CTR9 Counteracts EZH2 Activity in Breast Cancer Cells and Mesenchymal Stem/Stromal Cell Differentiation

By Ngai Ting Chan

A dissertation submitted in partial fulfillment of
the requirements for the degree of

Doctor of Philosophy
(Cancer Biology)

at the
UNIVERSITY of WISCONSIN-MADISON
2021

Date of final oral examination: August 18th, 2021

The dissertation is approved by the following members of the Final Oral Committee:

Wei Xu, Professor, Oncology
Paul G. Ahlquist, Professor, Oncology and Molecular Virology
Bill Sugden, Professor, Oncology
Shannon Kenney, Professor, Oncology and Medicine
Jacques Galipeau, Professor, Stem Cell & Regenerative Medicin

Table of Contents

Chapter 1: Introduction

Chapter 2: The transcriptional elongation factor CTR9 demarcates PRC2-mediated H3K27me3 domains by altering PRC2 subtype equilibrium

Chapter 3: CTR9 drives osteochondral lineage differentiation of human mesenchymal stem/stromal cells (MSCs) via counteracting EZH2 activity

Chapter 4: Conclusion, Discussion and Future Directions

CTR9 COUNTERACTS EZH2 ACTIVITY IN BREAST CANCER CELLS AND MESENCHYMAL STEM/STROMAL CELL DIFFERENTIATION

Ngai Ting Chan
Under the supervision of Professor Wei Xu
At the University of Wisconsin – Madison

Abstract

Dysregulation of transcription factors and epigenetic modifiers is increasingly recognized to play causal roles in carcinogenesis and developmental defects. We previously identified CTR9, a key scaffold subunit of human PAFc, as a master regulator of ER-mediated transcription in breast cancer cells. Moreover, CTR9 is required for ERα-positive breast cancer growth and tamoxifen sensitivity. In this study, I found that H3K27me3, a PRC2-mediated repressive marker, was significantly increased and expanded on chromatin upon loss of CTR9. Mechanistically, CTR9 depletion triggers a PRC2 subtype switch, from less active PRC2.2 to PRC2.1 with higher H3K27 methyltransferase activity. Consequently, CTR9 depleted cells become addicted to H3K27me3, and hypersensitive to PRC2 inhibitors. Our data uncover that CTR9 acquires novel chromatin regulatory functions by demarcating the PRC2-mediated H3K27me3 domains and affects cellular responses to PRC2 inhibition in breast cancer.

Because several studies have shown that PRC2-H3K27me3 contributes critical functions in skeletal development and osteoblast differentiation, I went on to investigate if CTR9 is involved in the lineage-specific differentiation of MSCs. Using loss- and gain-of-function approaches, I found that CTR9 regulates osteogenesis but not adipogenic differentiation. An *in vivo* ectopic osteogenesis assay confirmed the essentiality of CTR9 in hMSCs-derived bone formation. The lineage-specific differentiation regulated by CTR9 is not due to the alteration of the stem cell properties of hMSCs. Instead, CTR9 counteracts EZH2, a crucial histone methyltransferase, to modulate MSC lineage-specific differentiation. In accordance with the gain of H3K27me3 in CTR9 KD MSCs, either restoring CTR9 expression or treatment with an EZH2 inhibitor partially rescues the osteogenic defects caused by CTR9 deficiency, suggesting that regulation of osteogenic differentiation of hMSCs by CTR9 can be likely attributed to counteracting PRC2 activity and restraining H3K27me3 deposition.

Our studies uncover the conserved epigenetic mechanism of CTR9 via counteracting PRC2/EZH2 activity in regulating ER-dependent transcription and hMSC lineage determination. Tazemetostat has been FDA-approved for treating follicular lymphoma, this discovery has a significant translational impact because EZH2 inhibitors may be applicable for treating endocrine-resistant, ER+ breast cancer, and bone-related skeletal diseases.

Abbreviations

AM	Adipogenic induction medium
AP	Alkaline Phosphatase
ATAC-seq	Assay for Transposase-Accessible Chromatin using sequencing
ATCC	American type Culture Collection
BART	Binding Analysis for Regulation of Transcription
BCOR	BCL-6 corepressor
BMP2	Bone morphogenetic protein 2
BrCa	Breast Cancer
CCNE1	Cyclin E1
CDK1	Cyclin-dependent kinase 1
CECM	Cartilaginous extracellular matrix
CGI	CpG island
ChIP-Rx	Chromatin immunoprecipitation followed by high throughput sequencing with incorporation of a reference exogenous genome
CPF	Cleavage and polyadenylation machinery

crRNA	CRISPR RNA
Cryo-EM	Cryo-electron microscopy
CT	Computed tomography
CTD	C-terminal domain
CUT&RUN	Cleavage Under Targets and Release Using Nuclease
DMEM	Dulbecco’s modified medium
DMSO	Dimethyl sulfoxide
Dox	Doxycycline
EC*	Activated Pol II elongation complex
ECM	Extracellular calcium matrix
ELISA	Enzyme-linked immunosorbent assay
ER	Estrogen Receptor
ESC	Embryonic stem cell
EZH2	Enhancer of zeste 2
EZHIP	EZH Inhibitory Protein
FACS	Fluorescence activated cell sorting
FBS	Fetal bovine serum

FFF	Fused filament fabrication
FFPE	Formalin-Fixed Paraffin-Embedded
fl	Lox P (flox sites)
GGH	Gamma glutamyl hydrolase
gRNA	Guide RNA
GFP	Green fluorescent protein
GWAS	Genome-Wide Association Studies
H&E	Hematoxylin and eosin
H2AK119ub	Histone H2A lysine 119 ubiquitination
H2BK34ub1	Histone H2B lysine 34 mono-ubiquitination
H2BK120/K123ub	Histone H2B lysine 120/123 ubiquitination
H3K4me1/me2/me3	Histone H3 lysine 4 mono-/di-/tri-methylation
H3K9me2/me3	Histone H3 lysine 9 di-/tri-methylation
H3K27me1/me2/me3	Histone H3 lysine 27 mono-/di-/tri-methylation
H3K36me1/me2/me3	Histone H3 lysine 36 mono-/di-/tri-methylation
H3K79me2/me3	Histone H3 lysine 79 di-/tri-methylation
H4K12Ac	Histone H4 lysine 12 acetylation

H4K16Ac	Histone H4 lysine 16 acetylation
H4R3me2a	Histone H4 arginine 3 asymmetric di-methylation
HDAC	Histone deacetylase
HDM	Histone demethylase
HER2	Human epidermal growth factor receptor 2
HMT	Histone methyltransferase
IgG	Immunoglobulin G
IGV	Integrative genomics viewer
IHC	Immunohistochemistry
IMC	Imaging mass cytometry
IMPC	International Mouse Phenotyping Consortium
IP	Immunoprecipitation
ISCT	International Society for Cellular Therapy
KD	Knockdown
KO	Knockout
LC-MS/MS	Liquid chromatography tandem mass spectrometry
MACS	Model-based analysis of ChIP-seq

MAPQ	Mapping Quality Score
MEMα	Modified Eagle’s medium α
MLL	Mixed lineage leukemia
MPNST	Malignant peripheral nerve sheath tumors
MSC	Mesenchymal stem/stromal cell
MTT	3-(4, 5-dimethylthiazolyl-2)-2, 5-diphenyltetrazolium
NELF	Negative elongation factor
NIB	Nuclei Isolation Buffer
NSD3L	Nuclear receptor binding SET domain protein 3 like
OCN	Osteocalcin
OFCD	Oculo-facio-cardio-dental
OM	Osteogenic induction medium
OPN	Osteopontin
OSX	Osterix
PAFc	Polymerase associated factor complex
PARP	Poly-ADP ribose polymerase
PCL (Chapter 2)	Polycomb-like

PCL (Chapter 3)	Polycaprolactone
PEC	Paused Pol II elongation complex
P-TEFb	Positive transcription elongation factor-b
PR	Progesterone receptor
PRC1	Polycomb Repressive Complex 1
PRC2	Polycomb Repressive Complex 2
PTM	Post-transcriptional modification
P/S	Penicillin-Streptomycin
REST	RE1 silencing transcription factor
RNAPII	RNA Polymerase II
RNAPII Ser2P	Ser2 phosphorylation form of RNAPII
RNP	Ribonucleoprotein particle
RT-PCR	Real-time polymerase chain reaction
RUNX2	Run related transcription factor
SAH	S-adenosyl-l-homocysteine
SAH-EZH2	Stabilized α-helix of EZH2
SAM	S-adenosyl-l-methionine

scRNA-seq	single cell RNA-seq
shRNA	Small hairpin RNA
SNP	Single nucleotide polymorphism
SOX9	SRY-box transcription factor 9
T-ALL	T-cell acute lymphoblastic leukemia
tracrRNA	trans-activating CRISPR RNA
TES	Transcription end site
TF	Transcription factor
TGFβ	Transforming growth factor-β
TNBC	Triple-negative breast cancer
TPR	Tetratricopeptide repeats
TSS	Transcription start site
v-MYB	Avian myeloblastosis viral oncogene homolog
WNT	Wingless type
WT	Wild type
w/v	Weight per volume
YBX1	Y-box binding protein 1

Acknowledgments

I am so grateful that I was accepted into the Cancer Biology Program as a graduate student at the University of Wisconsin-Madison. Despite the hardships of graduate school, with continuous encouragement and support from many professors, peers, departmental staff, family members, and friends, my six years in graduate school have become the most memorable journey in my career.

I have many people to thank. First, I need to thank my advisor, Professor Wei Xu, for all her patience, guidance, and support. Wei has been an amazing teacher, mentor, and thesis supervisor, and kept me motivated throughout my studies. Her consistent approach to research and science is a source of inspiration. She has the characteristics of a true leader and set an excellent example of how to be a scientist. This thesis would not have been possible without her, and her guidance from day one has enabled me to develop my thesis project into what it is today. I am thankful for the extraordinary experiences and opportunities she provided for me to grow professionally and personally. She has witnessed me transform from a mediocre undergraduate to an accomplished PhD student. This thesis is not only a reflection of my efforts, but also hers.

The Xu lab has been a wonderful lab to work in, with so many nice colleagues who all contributed to creating an intellectually stimulating, productive, and enjoyable environment. I received many helpful comments and suggestions from all of my current and former lab mates, including Hao Zeng, Yidan Wang, Fabao Liu, Eui-Jun Kim, Ang Gao, Gui Ma, Kristine Donahue, and Megan Bacabac. They have played an integral role in the progression of my research. I would especially like to recognize the time and help I received from Dr. Hao Zeng and Kristine Donahue, who both spent a great deal of time proof-reading and editing my research proposals, manuscripts, as well as this thesis. Also, I would like to extend my thanks to Dr. Fabao Liu for generously sharing several critical plasmids, as well as his advice and insight on many experiments presented in this thesis. My appreciation also goes out to Dr. Gui Ma, who contributed to construction and validation of pivotal cell lines for my functional studies in this thesis. Without their collaboration, this thesis would not have been completed in a timely manner.

Professors Paul Ahlquist, Bill Sugden, Shannon Kenney, and Jacques Galipeau, who served as my thesis committee for the past six years, provided invaluable feedback on my analyses and how to frame my research. Their encouragement and assistance made me confident that this topic was worthy of my investigation, and that my investigation was a worthy pursuit. I especially would like to express my gratitude to Professor Jacques Galipeau for generously sharing his human primary mesenchymal stem cells, which were indispensable for my studies in Chapter 3.

I am also indebted to our collaborators for their tremendous support, which made my project more meaningful and impactful. I would especially like to acknowledge Dr. Junfeng Huang for performing mass spectrometry analysis of my samples, and Dr. Siddhant U. Jain, formally of Dr. Peter Lewis's lab, for kindly sharing *Drosophila* S2 cells and providing suggestions for optimizing my ChIP-Rx experiments. I would also like to thank Ming-Song Lee from Dr. Wan-Ju Li's lab for his help with my animal studies, and for skillfully preparing FFPE slides of 3D spheroids.

Lastly, I would like to give my deepest and heartfelt thanks to my family (Mom & Dad) for their unfailing support and love, day after day, year after year. Most importantly, I would like to express my greatest appreciation to my loving and patient girlfriend Xiaodan who, throughout this PhD, has seen the best and worst of me, and still loves me anyway. She is an expert at managing and organizing mega data and helped me tackle my bioinformatic analyses. The time and care she dedicated to housework made it possible for me to concentrate on my research. Her cheerful disposition is always the panacea for when I lose my confidence and feel uncertain about the future.

This thesis is dedicated to all who encouraged and helped me throughout graduate school.

Chapter 1

Introduction

1.1 Breast cancer molecular subtypes

Breast cancer is the most common cancer in American women. About 1 in 8 U.S. women (about 13%) will develop invasive breast cancer during their lifetime. As of January 2021, more than 3.8 million women have had a history of breast cancer in the U.S. (1). Because breast cancer is a highly heterogeneous diseases, there is no uniform treatment for all patients. The treatment has revolutionized in the last two decades since characterization of breast cancer has evolved from biochemical subtypes to molecular subtypes based on gene expression profiling.

In late 1980s, breast cancer was characterized depending on the expression of hormone receptors and HER2 in three major subtypes: estrogen receptor (ER)-positive, HER2-positive, and triple-negative which lacks the expression of ER, progesterone receptor (PR) and HER2. In 2000, Perou et. al. pioneered the molecular characterization of breast cancer into four main subtypes: ER + luminal-like, basal-like, HER2/ErbB2+ and normal breast-like groups (Figure 1-1) based on gene expression profiling of breast tumors (2). The biochemical and molecular characterizations of breast cancer largely align with each other. For example, the ER+ tumors express ER, progesterone receptor (PR), ER responsive genes and other genes that encode typical proteins of luminal epithelial cells, so they are termed the luminal group (3). In 2006, Hu et. al. evaluated additional intrinsic gene sets from three independent studies and further divided the luminal-like group into two main subclasses: luminal-A and luminal-B (4). Approximately 75% of breast cancers are luminal types, among which luminal A subtype displays low histological grade, low degree of nuclear pleomorphism, low mitotic activity and expresses high levels of ER as well as low levels of proliferation markers (5). Immunohistochemistry studies further characterized the luminal-A subtype as ER-positive and/or PR-positive tumors with negative HER2 and low Ki67 index. Patients with luminal-A breast cancer have a good prognosis and the relapse rate is significantly lower than the other subtypes. Hormone therapies including selective estrogen receptor modulator tamoxifen and aromatase inhibitors are mainstays for treatment of luminal A tumors in pre- and post-menopausal women, respectively (6,7).

In contrast, luminal-B tumors are more aggressive, have higher histological grade and proliferative profile, and patients have a worse prognosis (8,9). Increased expression of proliferation-related genes in luminal B tumors, such as avian myeloblastosis viral oncogene homolog (v-MYB), gamma glutamyl hydrolase (GGH) and cyclin E1 (CCNE1), are observed as compared with the luminal A subgroup (10). Several studies have suggested that luminal-B breast cancer is relatively less sensitive to endocrine therapies but more sensitive to neoadjuvant chemotherapy as compared with the luminal-A breast cancer (11-13).

The HER2-positive subtype accounts for 15-20% of breast cancer. These tumors are characterized by high expression of the HER2 gene and other genes associated with the HER2 pathway and/or the HER2 amplicon located in the 17q12 chromosome. HER2-positive breast cancers are aggressive clinically and morphologically, and these tumors are highly proliferative (14). Nearly half of HER2-positive breast cancers are positive for ER, but the ER levels are usually lower than those of luminal subtypes. The biochemical and molecular characterization of HER2-positive tumors do not match perfectly since only 70% of HER2 tumors by gene expression profiling have HER2 protein detected by immunohistochemistry (15). Prior to anti-HER2 therapies using monoclonal antibodies and tyrosine kinase inhibitors, HER2-positive patients had a poor prognosis and tumors tended to metastasize to the brain and visceral organs. Because HER2 positive tumors are resistant to anti-hormonal therapies, they are treated with cytotoxic agents such as doxorubicin, in combination with anti-HER2 therapies (16,17).

The basal-like subtype represents approximately 15% of all breast cancers (18). The majority of these tumors have high recurrence rate due to brain and lung metastasis (19). The basal-like subgroup expresses high levels of basal myoepithelial markers, such as CK5, CK14, CK17 and laminin, and do not express ER, PR and HER2, and hence are referred to as triple-negative breast cancer (TNBC). Basal-like cancers present with frequent mutations in the tumor suppressor protein TP53, guardian of genomic stability. Dysregulated integrin expression has also been detected and may contribute to aggressive cell behaviors and progression in this subtype (20). TNBC is usually treated with chemotherapies. In certain circumstances, such as the presence of BRCA mutants, basal-like cancers respond to poly-ADP ribose polymerase (PARP) enzyme inhibitors (21), because loss of DNA repair in BRCA1 mutant tumors renders synthetic lethality for PARP inhibitors (22).

Normal breast-like tumors constitute around 5%-10% of all breast tumors. They are poorly characterized and have been grouped based on similarity to the fibroadenomas and normal breast samples. This type of breast cancers expresses genes normally expressed in adipose tissues and have an intermediate prognosis between luminal and basal-like cancers. Although normal breast-like tumors also lack the expression of ER, PR and HER2, these tumors are not classified as basal-like or triple-negative because they also do not express CK5 and EGFR (23,24). There are few studies on this subtype and their clinical significance remains undetermined.

Although the molecular characterization has greatly improved personalized breast cancer therapy, the expression of receptors is often spatial and dynamic due to tumor heterogeneity. Hartland et. al. recently developed a novel strategy using multiplexed imaging mass cytometry (IMC) in 352 breast cancer patients to resolve the spatially inter- and intracellular heterogeneity of breast tumors in cell types, organization, architecture as well as microenvironment at single-cell resolution (Figure 1-2-A) (25). In combination with the clinical data, this technology was used simultaneously to quantify 35 biomarkers which subsequently build up a comprehensive single-cell pathology landscape of breast cancer (Figure 1-2-B). As a result, refined characterization of breast cancer histologically and molecularly at single-cell levels will provide more accurate guidance for cancer diagnosis, prognosis, and treatment options.

1.2 Epigenetic dysregulation in breast cancer

Epigenetic changes refer to heritable yet reversible changes in chromatin without changes at DNA sequence, such as histone or DNA modifications. Epigenetic dysregulation has been increasingly appreciated as the key event during breast cancer progression. During transformation of mammary epithelial cells, coordinated DNA methylation and histone modifications across large regions of the chromatin were observed (26,27), suggesting that epigenetic modifications may be exploited as diagnostic and prognostic markers or as a therapeutic vulnerability for breast cancer (Figure 1-3).

Epigenetic modifications are an integral part of chromatin remodeling. Many histone modifying enzymes are components of or interact with the chromatin remodeling complexes that are recruited onto the target genes on chromatin in breast cancer cells (28). These complexes could either repress or stimulate gene expression by forming distinct sub-complexes and integrating with histone post-transcriptional modifications (PTMs) in cancer cells (27,29). Dysregulation of the chromatin remodeling components could affect the expression of genes with diverse roles in tumor suppression, transformation, DNA repair, cell cycle, metabolism, and proliferation (30). In addition to epigenetic alterations on specific target genes, dysregulated histone modifications could have a global impact on chromatin structure, leading to disease progression. For instance, reduction in the levels of active transcription marks such as H4K16Ac or H4K12Ac is observed in the early stages of breast cancer (31). A reduction in the genome-wide levels of histones H3K9me2 and H3K9me3 and an increased H3K4me3 level have been observed during transformation of breast cancer cells (32).

Among multiple histone modifications, histone methylation is an abundant histone PTM and dynamically regulated by enzymes depositing modifications and removing modifications, so called ‘writers’ and ‘erasers. The regulation of histone methylation and its biological consequences are complex. Histone methylation can occur at various sites in histone proteins, primarily on lysine and arginine residues, and it can be governed by positive and negative regulators, even at a single site, to either activate or repress transcription, and thus confer divergent effects during cancer progression.

Studies have identified widespread changes in histone methylation in breast cancer cells as compared to the nontumorigenic counterparts. For instance, there is a global reduction in H4K20me3 in multiple cancer types including breast cancer (33). A global reduction in H4K20me3 was also observed in human breast cancer cell lines compared to the nontumorigenic cells (34). Further, in a rat model of breast cancer, a global decrease in H3K9me3 and H4K20me3 was observed, indicating that these epigenetic changes may play a causal role in tumorigenesis (35). In addition, low levels of histone methylation on H3K4me2, H4K20me3 and H4R3me2a in human tumors are correlated with poorer prognosis and more aggressive subtypes of breast cancer, such as luminal B and HER2-positive tumors (36). These global alterations in the histone methylation are suggestive of the aberrant expression of histone methyltransferases (HMTs) and/or demethylases (HDMs), which are extensively studied as therapeutic targets.

HMTs and HDMs are subjected to genetic or epigenomic alterations. More than 100 frequently hyper- or hypo-methylated gene promoters that clustered in different HMTs and HDMs are dysregulated which leads to aberrant expression of HMT and HDMs in breast tumors (37,38). For example, frequent overexpression and amplification of the histone methyltransferase NSD3L have been observed in mammary carcinomas. Depletion of NSD3L decreased the invasiveness of breast cancer cells, implying NSD3L is an oncogene (39). Enhancer of zeste 2 (EZH2), a H3K27 methyltransferase in the Polycomb Repressive Complex 2 (PRC2), is found overexpressed in breast cancer (40). The high expression of EZH2 is correlated with aggressiveness of cancer and poor prognosis (41). Upregulation of JARID1C, a histone demethylase, correlates with increased metastasis in breast cancer lesions (42). KDM3A, which demethylates H3K9 mono and di-methyl moieties, is an activator of ER (43). The catalytic activity of many HMTs is essential for ER transcriptional activity and growth of breast cancer cells, highlighting the significance of histone methylation in promoting breast tumorigenesis.

1.3 Human Polymerase Associated Factor Complex (hPAFc)

Multistep regulation of RNA Polymerase II (RNAPII) transcription by accessory proteins is important for maintaining the steady state level of transcription as well as regulating hormone-dependent gene expression. The Polymerase-Associated Factor Complex (PAFc) is a highly conserved complex regulating multiple steps of RNAPII-mediated transcription. PAFc is largely associated with transcription activation. Whether PAFc controls the switch from transcriptionally active to repressive chromatin states remains unknown.

1.3.1 Composition of PAFc

PAFc was originally identified as a Pol II-interacting complex in the budding yeast *Saccharomyces cerevisiae* (44). Biochemical and genetic studies reveal that yeast PAFc contains five subunits: PAF1, CTR9, CDC73, RTF1, and LEO1, and functions to promote RNAPII-mediated transcriptional elongation (45-47). Subsequent studies revealed high conservation of PAFc subunits across eukaryotes, including humans, with variation in the stability and composition of the complex. WDR61/SKI8 (48), a known component of the SKI complex responsible for RNA surveillance, has also been found in PAFc in human cells (49,50). RTF1, on the other hand, is loosely associated with PAFc in organisms other than *S. cerevisiae* (Figure 1-4). Although a short form of hRTF1 was reported to associate with the hPAFc at higher affinity than full-length hRTF1n and reconstitute a stable hRTF1-containing six-subunit hPAFc in insect cells (51), the presence of hRTF1 and its functions within hPAFc remain debatable.

Recent biochemical and structural analyses of hPAFc have revealed the architecture of PAFc and intracellular subunit interactions (52,53). The human PAF1 and CTR9 subunits appear to be the scaffold proteins, in agreement with the studies of yeast PAFc which shows that loss of either

PAF1 or CTR9 results in severe phenotypes (54). In addition, hCTR9 interacts with the mammalian specific PAFc subunit SKI8 (55). The scaffold functions of PAF1/CTR9 in human PAFc or yeast PAFc are reinforced by the structural studies which show that PAF1 and CTR9 form heterodimers and these core components are essential for PAFc assembly and PAFc-mediated histone modifications (54). These structural studies further suggest that the PAF1/CTR9 subcomplex-mediated holo-complex assembly might be conserved among eukaryotic species.

1.3.2 Functional studies of PAFc

Deletion of PAFc subunits in yeast leads to a variety of phenotypes revealing subunit specificity (56-58). These phenotypes include transcription deficiency and chromatin disturbance, leading to sensitivity to nucleotide biosynthesis inhibitors, the Suppressor of Ty (Spt-) phenotype and cryptic transcription initiation (59-61). Because of dysregulated gene expression, yeast cells lacking certain PAFc subunits exhibit defects in cell cycle and cell wall integrity (61,62). Consistent with the pleiotropic functions, deletion of PAF1 causes widespread changes in the coding and noncoding transcriptome (62-64).

Accumulated evidence supports that PAFc regulates multiple phases of transcription, including transcription initiation, elongation, termination, and RNA 3' end polyadenylation. PAFc facilitates transcription elongation through promoting release and phosphorylation of paused RNA Pol II at the promoter-proximal pause sites, as binding of PAFc to Pol II requires eviction of NELF and recruitment of P-TEFb to from the elongation complex (65-67). Furthermore, PAFc is engaged in transcription termination and RNA 3'-end formation, through promoting co-transcriptional histone modifications (68,69). PAFc stimulates monoubiquitylation (ub1) of H2B at K123 in yeast (and K120 in humans) through interaction with RAD6, which cooperates with Bre1 to catalyze H2BK123ub1 (70). This mark is a prerequisite for di- and tri-methylation (me2/3) of H3K79 and H3K4, by the HMT DOT1 and COMPASS, respectively (71,72). PAFc also interacts with the MSL1/2 complex to activate H2BK34ub1 (73). In addition to H2BK120ub1 and H2BK34ub1, H4K16 acetylation by MOF is regulated by PAFc. In the absence of PAFc, H4K16Ac level is reduced (74). The PAF1, CDC73 and CTR9 subunits of PAFc are indispensable for H3K36me3 establishment (75). Together, these observations significantly expand the known connections between PAFc and chromatin status. At least some effects of PAFc on histone modifications are conserved between yeast and humans, while others appear specific to higher eukaryotes.

Since multiple subunits in PAFc have physical interactions with subunits of the core RNAP II elongation machinery, the recruitment of PAFc to Pol II appear to species- and context-dependent. In yeast, PAFc is largely enriched on gene bodies, with significantly less occupancy near promoters or in the termination regions (63,70). In metazoans, PAFc can be recruited to promoters and enhancers by transcriptional activators. Upon transition to elongation, PAFc directly binds to RNAP II C-terminal domain and outer surface, and to the elongation factor Spt 4/5 (DSIF in humans) (76). carboxy-terminal domain (CTD) of Pol II is phosphorylated at serine 2 (Ser2) during elongation. As transcription ends, the new transcript is polyadenylated and cleaved at sites defined in part by PAFc, which interacts with the cleavage and polyadenylation machinery (CPF) (77). In summary, PAFc recruitment to promoters and enhancers may represent a general mechanism for regulation of specific genes in higher organisms. However, how many genes depend on PAFc for their expression remains to be determined and likely depends on cell type-specific transcription factors.

1.3.3 Structural analyses of human PAFc in RNA Polymerase II transcription elongation

Transcription of metazoan protein-coding genes is precisely regulated by RNAPII promoter-proximal pausing and release of paused Pol II during elongation (78,79). The RNAPII-DSIF (SPT4/5)-NELF-P-TEFb axis was previously regarded as major regulator for a smooth transition from pause to release of RNAPII. Recently, structural studies revealed an essential role of PAFc in regulating RNAPII pause and release (52).

The cryo-EM structural studies from the Cramer laboratory have shown that formation of an activated Pol II elongation complex (EC*) from a paused status (PEC) not only requires the phosphorylation of DSIF, NELF and the carboxy-terminal domain (CTD) of the large RNAPII subunit RPB1 by P-TEFb, but also needs the incorporation of PAFc and SPT6, where PAFc sterically displaces NELF from the RNAP II funnel and recruits SPT6 to the phosphorylated CTD, which opens the RNA clamp formed by DSIF during pause release (52) (Figure 1-5-A).

Notably, the PAFc scaffold protein CTR9 bridges the RBP subunits of RNAPII and other members of PAFc through its 19 tetratricopeptide repeats (TPR). The CTR9 TPRs form a right-handed superhelix that stretches from the RPB8/11 of RNAPII via the polymerase funnel helices. A pair of helices that create a ‘vertex’ is extended after the TPRs and connect to a prominent ‘trestle’ helix in CTR9 (CTR9 residues 807–892), which further extends to the RNAP II subunit RPB5, where downstream DNA enters the RNAPII cleft. The vertex and TPRs 13, 14 and 18 withstand the PAF subunit SKI8/WDR61, where CDC73 is anchored at CTR9 TPR 17 in a helix conformation (Figure 1-5-B/C).

Moreover, recent evidence suggests that RTF1, a labile human PAFc subunit, stimulates RNAPII elongation through a ‘latch’ structure by the association between Plus3-Fastener domain of RTF1 and PAF1-DSIF (80).

In summary, biochemical and structural studies of PAFc with RNAP II provide the molecular basis for understanding RNAP II pausing and release which is indispensable for productive elongation. It also sheds light into the aberrant transcriptional regulation by PAFc subunit mutations.

1.3.4 PAFc in human disease

Although PAFc is not essential for the viability of yeast, mutations or depletion of PAFc subunits in higher eukaryotes lead to severe developmental defects, loss of stem cell pluripotency, altered immune responses to viral infections, and changes in neuronal migration associated with intellectual disability (81-86). Moreover, numerous clinical manifestations have been attributed to the overexpression or mutations of PAFc subunit genes in humans. For example, overexpression of PAF1 has been associated with pancreatic and ovarian cancer. Depletion of CTR9 decreases proliferation of breast cancer cells and promotes leukemia via disrupting the interactions between PAFc and MLL (87,88). CDC73 is a well-known tumor suppressor also named parafibromin (86). Heritable and somatic mutations in CDC73 cause hyperparathyroidism jaw tumor syndrome and parathyroid carcinomas (89). Recently, CTR9 was also identified as a putative tumor suppressor gene, with mutations predisposing to Wilms' tumor (90,91). Additionally, it has been shown that PAFc is recruited to p53 target genes upon transcription stress and is required for p53's full activation (92). PAFc has also been found to promote tumorigenesis in several cancers (93,94). In non-small cell lung cancer, PAF1 protein levels correlate negatively with survival, and interestingly, depletion of both PAF1 and c-MYC synergistically inhibit cell proliferation. All these studies support that PAFc mis-regulation can cause tumor progression.

1.4 Polycomb Repressive Complex 2 (PRC2)

The Polycomb Repressive Complex 2 (PRC2) is the sole mammalian multi-subunit complex responsible for trimethylation of histone H3 at lysine 27, that is essential for maintaining cell identity and development of multicellular organisms. Therefore, comprehensive elucidation of the molecular mechanisms governing PRC2 functions is crucial for a better understanding of its role in normal biology and human disease and guiding the novel therapeutic strategies targeting this complex.

1.4.1 Composition of PRC2

Mammalian PRC2 consists of three core subunits: SUZ12, EED and either EZH1 or EZH2 histone methyltransferase (HMT) (95,96). These core PRC2 proteins associate in a 1:1:1 stoichiometry and catalyze all mono-, di- and tri-methylation of histone H3 lysine 27 (H3K27) through the SET domain of the EZH1/2 subunit (97,98). Although the SET domain of EZH1/2 constitutes the catalytic center of PRC2, the SET domain is autoinhibited on its own (97). The catalytic activity and the *in vivo* stability of EZH1/2 require the association of EZH1/2 with other core PRC2 subunits. It is worth noting that H3K27me3, the catalytic product, interacts with the aromatic cage formed by the WD-40 repeats of EED (99,100), forming an auto-regulatory loop to stimulate PRC2 catalytic activity to methylate new substrates. The trimeric core of PRC2, as well as the subunit RbAp46 or its paralog, RbAp48 (101), is essential for the methyltransferase activity of PRC2. The PRC2 core complex forms distinct subcomplexes by incorporating different auxiliary interaction partners, which have putative roles in PRC2 recruitment or regulation of PRC2 activity. Proteomic studies have identified a set of non-core subunits with sub-stoichiometric association with core members. The mutually exclusive auxiliary subunits segregate PRC2 into two distinct subtypes: PRC2.1 includes EPOP (102,103) or PALI (104,105) paired with a PCL paralog (PCL1/PHF1, PCL2/MTF2, or PCL3/PHF19), and PRC2.2 includes JARID2 and AEBP2 (103) (Figure 1-6). Although these factors were initially identified and studied individually, it is becoming clear that PRC2.1 and PRC2.2 complexes are precisely regulated, and their balance regulates the overall PRC2 activity and H3K27me3 levels and distributions among genomic sites.

1.4.2 Regulation of PRC2 subtypes

Although the PRC2 core subunits are identical in PRC2.1 and PRC2.2, facultative subunits are mutually exclusive for individual complexes. The exact interplay between the two subcomplexes and their roles in distinct biological contexts have been intensively studied recently. Current studies show that PRC2.1 and PRC2.2 employ different mechanisms for target gene recruitment and have different roles in gene silencing. Perturbations of cellular state (e.g., differentiation of embryonic stem cells) can trigger both architectural and functional changes in the PRC2 subcomplexes.

Biochemical and genomic studies have begun to elucidate the contribution of the PRC2 facultative subunits to PRC2 activity and occupancy at genomic sites and the mechanisms regulating equilibrium of PRC2.1 and PRC2.2 subtypes (106). All PCL proteins harbor conserved Tudor domain and two PHD fingers, which stimulate the activity of PRC2.1. However, even the three PCL paralogs differentially regulate PRC2.1. PHF1/PCL1 associates with H3K36me3 and recruits PRC2.1 to genomic regions containing high H3K36me3 levels during embryonic stem cell (ESC) differentiation (107,108). In addition, PHF1/PCL1 can directly bind DNA, thereby increasing the residence time of PRC2 on the chromatin and stimulating H3K27me3 deposition (109). MTF2/PCL2, on the other hand, mediates the *de novo* recruitment of PRC2 by binding to the unmethylated CpG islands (CGI), which serve as nucleation sites to propagate H3K27me3 marks (110-112). This finding is supported by a structural study revealing an intrinsic PRC2 dimer scaffold by MTF2 protein which enhance PRC2-MTF2 binding to an endogenous CpG islands (CGIs) enriched DNA (113). Similar to PHF1/PCL1, PHF19/PCL3 associates with H3K36me3 and recruits NO66, which demethylates H3K36me3 and allows H3K27me3 deposition and further PRC2 recruitment (114,115). Unlike other PRC2.1 components, little is known about the structure and domain functions of EPOP, although EPOP is general thought to be a scaffolding protein to bridge PRC2.1 and EloB/C (102,116), which positively regulates RNA polymerase II elongation (117). The interaction between PRC2.1 and EloB/C may restrain the occupancy and activity of PRC2, thereby maintaining PRC2 target genes at basal levels of transcription and preserving transcription plasticity (102,118). In summary, PRC2 auxiliary proteins such as PCL and EPOP are important for the precise regulation of the recruitment and activity of PRC2.1 at target genes. PRC2.2 complexes contain the facultative subunits JARID2 and AEBP2. In contrast to PRC2.1, the stoichiometry of these PRC2.2-specific constituents in PRC2 is roughly equal, and their relative association with core PRC2 during essential cellular processes remains stable (98,119). These findings suggest that PRC2.2 complexes may be more uniform than PRC2.1. Either JARID2 or AEBP2 could individually or synergistically enhance the catalytic activity of EZH2 *in vitro*. For example, JARID2 stimulates the catalytic activity of PRC2 by increasing the recruitment of PRC2.2 through binding of H2AK119ub or the high affinity of AT-rich DNA motif (120,121). In a separate study, methylation of JARID2 at K116 by EZH2 is shown to facilitate docking of the WD40 domain of EED, which in turn stimulates EZH2's catalytic activity (122). Stimulation of EZH2's catalytic activity by AEBP2 is less understood. However, AEBP2 has been suggested to stabilize EZH2 through its three C2H2-type zinc fingers, which mimic the unmodified H3 tails (123). Moreover, AEBP2 stimulates PRC2's binding to nucleosomes, thereby enhancing H3K27me3 deposition by EZH2 (124).

It is worthy to note that our knowledge on facultative PRC2 subunits is largely derived from studies using mouse embryonic stem cells (ESCs), HEK293 cells, and HeLa cells. Therefore, additional, tissue-specific subunits may exist and regulate PRC2 recruitment and activity in a cell-type and tissue-specific manner.

1.4.3 Other mechanisms of PRC2 regulation

Emerging structural and functional studies of PRC2 reveal that, other than PRC2 subtype auxiliary factors, additional factors might modulate PRC2 residence time on chromatin or directly affect the catalytic activity of PRC2, thus affecting the genome-wide distribution of H3K27 methylation patterns and gene expression. The reciprocal recruitment of PRC1 and PRC2 constitutes one mechanism for establishing a H3K27me3 pattern, where the CBX subunit of the canonical PRC1 binds to histone H3K27me3 with high affinity, leading to subsequent PRC2-mediated deposition of H3K27me3. The reciprocal recruitment of PRC1 and PRC2 promotes propagation of H3K27me3 and establishes more stable transcriptional repression (125,126). Another study shows that H2AK119ub could serve as an efficient recruiter of the PRC2.2 complex containing AEBP2 and JARID2 (127). Interestingly, this mark appears to be generated largely by a non-canonical PRC1 complex containing RYBP, a subunit that is mutually exclusive with CBX (128,129). Moreover, the N-terminus of JARID2 harbors a ubiquitin-interacting motif, which recognizes H2AK119ub and recruits PRC2 (120).

Chromatin components including modified histones, RNA and DNA have also been reported to function as allosteric regulators of PRC2. The transcription coupled H3K4me3, and H3K36me2/3 marks inhibit the catalytic activity of PRC2 toward H3K27 on the same histone H3 polypeptide, restricting H3K27me3 deposition and propagation (130,131). The non-specific binding of RNA transcripts to PRC2 inhibits its chromatin association, thereby preventing it from being recruited to transcriptionally active loci (132,133). Moreover, the length of linker DNA between the adjacent nucleosomes affects binding of PRC2 to nucleosomes (124,134). More recent studies show that histone mutations and histone peptide mimetics could also regulate PRC2 activities. Onco-histone H3K27M mutation is inhibitory for PRC2 activity. EZHIP, a protein harboring a histone H3 peptide mimetic sequence, is also a negative regulator of PRC2 activity (135-139). These studies demonstrate that chromatin components play important regulatory functions for the PRC2 complex, especially in disease states.

Finally, the post-translational modification (PTM) of PRC2 subunits could also affect the stability and activity of the complex. For instance, methylation of EZH2 at K510/514/515 increases the accessibility of PRC2 to histone H3K27 substrate (135,140), whereas ubiquitination of EZH2 at K421 promotes EZH2 degradation and subsequent PRC2 disassociation (141). Phosphorylation of SUZ12 at S539/541/546 has been shown to disrupt the integrity of PRC2, leading to ubiquitin-mediated degradation of some PRC2 components (142).

In summary, the identification of PRC2.1 and PRC2.2, together with recent structural and functional studies, have uncovered the complexity of PRC2 regulation and the mechanisms that control its recruitment to the specific genomic regions. Negative regulators of PRC2 include newly synthesized RNA transcripts, transcriptional active histone modifications, histone mutations and mimetics, and some PTMs of PRC2 subunits. Conversely, other factors that colocalize with PRC2 at CGIs, such as PRC2 auxiliary factors and H2AK119ub1, are positive regulators of PRC2 activity and maintain chromatin in repressive states.

1.4.4 PRC2 in cancer

Cancer genome and epigenome profiling studies have revealed that PRC2 complex and H3K27 methylations are frequently dysregulated (143,144). EZH2 is overexpressed in multiple cancer types as it is an E2F-regulated gene (145). However, its elevated expression is generally not considered to lead to deregulation of H3K27 methylation because the stoichiometry of the PRC2 complex is strictly regulated. This phenotype is in contrast with the recurrent 'change-of-function' mutations in EZH2. The first EZH2 mutation was identified in B-cell lymphomas, conferring an enhanced ability to convert H3K27me2 to H3K27me3 (146,147). The consequence of the heterozygous mutations is to increase levels of H3K27me3 and to decrease H3K27me2. Like EZH2 amplifications, hyperactivating EZH2 mutants have been shown to be an early event through tracing of tumor clonality (148). These data collectively suggest that increased PRC2 activity is a cancer driving event. The discovery of deletion and inactivating mutations on *EZH2*, *EED* and *SUZ12* in T-cell leukemias (T-ALL) (149-152) and malignant peripheral nerve sheath tumors (MPNST) (153) was initially surprising, because PRC2 function was considered oncogenic. These 'loss-of-function' mutations result in reduced levels of both H3K27me2 and H3K27me3. Another example of apparent loss of PRC2 function in cancer was the discovery of pediatric gliomas with H3K27M mutations in two genes encoding histone H3, *H3F3A* (H3.3) or *HIST3H1B* (H3.1) (154-156) Many single cell DNA sequencing studies confirmed that genes encoding the PRC2 members are frequently mutated in many different cancers. Surprisingly, both loss- and gain-of-function mutations have been identified, indicating that PRC2 acts as a tumor suppressor in some cancers and an oncogene in others.

1.4.5 Targeting PRC2 using pharmacological inhibitors

Given the oncogenic activity, mutations, and overexpression of EZH2 in various cancers, EZH2 has become an attractive therapeutic target for cancer treatment. Three classes of PRC2 inhibitors have been developed in recent years. The first class represents non-EZH2-specific inhibitors (e.g., DZNep) which interferes with S-adenosyl-l-homocysteine (SAH) hydrolase to elevate cellular SAH levels. SAH, in turn, inhibits EZH2 via a product inhibition mechanism (157). DZNep, therefore, is not selective for EZH2, but rather a general histone methylation inhibitor. The second class constitutes direct small molecule inhibitors, including GSK126, EPZ6438 and UNC1999, which are S-adenosylmethionine (SAM)-competitive PRC2 inhibitors, thus are potent and selective (158-160). The last class is the peptide-like inhibitors. The first-generation agent by Kim et al. is a stabilized α-helix of EZH2 (SAH-EZH2) peptide, based on the EED-EZH2 complex structure. This peptide disrupts the EZH2–EED complex, reduces EZH2 protein levels and selectively inhibits H3K27me3 in a dose-dependent manner (161). With emergence of a PRC2 structure and the allosteric activation mechanism of EZH2 by EED, EED226, a potent and selective PRC2 inhibitor that directly binds to the H3K27me3 binding pocket of EED, became available. EED226 induces a conformational change upon binding to EED, leading to inhibition of PRC2 activity. ED226 has equivalent activity to the SAM-competitive inhibitors to block H3K27 methylation of PRC2 target genes, and to induce the regression of human lymphoma xenograft tumors *in vivo* (162).

The development of potent PRC2 inhibitors provides opportunities for mono- or combinatory therapy with other approved anti-cancer drugs for cancer treatment. Early clinical trial data show that the combination of a PRC2 inhibitor with other anti-cancer drugs improves efficacy of response, and sometimes overcome treatment resistance, indicating that PRC2/EZH2 inhibition elicits strong synergism with other drugs in cancer treatment. Fillmore et. al. reported that EZH2 inhibition by DZNep or GSK126 sensitizes *BRG1* and *EGFR* mutant-expressing lung tumors to topoisomerase II inhibitors (163). Moreover, EZH2 inhibition by GSK126 is synthetic lethal in ARID1A-mutated ovarian cancer cells, and that ARID1A mutational status correlates with the response to EZH2 inhibitor (164).

1.5 Mesenchymal stem cells (MSCs)

1.5.1 Overview (Isolation, Characterization and Clinical Applications)

Mesenchymal stem/stromal cells (MSCs) are fibroblastic, multipotent adult stem cells that possess a high self-renewal and differentiation capacities. These cells can be isolated from several human tissues, including bone marrow, adipose tissue, umbilical cord matrix, tendon, lung etc. (165). Recent studies on MSC origin point to the perivascular niche that coordinates the vasculature in human body (166). The perivascular cells do not express endothelial and hematopoietic markers, e.g., CD31, CD34 and CD45, however, they express CD146, PDGFR beta, and alkaline phosphatase (167). The definition of MSCs has been controversial. According to the International Society for Cellular Therapy (ISCT), MSCs express the surface markers CD73, CD90 and CD105 and lack expression of CD14 or CD11b, CD34, CD45, CD79α or CD19, and HLADR (168) . In addition to cell surface markers, the widely accepted means to characterize MSCs is by their multipotency. MSCs can differentiate into mesodermal cell types, such as adipocytes, osteoblasts, and chondrocytes *in vivo* and *in vitro* under appropriate stimulatory cues. Trans-differentiation of MSCs into cells of non-mesenchymal origin, such as hepatocytes, neurons, and cardiomyocytes, has also been observed *in vitro* under specific stimuli (169-171) (Figure 1-8).

Because of the plasticity of MSCs, they are widely explored for tissue regeneration and tissue repair. In fact, MSCs are the most popularly used stem cells in clinical applications. In addition to the advantage of obtaining MSCs from different sources and the multi-lineage differentiation potential of MSCs, the migratory ability of MSCs to injured sites in response to the environmental stimuli make them suitable for tissue regeneration (172-175). Among other pleiotropic activities, MSCs can inhibit the immune system, promote cell survival, and induce angiogenesis via interacting with the host niche. Furthermore, MSCs can be obtained less-invasively (e.g., peripheral blood, adipose tissue) from a patient and rapidly expanded for clinical use in an autologous manner (176-180). The feasibility of obtaining MSCs from adult tissues circumvents the ethical issues of using embryonic tissues. These advantages make MSCs important tools in the regenerative medicine and potentially in oncology. Based on the clinicalTrials.gov, up to 25 clinical trials pertinent to the oncology using MSCs have been registered, among which 14 trials explore MSCs as therapeutic agents. The majority of phase 1 and 2 clinical trials involving MSCs are designed to evaluate the safety and efficacy of MSCs in cancer patients (181,182).

1.5.2 Transcriptional regulation of lineage specification of MSCs

MSC lineage specification is controlled by designated transcription factors (TFs) that either activate or silence lineage specific signaling pathways (Figure 1-9). A range of TFs are involved in the regulation of osteogenesis, among these RUNX2 and Osterix, are best studied (183,184). RUNX2 is a member of the Runt-domain gene family which is expressed in mesenchymal cells early in skeletal development and throughout osteoblast differentiation. Molecular and genetic studies demonstrate its necessity in osteoblast differentiation of mesenchymal cells (185-188). RUNX2 is an important TF in osteogenesis that regulates the transcription of osteoblast specific genes, such as osteocalcin and collagen 1A (189,190). RUNX2-null mice showed a complete absence of ossification, due to the maturational arrest of osteoblasts (191-193). Osterix (OSX) is another important TF involved in osteoblast commitment. OSX-deficient mice lack osteoblasts and exhibit defective bone formation (194,195).

Peroxisome proliferator activated receptor-γ (PPAR γ) is a master transcription factor essential for adipogenesis. PPARγ is expressed very early during the differentiation of adipocytes. PPAR γ binds to the 5′-flanking region of the adipocyte P2 gene, leptin regulatory element 1, upstream of LDL receptor gene leptin, as well as to the distal promoter of adipokine SFPR5 gene which induces adipocyte specific gene expression (196-198). Overexpression of PPARγ induces adipogenesis in cultured fibroblasts. Conversely, deletion of PPARγ in fibroblasts results in reduced adipogenesis, even with the addition of C/EBPα, another adipogenesis regulator (199,200).

Different TFs regulate chondrogenesis from those regulating adipogenesis and osteogenesis. SOX9 is a master regulator of chondrogenesis. SOX9 contains an HMG-type DNA binding domain and is expressed throughout chondrogenic differentiation (201,202). Deletion of *SOX9* in the mesenchymal cells of limb buds lead to the complete absence of chondrogenic mesenchymal condensations in the developing limbs, while deletion of the *SOX9* in mesenchymal condensations lead to the arrest of chondrogenesis at this stage (203,204), demonstrating the necessity of SOX9 at different stages of chondrogenesis (i.e., in both mesenchymal condensation and for chondrogenic progression).

1.5.3 Epigenetic regulation of lineage specification of MSCs

Lineage-specific cellular differentiation requires not only lineage specific TFs but also epigenetic modulators. The interplay between lineage-specific TFs and epigenetic modulators is important in lineage specification of MSCs (Figure 1-9). Histone methylation is one of the epigenetic mechanisms underlying MSC osteogenic differentiation. For instance, Hassan et al. showed that HOXA10 (a gene necessary for embryonic patterning of skeletal elements) contributes to osteogenic lineage determination through activation of RUNX2, alkaline phosphatase, osteocalcin, and bone sialoprotein (205). They further showed that these effects depend on histone hyperacetylation and H3K4 hypermethylation on the genes (206). In accordance with this finding, Fan et. al. reported that the activation of transcription of osteo-dentinogenic gene in MSCs derived from a patient with oculo-facio-cardio-dental (OFCD) syndrome, which is caused by BCL-6 corepressor (BCOR) mutation that leads to increased histone H3K4 and H3K36 methylation in MSCs (207,208).

In addition to histone methylation, epigenetic enzymes and non-coding RNAs have also been shown to regulate MSC bone differentiation. EZH2 and KDM6A serve as ‘writer’ and ‘eraser’ of

H3K27me3, respectively. Overexpression of EZH2 in MSCs is inhibitory for bone differentiation, on the contrary, KDM6A promotes MSC bone differentiation (209,210) . Wei et. al. shows that the activation of cyclin-dependent kinase 1 (CDK1) promotes MSC bone differentiation through phosphorylation of EZH2, which inactivates EZH2 catalytic activity (211). EZH2 mediated H3K27me3 is required for repression of Osteopontin (OPN), whose level is induced during osteogenesis in bone marrow derived MSCs (212). Several long non-coding RNA (i.e., ANCR, HoxA-AS3) are also direct targets of EZH2-H3K27me3 during lineage commitment of MSCs (213,214).

In summary, MSC-based therapies hold great potential for tissue regeneration and cancer therapy, in particular for repairing the bone and cartilage defects. While it is still under debate whether MSCs should be transplanted at the pre- or post-differentiation stage, transplantation of MSCs at the differentiated state is thought to be advantageous over transplantation at the undifferentiated state, because precise control of MSCs to specific lineages *in vivo* remains challenging. Further mechanistic understanding of MSC osteogenic and chondrogenic differentiation are of utmost importance. We have learned that both lineage-specific TFs and epigenetic modulators are important for lineage specification of MSCs. However, lineage-specific TFs are typically hard to target, whereas great advances have been made in pharmacological modulation of epigenetic enzymes. Understanding transcriptional and epigenetic mechanisms underlying MSC differentiation will allow us to better control MSC differentiation to specific lineages in a temporally and spatial manner and provide precision medicine for those diseases previously defined as incurable.

1.6 Synopsis of research

The aim of this thesis is to define the functions of CTR9, the scaffold protein of PAFc, in both physiological (MSC differentiation) and pathological processes (breast cancer), given that both are controlled by integrated transcriptional and epigenetic mechanisms. Chapter 2 reveals the unknown role of CTR9 in restraining repressive histone markers. Using inducible and stable CTR9 knockdown breast cancer cell lines, we identified a striking increase in the H3K27me3 level upon loss of CTR9. Moreover, loss of CTR9 leads to genome-wide expansion of H3K27me3, as well as increased recruitment of PRC2 on chromatin. Mechanistically, CTR9 depletion triggers a PRC2 subtype switch from less active PRC2.2 to PRC2.1 with higher methyltransferase activity. Consequently, CTR9 depletion generates vulnerability that renders breast cancer cells hypersensitive to PRC2 inhibitors. Our findings that CTR9 demarcates PRC2-mediated H3K27me3 levels and genomic distribution through regulating equilibrium of PRC2 subtypes identifies a novel role of CTR9 in counteracting PRC2 activity, beyond its established role in transcriptional initiation and elongation.

Because the PRC2-H3K27me3 axis has been shown to be essential for MSC lineage differentiation and a CTR9 SNP is linked to osteoporosis in a Kashin-Beck disease patient in a Genome-Wide Association Studies (GWAS) (215), we next investigated whether CTR9 plays a role in regulating lineage specification of MSCs in Chapter 3. Using loss-of-function and gain-of-function approaches, CTR9 was found to selectively regulate human MSC (hMSC) differentiation to osteoblasts, chondrocytes, but not to adipocytes. *In vivo* ectopic osteogenesis assay confirms the essentiality of CTR9 expression for hMSC-derived bone formation. The lineage-specific role of CTR9 is not due to modulation of MSC stem properties. Rather, CTR9 counteracts EZH2 activity and reduces level of H3K27me3, the essential histone marker determining MSC lineage-specific differentiation. In accordance with the gain of H3K27me3 in CTR9 KD MSCs, the osteogenic differentiation defects of CTR9 KD MSCs can be partially rescued by treatment with

EZH2 inhibitors, supporting a CTR9-driven epigenetic mechanism in regulating MSC lineage differentiation.

Altogether, the research described in this thesis uncovers a unique, and conserved mechanism of CTR9 in controlling a transition from transcriptionally active to repressive chromatin states by counteracting PRC2 activity and sheds light on the biological functions of CTR9 in development, differentiation, and cancer. The acquired sensitivity to EZH2 inhibitors in CTR9 ^{low} or loss-of-function cells provides a therapeutic vulnerability for treating CTR9-associated human diseases (e.g., Wilms tumors).

1.7 Figure & Legends

Figure 1-1. Molecular subtypes of human breast cancer

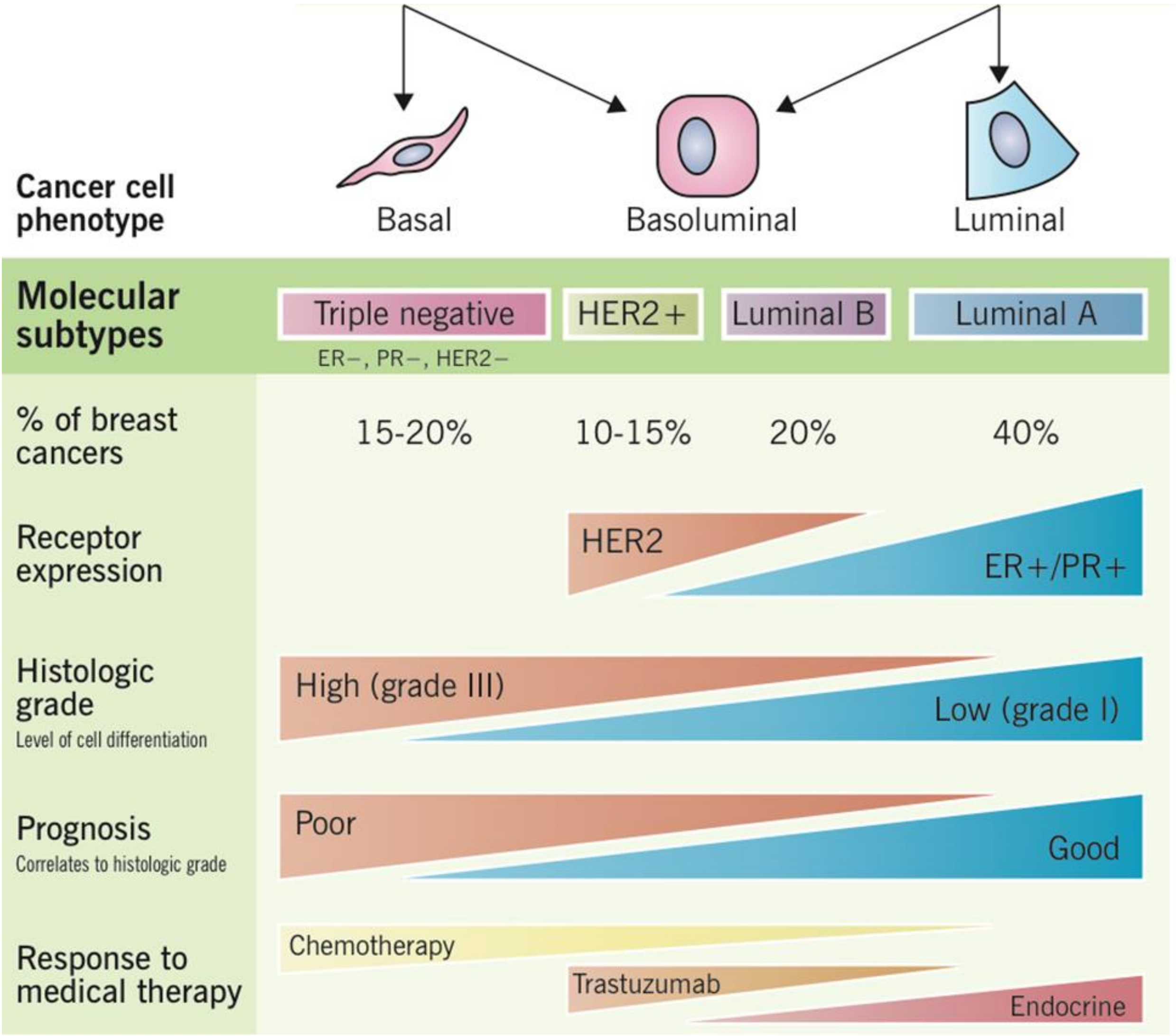

Figure 1-1. Summary of human breast cancer subtypes stratified by expression of ER, PR and HER2. The corresponding proportion, histologic grade, prognosis, and response to medical therapy were also shown in each individual subtype.

This figure was adopted from http://www.pathophys.org/breast-cancer/breastcancer-copy/.

Figure 1-2. Single-cell phenotypes in high-dimensional histopathology of breast cancer

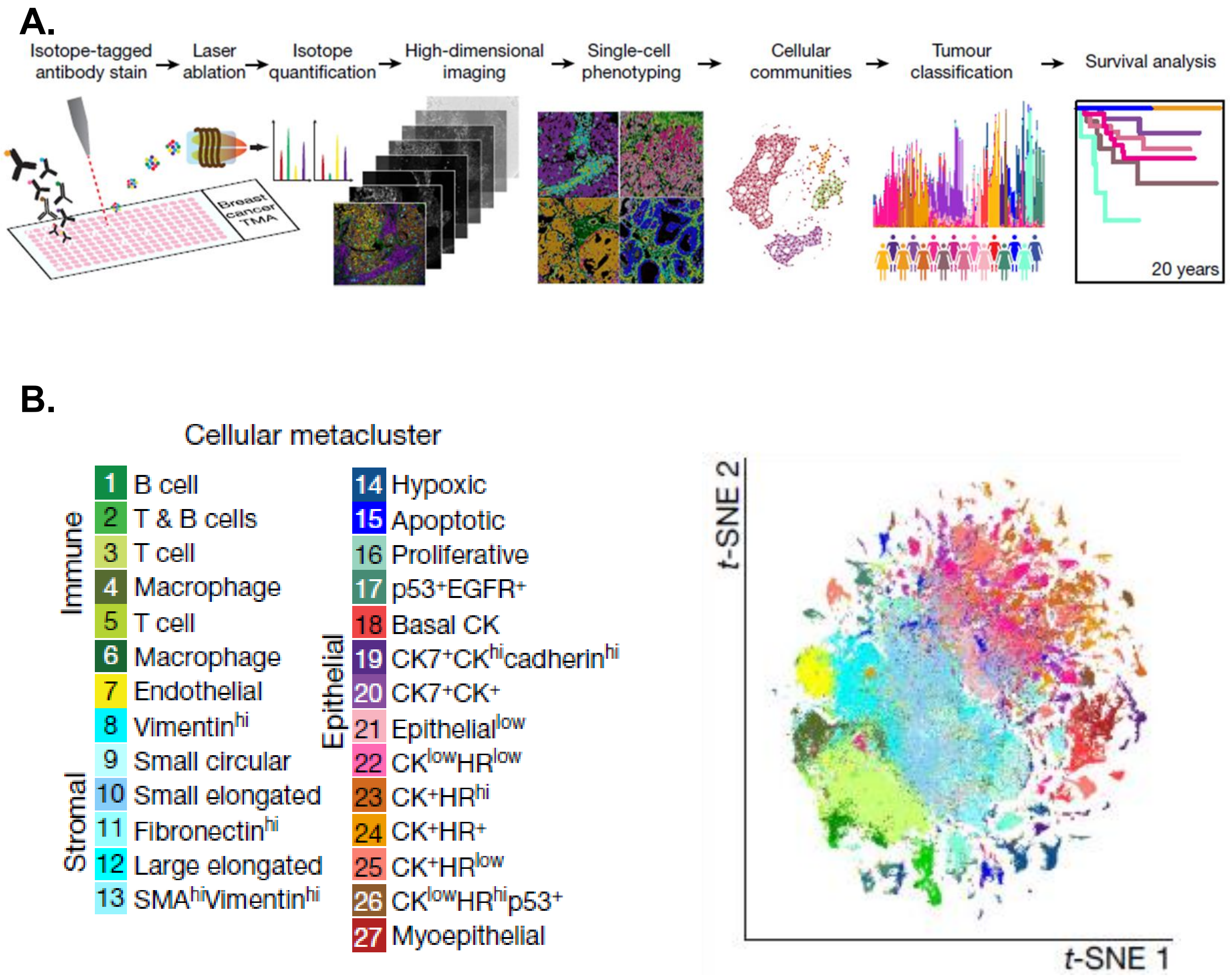

Figure 1-2.

A. Diagram shows the acquisition of single-cell images by imaging mass cytometry (IMC) from 281 breast cancer patients and its characterization of single-cell genomes, meta-clusters, stromal-cell architecture, and organization, subclassification of patients, and patient outcomes.

B. Map of 171,288 single cells color-coded in accordance with cell-type meta cluster identifier from high-dimensional images of breast tumors using t-distributed stochastic neighbor embedding (t-SNE).

This figure was adopted from (25).

Figure 1-3. Epigenetic dysregulations in cancer

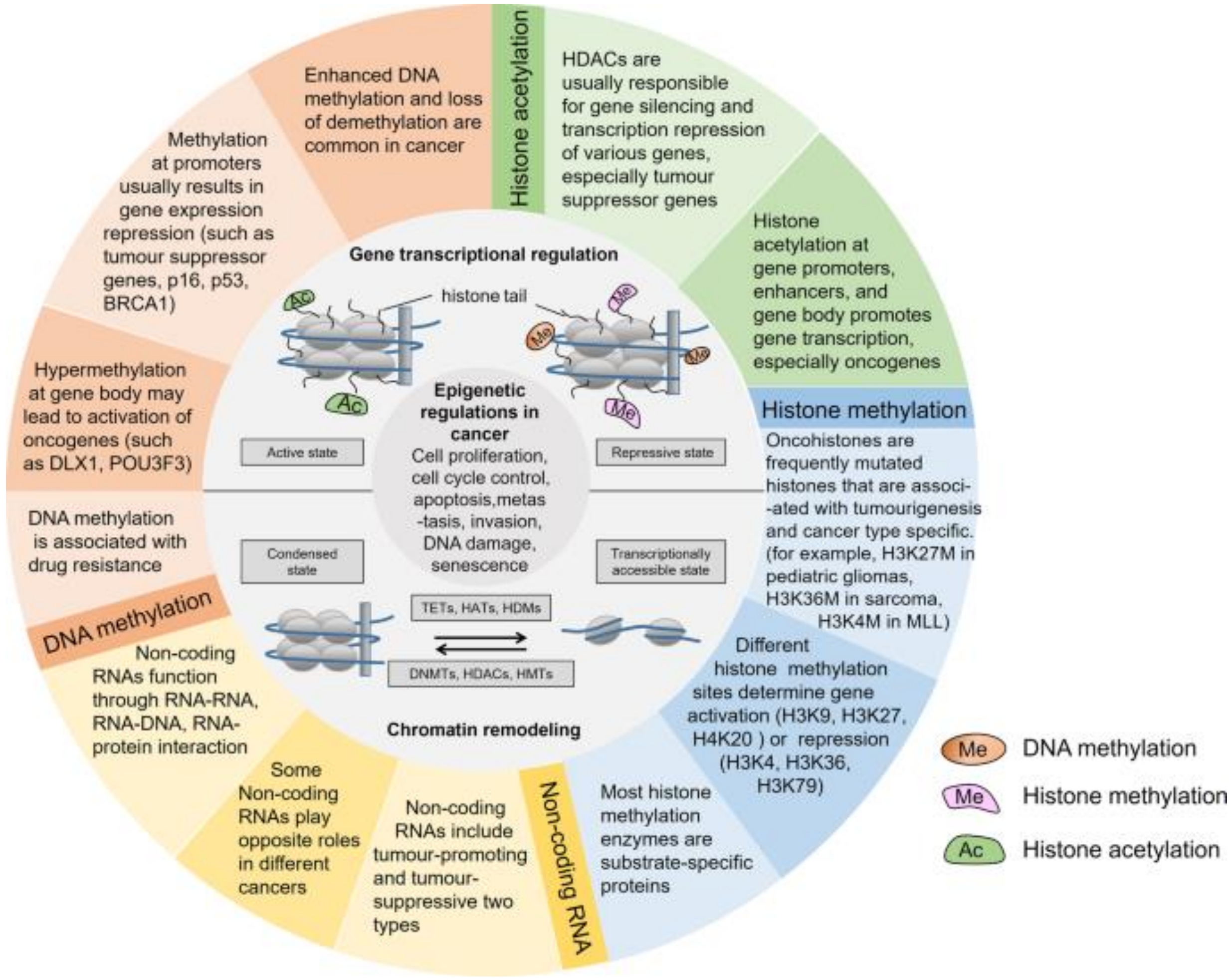

Figure 1-3. Breast cancer epigenetic changes affect a variety of cellular responses, including proliferation, apoptosis, invasion, and senescence. Among the epigenetic mechanisms contributing to tumorigenesis are DNA methylation, histone modification, chromatin remodeling, and noncoding RNA regulation. A major feature of epigenetics is the ability of epigenetic enzymes and proteins to silence and activate genes in a reversible manner.

This figure was adopted from (216).

Figure 1-4. Characterization of Native human PAFCs

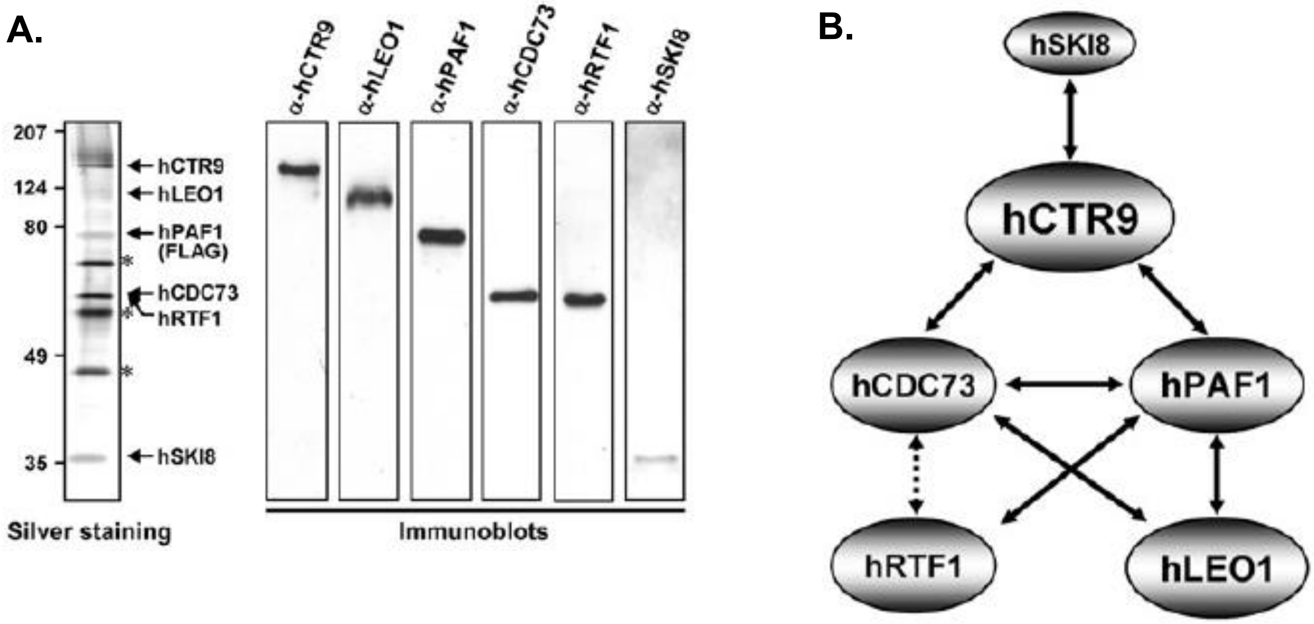

Figure 1-4.

A. Images showing silver staining and immunoblot analysis of native human PAFc purified from FLAG-hPAF1 HeLa cells.

B. The PAFc subunits interact with each other in a multivalent fashion. Direct interactions are indicated by arrows, while weak interactions are indicated by the dashed arrows.

This figure was adopted from (217).

Figure 1-5. Cryo-EM structure of EC* with PAFc.

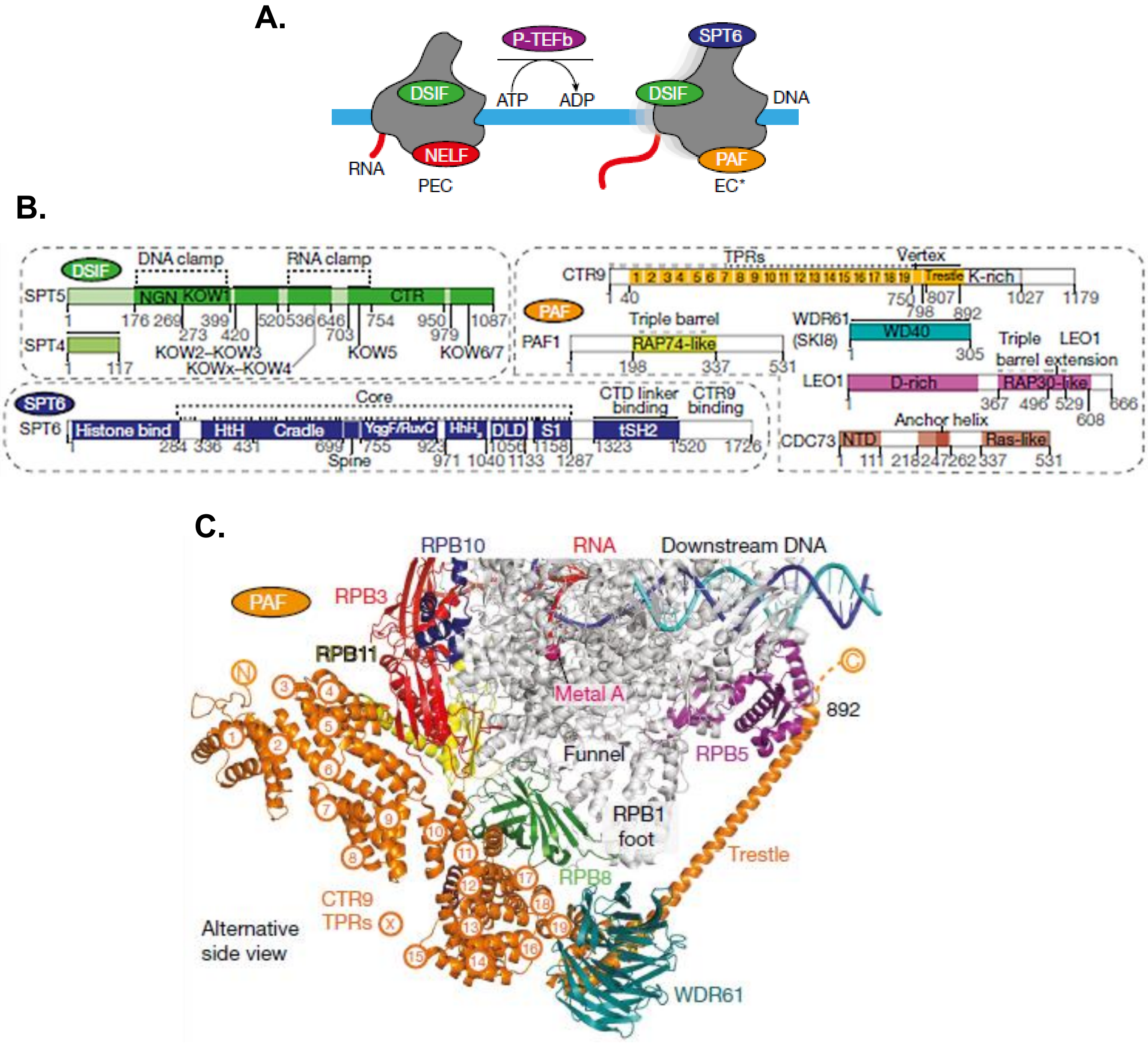

Figure 1-5.

A. Diagram showing the transition from paused Pol II–DSIF–NELF elongation complex (PEC) to activated Pol II–DSIF–PAFc–SPT6 elongation complex (EC*).

B. Diagrams illustrating the architectures of DSIF, PAF, and SPT6 with corresponding color codes.

C. Details of the cryo-EM structure of EC*.

This figure was adopted from (52).

Figure 1-6. Composition of two PRC2 subtypes

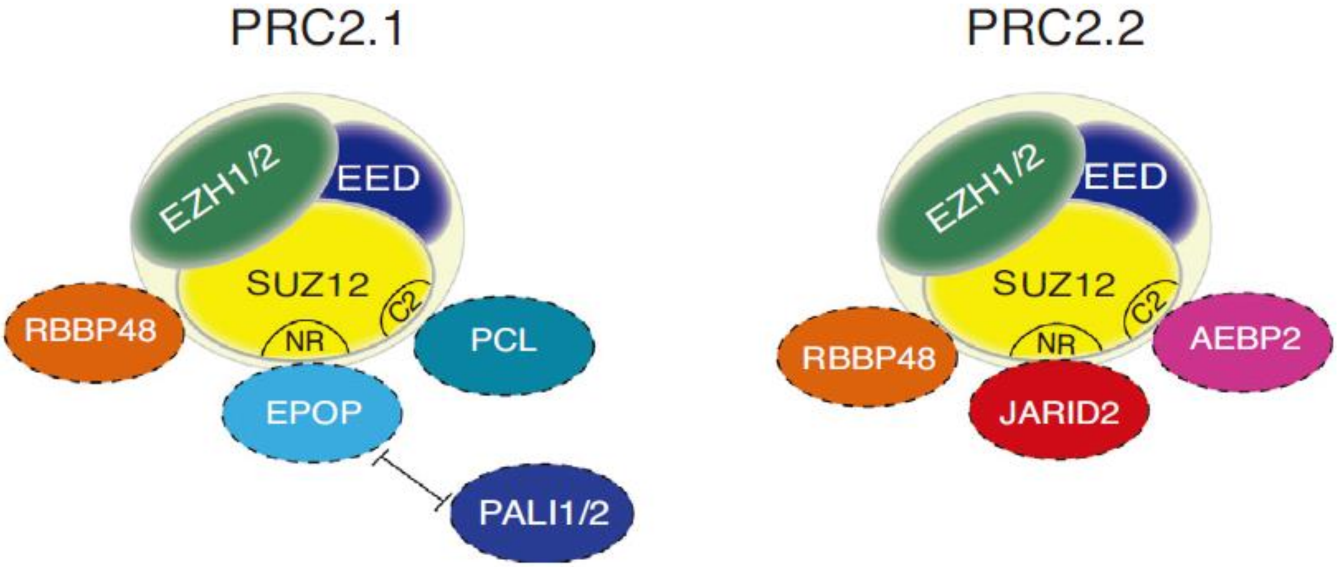

Figure 1-6. Schematic illustration of the PRC2.1 and PRC2.2 protein-composition. Mammalian PRC2.1 consists of a PCL protein (PHF1/PCL1, MTF2/PCL2, or PHF19/PCL3) bound to EPOP or PALI1/2 protein. JARID2 and AEBP2 are auxiliary proteins found in PRC2.2.

This figure was adopted from (218).

Figure 1-7. Schematic representation of factors with influencing PRC2 recruitment or catalytic activity

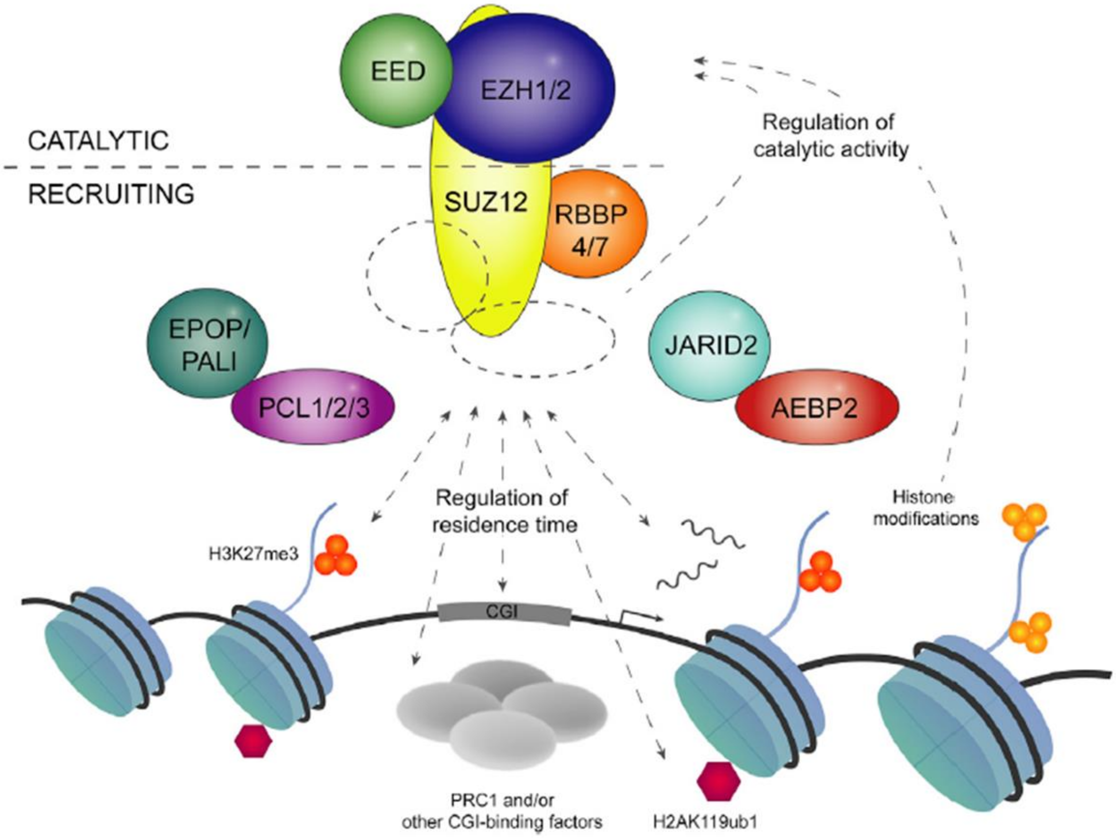

Figure 1-7. The structure of SUZ12 consists of a VEFS C-terminal domain that binds EED and EZH2/1 along with an N-terminal domain for the non-core components in PRC2. The N-terminal part of SUZ12 is required for chromatin binding, and transcriptional activity and co-localizing factors, including PRC1 and H2AK119ub1, influence CGI residence time. Moreover, non-core subunits of PRC2 as well as post-translational modifications of histone (H3K27me3, H3K4me3, and H3K36me2/me3) may affect the catalytic activity of PRC2.

This figure was adopted from (219).

Figure 1-8. Basic properties summary of human mesenchymal stem cells (MSCs)

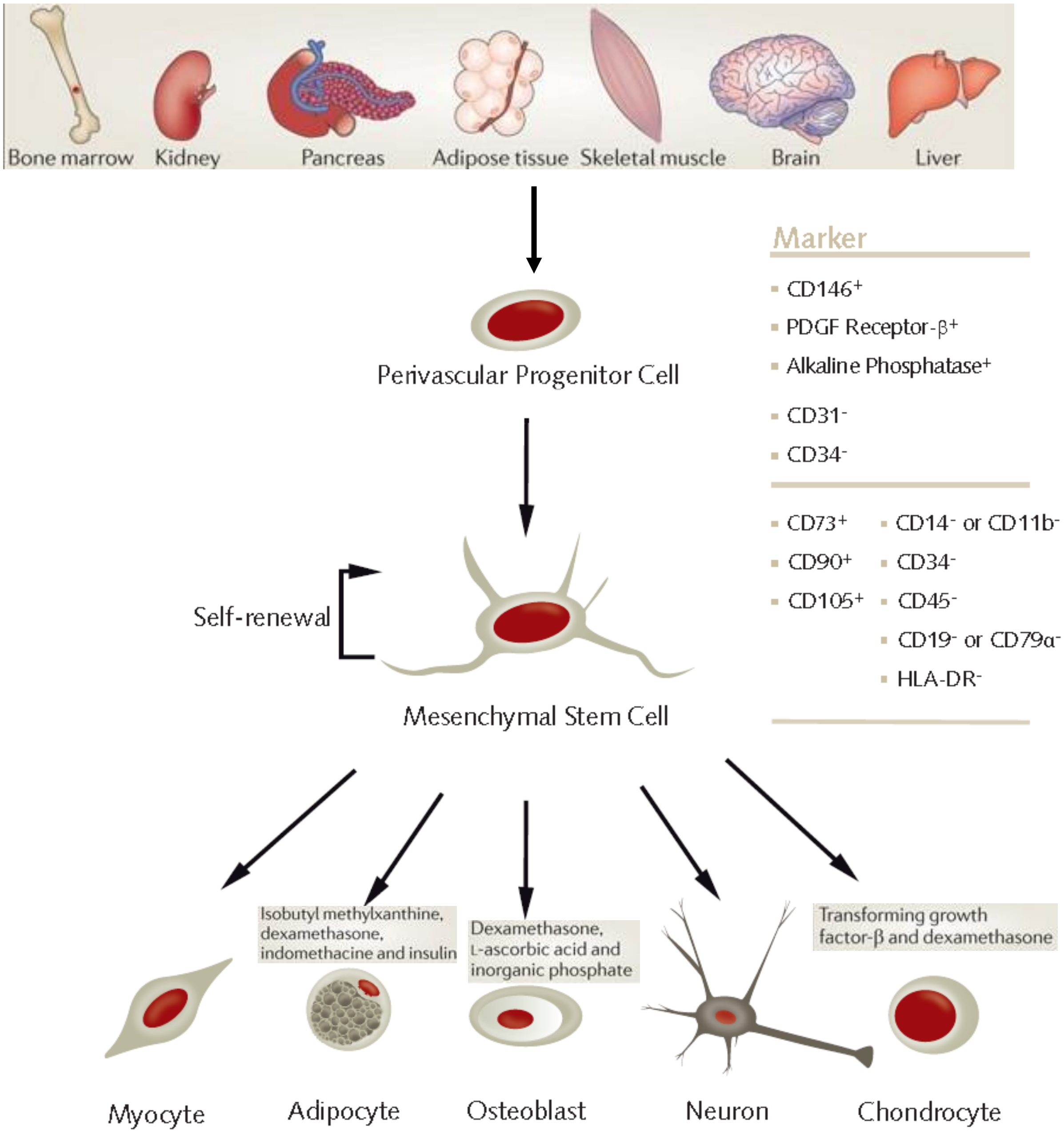

Figure 1-8. Under appropriate culture conditions, multipotent human mesenchymal stem cells can differentiate into osteoblasts, adipocytes, chondrocytes, even trans-differentiate into myocytes, and neurons regardless of origin organ sources.

This figure was adopted from a Scientific Poster from PromoCell© company (https://promocell.com/wp-content/uploads/2017/11/Osteogenic_Differentiation_and_Analysis_of_MSC-1.pdf).

Figure 1-9. The interplay between epigenetic modulators and transcription factors are determinant for lineage specification of MSCs

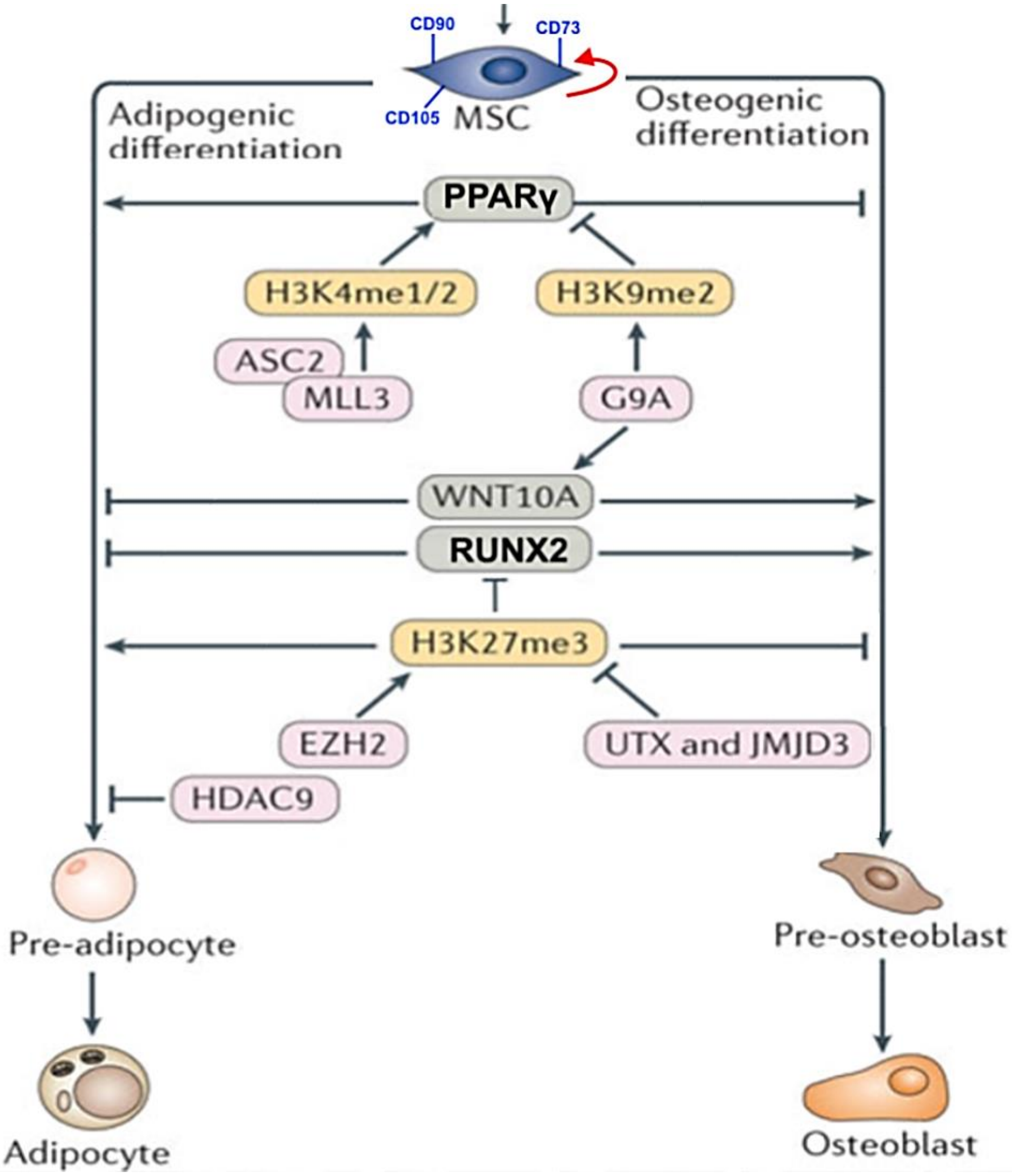

Figure 1-9. Typically, MSC lineage specification is controlled by specific transcription factors that either activate or silence lineage-specific signaling pathways in combination with precise epigenetic control based on a variety of histone modifications and their respective HMTs and HDMs. Adipocyte or osteoblast differentiation of MSC occurs in a critical balance, with induction of one lineage compromising induction of the other.

This figure was adopted from (220).

1.8 Reference

1. Ferlay, J., Colombet, M., Soerjomataram, I., Parkin, D.M., Pineros, M., Znaor, A. and Bray, F. (2021) Cancer statistics for the year 2020: An overview. *Int J Cancer*.
2. Perou, C.M., Sorlie, T., Eisen, M.B., van de Rijn, M., Jeffrey, S.S., Rees, C.A., Pollack, J.R., Ross, D.T., Johnsen, H., Akslen, L.A. *et al.* (2000) Molecular portraits of human breast tumours. *Nature*, **406**, 747-752.
3. Jha, S., Rajagopalan, D., Hora, S. and Jadhav, S.P. (2017), *Breast Cancer - From Biology to Medicine*.
4. Hu, Z., Fan, C., Oh, D.S., Marron, J.S., He, X., Qaqish, B.F., Livasy, C., Carey, L.A., Reynolds, E., Dressler, L. *et al.* (2006) The molecular portraits of breast tumors are conserved across microarray platforms. *BMC Genomics*, **7**, 96.
5. <Race, Breast Cancer Subtypes, and Survival in the Carolina Breast Cancer Study.pdf>.
6. An, K.C. (2016) Selective Estrogen Receptor Modulators. *Asian Spine J*, **10**, 787-791.
7. Ekpo, E.U., Brennan, P.C., Mello-Thoms, C. and McEntee, M.F. (2016) Relationship Between Breast Density and Selective Estrogen-Receptor Modulators, Aromatase Inhibitors, Physical Activity, and Diet: A Systematic Review. *Integr Cancer Ther*, **15**, 127-144.
8. Kennecke, H., Yerushalmi, R., Woods, R., Cheang, M.C., Voduc, D., Speers, C.H., Nielsen, T.O. and Gelmon, K. (2010) Metastatic behavior of breast cancer subtypes. *J Clin Oncol*, **28**, 3271-3277.
9. Yang, H., Wang, R., Zeng, F., Zhao, J., Peng, S., Ma, Y., Chen, S., Ding, S., Zhong, L., Guo, W. *et al.* (2020) Impact of molecular subtypes on metastatic behavior and overall survival in patients with metastatic breast cancer: A single-center study combined with a large cohort study based on the Surveillance, Epidemiology and End Results database. *Oncol Lett*, **20**, 87.
10. Creighton, C.J. (2012) The molecular profile of luminal B breast cancer. *Biologics*, **6**, 289-297.
11. Ellis, M.J., Tao, Y., Luo, J., A'Hern, R., Evans, D.B., Bhatnagar, A.S., Chaudri Ross, H.A., von Kameke, A., Miller, W.R., Smith, I. *et al.* (2008) Outcome prediction for estrogen receptor-positive breast cancer based on postneoadjuvant endocrine therapy tumor characteristics. *J Natl Cancer Inst*, **100**, 1380-1388.
12. Loi, S., Sotiriou, C., Haibe-Kains, B., Lallemand, F., Conus, N.M., Piccart, M.J., Speed, T.P. and McArthur, G.A. (2009) Gene expression profiling identifies activated growth factor signaling in poor prognosis (Luminal-B) estrogen receptor positive breast cancer. *BMC Med Genomics*, **2**, 37.
13. Reis-Filho, J.S., Weigelt, B., Fumagalli, D. and Sotiriou, C. (2010) Molecular profiling: moving away from tumor philately. *Sci Transl Med*, **2**, 47ps43.
14. Tsutsui, S., Ohno, S., Murakami, S., Kataoka, A., Kinoshita, J. and Hachitanda, Y. (2003) Prognostic significance of the coexpression of p53 protein and c-erbB2 in breast cancer. *Am J Surg*, **185**, 165-167.
15. de Ronde, J.J., Hannemann, J., Halfwerk, H., Mulder, L., Straver, M.E., Vrancken Peeters, M.J., Wesseling, J., van de Vijver, M., Wessels, L.F. and Rodenhuis, S. (2010) Concordance of clinical and molecular breast cancer subtyping in the

context of preoperative chemotherapy response. *Breast Cancer Res Treat*, **119**, 119-126.

16. Gabos, Z., Sinha, R., Hanson, J., Chauhan, N., Hugh, J., Mackey, J.R. and Abdulkarim, B. (2006) Prognostic significance of human epidermal growth factor receptor positivity for the development of brain metastasis after newly diagnosed breast cancer. *J Clin Oncol*, **24**, 5658-5663.
17. Ross, J.S., Fletcher, J.A., Linette, G.P., Stec, J., Clark, E., Ayers, M., Symmans, W.F., Pusztai, L. and Bloom, K.J. (2003) The Her-2/neu gene and protein in breast cancer 2003: biomarker and target of therapy. *Oncologist*, **8**, 307-325.
18. Rakha, E.A., Elsheikh, S.E., Aleskandarany, M.A., Habashi, H.O., Green, A.R., Powe, D.G., El-Sayed, M.E., Benhasouna, A., Brunet, J.S., Akslen, L.A. *et al.* (2009) Triple-negative breast cancer: distinguishing between basal and nonbasal subtypes. *Clin Cancer Res*, **15**, 2302-2310.
19. Heitz, F., Harter, P., Lueck, H.J., Fissler-Eckhoff, A., Lorenz-Salehi, F., Scheil-Bertram, S., Traut, A. and du Bois, A. (2009) Triple-negative and HER2-overexpressing breast cancers exhibit an elevated risk and an earlier occurrence of cerebral metastases. *Eur J Cancer*, **45**, 2792-2798.
20. Kreike, B., van Kouwenhove, M., Horlings, H., Weigelt, B., Peterse, H., Bartelink, H. and van de Vijver, M.J. (2007) Gene expression profiling and histopathological characterization of triple-negative/basal-like breast carcinomas. *Breast Cancer Res*, **9**, R65.
21. Anders, C.K. and Carey, L.A. (2009) Biology, metastatic patterns, and treatment of patients with triple-negative breast cancer. *Clin Breast Cancer*, **9 Suppl 2**, S73-81.
22. <The prognostic implication of the basal-like (cyclin E high-p27 low-p53+ glomeruloidmicrovascular- proliferation+) phenotype of BRCA1-related breast cancer.pdf>.
23. Parker, J.S., Mullins, M., Cheang, M.C., Leung, S., Voduc, D., Vickery, T., Davies, S., Fauron, C., He, X., Hu, Z. *et al.* (2009) Supervised risk predictor of breast cancer based on intrinsic subtypes. *J Clin Oncol*, **27**, 1160-1167.
24. Weigelt, B., Mackay, A., A'Hern, R., Natrajan, R., Tan, D.S., Dowsett, M., Ashworth, A. and Reis-Filho, J.S. (2010) Breast cancer molecular profiling with single sample predictors: a retrospective analysis. *Lancet Oncol*, **11**, 339-349.
25. Jackson, H.W., Fischer, J.R., Zanotelli, V.R.T., Ali, H.R., Mechera, R., Soysal, S.D., Moch, H., Muenst, S., Varga, Z., Weber, W.P. *et al.* (2020) The single-cell pathology landscape of breast cancer. *Nature*, **578**, 615-620.
26. Novak, P., Jensen, T.J., Garbe, J.C., Stampfer, M.R. and Futscher, B.W. (2009) Stepwise DNA methylation changes are linked to escape from defined proliferation barriers and mammary epithelial cell immortalization. *Cancer Res*, **69**, 5251-5258.
27. Karsli-Ceppioglu, S., Dagdemir, A., Judes, G., Lebert, A., Penault-Llorca, F., Bignon, Y.J. and Bernard-Gallon, D. (2017) The Epigenetic Landscape of Promoter Genome-wide Analysis in Breast Cancer. *Sci Rep*, **7**, 6597.
28. Berdasco, M. and Esteller, M. (2019) Clinical epigenetics: seizing opportunities for translation. *Nat Rev Genet*, **20**, 109-127.
29. Lo, P.K. and Sukumar, S. (2008) Epigenomics and breast cancer. *Pharmacogenomics*, **9**, 1879-1902.

30. Kumar, R., Paul, A.M., Rameshwar, P. and Pillai, M.R. (2019) Epigenetic Dysregulation at the Crossroad of Women's Cancer. *Cancers (Basel)*, **11**.
31. <H4K12ac is regulated by estrogen receptor-alpha and is associated with BRD4 function and inducible transcription of breast cancer subtypes.pdf>.
32. Zhao, Q.Y., Lei, P.J., Zhang, X., Zheng, J.Y., Wang, H.Y., Zhao, J., Li, Y.M., Ye, M., Li, L., Wei, G. *et al.* (2016) Global histone modification profiling reveals the epigenomic dynamics during malignant transformation in a four-stage breast cancer model. *Clin Epigenetics*, **8**, 34.
33. Elsheikh, S.E., Green, A.R., Rakha, E.A., Powe, D.G., Ahmed, R.A., Collins, H.M., Soria, D., Garibaldi, J.M., Paish, C.E., Ammar, A.A. *et al.* (2009) Global histone modifications in breast cancer correlate with tumor phenotypes, prognostic factors, and patient outcome. *Cancer Res*, **69**, 3802-3809.
34. <Loss of histone H4K20 trimethylation predicts poor prognosis in breast cancer and is associated with invasive activity.pdf>.
35. Kovalchuk, O., Tryndyak, V.P., Montgomery, B., Boyko, A., Kutanzi, K., Zemp, F., Warbritton, A.R., Latendresse, J.R., Kovalchuk, I., Beland, F.A. *et al.* (2007) Estrogen-induced rat breast carcinogenesis is characterized by alterations in DNA methylation, histone modifications and aberrant microRNA expression. *Cell Cycle*, **6**, 2010-2018.
36. Noberini, R., Restellini, C., Savoia, E.O., Raimondi, F., Ghiani, L., Jodice, M.G., Bertalot, G., Bonizzi, G., Capra, M., Maffini, F.A. *et al.* (2019) Profiling of Epigenetic Features in Clinical Samples Reveals Novel Widespread Changes in Cancer. *Cancers (Basel)*, **11**.
37. Hamamoto, R. and Nakamura, Y. (2016) Dysregulation of protein methyltransferases in human cancer: An emerging target class for anticancer therapy. *Cancer Sci*, **107**, 377-384.
38. Michalak, E.M. and Visvader, J.E. (2016) Dysregulation of histone methyltransferases in breast cancer - Opportunities for new targeted therapies? *Mol Oncol*, **10**, 1497-1515.
39. Zhou, Z., Thomsen, R., Kahns, S. and Nielsen, A.L. (2010) The NSD3L histone methyltransferase regulates cell cycle and cell invasion in breast cancer cells. *Biochem Biophys Res Commun*, **398**, 565-570.
40. Fujii, S., Tokita, K., Wada, N., Ito, K., Yamauchi, C., Ito, Y. and Ochiai, A. (2011) MEK-ERK pathway regulates EZH2 overexpression in association with aggressive breast cancer subtypes. *Oncogene*, **30**, 4118-4128.
41. Guo, S., Li, X., Rohr, J., Wang, Y., Ma, S., Chen, P. and Wang, Z. (2016) EZH2 overexpression in different immunophenotypes of breast carcinoma and association with clinicopathologic features. *Diagn Pathol*, **11**, 41.
42. Wang, Q., Wei, J., Su, P. and Gao, P. (2015) Histone demethylase JARID1C promotes breast cancer metastasis cells via down regulating BRMS1 expression. *Biochem Biophys Res Commun*, **464**, 659-666.
43. Wade, M.A., Jones, D., Wilson, L., Stockley, J., Coffey, K., Robson, C.N. and Gaughan, L. (2015) The histone demethylase enzyme KDM3A is a key estrogen receptor regulator in breast cancer. *Nucleic Acids Res*, **43**, 196-207.

44. Wade, P.A., Werel, W., Fentzke, R.C., Thompson, N.E., Leykam, J.F., Burgess, R.R., Jaehning, J.A. and Burton, Z.F. (1996) A novel collection of accessory factors associated with yeast RNA polymerase II. *Protein Expr Purif*, **8**, 85-90.
45. <Cdc73p and Paf1p are found in a novel RNA polymerase II-containing complex distinct from the Srbp-containing holoenzyme.pdf>.
46. Mueller, C.L. and Jaehning, J.A. (2002) Ctr9, Rtf1, and Leo1 are components of the Paf1/RNA polymerase II complex. *Mol Cell Biol*, **22**, 1971-1980.
47. Squazzo, S.L., Costa, P.J., Lindstrom, D.L., Kumer, K.E., Simic, R., Jennings, J.L., Link, A.J., Arndt, K.M. and Hartzog, G.A. (2002) The Paf1 complex physically and functionally associates with transcription elongation factors in vivo. *EMBO J*, **21**, 1764-1774.
48. Cao, Q.F., Yamamoto, J., Isobe, T., Tateno, S., Murase, Y., Chen, Y., Handa, H. and Yamaguchi, Y. (2015) Characterization of the Human Transcription Elongation Factor Rtf1: Evidence for Nonoverlapping Functions of Rtf1 and the Paf1 Complex. *Mol Cell Biol*, **35**, 3459-3470.
49. Mitchell, P. and Tollervey, D. (2003) An NMD pathway in yeast involving accelerated deadenylation and exosome-mediated 3'-->5' degradation. *Mol Cell*, **11**, 1405-1413.
50. Muhlemann, O., Mock-Casagrande, C.S., Wang, J., Li, S., Custodio, N., Carmo-Fonseca, M., Wilkinson, M.F. and Moore, M.J. (2001) Precursor RNAs harboring nonsense codons accumulate near the site of transcription. *Mol Cell*, **8**, 33-43.
51. Mayekar, M.K., Gardner, R.G. and Arndt, K.M. (2013) The recruitment of the Saccharomyces cerevisiae Paf1 complex to active genes requires a domain of Rtf1 that directly interacts with the Spt4-Spt5 complex. *Mol Cell Biol*, **33**, 3259-3273.
52. Vos, S.M., Farnung, L., Boehning, M., Wigge, C., Linden, A., Urlaub, H. and Cramer, P. (2018) Structure of activated transcription complex Pol II-DSIF-PAF-SPT6. *Nature*, **560**, 607-612.
53. Xu, Y., Bernecky, C., Lee, C.T., Maier, K.C., Schwalb, B., Tegunov, D., Plitzko, J.M., Urlaub, H. and Cramer, P. (2017) Architecture of the RNA polymerase II-Paf1C-TFIIS transcription elongation complex. *Nat Commun*, **8**, 15741.
54. Xie, Y., Zheng, M., Chu, X., Chen, Y., Xu, H., Wang, J., Zhou, H. and Long, J. (2018) Paf1 and Ctr9 subcomplex formation is essential for Paf1 complex assembly and functional regulation. *Nat Commun*, **9**, 3795.
55. Chu, X., Qin, X., Xu, H., Li, L., Wang, Z., Li, F., Xie, X., Zhou, H., Shen, Y. and Long, J. (2013) Structural insights into Paf1 complex assembly and histone binding. *Nucleic Acids Res*, **41**, 10619-10629.
56. Betz, J.L., Chang, M., Washburn, T.M., Porter, S.E., Mueller, C.L. and Jaehning, J.A. (2002) Phenotypic analysis of Paf1/RNA polymerase II complex mutations reveals connections to cell cycle regulation, protein synthesis, and lipid and nucleic acid metabolism. *Mol Genet Genomics*, **268**, 272-285.
57. Costa, P.J. and Arndt, K.M. (2000) Synthetic lethal interactions suggest a role for the Saccharomyces cerevisiae Rtf1 protein in transcription elongation. *Genetics*, **156**, 535-547.
58. Koch, C., Wollmann, P., Dahl, M. and Lottspeich, F. (1999) A role for Ctr9p and Paf1p in the regulation G1 cyclin expression in yeast. *Nucleic Acids Res*, **27**, 2126-2134.

59. Desmoucelles, C., Pinson, B., Saint-Marc, C. and Daignan-Fornier, B. (2002) Screening the yeast "disruptome" for mutants affecting resistance to the immunosuppressive drug, mycophenolic acid. *J Biol Chem*, **277**, 27036-27044.
60. Malik, I., Qiu, C., Snavely, T. and Kaplan, C.D. (2017) Wide-ranging and unexpected consequences of altered Pol II catalytic activity in vivo. *Nucleic Acids Res*, **45**, 4431-4451.
61. Riles, L., Shaw, R.J., Johnston, M. and Reines, D. (2004) Large-scale screening of yeast mutants for sensitivity to the IMP dehydrogenase inhibitor 6-azauracil. *Yeast*, **21**, 241-248.
62. Porter, S.E., Washburn, T.M., Chang, M. and Jaehning, J.A. (2002) The yeast pafl-rNA polymerase II complex is required for full expression of a subset of cell cycle-regulated genes. *Eukaryot Cell*, **1**, 830-842.
63. Fischl, H., Howe, F.S., Furger, A. and Mellor, J. (2017) Paf1 Has Distinct Roles in Transcription Elongation and Differential Transcript Fate. *Mol Cell*, **65**, 685-698 e688.
64. Penheiter, K.L., Washburn, T.M., Porter, S.E., Hoffman, M.G. and Jaehning, J.A. (2005) A posttranscriptional role for the yeast Paf1-RNA polymerase II complex is revealed by identification of primary targets. *Mol Cell*, **20**, 213-223.
65. <RNA polymerase II–associated factor 1 regulates the release and phosphorylation of paused RNA polymerase II.pdf>.
66. Hou, L., Wang, Y., Liu, Y., Zhang, N., Shamovsky, I., Nudler, E., Tian, B. and Dynlacht, B.D. (2019) Paf1C regulates RNA polymerase II progression by modulating elongation rate. *Proc Natl Acad Sci U S A*, **116**, 14583-14592.
67. Zhang, Y., Smith, A.D.t., Renfrow, M.B. and Schneider, D.A. (2010) The RNA polymerase-associated factor 1 complex (Paf1C) directly increases the elongation rate of RNA polymerase I and is required for efficient regulation of rRNA synthesis. *J Biol Chem*, **285**, 14152-14159.
68. <The tumor suppressor Cdc73 functionally associates with CPSF and CstF 3′ mRNA processing factors.pdf>.
69. Hazelbaker, D.Z., Marquardt, S., Wlotzka, W. and Buratowski, S. (2013) Kinetic competition between RNA Polymerase II and Sen1-dependent transcription termination. *Mol Cell*, **49**, 55-66.
70. Van Oss, S.B., Shirra, M.K., Bataille, A.R., Wier, A.D., Yen, K., Vinayachandran, V., Byeon, I.L., Cucinotta, C.E., Heroux, A., Jeon, J. *et al.* (2016) The Histone Modification Domain of Paf1 Complex Subunit Rtf1 Directly Stimulates H2B Ubiquitylation through an Interaction with Rad6. *Mol Cell*, **64**, 815-825.
71. Kim, J. and Roeder, R.G. (2009) Direct Bre1-Paf1 complex interactions and RING finger-independent Bre1-Rad6 interactions mediate histone H2B ubiquitylation in yeast. *J Biol Chem*, **284**, 20582-20592.
72. Wood, A., Schneider, J., Dover, J., Johnston, M. and Shilatifard, A. (2003) The Paf1 complex is essential for histone monoubiquitination by the Rad6-Bre1 complex, which signals for histone methylation by COMPASS and Dot1p. *J Biol Chem*, **278**, 34739-34742.
73. Wu, L., Zee, B.M., Wang, Y., Garcia, B.A. and Dou, Y. (2011) The RING finger protein MSL2 in the MOF complex is an E3 ubiquitin ligase for H2B K34 and is involved in crosstalk with H3 K4 and K79 methylation. *Mol Cell*, **43**, 132-144.

74. Wu, L., Li, L., Zhou, B., Qin, Z. and Dou, Y. (2014) H2B ubiquitylation promotes RNA Pol II processivity via PAF1 and pTEFb. *Mol Cell*, **54**, 920-931.
75. Chu, Y., Simic, R., Warner, M.H., Arndt, K.M. and Prelich, G. (2007) Regulation of histone modification and cryptic transcription by the Bur1 and Paf1 complexes. *EMBO J*, **26**, 4646-4656.
76. Qiu, H., Hu, C., Gaur, N.A. and Hinnebusch, A.G. (2012) Pol II CTD kinases Bur1 and Kin28 promote Spt5 CTR-independent recruitment of Paf1 complex. *EMBO J*, **31**, 3494-3505.
77. Nordick, K., Hoffman, M.G., Betz, J.L. and Jaehning, J.A. (2008) Direct interactions between the Paf1 complex and a cleavage and polyadenylation factor are revealed by dissociation of Paf1 from RNA polymerase II. *Eukaryot Cell*, **7**, 1158-1167.
78. Chen, F.X., Woodfin, A.R., Gardini, A., Rickels, R.A., Marshall, S.A., Smith, E.R., Shiekhattar, R. and Shilatifard, A. (2015) PAF1, a Molecular Regulator of Promoter-Proximal Pausing by RNA Polymerase II. *Cell*, **162**, 1003-1015.
79. Lu, X., Zhu, X., Li, Y., Liu, M., Yu, B., Wang, Y., Rao, M., Yang, H., Zhou, K., Wang, Y. *et al.* (2016) Multiple P-TEFbs cooperatively regulate the release of promoter-proximally paused RNA polymerase II. *Nucleic Acids Res*, **44**, 6853-6867.
80. Vos, S.M., Farnung, L., Linden, A., Urlaub, H. and Cramer, P. (2020) Structure of complete Pol II-DSIF-PAF-SPT6 transcription complex reveals RTF1 allosteric activation. *Nat Struct Mol Biol*, **27**, 668-677.
81. Akanuma, T., Koshida, S., Kawamura, A., Kishimoto, Y. and Takada, S. (2007) Paf1 complex homologues are required for Notch-regulated transcription during somite segmentation. *EMBO Rep*, **8**, 858-863.
82. Ding, L., Paszkowski-Rogacz, M., Nitzsche, A., Slabicki, M.M., Heninger, A.K., de Vries, I., Kittler, R., Junqueira, M., Shevchenko, A., Schulz, H. *et al.* (2009) A genome-scale RNAi screen for Oct4 modulators defines a role of the Paf1 complex for embryonic stem cell identity. *Cell Stem Cell*, **4**, 403-415.
83. Sobhian, B., Laguette, N., Yatim, A., Nakamura, M., Levy, Y., Kiernan, R. and Benkirane, M. (2010) HIV-1 Tat assembles a multifunctional transcription elongation complex and stably associates with the 7SK snRNP. *Mol Cell*, **38**, 439-451.
84. Zhang, C., Mejia, L.A., Huang, J., Valnegri, P., Bennett, E.J., Anckar, J., Jahani-Asl, A., Gallardo, G., Ikeuchi, Y., Yamada, T. *et al.* (2013) The X-linked intellectual disability protein PHF6 associates with the PAF1 complex and regulates neuronal migration in the mammalian brain. *Neuron*, **78**, 986-993.
85. Bai, X., Kim, J., Yang, Z., Jurynec, M.J., Akie, T.E., Lee, J., LeBlanc, J., Sessa, A., Jiang, H., DiBiase, A. *et al.* (2010) TIF1gamma controls erythroid cell fate by regulating transcription elongation. *Cell*, **142**, 133-143.
86. Wang, P., Bowl, M.R., Bender, S., Peng, J., Farber, L., Chen, J., Ali, A., Zhang, Z., Alberts, A.S., Thakker, R.V. *et al.* (2008) Parafibromin, a component of the human PAF complex, regulates growth factors and is required for embryonic development and survival in adult mice. *Mol Cell Biol*, **28**, 2930-2940.
87. <Ctr9, a key subunit of PAFc, affects global estrogen signaling and drives ERα-positive breast tumorigenesis.pdf>.
88. Muntean, A.G., Tan, J., Sitwala, K., Huang, Y., Bronstein, J., Connelly, J.A., Basrur, V., Elenitoba-Johnson, K.S. and Hess, J.L. (2010) The PAF complex synergizes

with MLL fusion proteins at HOX loci to promote leukemogenesis. *Cancer Cell*, **17**, 609-621.

89. Turchini, J. and Gill, A.J. (2020) Hereditary Parathyroid Disease: Sometimes Pathologists Do Not Know What They Are Missing. *Endocr Pathol*, **31**, 218-230.
90. Hanks, S., Perdeaux, E.R., Seal, S., Ruark, E., Mahamdallie, S.S., Murray, A., Ramsay, E., Del Vecchio Duarte, S., Zachariou, A., de Souza, B. *et al.* (2014) Germline mutations in the PAF1 complex gene CTR9 predispose to Wilms tumour. *Nat Commun*, **5**, 4398.
91. Martins, A.G., Pinto, A.T., Domingues, R. and Cavaco, B.M. (2018) Identification of a novel CTR9 germline mutation in a family with Wilms tumor. *Eur J Med Genet*, **61**, 294-299.
92. Albert, T.K., Antrecht, C., Kremmer, E. and Meisterernst, M. (2016) The Establishment of a Hyperactive Structure Allows the Tumour Suppressor Protein p53 to Function through P-TEFb during Limited CDK9 Kinase Inhibition. *PLoS One*, **11**, e0146648.
93. Moniaux, N., Nemos, C., Schmied, B.M., Chauhan, S.C., Deb, S., Morikane, K., Choudhury, A., Vanlith, M., Sutherlin, M., Sikela, J.M. *et al.* (2006) The human homologue of the RNA polymerase II-associated factor 1 (hPaf1), localized on the 19q13 amplicon, is associated with tumorigenesis. *Oncogene*, **25**, 3247-3257.
94. Zhi, X., Giroux-Leprieur, E., Wislez, M., Hu, M., Zhang, Y., Shi, H., Du, K. and Wang, L. (2015) Human RNA polymerase II associated factor 1 complex promotes tumorigenesis by activating c-MYC transcription in non-small cell lung cancer. *Biochem Biophys Res Commun*, **465**, 685-690.
95. Cao, R., Wang, L., Wang, H., Xia, L., Erdjument-Bromage, H., Tempst, P., Jones, R.S. and Zhang, Y. (2002) Role of histone H3 lysine 27 methylation in Polycomb-group silencing. *Science*, **298**, 1039-1043.
96. Chen, S., Jiao, L., Shubbar, M., Yang, X. and Liu, X. (2018) Unique Structural Platforms of Suz12 Dictate Distinct Classes of PRC2 for Chromatin Binding. *Mol Cell*, **69**, 840-852 e845.
97. Wu, H., Zeng, H., Dong, A., Li, F., He, H., Senisterra, G., Seitova, A., Duan, S., Brown, P.J., Vedadi, M. *et al.* (2013) Structure of the catalytic domain of EZH2 reveals conformational plasticity in cofactor and substrate binding sites and explains oncogenic mutations. *PLoS One*, **8**, e83737.
98. Smits, A.H., Jansen, P.W., Poser, I., Hyman, A.A. and Vermeulen, M. (2013) Stoichiometry of chromatin-associated protein complexes revealed by label-free quantitative mass spectrometry-based proteomics. *Nucleic Acids Res*, **41**, e28.
99. Xu, C., Bian, C., Yang, W., Galka, M., Ouyang, H., Chen, C., Qiu, W., Liu, H., Jones, A.E., MacKenzie, F. *et al.* (2010) Binding of different histone marks differentially regulates the activity and specificity of polycomb repressive complex 2 (PRC2). *Proc Natl Acad Sci U S A*, **107**, 19266-19271.
100. Margueron, R., Justin, N., Ohno, K., Sharpe, M.L., Son, J., Drury, W.J., 3rd, Voigt, P., Martin, S.R., Taylor, W.R., De Marco, V. *et al.* (2009) Role of the polycomb protein EED in the propagation of repressive histone marks. *Nature*, **461**, 762-767.
101. Cao, R. and Zhang, Y. (2004) SUZ12 is required for both the histone methyltransferase activity and the silencing function of the EED-EZH2 complex. *Mol Cell*, **15**, 57-67.

102. Beringer, M., Pisano, P., Di Carlo, V., Blanco, E., Chammas, P., Vizan, P., Gutierrez, A., Aranda, S., Payer, B., Wierer, M. *et al.* (2016) EPOP Functionally Links Elongin and Polycomb in Pluripotent Stem Cells. *Mol Cell*, **64**, 645-658.
103. Hauri, S., Comoglio, F., Seimiya, M., Gerstung, M., Glatter, T., Hansen, K., Aebersold, R., Paro, R., Gstaiger, M. and Beisel, C. (2016) A High-Density Map for Navigating the Human Polycomb Complexome. *Cell Rep*, **17**, 583-595.
104. Conway, E., Jerman, E., Healy, E., Ito, S., Holoch, D., Oliviero, G., Deevy, O., Glancy, E., Fitzpatrick, D.J., Mucha, M. *et al.* (2018) A Family of Vertebrate-Specific Polycombs Encoded by the LCOR/LCORL Genes Balance PRC2 Subtype Activities. *Mol Cell*, **70**, 408-421 e408.
105. Alekseyenko, A.A., Gorchakov, A.A., Kharchenko, P.V. and Kuroda, M.I. (2014) Reciprocal interactions of human C10orf12 and C17orf96 with PRC2 revealed by BioTAP-XL cross-linking and affinity purification. *Proc Natl Acad Sci U S A*, **111**, 2488-2493.
106. Healy, E., Mucha, M., Glancy, E., Fitzpatrick, D.J., Conway, E., Neikes, H.K., Monger, C., Van Mierlo, G., Baltissen, M.P., Koseki, Y. *et al.* (2019) PRC2.1 and PRC2.2 Synergize to Coordinate H3K27 Trimethylation. *Mol Cell*, **76**, 437-452 e436.
107. Musselman, C.A., Avvakumov, N., Watanabe, R., Abraham, C.G., Lalonde, M.E., Hong, Z., Allen, C., Roy, S., Nunez, J.K., Nickoloff, J. *et al.* (2012) Molecular basis for H3K36me3 recognition by the Tudor domain of PHF1. *Nat Struct Mol Biol*, **19**, 1266-1272.
108. Gatchalian, J., Kingsley, M.C., Moslet, S.D., Rosas Ospina, R.D. and Kutateladze, T.G. (2015) An aromatic cage is required but not sufficient for binding of Tudor domains of the Polycomblike protein family to H3K36me3. *Epigenetics*, **10**, 467-473.
109. Choi, J., Bachmann, A.L., Tauscher, K., Benda, C., Fierz, B. and Muller, J. (2017) DNA binding by PHF1 prolongs PRC2 residence time on chromatin and thereby promotes H3K27 methylation. *Nat Struct Mol Biol*, **24**, 1039-1047.
110. Li, H., Liefke, R., Jiang, J., Kurland, J.V., Tian, W., Deng, P., Zhang, W., He, Q., Patel, D.J., Bulyk, M.L. *et al.* (2017) Polycomb-like proteins link the PRC2 complex to CpG islands. *Nature*, **549**, 287-291.
111. Perino, M., van Mierlo, G., Karemaker, I.D., van Genesen, S., Vermeulen, M., Marks, H., van Heeringen, S.J. and Veenstra, G.J.C. (2018) MTF2 recruits Polycomb Repressive Complex 2 by helical-shape-selective DNA binding. *Nat Genet*, **50**, 1002-1010.
112. Casanova, M., Preissner, T., Cerase, A., Poot, R., Yamada, D., Li, X., Appanah, R., Bezstarosti, K., Demmers, J., Koseki, H. *et al.* (2011) Polycomblike 2 facilitates the recruitment of PRC2 Polycomb group complexes to the inactive X chromosome and to target loci in embryonic stem cells. *Development*, **138**, 1471-1482.
113. Chen, S., Jiao, L., Liu, X., Yang, X. and Liu, X. (2020) A Dimeric Structural Scaffold for PRC2-PCL Targeting to CpG Island Chromatin. *Mol Cell*, **77**, 1265-1278 e1267.
114. Brien, G.L., Gambero, G., O'Connell, D.J., Jerman, E., Turner, S.A., Egan, C.M., Dunne, E.J., Jurgens, M.C., Wynne, K., Piao, L. *et al.* (2012) Polycomb PHF19 binds H3K36me3 and recruits PRC2 and demethylase NO66 to embryonic stem cell genes during differentiation. *Nat Struct Mol Biol*, **19**, 1273-1281.

115. Ballare, C., Lange, M., Lapinaite, A., Martin, G.M., Morey, L., Pascual, G., Liefke, R., Simon, B., Shi, Y., Gozani, O. *et al.* (2012) Phf19 links methylated Lys36 of histone H3 to regulation of Polycomb activity. *Nat Struct Mol Biol*, **19**, 1257-1265.
116. Liefke, R., Karwacki-Neisius, V. and Shi, Y. (2017) EPOP Interacts with Elongin BC and USP7 to Modulate the Chromatin Landscape. *Mol Cell*, **65**, 202.
117. Aso, T., Haque, D., Barstead, R.J., Conaway, R.C. and Conaway, J.W. (1996) The inducible elongin A elongation activation domain: structure, function and interaction with the elongin BC complex. *EMBO J*, **15**, 5557-5566.
118. Ardehali, M.B., Anselmo, A., Cochrane, J.C., Kundu, S., Sadreyev, R.I. and Kingston, R.E. (2017) Polycomb Repressive Complex 2 Methylates Elongin A to Regulate Transcription. *Mol Cell*, **68**, 872-884 e876.
119. Kloet, S.L., Makowski, M.M., Baymaz, H.I., van Voorthuijsen, L., Karemaker, I.D., Santanach, A., Jansen, P., Di Croce, L. and Vermeulen, M. (2016) The dynamic interactome and genomic targets of Polycomb complexes during stem-cell differentiation. *Nat Struct Mol Biol*, **23**, 682-690.
120. Cooper, S., Grijzenhout, A., Underwood, E., Ancelin, K., Zhang, T., Nesterova, T.B., Anil-Kirmizitas, B., Bassett, A., Kooistra, S.M., Agger, K. *et al.* (2016) Jarid2 binds mono-ubiquitylated H2A lysine 119 to mediate crosstalk between Polycomb complexes PRC1 and PRC2. *Nat Commun*, **7**, 13661.
121. Peng, J.C., Valouev, A., Swigut, T., Zhang, J., Zhao, Y., Sidow, A. and Wysocka, J. (2009) Jarid2/Jumonji coordinates control of PRC2 enzymatic activity and target gene occupancy in pluripotent cells. *Cell*, **139**, 1290-1302.
122. Sanulli, S., Justin, N., Teissandier, A., Ancelin, K., Portoso, M., Caron, M., Michaud, A., Lombard, B., da Rocha, S.T., Offer, J. *et al.* (2015) Jarid2 Methylation via the PRC2 Complex Regulates H3K27me3 Deposition during Cell Differentiation. *Mol Cell*, **57**, 769-783.
123. Kim, H., Kang, K. and Kim, J. (2009) AEBP2 as a potential targeting protein for Polycomb Repression Complex PRC2. *Nucleic Acids Res*, **37**, 2940-2950.
124. Lee, C.H., Holder, M., Grau, D., Saldana-Meyer, R., Yu, J.R., Ganai, R.A., Zhang, J., Wang, M., LeRoy, G., Dobenecker, M.W. *et al.* (2018) Distinct Stimulatory Mechanisms Regulate the Catalytic Activity of Polycomb Repressive Complex 2. *Mol Cell*, **70**, 435-448 e435.
125. Min, J., Zhang, Y. and Xu, R.M. (2003) Structural basis for specific binding of Polycomb chromodomain to histone H3 methylated at Lys 27. *Genes Dev*, **17**, 1823-1828.
126. Connelly, K.E., Weaver, T.M., Alpsoy, A., Gu, B.X., Musselman, C.A. and Dykhuizen, E.C. (2019) Engagement of DNA and H3K27me3 by the CBX8 chromodomain drives chromatin association. *Nucleic Acids Res*, **47**, 2289-2305.
127. Kasinath, V., Beck, C., Sauer, P., Poepsel, S., Kosmatka, J., Faini, M., Toso, D., Aebersold, R. and Nogales, E. (2021) JARID2 and AEBP2 regulate PRC2 in the presence of H2AK119ub1 and other histone modifications. *Science*, **371**.
128. Zhao, J., Wang, M., Chang, L., Yu, J., Song, A., Liu, C., Huang, W., Zhang, T., Wu, X., Shen, X. *et al.* (2020) RYBP/YAF2-PRC1 complexes and histone H1-dependent chromatin compaction mediate propagation of H2AK119ub1 during cell division. *Nat Cell Biol*, **22**, 439-452.

129. Tavares, L., Dimitrova, E., Oxley, D., Webster, J., Poot, R., Demmers, J., Bezstarosti, K., Taylor, S., Ura, H., Koide, H. *et al.* (2012) RYBP-PRC1 complexes mediate H2A ubiquitylation at polycomb target sites independently of PRC2 and H3K27me3. *Cell*, **148**, 664-678.
130. Schmitges, F.W., Prusty, A.B., Faty, M., Stutzer, A., Lingaraju, G.M., Aiwazian, J., Sack, R., Hess, D., Li, L., Zhou, S. *et al.* (2011) Histone methylation by PRC2 is inhibited by active chromatin marks. *Mol Cell*, **42**, 330-341.
131. Yuan, W., Xu, M., Huang, C., Liu, N., Chen, S. and Zhu, B. (2011) H3K36 methylation antagonizes PRC2-mediated H3K27 methylation. *J Biol Chem*, **286**, 7983-7989.
132. Wang, X., Paucek, R.D., Gooding, A.R., Brown, Z.Z., Ge, E.J., Muir, T.W. and Cech, T.R. (2017) Molecular analysis of PRC2 recruitment to DNA in chromatin and its inhibition by RNA. *Nat Struct Mol Biol*, **24**, 1028-1038.
133. Yan, J., Dutta, B., Hee, Y.T. and Chng, W.J. (2019) Towards understanding of PRC2 binding to RNA. *RNA Biol*, **16**, 176-184.
134. Chammas, P., Mocavini, I. and Di Croce, L. (2020) Engaging chromatin: PRC2 structure meets function. *Br J Cancer*, **122**, 315-328.
135. Lee, C.H., Yu, J.R., Granat, J., Saldana-Meyer, R., Andrade, J., LeRoy, G., Jin, Y., Lund, P., Stafford, J.M., Garcia, B.A. *et al.* (2019) Automethylation of PRC2 promotes H3K27 methylation and is impaired in H3K27M pediatric glioma. *Genes Dev*, **33**, 1428-1440.
136. Nambirajan, A., Sharma, A., Rajeshwari, M., Boorgula, M.T., Doddamani, R., Garg, A., Suri, V., Sarkar, C. and Sharma, M.C. (2021) EZH2 inhibitory protein (EZHIP/Cxorf67) expression correlates strongly with H3K27me3 loss in posterior fossa ependymomas and is mutually exclusive with H3K27M mutations. *Brain Tumor Pathol*, **38**, 30-40.
137. Nambirajan, A., Sharma, A., Rajeshwari, M., Boorgula, M.T., Doddamani, R., Garg, A., Suri, V., Sarkar, C. and Sharma, M.C. (2021) Correction to: EZH2 inhibitory protein (EZHIP/Cxorf67) expression correlates strongly with H3K27me3 loss in posterior fossa ependymomas and is mutually exclusive with H3K27M mutations. *Brain Tumor Pathol*, **38**, 145.
138. Ishi, Y., Takamiya, S., Seki, T., Yamazaki, K., Hida, K., Hatanaka, K.C., Ishida, Y., Oda, Y., Tanaka, S. and Yamaguchi, S. (2020) Prognostic role of H3K27M mutation, histone H3K27 methylation status, and EZH2 expression in diffuse spinal cord gliomas. *Brain Tumor Pathol*, **37**, 81-88.
139. Harutyunyan, A.S., Chen, H., Lu, T., Horth, C., Nikbakht, H., Krug, B., Russo, C., Bareke, E., Marchione, D.M., Coradin, M. *et al.* (2020) H3K27M in Gliomas Causes a One-Step Decrease in H3K27 Methylation and Reduced Spreading within the Constraints of H3K36 Methylation. *Cell Rep*, **33**, 108390.
140. Wang, X., Long, Y., Paucek, R.D., Gooding, A.R., Lee, T., Burdorf, R.M. and Cech, T.R. (2019) Regulation of histone methylation by automethylation of PRC2. *Genes Dev*, **33**, 1416-1427.
141. Yu, Y.L., Chou, R.H., Shyu, W.C., Hsieh, S.C., Wu, C.S., Chiang, S.Y., Chang, W.J., Chen, J.N., Tseng, Y.J., Lin, Y.H. *et al.* (2013) Smurf2-mediated degradation of EZH2 enhances neuron differentiation and improves functional recovery after ischaemic stroke. *EMBO Mol Med*, **5**, 531-547.

142. Zhang, H., Diab, A., Fan, H., Mani, S.K., Hullinger, R., Merle, P. and Andrisani, O. (2015) PLK1 and HOTAIR Accelerate Proteasomal Degradation of SUZ12 and ZNF198 during Hepatitis B Virus-Induced Liver Carcinogenesis. *Cancer Res*, **75**, 2363-2374.
143. Helin, K. and Dhanak, D. (2013) Chromatin proteins and modifications as drug targets. *Nature*, **502**, 480-488.
144. Plass, C., Pfister, S.M., Lindroth, A.M., Bogatyrova, O., Claus, R. and Lichter, P. (2013) Mutations in regulators of the epigenome and their connections to global chromatin patterns in cancer. *Nat Rev Genet*, **14**, 765-780.
145. Bracken, A.P., Pasini, D., Capra, M., Prosperini, E., Colli, E. and Helin, K. (2003) EZH2 is downstream of the pRB-E2F pathway, essential for proliferation and amplified in cancer. *EMBO J*, **22**, 5323-5335.
146. McCabe, M.T., Graves, A.P., Ganji, G., Diaz, E., Halsey, W.S., Jiang, Y., Smitheman, K.N., Ott, H.M., Pappalardi, M.B., Allen, K.E. *et al.* (2012) Mutation of A677 in histone methyltransferase EZH2 in human B-cell lymphoma promotes hypertrimethylation of histone H3 on lysine 27 (H3K27). *Proc Natl Acad Sci U S A*, **109**, 2989-2994.
147. Sneeringer, C.J., Scott, M.P., Kuntz, K.W., Knutson, S.K., Pollock, R.M., Richon, V.M. and Copeland, R.A. (2010) Coordinated activities of wild-type plus mutant EZH2 drive tumor-associated hypertrimethylation of lysine 27 on histone H3 (H3K27) in human B-cell lymphomas. *Proc Natl Acad Sci U S A*, **107**, 20980-20985.
148. Bodor, C., Grossmann, V., Popov, N., Okosun, J., O'Riain, C., Tan, K., Marzec, J., Araf, S., Wang, J., Lee, A.M. *et al.* (2013) EZH2 mutations are frequent and represent an early event in follicular lymphoma. *Blood*, **122**, 3165-3168.
149. Score, J., Hidalgo-Curtis, C., Jones, A.V., Winkelmann, N., Skinner, A., Ward, D., Zoi, K., Ernst, T., Stegelmann, F., Dohner, K. *et al.* (2012) Inactivation of polycomb repressive complex 2 components in myeloproliferative and myelodysplastic/myeloproliferative neoplasms. *Blood*, **119**, 1208-1213.
150. Ernst, T., Chase, A.J., Score, J., Hidalgo-Curtis, C.E., Bryant, C., Jones, A.V., Waghorn, K., Zoi, K., Ross, F.M., Reiter, A. *et al.* (2010) Inactivating mutations of the histone methyltransferase gene EZH2 in myeloid disorders. *Nat Genet*, **42**, 722-726.
151. Jankowska, A.M., Makishima, H., Tiu, R.V., Szpurka, H., Huang, Y., Traina, F., Visconte, V., Sugimoto, Y., Prince, C., O'Keefe, C. *et al.* (2011) Mutational spectrum analysis of chronic myelomonocytic leukemia includes genes associated with epigenetic regulation: UTX, EZH2, and DNMT3A. *Blood*, **118**, 3932-3941.
152. Nikoloski, G., Langemeijer, S.M., Kuiper, R.P., Knops, R., Massop, M., Tonnissen, E.R., van der Heijden, A., Scheele, T.N., Vandenberghe, P., de Witte, T. *et al.* (2010) Somatic mutations of the histone methyltransferase gene EZH2 in myelodysplastic syndromes. *Nat Genet*, **42**, 665-667.
153. Lee, W., Teckie, S., Wiesner, T., Ran, L., Prieto Granada, C.N., Lin, M., Zhu, S., Cao, Z., Liang, Y., Sboner, A. *et al.* (2014) PRC2 is recurrently inactivated through EED or SUZ12 loss in malignant peripheral nerve sheath tumors. *Nat Genet*, **46**, 1227-1232.
154. Khuong-Quang, D.A., Buczkowicz, P., Rakopoulos, P., Liu, X.Y., Fontebasso, A.M., Bouffet, E., Bartels, U., Albrecht, S., Schwartzentruber, J., Letourneau, L. *et*

al. (2012) K27M mutation in histone H3.3 defines clinically and biologically distinct subgroups of pediatric diffuse intrinsic pontine gliomas. *Acta Neuropathol*, **124**, 439-447.

155. Gielen, G.H., Gessi, M., Hammes, J., Kramm, C.M., Waha, A. and Pietsch, T. (2013) H3F3A K27M mutation in pediatric CNS tumors: a marker for diffuse high-grade astrocytomas. *Am J Clin Pathol*, **139**, 345-349.
156. Wu, G., Broniscer, A., McEachron, T.A., Lu, C., Paugh, B.S., Becksfort, J., Qu, C., Ding, L., Huether, R., Parker, M. *et al.* (2012) Somatic histone H3 alterations in pediatric diffuse intrinsic pontine gliomas and non-brainstem glioblastomas. *Nat Genet*, **44**, 251-253.
157. Lee, J.K. and Kim, K.C. (2013) DZNep, inhibitor of S-adenosylhomocysteine hydrolase, down-regulates expression of SETDB1 H3K9me3 HMTase in human lung cancer cells. *Biochem Biophys Res Commun*, **438**, 647-652.
158. Konze, K.D., Ma, A., Li, F., Barsyte-Lovejoy, D., Parton, T., Macnevin, C.J., Liu, F., Gao, C., Huang, X.P., Kuznetsova, E. *et al.* (2013) An orally bioavailable chemical probe of the Lysine Methyltransferases EZH2 and EZH1. *ACS Chem Biol*, **8**, 1324-1334.
159. Knutson, S.K., Kawano, S., Minoshima, Y., Warholic, N.M., Huang, K.C., Xiao, Y., Kadowaki, T., Uesugi, M., Kuznetsov, G., Kumar, N. *et al.* (2014) Selective inhibition of EZH2 by EPZ-6438 leads to potent antitumor activity in EZH2-mutant non-Hodgkin lymphoma. *Mol Cancer Ther*, **13**, 842-854.
160. Chen, Y.T., Zhu, F., Lin, W.R., Ying, R.B., Yang, Y.P. and Zeng, L.H. (2016) The novel EZH2 inhibitor, GSK126, suppresses cell migration and angiogenesis via down-regulating VEGF-A. *Cancer Chemother Pharmacol*, **77**, 757-765.
161. Kim, W., Bird, G.H., Neff, T., Guo, G., Kerenyi, M.A., Walensky, L.D. and Orkin, S.H. (2013) Targeted disruption of the EZH2-EED complex inhibits EZH2-dependent cancer. *Nat Chem Biol*, **9**, 643-650.
162. Qi, W., Zhao, K., Gu, J., Huang, Y., Wang, Y., Zhang, H., Zhang, M., Zhang, J., Yu, Z., Li, L. *et al.* (2017) An allosteric PRC2 inhibitor targeting the H3K27me3 binding pocket of EED. *Nat Chem Biol*, **13**, 381-388.
163. Fillmore, C.M., Xu, C., Desai, P.T., Berry, J.M., Rowbotham, S.P., Lin, Y.J., Zhang, H., Marquez, V.E., Hammerman, P.S., Wong, K.K. *et al.* (2015) EZH2 inhibition sensitizes BRG1 and EGFR mutant lung tumours to TopoII inhibitors. *Nature*, **520**, 239-242.
164. Bitler, B.G., Aird, K.M., Garipov, A., Li, H., Amatangelo, M., Kossenkov, A.V., Schultz, D.C., Liu, Q., Shih Ie, M., Conejo-Garcia, J.R. *et al.* (2015) Synthetic lethality by targeting EZH2 methyltransferase activity in ARID1A-mutated cancers. *Nat Med*, **21**, 231-238.
165. Lv, F.J., Tuan, R.S., Cheung, K.M. and Leung, V.Y. (2014) Concise review: the surface markers and identity of human mesenchymal stem cells. *Stem Cells*, **32**, 1408-1419.
166. James, A.W. and Peault, B. (2019) Perivascular Mesenchymal Progenitors for Bone Regeneration. *J Orthop Res*, **37**, 1221-1228.
167. Li, H., Ghazanfari, R., Zacharaki, D., Lim, H.C. and Scheding, S. (2016) Isolation and characterization of primary bone marrow mesenchymal stromal cells. *Ann N Y Acad Sci*, **1370**, 109-118.

168. Dominici, M., Le Blanc, K., Mueller, I., Slaper-Cortenbach, I., Marini, F., Krause, D., Deans, R., Keating, A., Prockop, D. and Horwitz, E. (2006) Minimal criteria for defining multipotent mesenchymal stromal cells. The International Society for Cellular Therapy position statement. *Cytotherapy*, **8**, 315-317.
169. Song, L., Young, N.J., Webb, N.E. and Tuan, R.S. (2005) Origin and characterization of multipotential mesenchymal stem cells derived from adult human trabecular bone. *Stem Cells Dev*, **14**, 712-721.
170. Mackenzie, T.C. and Flake, A.W. (2001) Human mesenchymal stem cells persist, demonstrate site-specific multipotential differentiation, and are present in sites of wound healing and tissue regeneration after transplantation into fetal sheep. *Blood Cells Mol Dis*, **27**, 601-604.
171. Jing, Y., Zhang, J.C., Li, S.T., Zhao, J.H., Wang, J., Han, X.F. and Xing, Y. (2015) Wnt/beta-catenin pathway might underlie the MET in trans- differentiation from MSC to MSC-derived neuron. *Zhongguo Ying Yong Sheng Li Xue Za Zhi*, **31**, 572-576.
172. Li, X., Tan, J., Xiao, Z., Zhao, Y., Han, S., Liu, D., Yin, W., Li, J., Li, J., Wanggou, S. *et al.* (2017) Transplantation of hUC-MSCs seeded collagen scaffolds reduces scar formation and promotes functional recovery in canines with chronic spinal cord injury. *Sci Rep*, **7**, 43559.
173. Oh, E.J., Lee, H.W., Kalimuthu, S., Kim, T.J., Kim, H.M., Baek, S.H., Zhu, L., Oh, J.M., Son, S.H., Chung, H.Y. *et al.* (2018) In vivo migration of mesenchymal stem cells to burn injury sites and their therapeutic effects in a living mouse model. *J Control Release*, **279**, 79-88.
174. Magne, B., Dedier, M., Nivet, M., Coulomb, B., Banzet, S., Lataillade, J.J. and Trouillas, M. (2020) IL-1beta-Primed Mesenchymal Stromal Cells Improve Epidermal Substitute Engraftment and Wound Healing via Matrix Metalloproteinases and Transforming Growth Factor-beta1. *J Invest Dermatol*, **140**, 688-698 e621.
175. Hu, C., Yong, X., Li, C., Lu, M., Liu, D., Chen, L., Hu, J., Teng, M., Zhang, D., Fan, Y. *et al.* (2013) CXCL12/CXCR4 axis promotes mesenchymal stem cell mobilization to burn wounds and contributes to wound repair. *J Surg Res*, **183**, 427-434.
176. Negoro, T., Takagaki, Y., Okura, H. and Matsuyama, A. (2018) Trends in clinical trials for articular cartilage repair by cell therapy. *NPJ Regen Med*, **3**, 17.
177. Gaur, M., Dobke, M. and Lunyak, V.V. (2019) Methods and Strategies for Procurement, Isolation, Characterization, and Assessment of Senescence of Human Mesenchymal Stem Cells from Adipose Tissue. *Methods Mol Biol*, **2045**, 37-92.
178. Miao, Z., Jin, J., Chen, L., Zhu, J., Huang, W., Zhao, J., Qian, H. and Zhang, X. (2006) Isolation of mesenchymal stem cells from human placenta: comparison with human bone marrow mesenchymal stem cells. *Cell Biol Int*, **30**, 681-687.
179. Schuring, A.N., Schulte, N., Kelsch, R., Ropke, A., Kiesel, L. and Gotte, M. (2011) Characterization of endometrial mesenchymal stem-like cells obtained by endometrial biopsy during routine diagnostics. *Fertil Steril*, **95**, 423-426.
180. Francis, S.L., Duchi, S., Onofrillo, C., Di Bella, C. and Choong, P.F.M. (2018) Adipose-Derived Mesenchymal Stem Cells in the Use of Cartilage Tissue

Engineering: The Need for a Rapid Isolation Procedure. *Stem Cells Int*, **2018**, 8947548.

181. Hmadcha, A., Martin-Montalvo, A., Gauthier, B.R., Soria, B. and Capilla-Gonzalez, V. (2020) Therapeutic Potential of Mesenchymal Stem Cells for Cancer Therapy. *Front Bioeng Biotechnol*, **8**, 43.
182. Chan, T.S., Shaked, Y. and Tsai, K.K. (2019) Targeting the Interplay Between Cancer Fibroblasts, Mesenchymal Stem Cells, and Cancer Stem Cells in Desmoplastic Cancers. *Front Oncol*, **9**, 688.
183. Rauch, A. and Mandrup, S. (2021) Transcriptional networks controlling stromal cell differentiation. *Nat Rev Mol Cell Biol*, **22**, 465-482.
184. Nishimura, R., Hata, K., Matsubara, T., Wakabayashi, M. and Yoneda, T. (2012) Regulation of bone and cartilage development by network between BMP signalling and transcription factors. *J Biochem*, **151**, 247-254.
185. Sepulveda, H., Aguilar, R., Prieto, C.P., Bustos, F., Aedo, S., Lattus, J., van Zundert, B., Palma, V. and Montecino, M. (2017) Epigenetic Signatures at the RUNX2-P1 and Sp7 Gene Promoters Control Osteogenic Lineage Commitment of Umbilical Cord-Derived Mesenchymal Stem Cells. *J Cell Physiol*, **232**, 2519-2527.
186. Villanueva, F., Araya, H., Briceno, P., Varela, N., Stevenson, A., Jerez, S., Tempio, F., Chnaiderman, J., Perez, C., Villarroel, M. *et al.* (2019) The cancer-related transcription factor RUNX2 modulates expression and secretion of the matricellular protein osteopontin in osteosarcoma cells to promote adhesion to endothelial pulmonary cells and lung metastasis. *J Cell Physiol*, **234**, 13659-13679.
187. Jang, W.G., Kim, E.J., Kim, D.K., Ryoo, H.M., Lee, K.B., Kim, S.H., Choi, H.S. and Koh, J.T. (2012) BMP2 protein regulates osteocalcin expression via Runx2-mediated Atf6 gene transcription. *J Biol Chem*, **287**, 905-915.
188. Jeon, M.J., Kim, J.A., Kwon, S.H., Kim, S.W., Park, K.S., Park, S.W., Kim, S.Y. and Shin, C.S. (2003) Activation of peroxisome proliferator-activated receptor-gamma inhibits the Runx2-mediated transcription of osteocalcin in osteoblasts. *J Biol Chem*, **278**, 23270-23277.
189. Elango, J., Robinson, J., Zhang, J., Bao, B., Ma, N., de Val, J. and Wu, W. (2019) Collagen Peptide Upregulates Osteoblastogenesis from Bone Marrow Mesenchymal Stem Cells through MAPK- Runx2. *Cells*, **8**.
190. Xiao, G., Jiang, D., Gopalakrishnan, R. and Franceschi, R.T. (2002) Fibroblast growth factor 2 induction of the osteocalcin gene requires MAPK activity and phosphorylation of the osteoblast transcription factor, Cbfa1/Runx2. *J Biol Chem*, **277**, 36181-36187.
191. Shirai, Y., Kawabe, K., Tosa, I., Tsukamoto, S., Yamada, D. and Takarada, T. (2019) Runx2 function in cells of neural crest origin during intramembranous ossification. *Biochem Biophys Res Commun*, **509**, 1028-1033.
192. Tosa, I., Yamada, D., Yasumatsu, M., Hinoi, E., Ono, M., Oohashi, T., Kuboki, T. and Takarada, T. (2019) Postnatal Runx2 deletion leads to low bone mass and adipocyte accumulation in mice bone tissues. *Biochem Biophys Res Commun*, **516**, 1229-1233.
193. Xu, C., Wang, A., Zhang, L., Yang, C., Gao, Y., Dong, Z., Tian, Y., Li, C. and Gao, Y. (2021) Epithelium-Specific Runx2 knockout mice display junctional epithelium and alveolar bone defects. *Oral Dis*, **27**, 1292-1299.

194. Corps, K., Stanwick, M., Rectenwald, J., Kruggel, A. and Peters, S.B. (2021) Skeletal Deformities in Osterix-Cre;Tgfbr2(f/f) Mice May Cause Postnatal Death. *Genes (Basel)*, **12**.
195. Moon, Y.J., Yun, C.Y., Choi, H., Kim, J.R., Park, B.H. and Cho, E.S. (2018) Osterix regulates corticalization for longitudinal bone growth via integrin beta3 expression. *Exp Mol Med*, **50**, 1-11.
196. Zeng, J., Hu, J., Lian, Y., Jiang, Y. and Chen, B. (2018) SFRP5 is a target gene transcriptionally regulated by PPARgamma in 3T3-L1 adipocytes. *Gene*, **641**, 190-195.
197. Zhang, Y., Dallner, O.S., Nakadai, T., Fayzikhodjaeva, G., Lu, Y.H., Lazar, M.A., Roeder, R.G. and Friedman, J.M. (2018) A noncanonical PPARgamma/RXRalpha-binding sequence regulates leptin expression in response to changes in adipose tissue mass. *Proc Natl Acad Sci U S A*, **115**, E6039-E6047.
198. Zhu, D., Xu, L., Wei, X., Xia, B., Gong, Y., Li, Q. and Chen, X. (2021) PPARgamma enhanced Adiponectin polymerization and trafficking by promoting RUVBL2 expression during adipogenic differentiation. *Gene*, **764**, 145100.
199. Gabrielli, M., Romero, D.G., Martini, C.N., Raiger Iustman, L.J. and Vila, M.D.C. (2018) MCAM knockdown impairs PPARgamma expression and 3T3-L1 fibroblasts differentiation to adipocytes. *Mol Cell Biochem*, **448**, 299-309.
200. Sng, M.K., Chan, J.S.K., Teo, Z., Phua, T., Tan, E.H.P., Wee, J.W.K., Koh, N.J.N., Tan, C.K., Chen, J.P., Pal, M. *et al.* (2018) Selective deletion of PPARbeta/delta in fibroblasts causes dermal fibrosis by attenuated LRG1 expression. *Cell Discov*, **4**, 15.
201. Liu, C.F., Samsa, W.E., Zhou, G. and Lefebvre, V. (2017) Transcriptional control of chondrocyte specification and differentiation. *Semin Cell Dev Biol*, **62**, 34-49.
202. Jiang, X., Huang, X., Jiang, T., Zheng, L., Zhao, J. and Zhang, X. (2018) The role of Sox9 in collagen hydrogel-mediated chondrogenic differentiation of adult mesenchymal stem cells (MSCs). *Biomater Sci*, **6**, 1556-1568.
203. Kerney, R.R., Hanken, J. and Blackburn, D.C. (2018) Early limb patterning in the direct-developing salamander Plethodon cinereus revealed by sox9 and col2a1. *Evol Dev*, **20**, 100-107.
204. Liu, C.F., Angelozzi, M., Haseeb, A. and Lefebvre, V. (2018) SOX9 is dispensable for the initiation of epigenetic remodeling and the activation of marker genes at the onset of chondrogenesis. *Development*, **145**.
205. Hassan, M.Q., Tare, R., Lee, S.H., Mandeville, M., Weiner, B., Montecino, M., van Wijnen, A.J., Stein, J.L., Stein, G.S. and Lian, J.B. (2007) HOXA10 controls osteoblastogenesis by directly activating bone regulatory and phenotypic genes. *Mol Cell Biol*, **27**, 3337-3352.
206. Gordon, J.A., Hassan, M.Q., Koss, M., Montecino, M., Selleri, L., van Wijnen, A.J., Stein, J.L., Stein, G.S. and Lian, J.B. (2011) Epigenetic regulation of early osteogenesis and mineralized tissue formation by a HOXA10-PBX1-associated complex. *Cells Tissues Organs*, **194**, 146-150.
207. Fan, Z., Yamaza, T., Lee, J.S., Yu, J., Wang, S., Fan, G., Shi, S. and Wang, C.Y. (2009) BCOR regulates mesenchymal stem cell function by epigenetic mechanisms. *Nat Cell Biol*, **11**, 1002-1009.

208. Du, J., Ma, Y., Ma, P., Wang, S. and Fan, Z. (2013) Demethylation of epiregulin gene by histone demethylase FBXL11 and BCL6 corepressor inhibits osteo/dentinogenic differentiation. *Stem Cells*, **31**, 126-136.
209. Hemming, S., Cakouros, D., Isenmann, S., Cooper, L., Menicanin, D., Zannettino, A. and Gronthos, S. (2014) EZH2 and KDM6A act as an epigenetic switch to regulate mesenchymal stem cell lineage specification. *Stem Cells*, **32**, 802-815.
210. Dudakovic, A., Samsonraj, R.M., Paradise, C.R., Galeano-Garces, C., Mol, M.O., Galeano-Garces, D., Zan, P., Galvan, M.L., Hevesi, M., Pichurin, O. *et al.* (2020) Inhibition of the epigenetic suppressor EZH2 primes osteogenic differentiation mediated by BMP2. *J Biol Chem*, **295**, 7877-7893.
211. Wei, Y., Chen, Y.H., Li, L.Y., Lang, J., Yeh, S.P., Shi, B., Yang, C.C., Yang, J.Y., Lin, C.Y., Lai, C.C. *et al.* (2011) CDK1-dependent phosphorylation of EZH2 suppresses methylation of H3K27 and promotes osteogenic differentiation of human mesenchymal stem cells. *Nat Cell Biol*, **13**, 87-94.
212. Liu, L., Luo, Q., Sun, J., Ju, Y., Morita, Y. and Song, G. (2018) Chromatin organization regulated by EZH2-mediated H3K27me3 is required for OPN-induced migration of bone marrow-derived mesenchymal stem cells. *Int J Biochem Cell Biol*, **96**, 29-39.
213. Zhu, L. and Xu, P.C. (2013) Downregulated LncRNA-ANCR promotes osteoblast differentiation by targeting EZH2 and regulating Runx2 expression. *Biochem Biophys Res Commun*, **432**, 612-617.
214. Zhu, X.X., Yan, Y.W., Chen, D., Ai, C.Z., Lu, X., Xu, S.S., Jiang, S., Zhong, G.S., Chen, D.B. and Jiang, Y.Z. (2016) Long non-coding RNA HoxA-AS3 interacts with EZH2 to regulate lineage commitment of mesenchymal stem cells. *Oncotarget*, **7**, 63561-63570.
215. Wen, Y., Guo, X., Hao, J., Xiao, X., Wang, W., Wu, C., Wang, S., Yang, T., Shen, H., Chen, X. *et al.* (2016) Integrative analysis of genome-wide association studies and gene expression profiles identified candidate genes for osteoporosis in Kashin-Beck disease patients. *Osteoporos Int*, **27**, 1041-1046.
216. Cheng, Y., He, C., Wang, M., Ma, X., Mo, F., Yang, S., Han, J. and Wei, X. (2019) Targeting epigenetic regulators for cancer therapy: mechanisms and advances in clinical trials. *Signal Transduct Target Ther*, **4**, 62.
217. Kim, J., Guermah, M. and Roeder, R.G. (2010) The human PAF1 complex acts in chromatin transcription elongation both independently and cooperatively with SII/TFIIS. *Cell*, **140**, 491-503.
218. Glancy, E., Ciferri, C. and Bracken, A.P. (2021) Structural basis for PRC2 engagement with chromatin. *Curr Opin Struct Biol*, **67**, 135-144.
219. Laugesen, A., Hojfeldt, J.W. and Helin, K. (2019) Molecular Mechanisms Directing PRC2 Recruitment and H3K27 Methylation. *Mol Cell*, **74**, 8-18.
220. Chen, Q., Shou, P., Zheng, C., Jiang, M., Cao, G., Yang, Q., Cao, J., Xie, N., Velletri, T., Zhang, X. *et al.* (2016) Fate decision of mesenchymal stem cells: adipocytes or osteoblasts? *Cell Death Differ*, **23**, 1128-1139.

Chapter 2

The transcriptional elongation factor CTR9 controls PRC2-mediated H3K27me3 domains by altering PRC2 subtype equilibrium

This chapter is adapted from a manuscript under revision.

Quantification of histone modifications by LC-MS/MS is performed by Dr. Junfeng Huang from Prof. Lingjun Li's lab at Department of Pharmacy.

Construction and validation of MCF7-3xFlag-KI-CTR9 clonal cell line were performed by Dr. Gui Ma.

Data in Figure 2-9 B/C/E were generated by Dr. Gui Ma.

2.1 ABSTRACT

CTR9 is the scaffold subunit in Polymerase Associated Factor complex (PAFc), a multifunctional complex employed in multiple steps of RNA Polymerase II (RNAPII)-mediated transcription. CTR9/PAFc is well known as an evolutionarily conserved elongation factor that regulates gene activation via coupling with histone modification enzymes. However, little is known about its function to restrain repressive histone markers. Using inducible and stable CTR9 knockdown breast cancer cell lines, we discovered that the H3K27me3 levels are governed by CTR9. Quantitative profiling of histone modifications revealed a striking increase of H3K27me3 levels upon loss of CTR9. Moreover, loss of CTR9 leads to genome-wide expansion of H3K27me3, as well as increased recruitment of PRC2 on chromatin, which can be reversed by CTR9 restoration. Further, CTR9 depletion triggers a PRC2 subtype switch from the less active PRC2.2, to the more active PRC2.1 with higher methyltransferase activity. As a consequence, CTR9 depletion generates vulnerability that renders breast cancer cells hypersensitive to PRC2 inhibitors. Our findings that CTR9 demarcates PRC2-mediated H3K27me3 levels and genomic distribution provide a unique mechanism that explains the transition from transcriptionally active chromatin states to repressive chromatin states and shed light on the biological functions of CTR9 in development and cancer.

2.2 INTRODUCTION

The Polymerase-Associated Factor complex (PAFc) was originally identified as an RNA Polymerase II (RNAPII)-interacting complex in *Saccharomyces cerevisiae* over 20 years ago. PAFc has emerged as a highly conserved complex regulating multiple steps of RNA polymerase II (RNAPII)-mediated transcription (1). In budding yeast, PAFc consists of five subunits, including PAF1, CTR9, CDC73, LEO1 and RTF1. In higher eukaryotic organisms, RTF1 is loosely attached to PAFc, and SKI8/WDR61 is a new subunit of PAFc (2). PAFc regulates multiple phases of transcription, including transcription elongation, transcription termination, and RNA 3'-end polyadenylation (1). Recent studies show that PAF1 and CTR9 are essential for PAFc integrity (3-5). PAFc promotes RNAPII pause release (5) and regulates gene expression by controlling multiple transcription coupled histone modifications, including H2BK123ub, H3K4me2/3, and H3K36me2/3, via interaction with different histone modification enzymes (6). The defined functions of PAFc in chromatin modification and transcription elongation control have marked PAFc as an essential regulator of RNAPII-mediated transcription. Inactivation or overexpression of different subunits in PAFc has been found in various cancer types, and the oncogenic or tumor suppressor function of individual subunits appears to be context-dependent (7). For example, germline mutations in *CTR9* were identified in Wilms tumor families, implicating *CTR9* as a Wilms tumor predisposition gene (8). We have found that CTR9 is enriched in estrogen receptor α (ERα) positive breast cancers, and high expression of CTR9 correlates with poor prognosis and tamoxifen resistance (9). Knocking down CTR9 in ERα+ breast cancer cells erased >90% of estrogen-regulated transcriptional response, demonstrating CTR9's function in promoting breast cancer progression (10).

Polycomb repressive complex 2 (PRC2), the sole mammalian multi-subunit complex responsible for H3K27me3, is essential for maintaining cellular identity and development of multicellular organisms (11). PRC2 is comprised of the core subunits EZH1/2, EED, SUZ12, and RbAp46/48, as well as several sub-stoichiometric proteins (12,13). Though EZH2 is the catalytic subunit of PRC2 (14), the physical interaction of EZH2 with EED and SUZ12 is necessary for full H3K27 methylation activity, as well as for modulating complex stability, and nucleosome binding ability. In the absence of EED or SUZ12, EZH2 is autoinhibited (14-16). Distinct stimulatory models of PRC2 including allosteric activation by its own catalysis (17) as well as auto-methylation of EZH2 at several lysine residues (18) have been reported. Emerging evidence supports the existence of two different PRC2 complex subtypes in vertebrate. The subtype is determined by the auxiliary proteins associated with the core PRC2 complex (11,12). EPOP or PALI, and one of the Polycomb-like (PCL) proteins (either MTF2, PHF1, or PHF19) are found in PRC2.1, while AEBP2 and JARID2 are found in PRC2.2 (19). The auxiliary proteins are known to either promote PRC2 activity, facilitate its stability on chromatin, or both. For example, JARID2, a PRC2.2-specific subunit, is methylated by EZH2, and methylated JARID2 mimics the methylated H3 tail to stimulate PRC2 activity (20). MTF2, a protein that forms the PRC2.1 sub-complex, is required for sufficient recruitment of PRC2 to CpG islands in mouse embryonic stem cells (mESCs) (21). Although PRC2.1 seems to have higher enzymatic capacity to catalyze H3K27me3 propagation along genome than PRC2.2 during the *de novo* establishment of H3K27me2/3 repressive domains (22), the mechanisms of PRC2 recruitment to CpG islands in human, especially in cancer environment, remain unclear (11). The overall H3K27me3 levels are thought to be deliberately balanced by PRC2.1

and PRC2.2, to achieve an optimized H3K27me3 concentration either at nucleation or proximal/distal spreading sites (23).

The mutations on PRC2 members are frequently found in human cancers, which are often accompanied by the alteration of global levels of H3K27me2/3 (24). Elevated EZH2 levels in breast cancer are associated with poor prognosis (25,26). Pharmacological inhibition of EZH2 is under intensive investigation for combating cancers with aberrant PRC2 activity (27). Tazemetostat, an EZH2 inhibitor, was recently approved by the FDA for the treatment of adult patients with relapsed follicular lymphoma (28). Single-cell analysis showed that loss of H3K27me3 was associated with treatment-resistant breast cancer (29), highlighting the need to further understand how chromatin states affect drug sensitivity.

This study uncovers that H3K27me3 levels are precisely controlled by CTR9 levels in breast cancer cells. Global quantitative analyses of histone modifications reveal a significant increase of H3K27me3 levels and genome-wide spreading of H3K27me3 upon depletion of CTR9. This is partially attributed to the moderate increase of PRC2 recruitment, but more significantly, to switch from PRC2.2 to PRC2.1, of which PRC2.1 has stronger H3K27me3 methylation activity and propagation capability. Genes harboring CTR9 binding sites are often found to possess the gain of H3K27me3 repressive signals upon loss of CTR9. Finally, CTR9 depleted cells become addicted to H3K27me3 and are hypersensitive to PRC2 inhibition. Collectively, our study uncovers a unique mechanism by which a transcriptional elongation factor demarcates the PRC2-mediated H3K27me3 domains in breast cancer cells and provides a molecular basis for therapeutically targeting CTR9-low breast tumors with EZH2 inhibitors.

2.3 RESULTS

2.3.1 CTR9 is a determinant of cellular H3K27me3 levels

CTR9/PAFc has been shown to regulate ERα mediated transcription via coupling multiple histone modifications in breast cancer cells. We sought to achieve a comprehensive understanding on how the global histone modification landscape is altered, as well as whether specific histone modifications are more sensitive to CTR9 depletion than others. To address these questions, we employed a Dox-inducible CTR9 knockdown (KD) cell line (i.e., MCF7-tet-on-shCTR9) where shRNA expression can be monitored by expression of eGFP marker (Fig. 2-1-A). Western blotting results showed that treatment with Dox for 7 days (+Dox 7D) was sufficient to deplete CTR9. Beginning on day 8, Dox was removed for 0 day (-Dox 0D) and up to 7 days (-Dox 7D) to allow CTR9 to recover to basal level (Fig. 2-1-B). To measure the levels of histone modifications, total histones were extracted from the nuclear pellets of MCF7-tet-on-shCTR9 cells after treatment with Dox on Day 0 and Day 7, followed by liquid chromatography and tandem mass spectrometry (LC-MS/MS). The transcription-coupled histone modifications such as H3K4me3 and H3K36me3 were decreased by CTR9 depletion, as we reported previously (9). Surprisingly, H3K27me2 and H3K27me3, two transcriptional repressive histone markers, were robustly increased (Fig. 2-1-C, Table 1). The histone modification changes in response to CTR9 KD were validated by western blotting (Fig. 2-1-D) where a significant increase of H3K27me3 was observed after a 7-day Dox treatment. This result suggests that loss of CTR9 results in a global increase of H3K27me3 levels in MCF7 cells. Furthermore, similar observation was made in MCF7, T47D, and BT474 cells stably expressing two distinct CTR9-targeting shRNAs (shCTR9#3 or #5) (Fig. 2-2-A), as measured by western blotting of purified histones and ELISA assays (Fig. 2-2-B/C). To interrogate whether elevation of H3K27me3 levels in CTR9 KD cells can be reversed by re-expressing CTR9 when Dox was removed, we performed a time-course Dox addition and removal experiment as described above (Fig. 2-1-B). Figure 2-3-A shows that H3K27me3 levels increased when CTR9 was depleted, and that H3K27me3 returned to its original levels when CTR9 levels were restored. The dynamic changes of H3K27me3 in response to CTR9 levels were further confirmed by flow cytometry using an Alexa Fluor®647-labelled H3K27me3 antibody (Fig. 2-3-B) as well as an H3K27me3 ELISA assay (Fig. 2-3-C). To visualize the H3K27me3 changes in individual cells, we performed immuno-fluorescence staining of H3K27me3 using confocal microscopy (Fig. 2-3-E). The results showed that, although the response of individual cells varies, possibly due to the heterogeneous expression of shCTR9 (expression indicated by eGFP), the overall intensity of H3K27me3 staining was inversely correlated with CTR9 levels in a dynamic manner (Fig. 2-3-F). Together, these data strongly suggest that CTR9 is a *bona fide* regulator of cellular H3K27me3 levels.

2.3.2 CTR9 confines the intensities and genome-wide distribution of H3K27me3 peaks

PRC2 deposits H3K27me3 marks in spatially defined chromatin domains to repress gene expression. Since CTR9 KD leads to a global increase of H3K27me3 levels, we examined whether CTR9 demarcates the enrichment and distribution of H3K27me3 on chromatin. To quantify the histone modification changes in MCF7-tet-on-shCTR9 cells under the treatment conditions depicted in Figure 2-1-B, we performed chromatin immunoprecipitation followed by high throughput sequencing with incorporation of a reference exogenous genome (ChIP-Rx) using an antibody against H3K27me3.

In response to the decrease of CTR9 to a non-detectable level after a 7-day Dox treatment (Fig. 2-1-B), total H3K27me3 peak numbers increased nearly two-fold (Fig. 2-4-A). The H3K27me3 peaks under the '-Dox 0D' condition significantly overlapped with those of the '+Dox 7D' condition (Fig. 2-4-A), explained by their similar CTR9 KD status. Notably, the H3K27me3 peak numbers decreased to nearly basal levels in responsive to CTR9 restoration by removing Dox for another 7 days (-Dox 7D) (Fig. 2-4-A). The increased H3K27me3 peaks in response to CTR9 depletion did not display a genome-specific enhancement, but rather, the peaks distributed across broad chromatin regions (i.e., promoter, exon, intron and intergenic regions) (Fig. 2-4-B). The H3K27me3 ChIP-Rx results demonstrate that the peak numbers of H3K27me3 are inversely and dynamically regulated by CTR9 levels. Next, we interrogated the peak distribution around transcription start sites (TSS) and found that H3K27me3 peaks in '+Dox 7D' condition have a higher frequency to cluster near the TSS or TSS proximal regions as compared to the '+Dox 0D' condition, implying that CTR9 depletion might trigger H3K27me3 nucleation near the TSS (Fig. 2-4-C). By overlapping H3K27me3 peaks under the basal and CTR9 KD conditions (+Dox 0D vs +Dox 7D), we categorized H3K27me3 peaks into three clusters based on the peak intersection (Fig. 2-5-A). Cluster I contains 10,563 H3K27me3 peaks that only exist in the '+Dox 0D' group. Cluster II encompasses overlapping H3K27me3 peaks (71,098) of both groups. Cluster III contains H3K27me3 peaks (93,180) that are unique to the '+Dox 7D' group. It is noteworthy that the number of peaks in Cluster III is significantly higher than in Cluster I. Figure 2-5-B depicts clustered heatmaps (left) and line plots (right) of the average ChIP-Rx signals around the peak center with ± 5.0kb expansion. Representative snapshots of the genome browser for each cluster are shown in Supplemental Figure 2-B-C. The H3K27me3 peak intensities in cluster I (Fig. 2-5-C, depicted in blue triangles) are similar between the '+Dox 0D' and '+Dox 7D' groups, even though those peaks are only detected in the '+Dox 0D' group by the peak calling algorithm. In contrast, upon CTR9 knockdown, the intensities of H3K27me3 peaks were significantly increased in cluster II (Fig. 2-5-C, black triangles). In addition, new peaks emerged and were classified as cluster III (red triangles). To determine if H3K27me3 peak intensity and peak width are responsive to the dynamic changes in CTR9 levels, we normalized read counts across all three clusters of H3K27me3 peaks in MCF7 CTR9 inducible KD cells. A scatter plot (Fig. 2-5-D) showed that CTR9 loss had negligible effect on cluster I peaks when comparing the basal (+Dox 0D) and CTR9 KD state (+Dox 7D), indicating that these H3K27me3 peaks represent basal H3K27me3 levels in both conditions. In contrast, cluster II/III peaks were skewed towards the CTR9 KD state (+Dox 7D), revealing a significant increase of H3K27me3 levels in the CTR9 KD state (+Dox 7D) as compared to the basal level (+Dox 0D) (Fig. S2D). In addition to the two-fold increase of H3K27me3 peak numbers and the increased peak intensities upon CTR9 depletion, the peak widths were broadened (Fig. 2-5-E). Importantly, these changes were all reversible upon CTR9 recovery. These results demonstrate that loss of CTR9 results in significant expansion of steady state H3K27me3 domains, as well as increased H3K27me3 peak intensities on chromatin, and these changes can be reversed by CTR9 re-expression.

2.3.3 CTR9-responsive H3K27me3 peak genes are likely regulated by PRC2

Despite the genome-wide enhancement of H3K27me3 upon CTR9 depletion, the tendency of H3K27me3 peaks to cluster in the TSS proximal regions (Fig. 2-4-C) prompted us to analyze genes putatively regulated by H3K27me3. Because H3K27me3 peaks are in general broad, we assigned each individual H3K27me3 peak merged from '+Dox 0D' and '+Dox 7D' groups to the nearest genes within the range of TSS-TES±2.5kb (30). Among ~14,000 H3K27me3 peak genes that meet these criteria, 11,483 genes displayed at least a two-fold increase in normalized H3K27me3 ChIP-Rx signals after CTR9 knockdown (+Dox 7D/+Dox 0D, Fig. 2-6-A). Further examination revealed a significant increase of H3K27me3 ChIP-Rx signals from TSS-2.5kb to TES + 2.5kb on these genes upon CTR9 loss, as well as a decrease in H3K27me3 ChIP-Rx signals upon CTR9 restoration. We thus classified them as strong H3K27me3 peak associated genes (Fig. 2-6-B/C). Notably, over 75% of these genes code for proteins (Fig. 2-6-D) whose functions are related to general transcriptional regulation, such as transcriptional activator/repressor activity and RNA Polymerase II mediated DNA binding (Fig. 2-6-E). To deduce their regulation by potential transcription factors (TFs) as well as epigenetic modulators, we performed a *cis*-regulatory factor prediction for the strong H3K27me3 peak associated genes using *BART* tool (Binding Analysis for Regulation of Transcription) (31)(Fig. 2-6-F, Table 2). Among over 900 TFs and epigenetic modulators, YBX1 (Y-box binding protein 1) and REST (RE1 silencing transcription factor) were the top two predicted TFs, and both have been implicated in breast cancer progression (32,33). Interestingly, several PRC2 subunits including EED, EZH2, SUZ12 and JARID2 were identified among the top hits. These results indicate that CTR9 manifests a strong effect on genes that are regulated by PRC2 complex and H3K27me3.

2.3.4 Loss of CTR9 results in enhanced PRC2 chromatin association

H3K27me3 is mainly established by the PRC2-EZH2 complex in human. Given that *cis*-regulatory factor prediction identified several PRC2 subunits at H3K27me3 regulated genes, we examined if CTR9 loss affects PRC2 chromatin recruitment. We performed ChIP-Rx using an antibody against SUZ12, the core subunit of PRC2, in MCF7-tet-on-shCTR9 cells, under the aforementioned treatment conditions (Fig. 2-1-B). We found that the peak numbers of SUZ12 increased by 4-fold from '+Dox 0D' to '+Dox 7D' in response to CTR9 depletion (Fig. 2-7-A), which resembles the changes of H3K27me3 (Fig. 2-4-A). Notably, ~90% of SUZ12 peaks found in '+Dox 0D' condition were also detected in the '+Dox 7D' group (Fig. 2-7-B), suggesting that the new PRC2 binding sites may expand from the pre-existing binding sites. As observed with the change of H3K27me3, CTR9 re-expression (-Dox 7D) led to decreased SUZ12 peak numbers (Fig. 2-7-A). Importantly, around 50%-70% of SUZ12 peaks overlapped with H3K27me3 peaks under each condition (Fig. 2-7-C), demonstrating a strong genome-wide association between PRC2 (enzyme) and H3K27me3 (substrate). To determine how CTR9 refines global H3K27me3 distribution on chromatin, we allocated the SUZ12 ChIP-Rx signal on H3K27me3 peaks as well as the putative H3K27me3 regulated genes. H3K27me3 peak regions (Fig. 2-7-D) and over 11,000 strong H3K27me3 peak genes concurrently displayed dynamic SUZ12 changes in response to CTR9 levels by Dox treatment (Fig. 2-7-E/F), as depicted by an example captured from genome-browser (Fig. 2-7-G). We noted, however, that the magnitude of changes of SUZ12/PRC2 binding intensities were less pronounced as compared to those of H3K27me3 (compare Fig. 2-7-E with Fig. 2-6-B), especially around the newly gained H3K27me3 peak regions (Fig. 2-7-G), when CTR9 was knocked down or re-expressed. Similar to our analyses of H3K27me3 peak associated genes, we found that CTR9 loss led to increased SUZ12 peak width (Fig. 2-7-H), which further consolidates the idea that increased PRC2 binding, at least in part, accounts for increased H3K27me3 deposition. Using the peak-annotation method (Fig. 2-6-A) to assign SUZ12 peaks to the putative regulated genes, we identified > 17,000 putative SUZ12 peak genes, among which 85% are protein-coding genes (Fig. 2-8-A). Moreover, 9,368 SUZ12 peak genes overlapped with H3K27me3 peak genes (Fig. 2-8-B). Notably, a significant number of genes (2115) were identified as H3K27me3 peak genes but lacked SUZ12 binding peaks (Fig. 2-8-B). The reason for 2155 genes harboring strong H3K27me3 signal but weak SUZ12 signals is unclear. Nevertheless, the significant overlap between SUZ12 and H3K27me3 peak associated genes underscore the concordant PRC2 complex binding and histone H3K27me3 deposition that occurs in a CTR9-dependent manner.

2.3.5 CTR9 regulated genes are subjected to epigenetic regulation by PRC2, and CTR9 counteracts the establishment of H3K27me3 repressive domains

To investigate if genes harboring CTR9 binding sites are more likely to be subjected to H3K27me3 regulation than genes without CTR9 binding, we sought to map CTR9 genomic binding sites and derive CTR9 regulated genes from ChIP-Rx binding peaks. Because ChIP-grade CTR9 antibody is not available, we first generated a 3xFlag knock-in MCF7 clonal cell line using CRISPR/Cas9 (Fig. 2-9-A). PCR and sequencing results confirmed the correct insertion of 3 x Flag epitope tag before the translation start codon of CTR9 loci (MCF7-3xFlag-KI-CTR9; Clone#5) (Fig. 2-9-B/C). To verify that the Flag-tagged CTR9 protein was successfully incorporated into PAFc, we performed pull-down using an anti-Flag antibody. The results showed that Flag-CTR9 was enriched in chromatin extract (Fig. 2-9-D), and co-immunoprecipitated with other PAFc subunits (Fig. 2-9-E). The Flag-tag knock-in does not appear to affect cell growth, since the growth rate of the MCF7-3xFlag-KI-Ctr9 clone was similar to that of the parental MCF7 cells (Fig. 2-9-F). To identify highly confident genes regulated by CTR9, we performed ChIP-Rx using two different, commercial Flag antibodies (Cell signaling technology and Sigma). 6,750 genes were identified by overlaying Flag-CTR9 binding peaks using two Flag antibodies, over 85% of which are protein-coding genes (Fig. 2-10-A). TF motif analyses identified COUP-TFII and FOXO3, both of which are TFs that regulate gene expression of multiple pathways in breast cancer (34,35). Interestingly, PRC2 proteins (i.e., SUZ12 and EZH2) were predicted as *cis*-regulatory factors enriched on the putative CTR9 regulated genes (Fig. 2-10-B, Table 3), resembling the regulatory pattern of H3K27me3 peaks associated genes (Fig. 2-6-F). Around 50% of genes with Flag-CTR9 binding sites overlap with those harboring strong H3K27me3 peaks (Fig. 2-10-C). Moreover, the level of H3K27me3 was responsive to CTR9 level changes on the genes containing Flag-CTR9 binding peaks, as shown in an example (Fig. 2-10-D). In addition, the pathway enrichment analysis revealed that genes harboring high confidence Flag-CTR9 binding sites are often linked to pathways of transcriptional regulation (Fig. 2-10-E), in keeping with the known functions of CTR9. Together, our results reveal a potential link between CTR9 binding and PRC2 regulation. To directly examine if CTR9 regulated genes are subjected to PRC2 and

H3K27me3 regulation, we analyzed the ChIP-Rx signals of H3K27me3 and SUZ12, as well as transcriptional active histone marks (H3K4me3 and H3K36me3) on previously identified 240 CTR9 regulated genes (10). These genes were derived from our integrated analysis of microarray gene expression and RNA Polymerase II ChIP-seq signal changes in MCF7-tet-on-shCTR9 cell line (9,10), and thus are classified as high-confident CTR9 target genes. The results showed that CTR9 target genes are highly responsive to H3K27me3 and PRC2 regulation (Fig. 2-11-A). Increased H3K27me3/SUZ12 ChIP-Rx signals were accompanied by decreased H3K4me3/H3K36me3 signals upon CTR9 depletion (Fig. 2-11-A/B), and conversely, H3K27me3/SUZ12 binding on these genes were diminished by re-expression of CTR9, along with the concomitant increase of H3K4me3 and H3K36me3 signals. The H3K27me3, H3K4me3 and H3K36me3 ChIP-Rx signal intensities on an example gene in response to CTR9 loss was illustrated in Fig. 2-11-C. Together, our results strongly support the notion that the CTR9 and PRC2 intricately counteracts each other to establish transcriptionally active or repressive domains. This epigenetic regulation engages multiple histone modifications (e.g., H3K27me3, H3K4me3 and H3K36me3), and is reversible and highly dependent on CTR9 levels.

2.3.6 CTR9 level is a determinant of PRC2 complex subtype

The increased total H3K27me3 levels and broadened H3K27me3 peak-width (Fig. 2-5-B and Fig. 2-5-E) in CTR9 KD cells are in conformity with increased PRC2 recruitment and enhanced PRC2 activity. Although SUZ12 changes coincide with H3K27me3 in response to CTR9 levels, the extent of increase of SUZ12/PRC2 peaks was modest as compared to the increased H3K27me3 intensities (Fig. 2-6-B vs. 2-7-E). Hence, we postulated that CTR9 knockdown might also lead to enhanced PRC2 activity. There are two mutually exclusive subtypes of PRC2: PRC2.1 and PRC2.2, which have been shown to antagonize each other and elicit different capacity for H3K27me3 deposition and propagation. For instance, loss of PRC2.2 specific subunit AEBP2 led to an increase in the amount of PALI1-containing PRC2.1 (23). Moreover, H3K27me3 levels are greatly receded in either MTF2 single KO or PCL proteins triple KO ESCs (36). Because the levels of JARID2, a PRC2.2-specific subunit, is positively correlated with CTR9 expression in our transcriptome studies (9), we surmise that CTR9 KD may cause a PRC2 subtype switch through affecting the expression of PRC2 facultative components. Indeed, depleting CTR9 in MCF7 cells resulted in a dramatic increase in PRC2.1 facultative subunits MTF2, PHF19, and EPOP, and a decrease in JARID2 and AEBP2, the PRC2.2 facultative subunits (Fig. 2-12-A), in total cell lysates and chromatin fractions, whereas the levels of four core subunits remained unchanged. Similar observations were made in two stable MCF7 CTR9 KD cell lines (Fig. 2-12-B). To investigate if the regulation of PRC facultative subunits by CTR9 is reversible, we measured the expression of five facultative subunits of respective PRC2 subtypes in MCF7-tet-on-shCTR9 cells. The expression of PRC2 facultative subunits, and CTR9 protein levels was strongly correlated (Fig. 2-12-C). The decrease of PRC2.2-specific subunits JARID2 and AEBP2 could be partially restored by CTR9 re-expression and was accompanied by the opposite changes in PRC2.1-specific MTF2, PHF19 and EPOP proteins (Fig. 2-12-C). The negative correlation between CTR9 and PRC2.1 facultative subunits (PHF1/MTF2/PHF19 and EPOP) at the mRNA level was also observed in 817 ER-positive primary breast tumor samples in TCGA

(Fig. 2-12-D). To test if loss of CTR9 is sufficient to alter PRC2 subtype equilibrium, we performed glycerol gradient sedimentation to separate two PRC2 subcomplexes from nuclear fractions, based on their difference in molecular weights (i.e., calculated PRC2.2 molecular weight is nearly 100 KDa larger than PRC2.1). When CTR9 was knocked down (+Dox 7D), the PRC2 complex changed from the heavy form of PRC2.2 to the light form of PRC2.1, as detected by subtype-specific subunit levels by western blotting (Fig. 2-12-E). Co-immunoprecipitation using antibodies against EZH2 and SUZ12, the core subunits of the PRC2, was able to pull down other core and auxiliary proteins from nuclear extract, and the results were in conformity with PRC2.2 to PRC2.1 subtype switching in response to depletion of CTR9. Specifically, PRC2 core subunits tended to co-precipitate PRC2.2-specific JARID2 and AEBP2 proteins when CTR9 was expressed. Knocking down CTR9 resulted in enrichment of PRC2.1-specific subunits MTF2/PHF19 and EPOP (Fig. 2-12-F). Biotinylated H3K27me3 peptide pulldown (Fig. 2-12-G) further confirmed the PRC2.2 to PRC2.1 switch. Thus, we conclude that this PRC2 subtype switch is likely due to the relative abundance of facultative subunits, which are highly responsive to CTR9 levels. Because PRC2.1 was proposed to elicit higher histone methylation activity than PRC.2.2, we prepared nuclear extract from CTR9 inducible KD MCF7 cells with and without Dox treatment and used them as enzyme sources for the *in vitro* methylation assay. Recombinant histone H3.1 or recombinant poly-nucleosome were used as substrates (Fig. 2-13-A). The results showed that nuclear extract from ‘+Dox 7D’ cells elicited higher histone methyltransferase (HMT) activity than that from ‘+Dox 0D” cells on H3K27, regardless of the substrates used (Fig. 2-13-A). In addition to HMT activity changes *in vitro*, we performed ChIP-Rx for JARID2, a PRC2.2 specific subunit, and MTF2, a PRC2.1

specific subunit. Upon CTR9 depletion (+Dox 7D), decreased JARID2 and increased MTF2 genomic association were observed across the SUZ12 peaks (Fig. 2-13-B). Despite the inverse intensities of JARID 2 and MTF2 ChIP-Rx, their binding peaks overlap with those of SUZ12 and H3K27me3, as shown by an example gene (Fig. 2-13-C). Further analyses of the global JARID2, MTF2 and H3K27me3 normalized read counts across all SUZ12 peaks confirmed a substantial shift from JARID2 containing PRC2.2 to MTF2 containing PRC2.1 in response to CTR9 depletion, as illustrated in the scatter plot (Fig. 2-13-D). These data collectively support the model that CTR9 loss triggers the expression changes of PRC2 facultative subunits, leading to a switch from the enzymatically less active PRC2.2 to more active PRC2.1, which facilitates the propagation of H3K27me3 repressive domains.

2.3.7 CTR9 depletion sensitizes breast cancer cells to PRC2 complex inhibitors

High levels of EZH2 and H3K27me3 in ER-negative breast cancer patients predict poor overall survival, and EZH2 inhibitor GSK343 has been shown eliciting robust inhibition of ER-negative breast tumor growth in a preclinical model (37). The remarkable increase of total H3K27me3 levels upon depletion of CTR9 implies an addiction of cells to H3K27me3 for survival. If this were true, we expect that CTR9 knockdown cells would elicit higher sensitivity to EZH2 inhibitors than the parental cells. Cell viability was measured after treatment with UNC1999, a chemical inhibitor targeting both EZH2 and EZH1, and UNC2400, a structurally similar but inactive analog compound, to exclude the possibility of off-target effects (38). As expected, CTR9 KD MCF7 cells were more sensitive to UNC1999 than parental MCF7 cells, as shown by MTT assays. EZH2 KD MCF7 cells (shEZH2) were included as a negative control (Figure 2-14-A), and, indeed, were insensitive to UNC1999. To exclude a drug-specific effect, we examined two additional mechanistically distinct PRC2 inhibitors, GSK343 and EED 226 (39,40). The results (Fig. 2-14-B) were similar to those of UNC1999. In addition to MTT assays, we counted EdU positive proliferating cells in the presence of DMSO, UNC1999 and UNC2400. The results confirmed that CTR9 KD MCF7 cells were more sensitive to EZH2 inhibitors than parental cells (Fig. 2-14-C). Collectively, our results demonstrate that depletion of CTR9 leads to increased sensitivity towards PRC2 inhibitors. To determine whether UNC1999 causes elevated apoptosis or necrosis upon CTR9 depletion, we performed flow cytometry analyses after labeling cells with propidium iodide (PI) and annexin V-FITC (Fig. 2-14-D). The dose-responsive increase of apoptosis and necroptosis by UNC1999 was quantified in Figure 2-14-E. Both apoptotic and necrotic cells were largely detected in CTR9 KD cells, but not in the shControl cells after 1 - 5 μM UNC1999 treatment for 2 days. When the concentration of UNC1999 increased to 12.5 μM, nearly all the CTR9 KD MCF7 cells became apoptotic or necrotic; however, ~30% of control KD cells remained viable (Fig. 2-14-D). Next, we employed a duo-fluorescence based cell cytotoxicity kit to quantify the differential cytotoxic response between Control KD and CTR9 KD cells towards UNC1999, both in 2D monolayer (Fig. 2-14-F) and in 3D tumor spheroids (Fig. 2-14-G). When treated with ascending concentrations of UNC1999 from 1 μM to 50 μM for 24 hours, CTR9 KD MCF7 3D spheroids (shCTR9#3/shCTR9#5) elicited stronger cytotoxic response (more red cells and less green cells) than the control group (shControl). UNC2400 (50 μM) serves as a negative control (Fig. 2-14-G), and no cytotoxic effect was detected. Differences in the percentage of live and dead cells were quantified (Fig. 2-14-H). These results reinforced that CTR9 KD cells are more sensitive to EZH2 inhibitors. Collectively, CTR9 depletion renders cells more sensitive to EZH2 inhibitors, as measured by the inhibition of growth/proliferation, as well as induction of apoptosis and necrosis in MCF7 cells.

2.4 DISCUSSION

In this study, we reported that CTR9 governs the establishment of H3K27me3 repressive domains, beyond its well-characterized functions in transcriptional regulation and modulation of transcription-coupled histone modifications (i.e., H2Bub, H3K4me3, H3K36me3). This discovery provides an explanation for the discrepancy between the phenotypes observed in lower eukaryotes (i.e., yeast) and multicellular organisms when CTR9 is depleted. While CTR9 is not an essential gene in *S. cerevisiae* (41,42), CTR9 knockout causes early embryonic lethality in higher eukaryotic organisms such as *Drosophila*, zebrafish and mouse (43-45). The requirement of CTR9 in preimplantation development of mice resembles the phenotypes that result from lacking core PRC2 subunits SUZ12, EZH2 and EED (46). While PRC2 and H3K27me3 play crucial roles in establishing repressive chromatin regions, and safeguarding cell identity in multicellular organisms (12), neither PRC2, nor histone H3K27me3, exists in yeast. Our results indicate that while CTR9 maintains transcriptional control across species, controlling PRC2-repressive domains is a new function acquired over the course of evolution. We surmise that the embryonic lethality of CTR9-null metazoans is more likely attributed to deregulated H3K27me3 than the transcription inhibition *per se*.

CTR9 is not among the 148 PRC2 interaction partners that are enriched in EZH2 and SUZ12 immunoprecipitants in ESCs (47). Therefore, the significantly elevated levels and genome-wide distribution of H3K27me3 upon loss of CTR9 is unexpected, which implies that, despite no physical interaction, CTR9 is functionally related to PRC2. Given that CTR9 is the scaffold protein of PAFc which regulates multiple steps of transcription, and that the switch of PRC2 subtypes is accompanied by loss of CTR9, we envision that at least three mechanisms may collectively contribute to the establishment of H3K27me3 domains: inhibition of transcription, enhanced PRC2 recruitment, and alteration of PRC2 activity.

First, inhibition of transcription alone has been shown to be sufficient for gain of H3K27me3 in the gene bodies (48,49). In mouse ESCs, transcriptional inhibition by RNAPII inhibitors 5,6-dichloro-1-beta-D-ribofurano-sylbenzimidazole riboside (DRB), and triptolide, induces genome-wide ectopic PRC2 recruitment (49). Hosogane M. *et al.* also reported that abrogation of transcription induces accumulation of H3K27me3 in the gene bodies (48). Emerging evidence have shown that the active histone marks inhibit PRC2 activity in transcribed regions (50) and that both H3K4me3 and H3K36me2/3 are inhibitory to PRC2 activity (51,52). Because H3K4me3 and H3K36me3 are associated with actively transcribed genes, transcription inhibition by loss of CTR9 could result in H3K27me3 accumulation in gene bodies. Indeed, we have previously shown that RNAPII binding, H3K4me3, and H3K36me3, are drastically decreased by knocking down CTR9 in MCF7 cells (9,10) (Fig. 2-15). Henceforth, disruption of active transcription favored H3K4me3/H3K36me3 marks by CTR9/PAFc eviction will inevitably results in precedence of H3K27me3 in the gene proximal regions.

Second, H3K27me3 levels are correlated with PRC2 duration on chromatin. PRC2 alone exhibits the lowest residency time on chromatin through a hit & run mechanism, but PRC2-chromatin association could be stabilized when complexed with JARID2 when forming PRC2.2 or stabilized by MTF2 in the PRC2.1 at an even greater level (22). As expected, our ChIP-Rx results showed that although >50% of genes harboring SUZ12/PRC2 binding sites overlap with those containing H3K27me3, some genes contain only H3K27me3 or SUZ12 (Fig. 2-8-B). Those potent H3K27me3 responsive regions without an obvious increase of SUZ12/PRC2 binding could be due to the dissociation of SUZ12 after marking H3K27me3, the efficacy of ChIP-Rx using SUZ12, or corresponding to the distal spreading sites with attenuated PRC2 binding. Additional H3K27me3 and SUZ12 ChIP-Rx experiments with the gradual decline of CTR9 expression will help distinguishing the initiation or propagation of PRC2 association events.

Third, we envision that the PRC2 subtype switching is the major mechanism for the global H3K27me3 increase observed. JARID2, a PRC2.2-specific subunit, contains a Jumonji-C domain, but it has no enzymatic activity of its own (53). A previous study showed that depletion of AEBP2 results in up-regulation of PALI1/2 (23), and conversion from JARID2-containing PRC2.2, to the MTF2-containing PRC2.1 complex (54). Moreover, JARID2 knockout in differentiated ESCs causes aberrant deposition of H3K27me3 in intergenic regions of the genome (55). This is analogous to the effects of loss of CTR9, where a decrease in JARID2 and AEBP2 levels is accompanied by an increase of H3K27me3 domains in the intergenic regions (Fig. 2-16), and concomitantly, PRC2 subtype switching from PRC2.2 to PRC2.1 (Figure 2-12/13). Therefore, we reason that the loss of CTR9 resulted in a decrease of JARID2, leading to the formation of the more active PRC2.1 complex, and thus the elevated H3K27me3 levels. In support of this model, MTF2 and other PCL proteins have been shown to bind CpG-rich DNA, and knockout of MTF2 in mESCs leads to reduced SUZ12 binding at CpG islands and concomitant depletion of H3K27me3 (56). Our data infer a chromatin surveillance mechanism: In the presence of CTR9, the predominant form of PRC2 is PRC2.2 to maintain the basal levels of H3K27me3. When CTR9 is removed, PRC2.1 replaces the PRC2.2 to effectively establish and expand the H3K27me3 repressive domains, including regions with stalled transcriptional machinery due to loss of CTR9. Collectively, our studies reveal the complex mechanisms by which CTR9 demarcates PRC2-mediated H3K27me3 domains, and the previously unidentified interplay between transcriptional activation machinery and transcriptional repressive complexes. Although these findings were made in breast cancer cell lines, the general principal for the establishment of H3K27me3 domains governed by CTR9 is likely conserved in other biological systems (e.g., ESCs).

Mutations in subunits of PRC2 have been increasingly identified in multiple cancers, resulting in changes in the global levels, as well as the genome-wide distribution of H3K27me3 (24). These changes in cancer cells often confer context- dependent blocks to cellular differentiation and promote oncogenic signaling pathways. Either overexpression of EZH2, or inactivation of negative regulators of PRC2, augments the dependency of cancer cells on H3K27me3 and PRC2, indicating that PRC2 inhibition can augment the therapeutic vulnerability of cancer cells (57). For example, acute myeloid leukemia and multiple myeloma cell lines with KDM6A mutations are more sensitive to EZH2 inhibitors than KDM6A wild type expressing lines (58,59). We found that either inducible or permanent CTR9 KD MCF7 cells elicit increased sensitivity to PRC2 inhibition, indicating that loss of CTR9 renders cells more addicted to H3K27me3 and PRC2. GSK126 and EPZ-6438, two EZH2 specific inhibitors, are under clinical investigation for treating lymphomas (27). In 2020, a first-in-class, orally bioavailable EZH2 inhibitor – tazemetostat, received accelerated approval by FDA, for treatment of epithelioid sarcoma. Furthermore, tazemetostat appears to be promising to treat patients with B-Cell NHL and other solid tumors (60). Because depletion of EZH2 suppressed ER-negative tumor growth and metastasis in preclinical models (61), EZH2 has emerged as a potential therapeutic target for triple-negative breast cancer (TNBC). Our data that TNBC cell lines display higher levels of EZH2 and H3K27me3 (Fig. 2-17) support the application of PRC2 inhibitors in treating TNBC. Moreover, depletion of CTR9 in ER-positive cells increase sensitivity of cells to PRC2 inhibition by >10 fold, which suggests that EZH2 inhibitors may also be applicable to CTR9 low expressing, ER-positive breast cancer. We speculate that CTR9 levels, rather than ER status, is a predictive biomarker for PRC2 dependency in breast cancer cells. Since CTR9 depletion generates therapeutic vulnerability to pharmacological inhibition of PRC2, the CTR9 expression levels may be used as a biomarker for predicting PRC2 dependency and EZH2 inhibitor sensitivity in broad cancer types.

Our findings that CTR9 demarcates PRC2-mediated H3K27me3 levels and genomic distribution provide unique insights as to how transcriptionally active states are converted to repressive chromatin regions. CTR9 silencing results in the loss of imprinted genes during preimplantation development in mice (45), which may cause genome instability. Exon 9 deletion of *CTR9* were recently discovered in Wilms tumors. Whether H3K27me3 is elevated in CTR9-mutated Wilms tumors, and whether CTR9-mutant expressing tumors are sensitive to EZH2 inhibitors, awaits investigation. The new function of CTR9 in regulating PRC2-repressive H3K27me3 domains opens new avenues for understanding the biological functions of CTR9 in development and broad cancer types, and for exploring the possibility of using CTR9 as a biomarker to select cancer patients who are responsive to epigenetic therapies targeting PRC2 complex.

2.5 MATERIALS & METHODS

Cell lines and Cell Culture

HEK293T, MCF7, T47D cell lines were obtained from American Type Culture Collection (ATCC) and maintained in Dulbecco's modified medium (DMEM) (Gibco) supplemented with 10% fetal bovine serum (FBS) (VWR) and 1% Penicillin-Streptomycin (P/S) (Gibco). BT474 cell lines were obtained from ATCC and maintained in RPMI 1640 medium (Gibco) supplemented with 10% FBS and 1% P/S. MCF7-tet-on-parental cells and MCF7-tet-on-shCTR9 cells were generated previously (9) and maintained in DMEM supplemented with 10% FBS and 1% P/S. All cells were cultured at 37°C in a humidified atmosphere containing 5% CO_2.

Construction of MCF7-3xFlag-KI-CTR9 cell line

Guide RNA (gRNA) targeting Exon1 of CTR9 was prepared by mixing CRISPR RNA (crRNA) and trans-activating CRISPR RNA (tracrRNA) in equimolar concentrations in a sterile microcentrifuge tube to a final duplex concentration of 100 µM. RNAs were heated at 95ºC for 5 min and allow to cool to room temperature (15–25ºC) on the bench top. The ribonucleoprotein particles (RNP) were formed by mix the Cas9 enzyme and gRNA targeting Exon1 of CTR9 and incubated at room temperature for 10 min. MCF7 cells were transfected with the RNPs and ssDNA for Flag by using Lonza 4D-Nucleofector system. Single cells were plated in 96 well plates, after single colony formation, genomic DNA of each single clone were purified and PCR were performed to detect whether flag tag was knocked in the N-terminal of CTR9 gene, PCR products were also sequenced. To further confirm that Flag was successfully knocked in, proteins of MCF7-flag-KI-CTR9 cells and MCF7 parental cells were extracted, and IP was performed by using Flag antibody, the results showed that CTR9 as well as other PAFc components could be pulled down in MCF7-3xFlag-KI-CTR9 cells rather than in parental cells.

Primers and oligonucleotides for construction of MCF7-3xFlag-KI-CTR9 cell line are shown below.

Flag ssDNA:

GCTGCGGAGCGGCGGGGCGAGACACTTGCTCGCCTTTTGACCCCATCATGGACTACAAAG
ACCATGACGGTGATTATAAAGATCATGACATCGATTACAAGGATGACGATGACAAGCTCAT
GTCGCGGGGCTCCATCGAGATTCCCCTCCGGGACACTGACGAGGTAAGTGTCGTGTATGG

gRNA sequence: CTTTTGACCCCATCATGTCG

Flag-seq Forward: TTGTTTAAGCGGCTGACGGG

Flag-seq Reverse: CCCGGAGGGGAATCTCGATG

3D spheroids formation

100,000 — 300,000 cells of MCF7-shControl/shCTR9#3/shCTR9#5 were fully resuspended in 200 – 250 µl of DMEM media and seeded in 96-well round bottom plates with ultralow attachment (Corning, Product# 4515), followed by centrifugation at 500g for 10 minutes. 3D spheroid cultures were grown at 37°C up to 4 days in a humidified atmosphere with 5% CO_2.

Virus packaging, infection and preparation of stable knockdown cell line

Stable knockdown cell lines were generated by lentivirus infection. The virus packaging vectors pME-VSVG and psPAX2 were purchased from Open Biosystems. For lentivirus packaging, 2 µg pME-VSVG, 2 µg psPAX2 and 4 µg lentiviral shRNA expression vectors were co-transfected into HEK293T cells cultured in one 10-cm dish using transIT-LT1 reagent (Mirus Bio) according to the manufacturer’s protocol. Medium was replaced with fresh DMEM supplemented with 10% FBS/ 1%P/S 8-10 hours post transfection. 48 hours after transfection, the supernatant containing the virus particles was collected by centrifugation (1500 rpm, 5 minutes) and subsequent filtered through a 0.45 µm syringe filter (Thermo Scientific). Approximately 1/5 volume of Lenti-X concentrator (Clonetech) was added to concentrate the virus tilter overnight at 4°C. For infection, 1 mL of virus was mixed with 1 mL of fresh cell culture medium, and polybrene was added at a final concentration of 8 μg/mL in order to increase the infection efficiency. After overnight infection, the culture medium was changed. Cells were infected overnight, followed by changing of culture medium. Cells were selected with 2 μg/mL puromycin for at least one week to generate stable cell lines.

Preparation of the chromatin fraction

Cells were harvested after trypsinization. After washing with 1X PBS, two to five volumes of lysis buffer were added to the cell pellet [10 mM HEPES pH7.4, 10 mM KCl and 0.05% NP-40, 1X protease inhibitor cocktail (Sigma-Aldrich), phosphatase inhibitor (1 mM $NaVO_4$) and deacetylase (5 mM TSA, Sigma-Aldrich)], and then incubated on ice for 20 mins. Nuclei pellets were separated by centrifugation at 14,000 rpm at 4°C for 10 mins. Subsequently, nuclei pellets were washed once with lysis buffer, resuspended in two to five volumes of low salt buffer [10 mM Tris-HCl pH7.4, 0.2 mM $MgCl_2$, 1X protease inhibitor cocktail phosphatase inhibitor (1 mM $NaVO_4$) and deacetylase (5 mM TSA), and 1% Triton X-100], and incubated on ice for 15 minutes. Chromatin fractions were separated by centrifugation at 14,000 rpm at 4°C for 10 mins, resuspended with two to five volumes of 0.2N HCl, and incubated on ice for 20 minutes. After centrifugation, the supernatant containing chromatin associated proteins was neutralized with an equal volume of 1 M Tris-HCl pH 8.0.

Histone extraction and purification

MCF7/BT474/T47D cells were harvested after trypsinization. After washing with 1X PBS, cell pellets were resuspended in two volumes of lysis buffer [50 mM Tris-HCl pH7.4, 150 mM NaCl ,10% Glycerol and 0.05% NP-40]. Protease Inhibitors (1X protease inhibitor cocktail) and HDAC inhibitor (10 mM sodium butyrate) were added before use. The cell pellets were incubated on ice for 30 mins, followed by a brief sonication. After 15 mins of centrifugation at 13,000 rpm at 4°C, the supernatant was saved as whole cell lysate and the pellet was used for histone extraction. Pellets were washed twice using NIB buffer [10 mM Tris-HCl pH7.5, 2 mM $MgCl_2$, 3 mM $CaCl_2$ and 1% NP40] containing 100 mM NaCl, and once with NIB buffer containing 400 mM NaCl. The pellet was finally resuspended in NIB buffer (400 mM NaCl) without NP40. For acid extraction of histones, double volume of 0.2N HCl was added and incubated overnight at 4°C. After centrifugation at 13,000 rpm for 15 mins at 4°C, solubilized histone in supernatant was dialyzed in ddH_2O overnight at 4°C using 10K MWCO Dialysis Tubing (Thermo). Histones were lyophilized and dissolved in ddH_2O.

Liquid Chromatography and Quantitative Histone Mass Spectrometry (LC-MS/MS)

1. Chemical derivatization of histones and tryptic digestion: Take 25 µg of purified histone samples and dissolve them in 100µL 100 mM TEAB buffer (pH 8.0). Add 4µL 4% $^{13}CD_2O$ (w/v) and 4µL 600 mM $NaBD_3CN$ to the samples and vortex them at room temperature for 1h to label the free and mono-methylated lysine with heavy isotopic methyl. Terminate the reaction by acidifying the sample with TFA. Transfer the samples to 10K MWCO ultracentrifuge tube (Millipore) and centrifuge the samples for 15 min at 14,000 g at 4°C to remove the reaction reagents. Continually add 200 µL 100 mM TEAB buffer in the ultracentrifuge tube and centrifuge the samples for 15 min at 14,000 g at 4°C to wash histone sample for 3 times. Add 100 µL 100mM TEAB buffer and 1µg trypsin in the ultracentrifuge tube and put the samples at 37°C incubators for 16 h. Collect the digested sample by centrifuging the samples for 15 min at 14,000 g at 4°C. Wash the ultracentrifuge tube two times with 100µL 100 mM TEAB buffer and combine the follow-through with digested sample and dry down. Resolve the dry down sample with 100 µL 50 mM TEAB buffer and add 15µL 25% propionic anhydride buffer (v/v in ACN) in the sample, add 10-15 µL 28% NH_4OH to keep the pH of the sample reaction to be around 8.0. Put the sample tube on vortex for 20 min to label the N-termini of digested histone peptides with propionyl. After propionylation, the sample was desalted with Sep-Pak cartridge (Waters) and lyophilized.

2. LC-MS/MS for histone modification: Lyophilized histone peptides were resuspended in 0.1% formic acid (FA) and analyzed on a Dionex U3000 ultra performance liquid chromatography system coupled to a Q-Exactive HF quadrupole orbitrap mass spectrometer (Thermo Fisher Scientific). A Waters BEH 300Å C18 reversed phase capillary column (150 mm x 75 µm, 1.7 µm) was used for separation. Water with 0.1% FA and acetonitrile with 0.1% FA were used as mobile phases A and B, respectively. The flow rate was set to 0.300 µL/min. 2 µL of peptide sample was injected onto the column and separated over a 120-minute gradient as follows: 0-1 min 3-10% B; 1-90 min 10-35% B; 90-92 min 35-95% B; 92-102 min 95% B; 102-105 min 95-3% B; 105-120 min 3% B. The data was acquired under data dependent acquisition mode (DDA, top 20). Mass spectrometric conditions were as follows: spray voltage of 2.8 kV, no sheath and auxiliary gas flow; heated capillary temperature of 275°C, normalized high-energy collision dissociation (HCD) collision energy of 33%, resolution of 120, 000 for full scan, resolution of 60, 000 for MS/MS scan, automatic gain control of 2e5, maximum ion injection time of 100 ms, isolation window of 1.6, and fixed first mass of 110 m/z

3. Data analysis and relative quantification of histone PTMs: Because histones possess multiple post-translational modifications, and after heavy isotopic di-methylation and propionylation they are even more heavily modified and may contain several isoforms for the same peptide sequence with different modifications, it is challenging to identify all different forms of histone modification peptides. Here in this work, the most frequently observed modifications including the mono-methylation, di-methylation, tri-methylation, and acetylation on lysine residue of histone H3 were analyzed. The same histone peptide possess different modifications can firstly be identified according to their difference in mass over charge (m/z). Then the peptide can be additionally distinguished according to their retention time difference on the RP-HPLC column (trimethylated peptide ≈ unmodified (possesses two heavy isotopic methyl), mono (possesses one heavy isotopic methyl), and di-methylated peptide < acetylated peptides. To relatively quantify the abundance of histone PTMs, we used the area of each identified peptide peak in the MS chromatogram for comparison. Normally same peptide may have different charge state ions in LC-MS analysis. We only choose the highest intensity ions to measure their peak area. The total peak area of a histone peptide with all different PTM forms is regarded as 100%, and the percentage of each PTM on the peptide is calculated by dividing the area of the PTM peak area by the total peak area. To distinguish histone peptide isoform, we also investigate the MS/MS spectrum to calculate the ratios of b and/or y ions that were different between the two or more peptide isoforms, and the ratio is used to continually calculate the relative quantity of the peptide isoforms.

Preparation of nuclear lysates

Nuclear lysates were prepared as described (62) and used for co-immunoprecipitation and peptide pulldown experiments. Cells were harvested in ice-cold PBS and extracted at 4°C in buffer containing 50 mM Tris-HCl pH7.5, 5 mM EDTA, 250 mM NaCl and 0.1% NP-40 supplemented with protease and phosphatase inhibitors for 30 mins. After centrifugation at 13,000 rpm at 4°C for 1 hour, the supernatant was collected, and mixed with two volumes of buffer containing 50 mM Tris-HCl pH7.5, 5 mM EDTA, 100 mM NaCl, 0.1% NP-40 and 10% glycerol.

Co-Immunoprecipitation using nuclear extract

Co-IP was performed as previously described (63). Briefly, immunoprecipitations were performed in IP buffer [50 mM Tris-HCl pH7.5,150 mM NaCl, 2 mM $MgCl_2$, 0.5% NP-40 and 10% Glycerol] supplemented with protease and phosphatase inhibitors before use. Approximately 1.5 - 2 mg nuclear protein extract, as quantified by a Bradford assay, was mixed with 5 μg of antibody and 50 μl of protein A magnetic Dynabeads (Invitrogen, washed previously 3x in IP buffer) per IP reaction in 750 μl total volume. Beads were washed three times with IP buffer, and once with PBST the following day. Proteins were eluted in 75 μl 2X SDS loading buffer with 50nM DTT and heated at 95°C for 15 mins before loading on an SDS-PAGE gel.

Peptide pull-down using nuclear extract

Peptide pulldown was adapted from published protocol (63). Lysine methylated peptide with a C-terminal biotin tag ATKAAR-Kme3-SAPSTGGVKKPHRYRPG-GGK(Biotin)-NH_2 was synthesized by Active Motif®. For each peptide pull down, 50 μg of magnetic streptavidin beads (Medchem Express) were incubated with 5 μg of peptide in 500 μl of binding buffer [50 mM Tris-HCl pH7.5, 150 mM NaCl, 1 mM EDTA and 1% NP40] for three hours, rotating at room temperature. Peptide-bound beads were washed three times in wash buffer I [50 mM Tris-HCl pH7.5, 150 mM NaCl, 1 mM EDTA and 0.05% Triton X-

100], twice in wash buffer II [50 mM Tris-HCl pH7.5, 150 mM NaCl and 1 mM EDTA]. Samples were vortexed twice with 50 μl U/T buffer [6 M urea, 2 M thiourea, 150 mM NaCl, 30 mM biotin in 10 mM HEPES pH 8.0] at room temperature for 10 min and at 95℃ for 15 min. The two eluates were combined for western blot analysis.

In-vitro **histone methyltransferase assay (HMT) using nuclear extract as enzyme resource**

10 µg of biotinylated histones or poly-nucleosome are bound to pre-equilibrated streptavidin beads for 1 hour at room temperature. Wash the beads with reaction buffer [50 mM Tris-HCl pH8.6, 0.02% Triton X-100, 2 mM $MgCl_2$, 1 mM TCEP] twice after incubation. Pre-bound biotinylated histones or poly-nucleosome were equally aliquoted to each HMT reaction. Nuclear extract pre-cleaned with 1/500 volume of blank streptavidin beads is followed by buffer exchange to reaction buffer using 3 KDa Ultra centrifuge filter. Concentration of pre-cleaned nuclear were then measured by regular Bradford assay. Ascending amount of pre-cleaned nuclear extract were incorporated in the HMT reaction with additional supplement of 100 nM ATP and 100 µM S-adenosyl Methionine (SAM). Incubate the reaction mix at 37°C for 1 hour. Discard the supernatant and wash the streptavidin beads with strong wash buffer 3 times. Biotinylated histones or poly-nucleosome were eluted in equal volume of 2X SDS loading buffer with 50 nM DTT and heated at 95°C for 15 mins before loading on an SDS-PAGE gel.

Glycerol gradient sedimentation

To prepare glycerol gradient in a 5 mL polyallomer tubes (Beckman), pre-filtered K150 buffer [50 mM HEPES pH7.9, 1 mM EGTA pH8.0, 2 mM $MgCl_2$, 600 mM KCl and freshly added protease inhibitors] containing 30% -- 50% glycerol (v/v) were layered from bottom to top. Freshly prepared nuclear extracts were concentrated and resuspended in K150 buffer without glycerol. After Bradford quantification, about 150-200 µg (< 200 µl) of nuclear extract were gently layered on the top of the glycerol gradient. Insert the 5 mL polyallomer tubes in a pre-chilled SW28 rotor and ultracentrifuge at 25,000 g X 14.5 hrs at 4°C (Beckman Optima XPN). Fractionize the glycerol gradient by repeatedly removing

200µl from the top to the bottom without disturbing the tube. Add equal volume of 2X SDS loading dye to each fraction before SDS-PAGE analysis.

Western blotting and Ponceau S staining

Cells were harvested after trypsinization, washed with 1x Dulbecco's phosphate buffer saline (DPBS) (Life Technologies), and lysed in lysis buffer [50 mM Tris-HCl pH 8.0, 400 mM NaCl, 10% glycerol, 0.5% Triton X-100 and 1 x protease inhibitor cocktail (Sigma-Aldrich)]. After a brief sonication, total lysate was centrifuged, and the supernatant was quantified using the BioRad Protein Assay (BioRad). Approximately 30 µg protein was resolved by SDS-PAGE. Proteins were transferred to a nitrocellulose membrane for 1.5 hours at 350 mA. Membranes were blocked with 5% nonfat milk or 5% BSA at room temperature for 1 hour and incubated overnight with diluted primary antibody at 4°C. Membranes were then washed and incubated with HRP-conjugated goat-anti-rabbit or mouse IgG secondary antibody for 1 hour at room temperature. Membrane was incubated with enhanced chemiluminescence reagents (Thermo Scientific) followed by exposure to X-ray films.

For ponceau S staining of histone extraction, the transferred membranes were first briefly wash with ddH_2O. The membranes were then soaked into Ponceau S staining dye and shake for 20 mins at room temperature. Finally, the membranes were washed by de-staining buffer [2% Acetic Acid] till the background turn clean.

ELISA assays for quantification of histone modifications

ELISA measurement of specific Histone H3 modification was performed using Histone H3 Modification Multiplex Assay Kit (abcam) according to manufacturer’s protocol. In brief, extracted histone mixture in Antibody Buffer (provided in kit) was aliquoted to wells coated with specific Histone H3 modification antibodies. After incubation at 37°C for 2hrs, solution in wells was removed and wells were washed 3X in wash buffer (provided in kit). Diluted detection antibody solution (provide in kit) was added and incubated at room temperature for 1hr. After 2x brief wash in wash buffer, developer solution was added followed by incubation at room temperature for 2-10 mins until wells sufficiently turn into blue while blank wells with no histone extract added remain transparent. The reaction was stopped by stop solution (provided in kit), and the wells turned into yellow. The absorbance of each well was read on a microplate reader at 450 nm with an optional reference wavelength of 655 nm. Absorbance output among different samples will first eliminate the background noise measured by the blank wells and subsequently normalized by corresponding absorbance in control wells coated with H3-total antibody.

Cell proliferation and Cell cycle analyses using flow cytometry

For cell counting-based proliferation assays, 1 × 10^5 cells were seeded into six 3.5 cm petri dishes for compound treatment. MCF7-tet-on–shCtr9 cells were pretreated with vehicle or 500 ng/mL Dox for 5 days before seeding to 3.5 cm petri dishes. Media were changed every 48 hours. Cells were trypsinized and counted after Trypan blue exclusion using an automated cell counter (Bio-Rad).

For 3-(4,5-dimethylthiazol-2-yl)-2,5-diphenyltetrazolium (MTT)-based (Sigma-Aldrich) proliferation assays, 2 × 10^3 cells were seeded into 96-well plates for compound treatment. 15 μl MTT (5 mg/mL in DPBS) was added to the cells followed by incubation at 37°C for 1 h. After removing cell culture medium, 50 μL of DMSO was added. The absorbance of the color substrate was measured with a 540-nm filter on a VictorX5 microplate reader (Perkin Elmer), and data were plotted and analyzed using GraphPad Prism 8 software (GraphPad Software, Inc.).

Edu staining-based cell proliferation analysis was performed by using the Click-iT^{TM} Plus Edu Flow Cytometry Assay Kit (Invitrogen) according to manufacturer’s protocol. In brief, cells were labeled with 10 μM Edu staining buffer in culture medium for 2 hours. After a brief wash with 1% BSA in DPBS, cells were harvested by centrifugation. Cells were then fixed in fixative buffer (provided in kit) at room temperature for 15 mins. After washing with 1% BSA in DPBS twice, cells were resuspended in saponin-based permeabilization buffer (provided in kit) at room temperature for 15 mins. 500 μl Click-iT^{TM} Plus reaction cocktail was added to each sample, followed by incubation of the reaction mixture in dark at room temperature for 30 mins. Cells were washed with permeabilization buffer, wash buffer (provided in kit), and then subjected to flow cytometry analysis.

Annexin V and PI Staining by Flow Cytometry

Collect 1-5 x10^5 trypsinizied cells by centrifugation. Wash cells with 1X cold PBS and carefully remove the supernatant. Re-suspend the cells in binding buffer [10 mM HEPES pH 7.4, 140 mM NaCl and 2.5 mM $CaCl_2$] at a concentration of ~1 × 10^6 cells/mL. After a brief centrifugation, cells were resuspended and incubated for 10 min with 0.5 µg/mL Annexin V-FITC and 2 µg/mL PI in 400 µL binding buffer. The cells were immediately placed on ice and analyzed by flow cytometry. Cell fragments were removed by morphological gating. Cells negative for Annexin V-FITC and PI were considered viable, Annexin V-FITC positive and PI negative considered apoptotic, and Annexin V-FITC positive and PI positive considered necrotic.

Cytotoxicity assay of 3D spheroids

Assay was performed according to manufacturer's instruction (Invitrogen, Cat# L3224). In brief, optimized concentration of Calcein AM and Ethidium homodimer-1 as well as 1 µM Hoechest 33342 were added in DMEM media and incubated with spheroids at 37°C for 30 mins. After incubation, those 3D spheroids were immediately subjected to confocal imaging (Nikon W1 confocal) in a live cell incubating chamber. The area of 3D spheroids was measured using NIS-A1R Advanced Research Imaging Software (Nikon - Mager Science) with nuclei annotation.

Immunofluorescence staining of H3K27me3

MCF7-tet-on-shCTR9 cells were seeded on glass bottom 3.5 cm petri dishes and cultured in DMEM supplemented with 10% FBS in the absence or presence of 500 ng/mL Dox. Cells were fixed in 4% formaldehyde for 15 mins, and then washed with DPBS three times. Subsequently, cells were permeabilized in 0.3% Triton X-100 in PBS for 10 mins, blocked with 3% BSA in PBST [PBS + 0.1% Triton X-100] for 1hr, and incubated with H3K27me3 primary antibody (Cell signaling technology) at room temperature for 2 hours or overnight at 4°C. Cells were then washed with PBST, followed by incubation with secondary antibody (Cy5-goat anti-rabbit IgG (H+L), 1:250; Bethyl) for 1 hr at room temperature. After being washed twice in PBST, cells were incubated with 50 nM Alexa Fluor 555 Phalloidin (Cell Signaling Technology) and 1 μg/ml of Hoechest 33342 (Cell Signaling

Technology) at 37°C for 15 mins, then washed twice in DPBS. Fluorescence was detected using a Nikon A1R confocal microscope at appropriate wavelengths at the UW imaging core. Signal intensity was analyzed in NIS-A1R Advanced Research Imaging Software (Nikon - Mager Science)

Quantification of H3K27me3 intensity using flow cytometry

The Dox treatment of MCF7-tet-on-shCTR9 cells was performed as previously described above. Cells were harvested after trypsinization, washed in PBS, and fixed in 4% paraformaldehyde for 15 mins. Subsequently, cells were permeabilized with 0.3% Triton X-100 in PBS for 10 mins, blocked with 3% BSA in PBST for 1 hour, and incubated with Cy5 conjugated H3K27me3 antibody (abcam) in 1% BSA in PBST for 1hr. After washing with PBST, cells were subjected to flow cytometry analysis.

Chromatin immunoprecipitation with exogenous reference genome (ChIP-Rx)

Cells in 15-cm dishes were washed once with PBS before cross-linking with PBS containing 1% formaldehyde for 15mins at room temperature. Crosslinking was quenched with 0.125 M glycine for 5 minutes at room temperature before two washes with ice-cold PBS. Cells were scraped, harvested by centrifugation, and subjected to ChIP assays. Crosslinked cells were lysed with lysis buffer 1 [10 mM HEPES pH 7.0, 10 mM EDTA, 0.5 mM EGTA, 0.25% Triton X-100, supplemented with 0.5 mM PMSF before use] with rotation at 4 °C for 10 minutes. The crude nuclear pellets were collected by centrifugation at 1500 rpm for 4 minutes at 4 °C. The supernatant was discarded, and the chromatin was washed with lysis buffer 2 [10 mM HEPES pH 7.0, 200 mM NaCl, 1 mM EDTA, 0.5 mM EGTA, supplemented with 0.5 mM PMSF before use] for 10 minutes at 4°C with rotation. Nuclear pellets were collected by centrifugation (1500 rpm, 4°C, 4 minutes), resuspended in nuclear lysis buffer [50 mM Tris-HCl pH 8.1, 10 mM EDTA, 1% SDS, supplemented with 1 mM PMSF and 1 x protease inhibitor cocktail (Sigma-Aldrich) before use], and incubated on ice for 10 minutes. Chromatin was sheared to approximately 100bp-1000bp fragments by sonication in ice-water bath at 4°C using a Branson Sonifier 450 with a microtip (40% amplitude, 3 seconds on, 10 seconds off, 5 minutes total pulse time). Sonicated chromatin was centrifuged at 15,000 rpm for 15 minutes at 10°C, and concentration of nuclear proteins was determined using the BioRad Protein Assay (BioRad). Equal amounts of total nuclear proteins were used for ChIP. Nuclear proteins were supplemented with nuclear lysis buffer to achieve equal volumes for different samples, and then diluted 1:10 with dilution buffer [20 mM Tris-HCl pH 8.1, 150 mM NaCl, 2 mM EDTA, 1% Triton X-100, supplemented with 1 x protease inhibitor cocktail before use]. 20 µg of sheared *Drosophila* chromatin derived from S2 cells plus 2 µg H2A.V antibody were supplied. Five percent of the chromatin fraction was removed and saved as input, and the rest was pre-cleared with a normal IgG control before incubating with the antibody of interest overnight at 4°C.

On the following day, the immune complexes were incubated with Dynabeads^{TM} Protein A/G or Dynabeads^{TM} M-280 Sheep anti-Mouse IgG (Life Technologies) (beads were pre-washed with ChIP dilution buffer three times before use) while rotating at 4 °C for 2 hours. The immunoprecipitated materials were subsequently washed once with low salt wash buffer [20 mM Tris-HCl pH 8.1, 150 mM NaCl, 2 mM EDTA, 0.1% SDS, 1% Triton X-100], once with high salt wash buffer [20 mM Tris-HCl pH 8.1, 500 mM NaCl, 2 mM EDTA, 0.1% SDS, 1% Triton X-100], once with LiCl wash buffer [10 mM Tris-HCl pH 8.1, 0.25 M LiCl, 1 mM EDTA, 1% NP-40, 1% deoxycholate], and twice with TE buffer [10mM Tris-HCl pH 8.0, 1 mM EDTA pH 8.0]. Each wash was done with rotation at 4 °C for 5 minutes followed by separation on magnetic stand. The immunoprecipitated material was eluted twice in freshly prepared elution buffer [1% SDS, 0.1 M NaHCO3] with shaking on a vortexer for 20 minutes at room temperature. The eluted and input materials were then digested with proteinase K (200 µg/ml final concentration) at 55°C for 2 hours. The crosslinking materials were reversed by incubating at 65°C in a hybridization oven overnight. DNA was purified using a Qiagen PCR Purification Kit per manufacturer’s protocol.

ChIP-seq library preparation

Prior to ChIP-seq library preparation, the concentration and size distribution of the ChIPed DNA samples was determined using a Qubit Fluorometer (Thermo Fisher Scientific) and the Agilent High Sensitivity DNA Kit (Agilent Technologies), respectively at the Sequencing Facility at the Northwestern University (NUseq core). Approximately 10-100 ng of ChIPed DNA from each condition was used to generate the ChIP-seq library using the Ovation Ultralow System V2 1-16 Kit (NuGEN Technologies), according to the manufacturer's protocol. Briefly, the DNA was end-repaired and ligated to Illumina sequencing adaptors. The ligated DNA was purified using Agencourt RNAClean XP beads (Beckman Coulter). A subsequent PCR amplification step (8-15 cycles) was performed to add linker sequence to the purified fragments for annealing to the Genome Analyzer flow-cell. Following PCR amplification, the library was separated on a 2% agarose gel (120 V, 1.5 hours) to select a narrow range of fragment sizes, and bands between 200-500 bp were excised. The library was purified from the excised agarose gel using the Qiagen MiniElute PCR Purification Kit following the manufacturer's protocol. Quality control for the size, purity, and concentration of the final ChIP-seq libraries was performed at the Sequencing Facility at University of Wisconsin-Madison Biotechnology Center. Qualified libraries were deep sequenced using an Illumina HiSeq 4000 per the manufacturer's instructions at the Northwestern University (NUseq core).

Bioinformatic analyses of ChIP-Rx datasets

ChIP sequencing reads that passed quality score were aligned to the human reference genome (hg38) using Bowtie2 (v2.4.1) (64). Only unique alignments that passed high mapping quality (MAPQ>30) were retained for downstream analysis. Duplicated reads and reads resides in hg38 blacklist regions (https://github.com/Boyle-Lab/Blacklist/tree/master/lists) were eliminated by sambamba tools (v0.7.1). Sequencing reads were also aligned to the *Drosophila* genome (dm6) and normalization factors (Rx factor) were calculated after removing multi-mapping and duplicated reads. Bigwig files were generated at a resolution of 20bp using the bamCoverage utility from the deepTools (v3.4.3) suits (65) and data were subsequently visualized as ChIP-Rx normalized tracks using IGV genome browser (v2.8.9). Wiggletools (v1.2.3) was used to generate the mean of bigwig files from two biological replicates. Peaks were called using MACS2 (v2.1.4) (66) with FDR<0.01 for narrow beaks and FDR<0.05 for broad peaks. Peaks intersection was performed by bedtools (v2.29.2). Overlapped peaks that shorter than sequencing tag (100bp) will be discarded. Average ChIP-Rx signal on particular regions or genes were calculated by multiBamSummary/ multiBigwigSummary utility from the deepTools (v3.4.3) suits. All heatmap and average line-profile plots were made using plotHeatmap/ plotProfile utility also in deepTools (v3.4.3) suits.

Peaks annotation was performed by ChIPseeker (v1.26.0) package in R. Peak associated genes are assigned to a nearest peak if it is within the range of TSS-TES±2.5kb

Pathway enrichment (GO) and Motif analysis were performed by functional annotation tool in DAVID Bioinformatics Resources (v6.8) and Homer Motif Analysis in Homer software (v4.11)

mRNA expression correlation analysis using the published breast tumor RNA-seq data from TCGA

For Figure 5C, TCGA Breast Cancer clinical records and RNA-seq datasets were downloaded from cBioPortal (https://www.cbioportal.org). Estrogen receptor (ER) status was determined by the entry 'breast_carcinoma_estrogen_receptor_status' in patient's clinical record. There are 817 ER positive patients have primary tumor RNA-seq data. RNA-Seq by Expectation Maximization (RSEM) to all samples were used to study gene expression levels. Pearson correlation was calculated between two genes' $\log_{10}$ (RSEM). P-values were adjusted by Benjamini & Hochberg procedure to account for multiple hypothesis testing.

Statistical analysis

Statistical comparisons between two groups for ChIP-Rx data were performed with Graphpad Prism software 8.0 using an unpaired two tails t-test with Welch correction or paired two tails student's t-test correspondingly. The sample size (n) is indicated in the figure legends and represents peak or gene numbers. Details for sequence data analyses and statistical significance are described in the specific **METHOD** section.

2.6 FIGURES & LEGENDS

Figure 2-1.

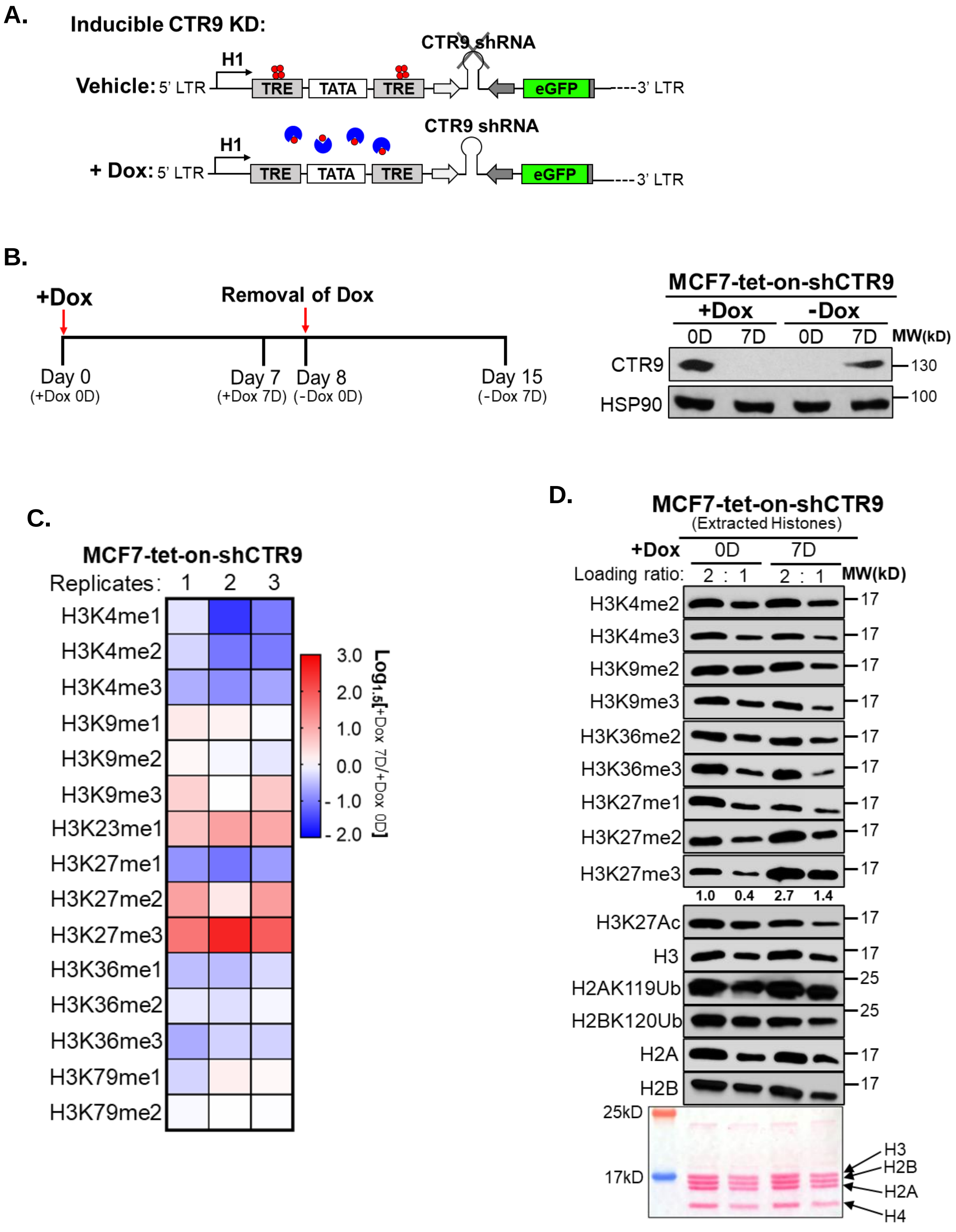

Figure 2-1.

- **A.** Schematic design of doxycycline inducible CTR9 knockdown cell line MCF7-tet-on-shCTR9.
- **B.** Schematic workflow of inducible CTR9 knockdown in MCF7 cells by treatment with doxycycline (Dox) for 0 to 7 days and Dox removal for 0 to 7 days (*Left*). Western blotting showed the depletion of CTR9 by Dox treatment for 7 days and recovery of CTR9 protein by removal of Dox after 7 days (*Right*).
- **C.** Heatmap showing the Log1.5 relative fold-change of histone methylation levels on '+Dox 7D (7 days)' over '+Dox 0D (0 day)' measured by liquid chromatography tandem mass spectrometry (LC-MS/MS) in MCF7-tet-on–shCTR9 cells.
- **D.** Western blot analyses of extracted histones after treatment with Dox for 0 day or 7 days in MCF7-tet-on–shCTR9 cells (*Top*). Ponceau S staining of histones (*Bottom*). Each sample is loaded in two-fold dilution. The bands intensity of H3K27me3 are quantified by ImagePro after normalizing with H3 loading controls.

Figure 2-2.

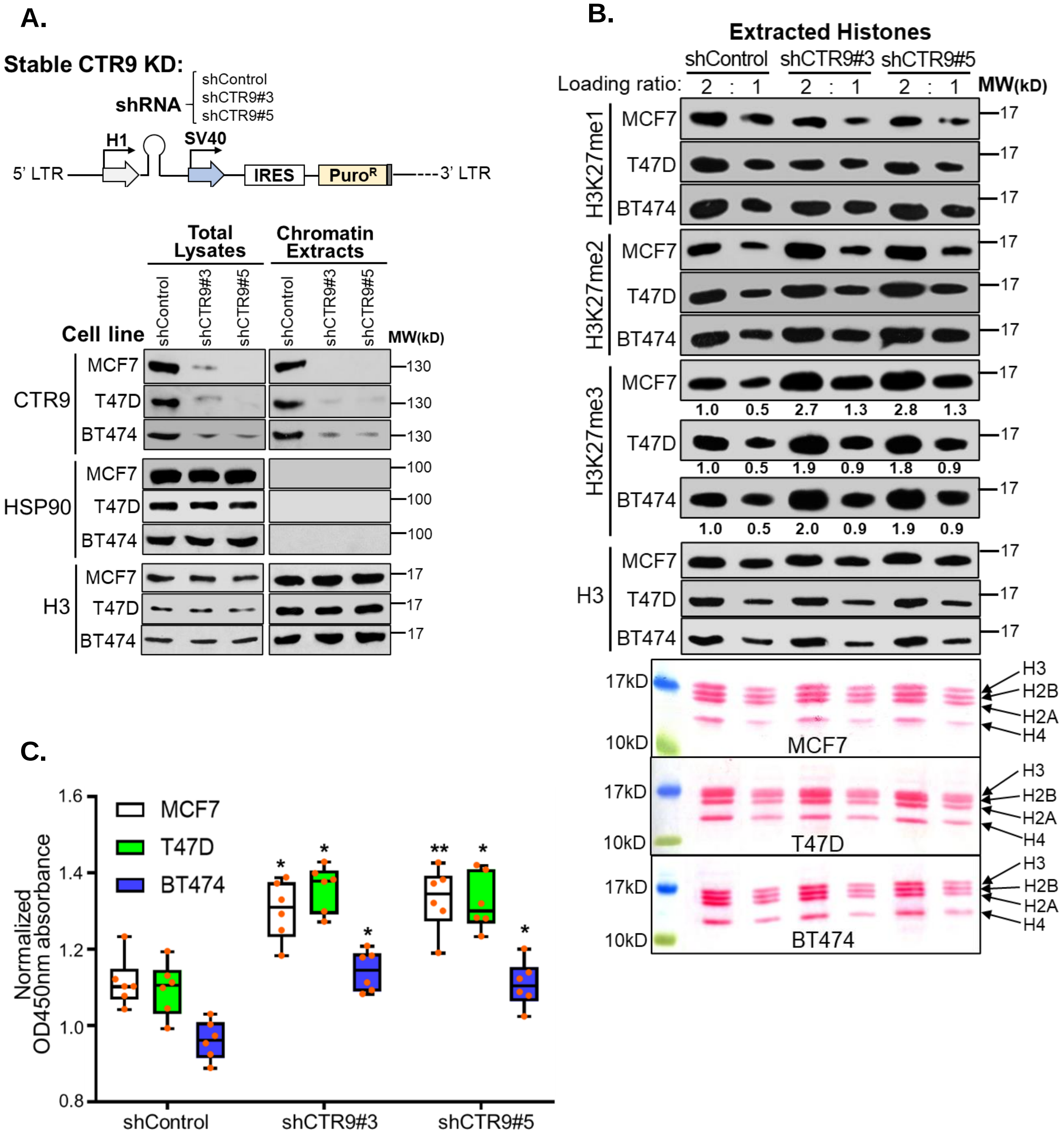
A.
Stable CTR9 KD:
shRNA
shControl
shCTR9#3
shCTR9#5
H1
SV40
5' LTR
IRES
Puro^R
3' LTR
Total Lysates
Chromatin Extracts
Cell line
shControl
shCTR9#3
shCTR9#5
shControl
shCTR9#3
shCTR9#5
MW(kD)
CTR9
HSP90
H3
MCF7
T47D
BT474
130
100
17
B.
Extracted Histones
shControl
shCTR9#3
shCTR9#5
Loading ratio: 2 : 1 2 : 1 2 : 1
MW(kD)
H3K27me1
H3K27me2
H3K27me3
H3
MCF7
T47D
BT474
17
1.0 0.5 2.7 1.3 2.8 1.3
1.0 0.5 1.9 0.9 1.8 0.9
1.0 0.5 2.0 0.9 1.9 0.9
17kD
10kD
H3
H2B
H2A
H4
MCF7
T47D
BT474
C.
Normalized OD450nm absorbance
1.6
1.4
1.2
1.0
0.8
MCF7
T47D
BT474
*
**
shControl
shCTR9#3
shCTR9#5

Figure 2-2.

- **A.** Schematic design of the stable CTR9 knockdown using shCTR9#3 and shCTR9#5 (*Up*). Western blotting results showed the levels of CTR9 in total lysates and chromatin extracts in MCF7, T47D or BT474 cell lines stably expressing shCTR9#3 and ShCTR9#5 (*Bottom*).
- **B.** Western blot analyses of H3K27me1, 2, 3 levels in MCF7 (top), T47D (middle) and BT474 (bottom) cells stably expressing shControl, shCTR9#3, or shCTR9#5. The bands intensities of H3K27me3 are quantified by ImagePro after normalizing with H3 loading controls and shown in two-fold dilution.
- **C.** H3K27me3 levels measured by ELISA assays in MCF7, T47D and BT474 cells expressing shControl, shCTR9#3 or shCTR9#5. Data were normalized to the respective total histone H3 levels and represented as mean ± SD (n = 6). P-values were calculated using two tails t-test with Welch's correction (*: $p < 0.05$; **: $p < 0.01$).

Figure 2-3.

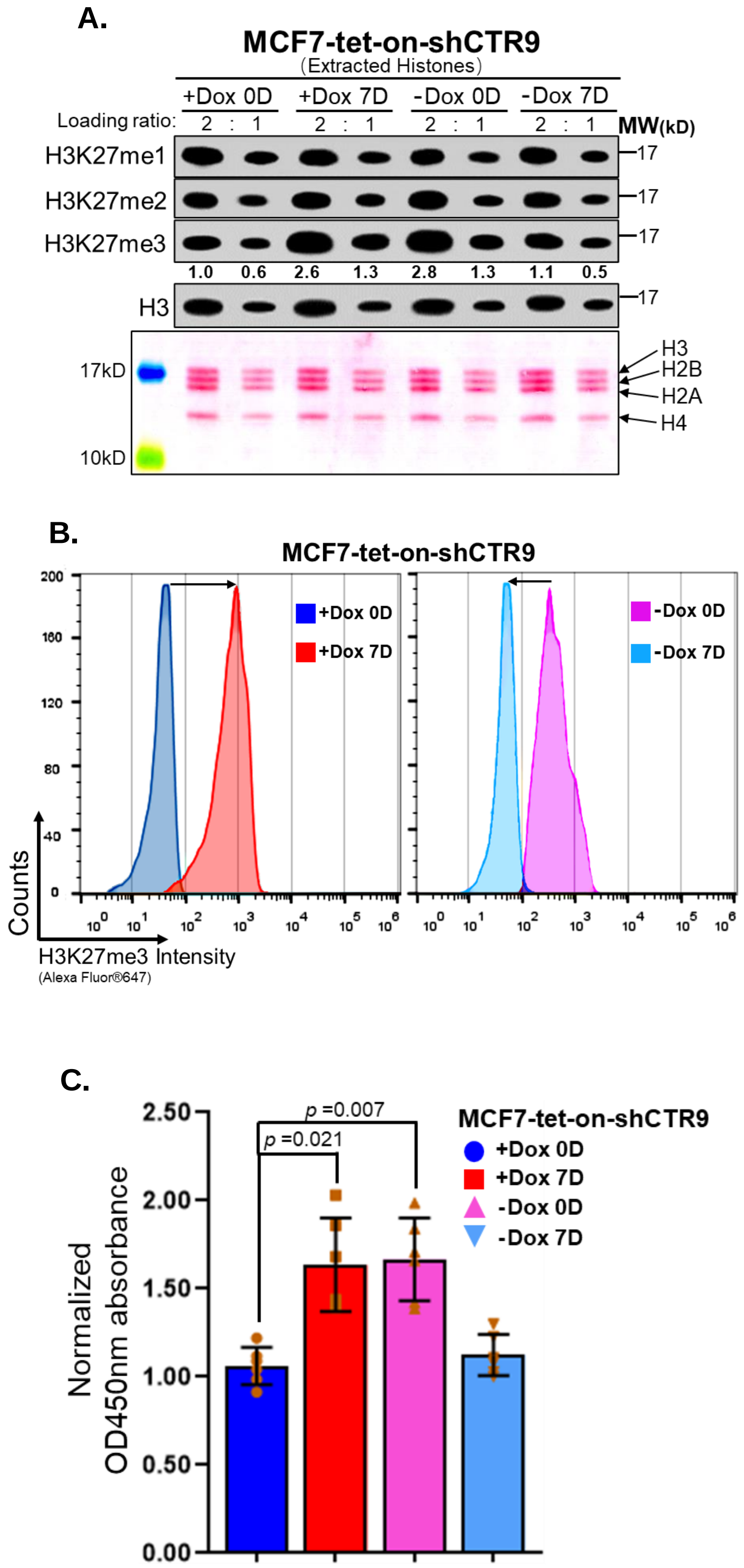
A.
MCF7-tet-on-shCTR9
(Extracted Histones)
+Dox 0D
+Dox 7D
-Dox 0D
-Dox 7D
Loading ratio:
2 : 1
2 : 1
2 : 1
2 : 1
MW(kD)
H3K27me1
H3K27me2
H3K27me3
17
17
17
1.0
0.6
2.6
1.3
2.8
1.3
1.1
0.5
H3
17
17kD
10kD
H3
H2B
H2A
H4
B.
MCF7-tet-on-shCTR9
200
160
120
80
40
0
Counts
+Dox 0D
+Dox 7D
-Dox 0D
-Dox 7D
10^0
10^1
10^2
10^3
10^4
10^5
10^6
H3K27me3 Intensity
(Alexa Fluor®647)
C.
2.50
2.00
1.50
1.00
0.50
0.00
Normalized
OD450nm absorbance
p =0.007
p =0.021
MCF7-tet-on-shCTR9
● +Dox 0D
■ +Dox 7D
▲ -Dox 0D
▼ -Dox 7D

Figure 2-3.

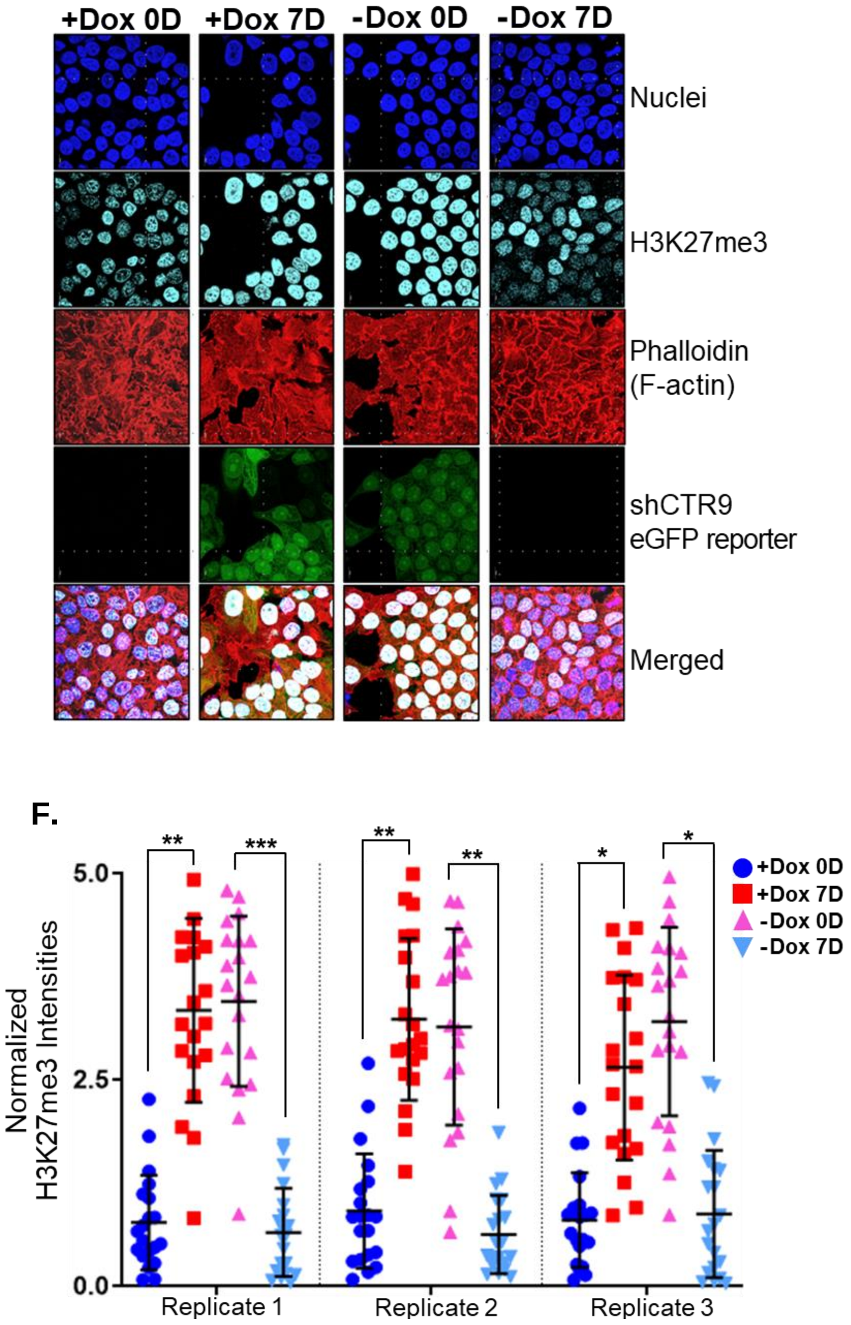
+Dox 0D
+Dox 7D
-Dox 0D
-Dox 7D
Nuclei
H3K27me3
Phalloidin (F-actin)
shCTR9 eGFP reporter
Merged
F.
Normalized H3K27me3 Intensities
5.0
2.5
0.0
**
***
**
**
*
*
Replicate 1
Replicate 2
Replicate 3
+Dox 0D
+Dox 7D
-Dox 0D
-Dox 7D

Figure 2-3.

- **A.** Western Blot analyses of H3K27me1, 2, 3 in MCF7-tet-on–shCTR9 cells under treatment scheme in Fig. 1A (*Top*). Ponceau S staining of histones were shown in two-fold loading ratio (*Bottom*). The bands intensity of H3K27me3 are quantified by ImagePro after normalizing with H3 loading controls.
- **B.** Flow cytometry quantification of H3K27me3 intensity in MCF7-tet-on–shCTR9 cells upon addition and removal of Dox for 0 and 7 days.
- **C.** H3K27me3 levels measured by ELISA assays in MCF7-tet-on–shCTR9 upon addition and removal of Dox. Data were normalized to the respective total histone H3 levels and represented as mean ± SD (n = 6). P-values were calculated using two tails t-test with Welch's correction.
- **D.** Representative images of Immuno-fluorescence staining of H3K27me3 (cyan), nuclei (blue), and F-actin (red) in MCF7-tet-on–shCTR9 cells under treatment scheme in Fig. 2-1-B.
- **E.** Ratios of H3K27me3 to nuclei staining intensity in 20 selected cells with complete nuclei. Difference in ratios were significant (*p<0.05; **p<0.01; ***p<0.001) by two-tailed t-test with Welch's correction; error bars show the standard deviation across triplicates.

Figure 2-4.

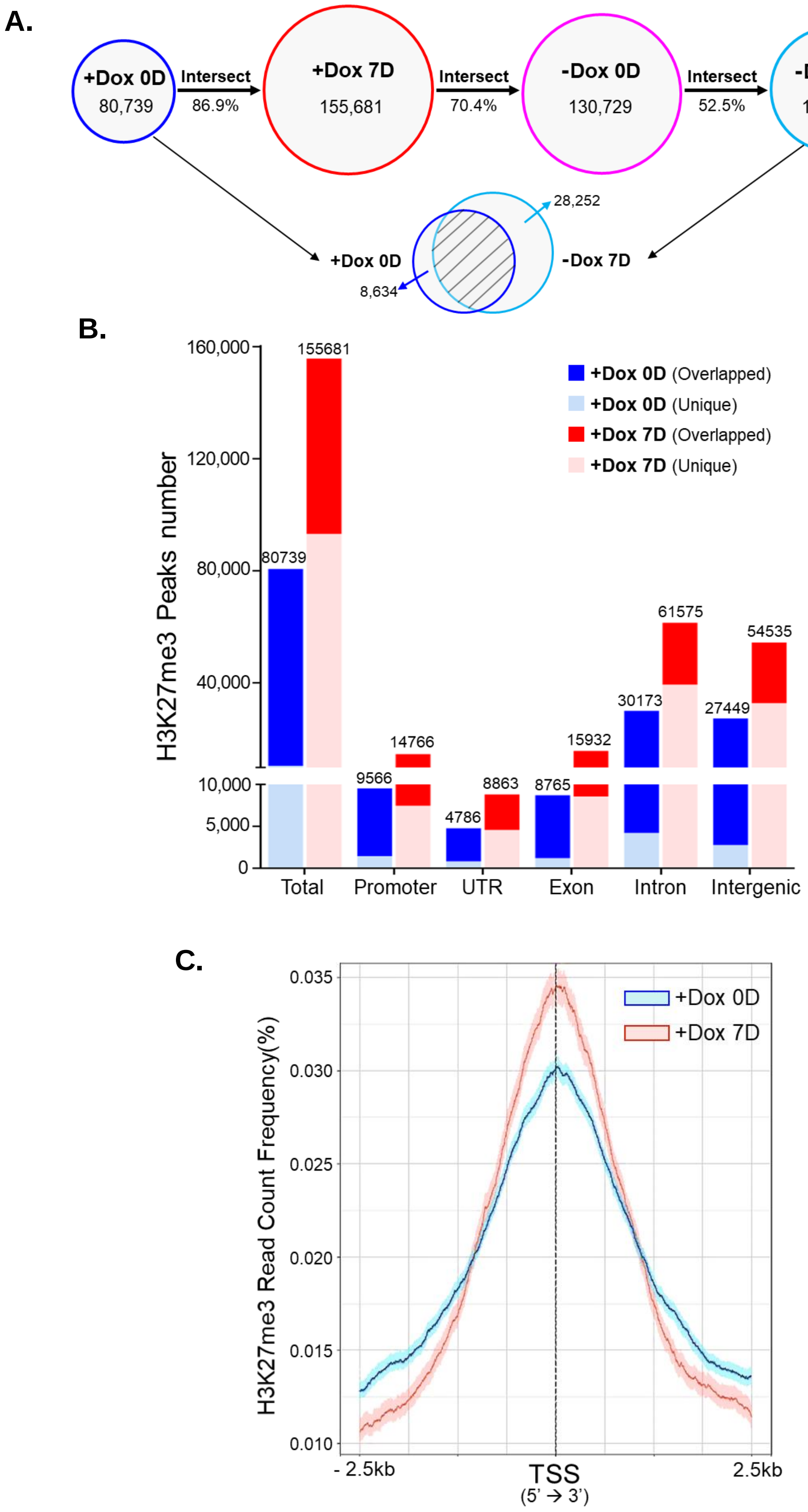
A.
+Dox 0D
80,739
Intersect
86.9%
+Dox 7D
155,681
Intersect
70.4%
-Dox 0D
130,729
Intersect
52.5%
-Dox 7D
101,332
28,252
+Dox 0D
-Dox 7D
8,634
B.
H3K27me3 Peaks number
160,000
120,000
80,000
40,000
10,000
5,000
0
155681
80739
9566
14766
4786
8863
8765
15932
30173
61575
27449
54535
+Dox 0D (Overlapped)
+Dox 0D (Unique)
+Dox 7D (Overlapped)
+Dox 7D (Unique)
Total
Promoter
UTR
Exon
Intron
Intergenic
C.
H3K27me3 Read Count Frequency(%)
0.035
0.030
0.025
0.020
0.015
0.010
+Dox 0D
+Dox 7D
- 2.5kb
TSS
(5' → 3')
2.5kb

Figure 2-4.

- **A.** H3K27me3 peak numbers in MCF7-tet-on-shCTR9 cells after addition and removal of Dox for 0 day and 7 days. Peak numbers and percent of intersection between groups are shown.
- **B.** Respective genome-wide distribution of the overlapped (Light Blue) and unique (Blue) H3K27me3 peak numbers in MCF7-tet-on-shCTR9 cells treated with Dox for 0 day. After 7-day treatment with Dox, the overlapped (Light Red) and unique H3K27me3 peaks (Red) were shown. Total peak numbers for each group and their distribution to promoter, UTR, exon, intron and intergenic regions were indicated.
- **C.** Continuous read count frequency (%) of H3K27me3 peak distributed around the TSS regions (TSS ± 2.5kb).

Figure 2-5.

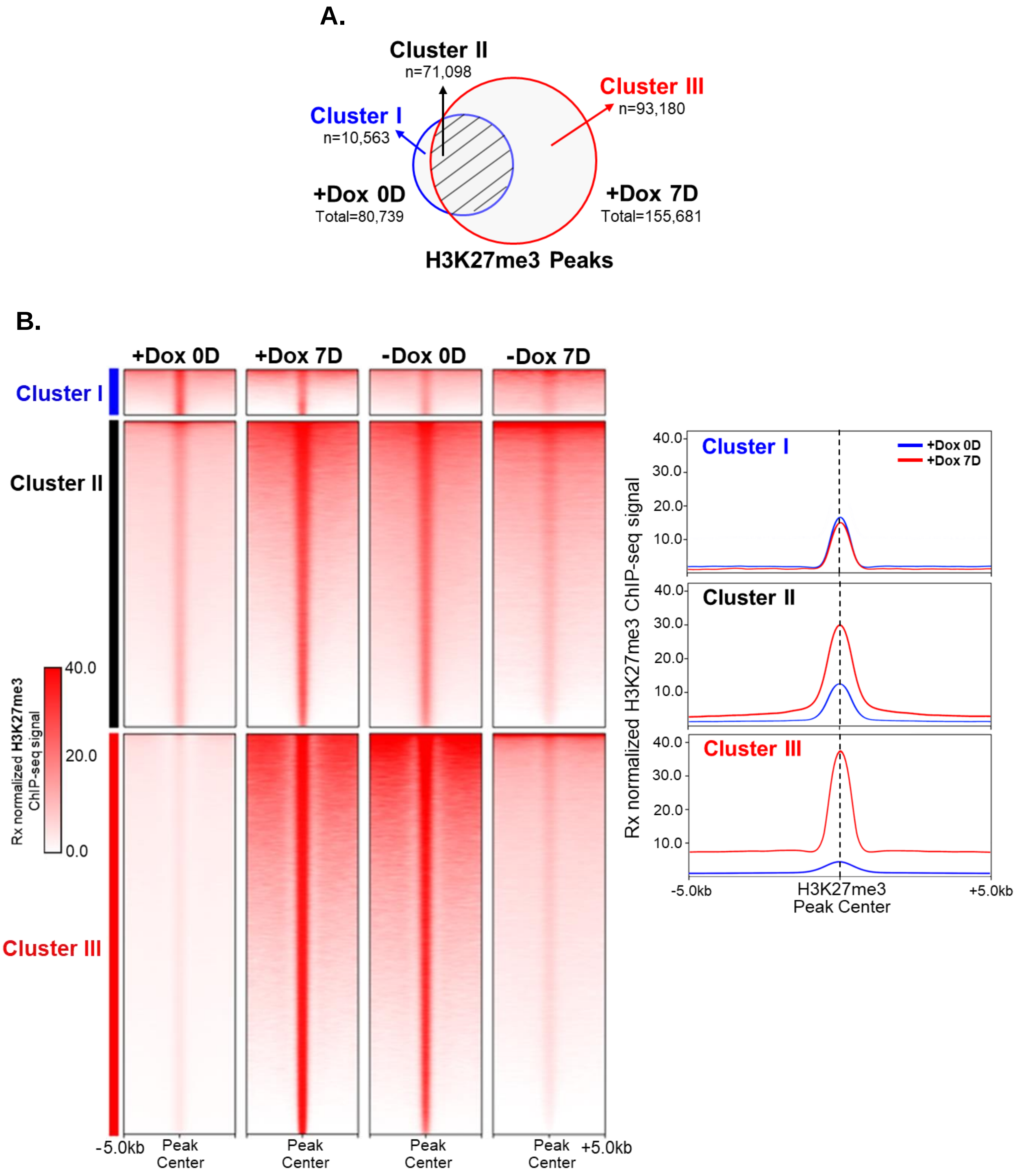
A.
Cluster II
n=71,098
Cluster I
n=10,563
Cluster III
n=93,180
+Dox 0D
Total=80,739
+Dox 7D
Total=155,681
H3K27me3 Peaks
B.
+Dox 0D
+Dox 7D
-Dox 0D
-Dox 7D
Cluster I
Cluster II
Cluster III
Rx normalized H3K27me3 ChIP-seq signal
40.0
20.0
0.0
-5.0kb
Peak Center
Peak Center
Peak Center
Peak Center
+5.0kb
Rx normalized H3K27me3 ChIP-seq signal
Cluster I
+Dox 0D
+Dox 7D
Cluster II
Cluster III
40.0
30.0
20.0
10.0
-5.0kb
H3K27me3 Peak Center
+5.0kb

Figure 2-5.

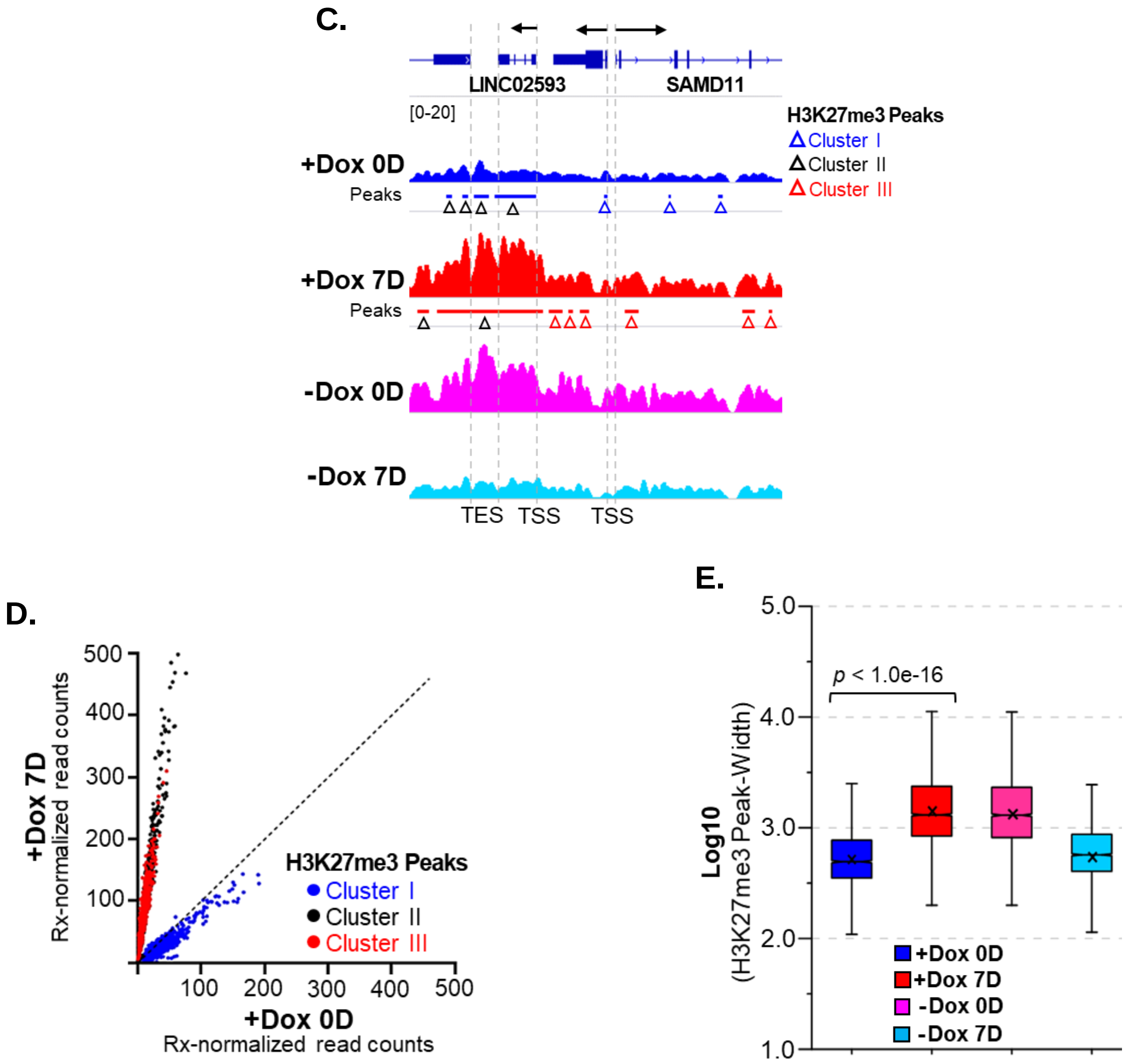
C.
LINC02593
SAMD11
[0-20]
H3K27me3 Peaks
Cluster I
Cluster II
Cluster III
+Dox 0D
Peaks
+Dox 7D
Peaks
-Dox 0D
-Dox 7D
TES
TSS
TSS
D.
500
400
300
200
100
+Dox 7D
Rx-normalized read counts
H3K27me3 Peaks
Cluster I
Cluster II
Cluster III
100
200
300
400
500
+Dox 0D
Rx-normalized read counts
E.
5.0
4.0
3.0
2.0
1.0
p < 1.0e-16
Log10
(H3K27me3 Peak-Width)
+Dox 0D
+Dox 7D
-Dox 0D
-Dox 7D

Figure 2-5.

- **A.** Venn Diagram of H3K27me3 peaks between '+Dox 0D' and '+Dox 7D' groups and the designated Clusters.
- **B.** Heatmap of Rx-normalized H3K27me3 ChIP-seq profiles at peak center ±5.0kb regions after addition and removal of Dox for 0 day and 7 days in the designated clusters (*Left*). Composite profile of Rx-normalized H3K27me3 ChIP-seq signals in ±5.0kb range of peak centers for different clusters (*Right*).
- **C.** Representative genome-browser snapshot of Rx-normalized H3K27me3 ChIP-Rx signals in MCF7-tet-on-shCTR9 cells under indicated treatment conditions. Each signal-track represents the mean of two biological replicates. Peaks classified to three clusters were denoted with blue, red, or black triangles, respectively.
- **D.** Dot plot of Rx-normalized read counts of H3K27me3 peaks from MCF7-tet-on-shCTR9 cells treated with Dox for 0 day and 7 days. Peaks from three clusters were represented with blue, black and red dots, respectively.
- **E.** Notched box plot showing the peak width of H3K27me3 from MCF7-tet-on-shCTR9 cells upon addition or removal of Dox for 0 day or 7 days. P-value of Welch's t-test was calculated.

Figure 2-6.

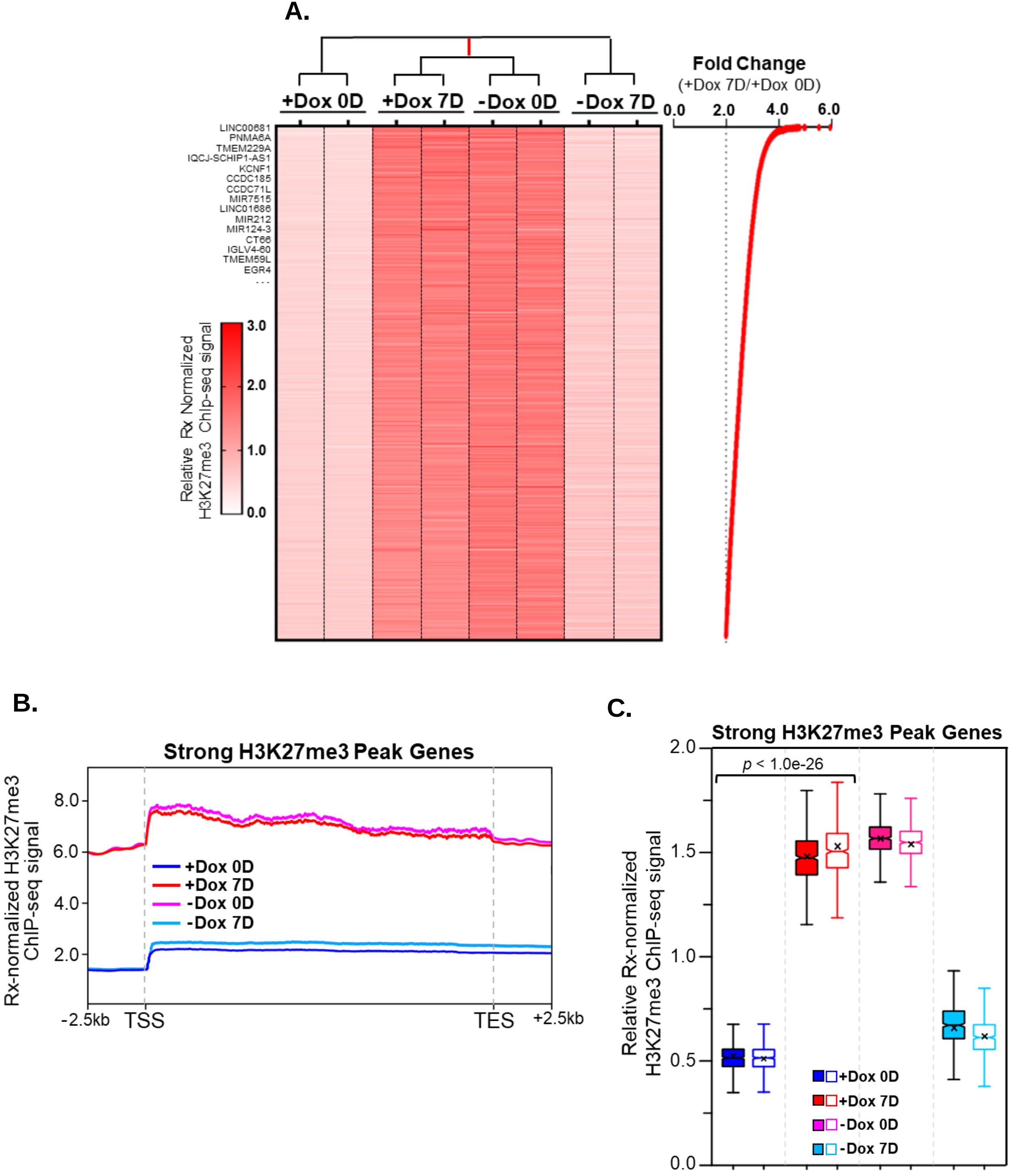
A.
+Dox 0D
+Dox 7D
-Dox 0D
-Dox 7D
LINC00681
PNMA6A
TMEM229A
IQCJ-SCHIP1-AS1
KCNF1
CCDC185
CCDC71L
MIR7515
LINC01686
MIR212
MIR124-3
CT66
IGLV4-60
TMEM59L
EGR4
. . .
Relative Rx Normalized H3K27me3 ChIp-seq signal
3.0
2.0
1.0
0.0
Fold Change
(+Dox 7D/+Dox 0D)
0.0
2.0
4.0
6.0
B.
Strong H3K27me3 Peak Genes
Rx-normalized H3K27me3 ChIP-seq signal
8.0
6.0
4.0
2.0
+Dox 0D
+Dox 7D
-Dox 0D
-Dox 7D
-2.5kb
TSS
TES
+2.5kb
C.
Strong H3K27me3 Peak Genes
p < 1.0e-26
Relative Rx-normalized H3K27me3 ChIP-seq signal
2.0
1.5
1.0
0.5
0.0
+Dox 0D
+Dox 7D
-Dox 0D
-Dox 7D

Figure 2-6.

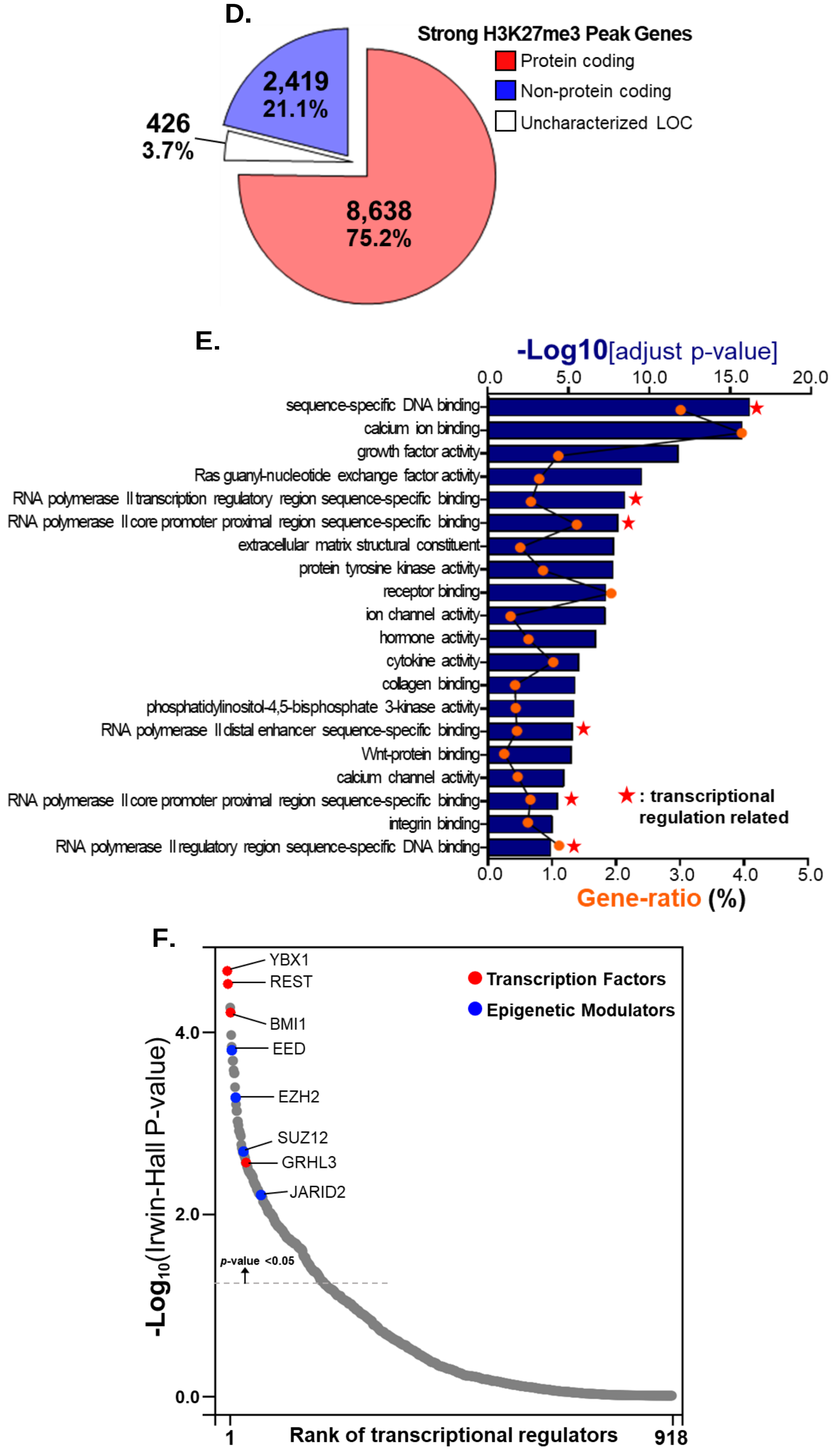
D.
Strong H3K27me3 Peak Genes
Protein coding
Non-protein coding
Uncharacterized LOC
2,419
21.1%
426
3.7%
8,638
75.2%
E.
-Log10[adjust p-value]
0.0
5.0
10.0
15.0
20.0
sequence-specific DNA binding
calcium ion binding
growth factor activity
Ras guanyl-nucleotide exchange factor activity
RNA polymerase II transcription regulatory region sequence-specific binding
RNA polymerase II core promoter proximal region sequence-specific binding
extracellular matrix structural constituent
protein tyrosine kinase activity
receptor binding
ion channel activity
hormone activity
cytokine activity
collagen binding
phosphatidylinositol-4,5-bisphosphate 3-kinase activity
RNA polymerase II distal enhancer sequence-specific binding
Wnt-protein binding
calcium channel activity
RNA polymerase II core promoter proximal region sequence-specific binding
integrin binding
RNA polymerase II regulatory region sequence-specific DNA binding
★ : transcriptional regulation related
0.0
1.0
2.0
3.0
4.0
5.0
Gene-ratio (%)
F.
YBX1
REST
BMI1
EED
EZH2
SUZ12
GRHL3
JARID2
Transcription Factors
Epigenetic Modulators
4.0
2.0
0.0
-Log10(Irwin-Hall P-value)
p-value <0.05
1
Rank of transcriptional regulators
918

Figure 2-6.

- **A.** Heatmap of the relative Rx-normalized H3K27me3 ChIP-Rx profiles (n=2) at strong H3K27me3 peak genes (*Left*). The Dox-induced H3K27me3 peak fold-changes were plotted (*Right*).
- **B.** Average profiles of Rx-normalized H3K27me3 ChIP-seq signals at ±2.5kb of TSS-TES regions of the strong H3K27me3 peak associated genes.
- **C.** Notched boxplot of relative Rx-normalized H3K27me3 ChIP-seq signals of strong H3K27me3 peak genes (n=2). Paired Student's t test was used to calculate statistical significance among groups.
- **D.** Genomic distribution of the strong H3K27me3 peak genes (11,483).
- **E.** Gene Ontology pathway analysis (molecular function) of strong H3K27me3 peak genes.
- **F.** Ranked dot plot of *cis*-regulatory factor prediction of 11,483 strong H3K27me3 peak associated genes by *BART* (Binding Analysis for Regulation of Transcription). The top ranked transcription factors and epigenetic modulators were highlighted in red and blue.

Figure 2-7.

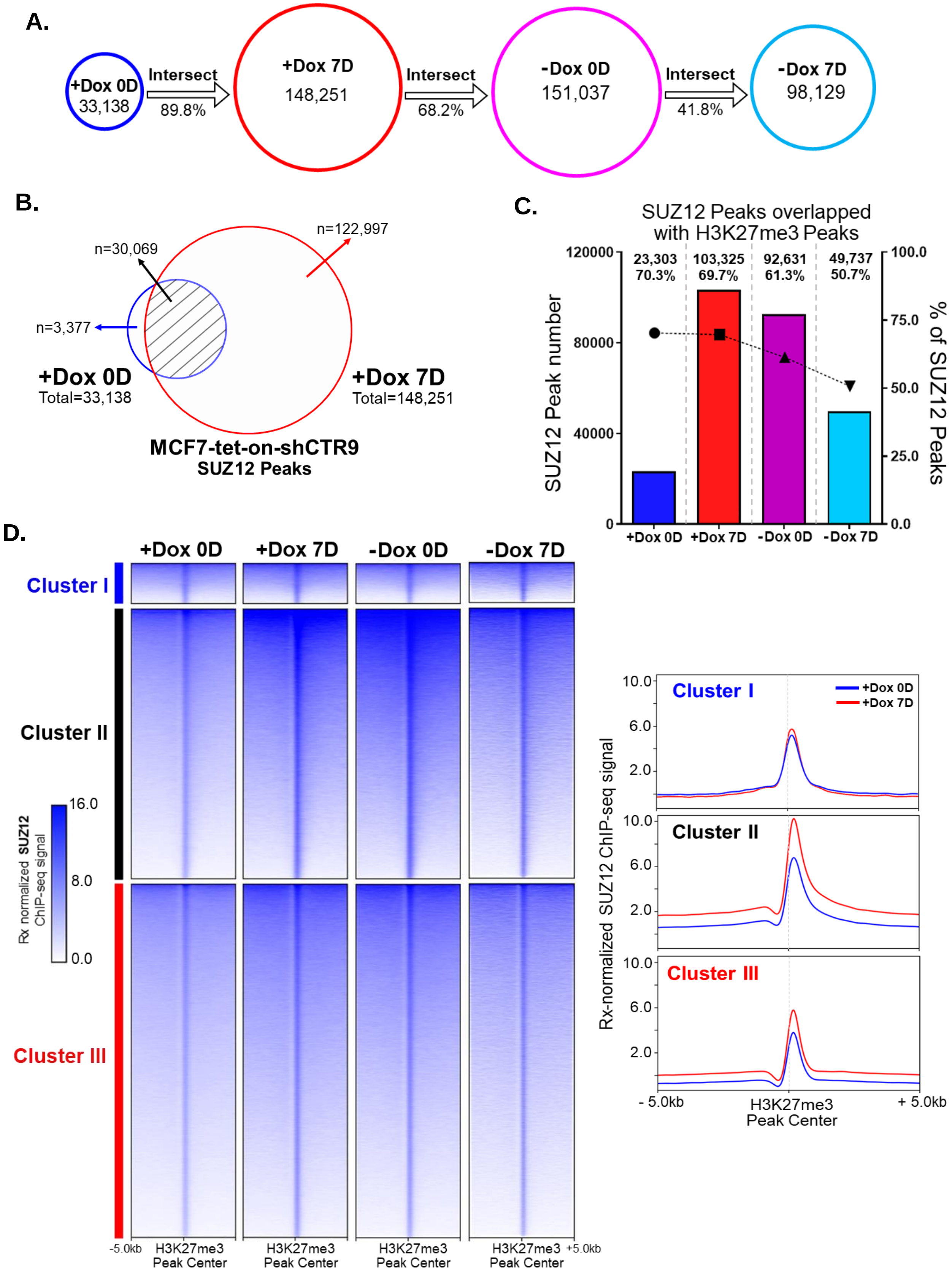
A.
+Dox 0D
33,138
Intersect
89.8%
+Dox 7D
148,251
Intersect
68.2%
-Dox 0D
151,037
Intersect
41.8%
-Dox 7D
98,129
B.
n=30,069
n=122,997
n=3,377
+Dox 0D
Total=33,138
+Dox 7D
Total=148,251
MCF7-tet-on-shCTR9
SUZ12 Peaks
C.
SUZ12 Peaks overlapped with H3K27me3 Peaks
SUZ12 Peak number
% of SUZ12 Peaks
120000
80000
40000
0
100.0
75.0
50.0
25.0
0.0
23,303
70.3%
103,325
69.7%
92,631
61.3%
49,737
50.7%
+Dox 0D
+Dox 7D
-Dox 0D
-Dox 7D
D.
+Dox 0D
+Dox 7D
-Dox 0D
-Dox 7D
Cluster I
Cluster II
Cluster III
Rx normalized SUZ12 ChIP-seq signal
16.0
8.0
0.0
-5.0kb
H3K27me3 Peak Center
H3K27me3 Peak Center
H3K27me3 Peak Center
H3K27me3 Peak Center
+5.0kb
Rx-normalized SUZ12 ChIP-seq signal
10.0
6.0
2.0
Cluster I
+Dox 0D
+Dox 7D
10.0
6.0
2.0
Cluster II
10.0
6.0
2.0
Cluster III
- 5.0kb
H3K27me3 Peak Center
+ 5.0kb

Figure 2-7.

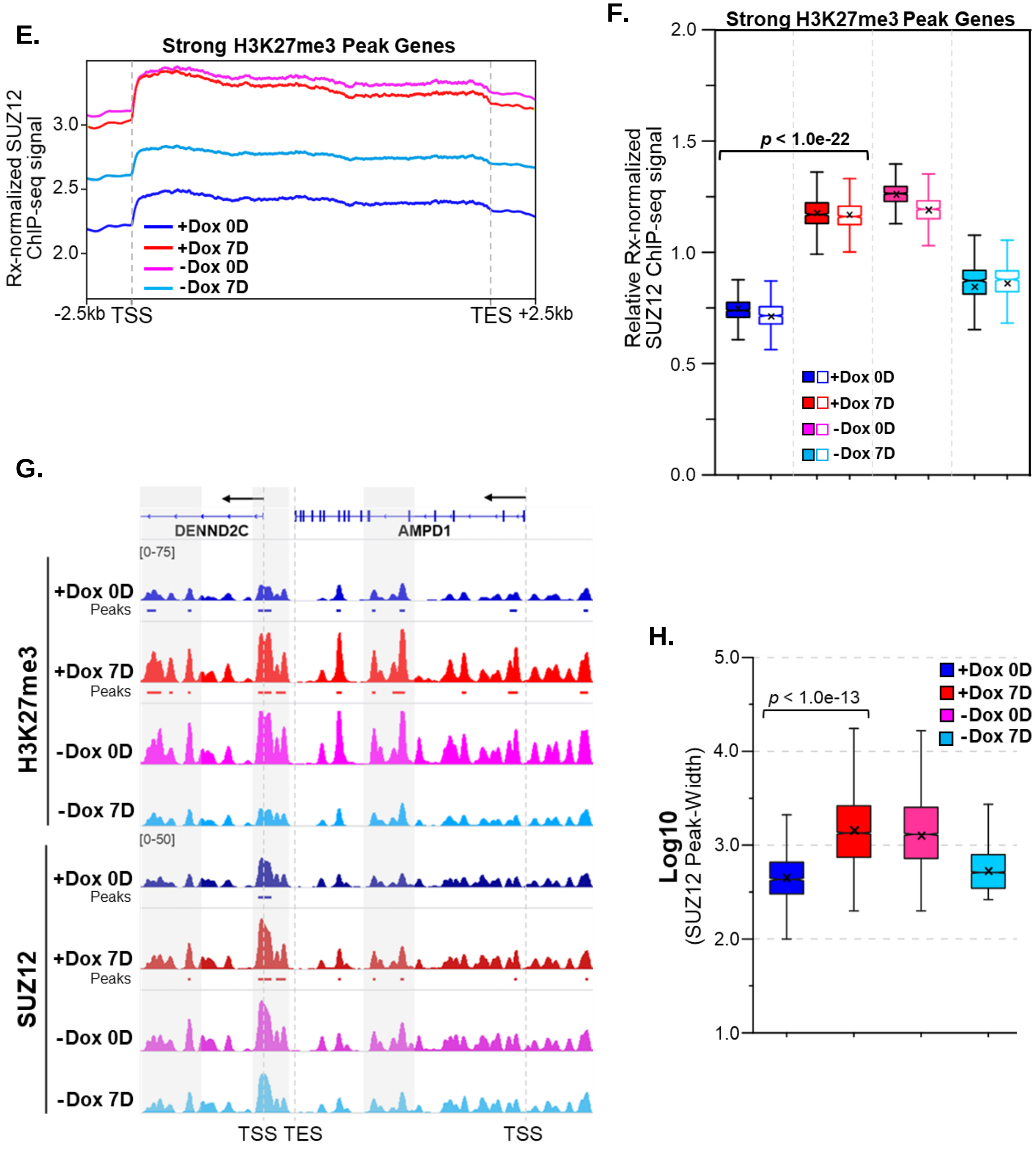
E.
Strong H3K27me3 Peak Genes
Rx-normalized SUZ12 ChIP-seq signal
3.0
2.5
2.0
+Dox 0D
+Dox 7D
-Dox 0D
-Dox 7D
-2.5kb TSS
TES +2.5kb
F.
Strong H3K27me3 Peak Genes
Relative Rx-normalized SUZ12 ChIP-seq signal
2.0
1.5
1.0
0.5
0.0
p < 1.0e-22
+Dox 0D
+Dox 7D
-Dox 0D
-Dox 7D
G.
DENND2C
AMPD1
[0-75]
H3K27me3
+Dox 0D
Peaks
+Dox 7D
Peaks
-Dox 0D
-Dox 7D
[0-50]
SUZ12
+Dox 0D
Peaks
+Dox 7D
Peaks
-Dox 0D
-Dox 7D
TSS TES
TSS
H.
Log10 (SUZ12 Peak-Width)
5.0
4.0
3.0
2.0
1.0
p < 1.0e-13
+Dox 0D
+Dox 7D
-Dox 0D
-Dox 7D

Figure 2-7.

- **A.** SUZ12 peak numbers in MCF7-tet-on-shCTR9 cells under the indicated treatment conditions.
- **B.** Venn Diagram of the SUZ12 peaks between ‘+Dox 0D’ and ‘+Dox 7D’ groups in MCF7-tet-on-shCTR9 cells.
- **C.** SUZ12 peak numbers (bar-graph) and percentage% (dot-plot) of total SUZ12 peaks that overlapped with H3K27me3 peaks under each treatment condition. Peak numbers were indicated on the top of each bar.
- **D.** Heatmap of Rx-normalized SUZ12 ChIP-seq profiles at ±5.0kb regions after addition and removal of Dox for 0 day and 7 days in the designated clusters (*Left*). Composite profile of Rx-normalized SUZ12 ChIP-seq signals in ±5.0kb range of H3K27me3 peak centers for different clusters (*Right*).
- **E.** Average profiles of Rx-normalized SUZ12 ChIP-seq signals at ±2.5kb of TSS-TES regions of 11,483 strong H3K27me3 peak genes.
- **F.** Notched boxplot of relative Rx-normalized SUZ12 ChIP-seq signals of strong H3K27me3 peak genes (n=2). Paired Student’s t test was used to calculate statistical significance among groups.
- **G.** Representative genome-browser snapshot of Rx-normalized H3K27me3 (top) and SUZ12 (bottom) ChIP-seq signals in MCF7-tet-on-shCTR9 cells under treatment conditions indicated. Each signal-track represents the mean of two biological replicates.
- **H.** Notched box plot showing the peak width of SUZ12 from MCF7-tet-on-shCTR9 cells upon the addition or removal of Dox for 0 day or 7 days. P-value of Welch’s t-test was calculated.

Figure 2-8.

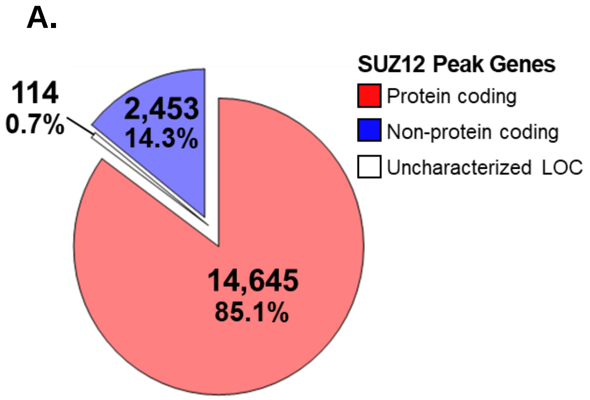

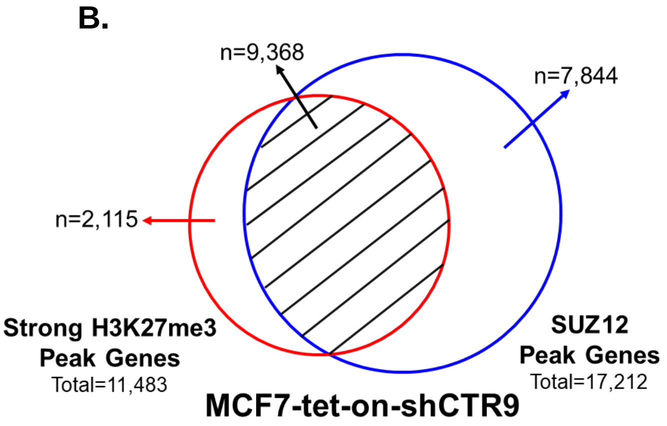

Figure 2-8.

A. Genomic distribution of SUZ12 peak genes (17,212).

B. Venn Diagram showing a large overlap between the strong H3K27me3 peak genes and SUZ12 peak genes.

Figure 2-9.

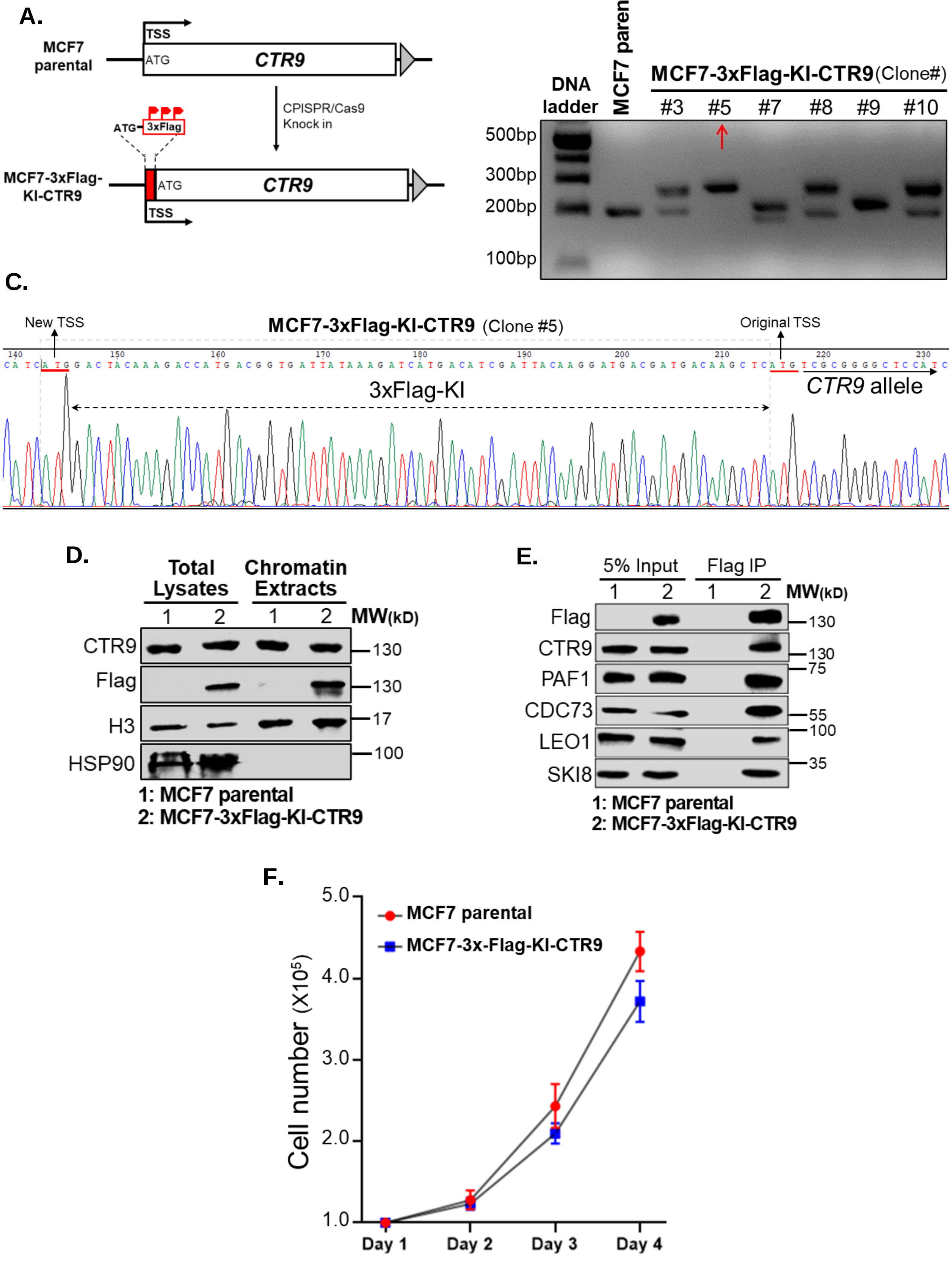
A.
MCF7 parental
TSS
ATG
CTR9
CPISPR/Cas9
Knock in
ATG
3xFlag
MCF7-3xFlag-KI-CTR9
ATG
CTR9
TSS
B.
DNA ladder
MCF7 parental
MCF7-3xFlag-KI-CTR9 (Clone#)
#3
#5
#7
#8
#9
#10
500bp
300bp
200bp
100bp
C.
New TSS
MCF7-3xFlag-KI-CTR9 (Clone #5)
Original TSS
3xFlag-KI
CTR9 allele
D.
Total Lysates
Chromatin Extracts
1
2
1
2
MW(kD)
CTR9
Flag
H3
HSP90
130
130
17
100
1: MCF7 parental
2: MCF7-3xFlag-KI-CTR9
E.
5% Input
Flag IP
1
2
1
2
MW(kD)
Flag
CTR9
PAF1
CDC73
LEO1
SKI8
130
130
75
55
100
35
1: MCF7 parental
2: MCF7-3xFlag-KI-CTR9
F.
MCF7 parental
MCF7-3x-Flag-KI-CTR9
Cell number (X10^5)
5.0
4.0
3.0
2.0
1.0
Day 1
Day 2
Day 3
Day 4

Figure 2-9.

- **A.** Scheme of 3xFlag knock-in CTR9 in MCF7 cells. (TSS: translation start site)
- **B.** Selection of homozygous 3xFlag knock-in (KI) clones using PCR identified clone #5 as a correctly engineered MCF7-3xFlag-KI-CTR9 clone.
- **C.** Sequencing verification of 3xFlag knock-in of clone #5.
- **D.** Western blotting demonstrates the expression of 3xFlag CTR9 protein. HSP90 and histone H3 were used as loading controls for total lysates and chromatin extracts, respectively.
- **E.** CTR9 was pulled down using anti-Flag antibody in MCF7-3xFlag-KI-CTR9 cells. Western blotting results showed co-immunoprecipitation of other subunits of PAFc with CTR9. MCF7 parental cells served as negative control.

Figure 2-10.

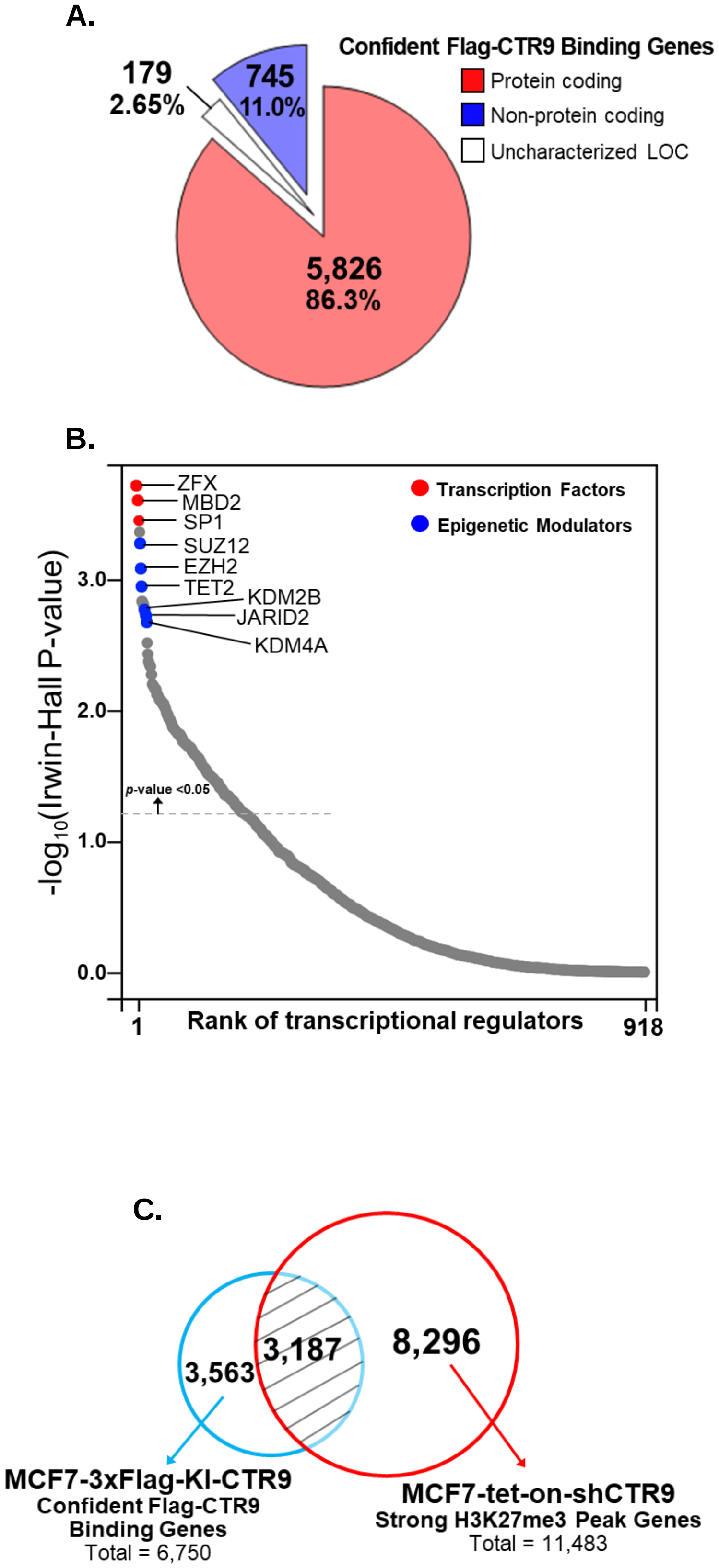
A.
Confident Flag-CTR9 Binding Genes
Protein coding
Non-protein coding
Uncharacterized LOC
179
2.65%
745
11.0%
5,826
86.3%
B.
-log10(Irwin-Hall P-value)
3.0
2.0
1.0
0.0
ZFX
MBD2
SP1
SUZ12
EZH2
TET2
KDM2B
JARID2
KDM4A
Transcription Factors
Epigenetic Modulators
p-value <0.05
1
Rank of transcriptional regulators
918
C.
3,563
3,187
8,296
MCF7-3xFlag-KI-CTR9
Confident Flag-CTR9
Binding Genes
Total = 6,750
MCF7-tet-on-shCTR9
Strong H3K27me3 Peak Genes
Total = 11,483

Figure 2-10.

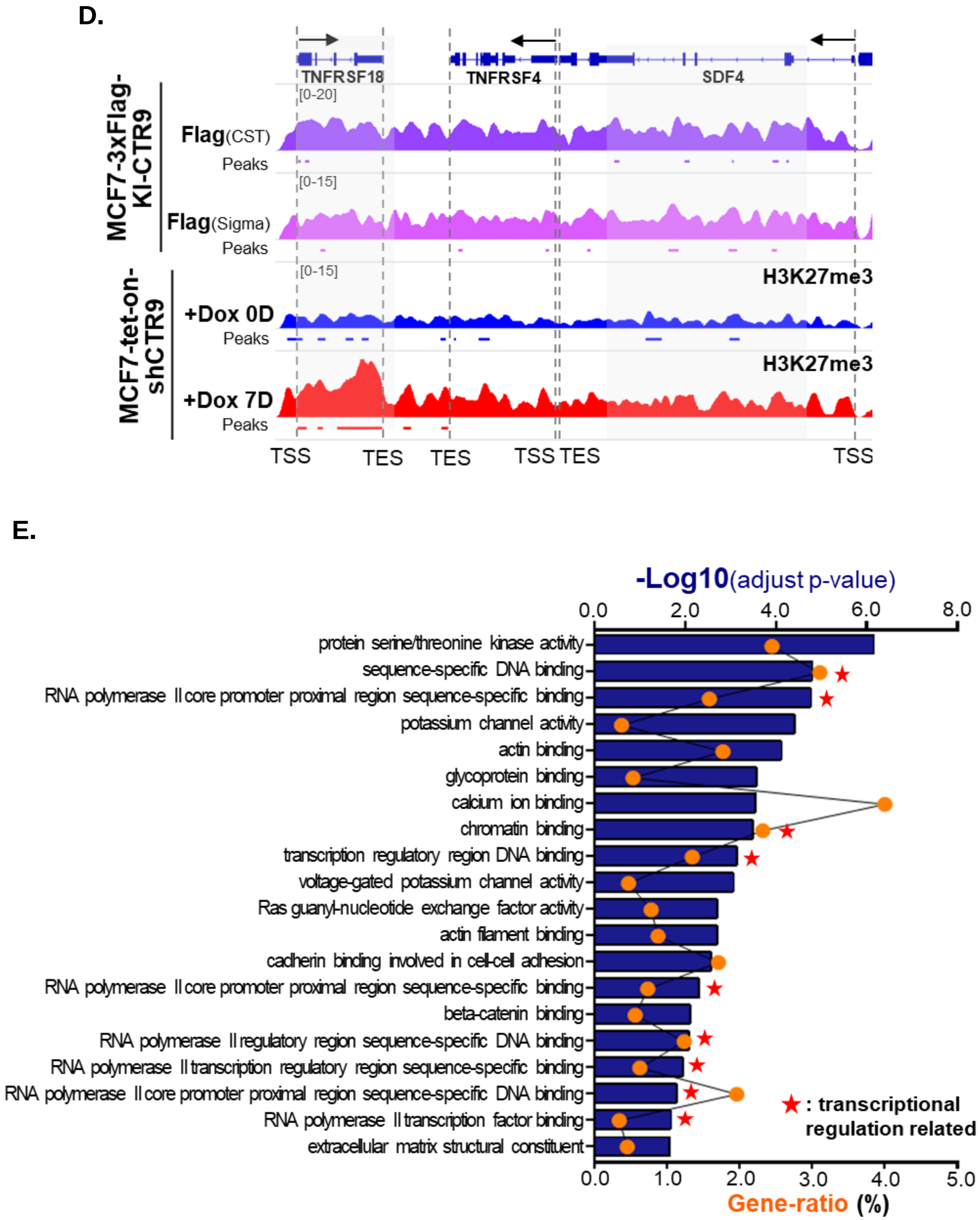
D.
TNFRSF18
TNFRSF4
SDF4
MCF7-3xFlag-KI-CTR9
[0-20]
Flag(CST)
Peaks
[0-15]
Flag(Sigma)
Peaks
MCF7-tet-on-shCTR9
[0-15]
H3K27me3
+Dox 0D
Peaks
H3K27me3
+Dox 7D
Peaks
TSS
TES
TES
TSS TES
TSS
E.
-Log10(adjust p-value)
0.0
2.0
4.0
6.0
8.0
protein serine/threonine kinase activity
sequence-specific DNA binding
RNA polymerase II core promoter proximal region sequence-specific binding
potassium channel activity
actin binding
glycoprotein binding
calcium ion binding
chromatin binding
transcription regulatory region DNA binding
voltage-gated potassium channel activity
Ras guanyl-nucleotide exchange factor activity
actin filament binding
cadherin binding involved in cell-cell adhesion
RNA polymerase II core promoter proximal region sequence-specific binding
beta-catenin binding
RNA polymerase II regulatory region sequence-specific DNA binding
RNA polymerase II transcription regulatory region sequence-specific binding
RNA polymerase II core promoter proximal region sequence-specific DNA binding
RNA polymerase II transcription factor binding
extracellular matrix structural constituent
★ : transcriptional regulation related
0.0
1.0
2.0
3.0
4.0
5.0
Gene-ratio (%)

Figure 2-10.

- **A.** Genomic distribution of high confident genes (n=6,750) regulated by CTR9 based on Flag ChIP-Rx signals in MCF7-3xFlag-KI-CTR9 cells.
- **B.** Ranked dot plot of *cis*-regulatory factors prediction for Flag-CTR9 binding genes by *BART*. Top transcription factors and epigenetic modulators were highlighted in red and blue.
- **C.** Venn Diagram showing the overlap between the 6,750 genes harboring Flag-CTR9 binding sites and 11,483 strong H3K27me3 peak associated genes identified in Figure 2-6-A.
- **D.** Representative genome-browser snapshot of the averaged Flag (CST/Sigma) ChIP-Rx signals (n=2) in MCF7-3xFlag-KI-CTR9 cells (top) and H3K27me3 ChIP-Rx signals (n=2) in MCF7-tet-on-shCTR9 cells (bottom)**.**
- **E.** Gene Ontology pathway analysis (Molecular Function) of 6,750 highly confident Flag-CTR9 binding genes. The top 20 identified pathways were sorted according to Bonferroni adjusted p-value followed by –log10 transformation.

Figure 2-11.

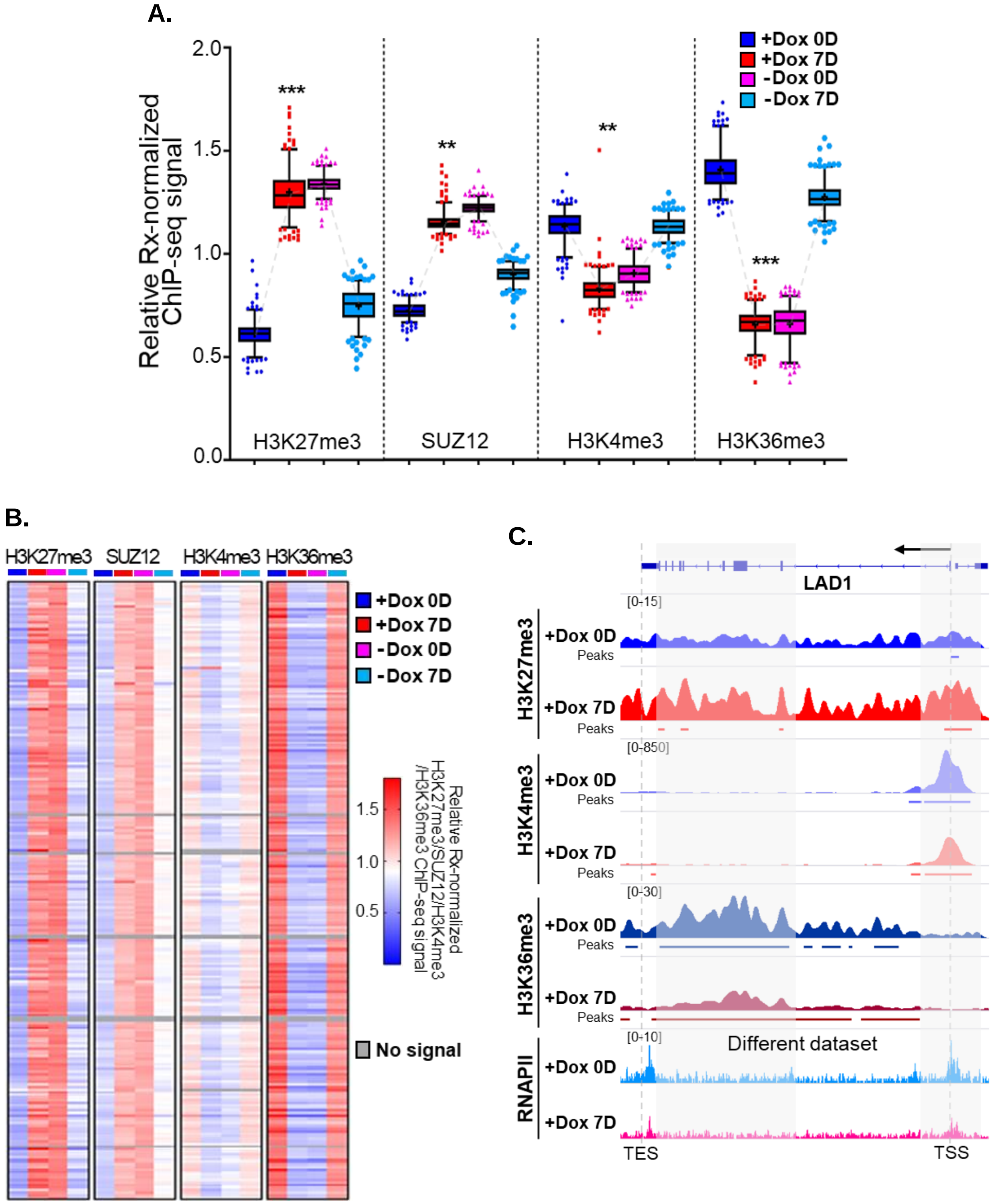
A.
Relative Rx-normalized ChIP-seq signal
2.0
1.5
1.0
0.5
0.0
***
**
**
***
H3K27me3
SUZ12
H3K4me3
H3K36me3
+Dox 0D
+Dox 7D
-Dox 0D
-Dox 7D
B.
H3K27me3
SUZ12
H3K4me3
H3K36me3
+Dox 0D
+Dox 7D
-Dox 0D
-Dox 7D
1.5
1.0
0.5
Relative Rx-normalized H3K27me3/SUZ12/H3K4me3 /H3K36me3 ChIP-seq signal
No signal
C.
LAD1
[0-15]
H3K27me3
+Dox 0D
Peaks
+Dox 7D
Peaks
[0-850]
H3K4me3
+Dox 0D
Peaks
+Dox 7D
Peaks
[0-30]
H3K36me3
+Dox 0D
Peaks
+Dox 7D
Peaks
[0-10]
Different dataset
RNAPII
+Dox 0D
+Dox 7D
TES
TSS

Figure 2-11.

- **A.** Box plot of relative Rx-normalized H3K27me3, SUZ12, H3K4me3, and H3K36me3 ChIP-Rx signals of 240 CTR9 regulated genes. Difference in ratios were significant (*p<0.05; **p<0.01; ***p<0.001) by two-tailed t-test with Welch’s correction.
- **B.** Heatmap of changes of H3K27me3, SUZ12, H3K4me3 and H3K36me3 ChIP-Rx signals on 240 CTR9 regulated genes in MCF7 cells.
- **C.** Representative genome browser snapshot of normalized ChIP-Rx signals for H3K27me3, H3K4me3, H3K36me3 and RNAPII on LAD1, a previously identified CTR9 regulated gene, in Dox 0D and Dox 7D conditions.

Figure 2-12.

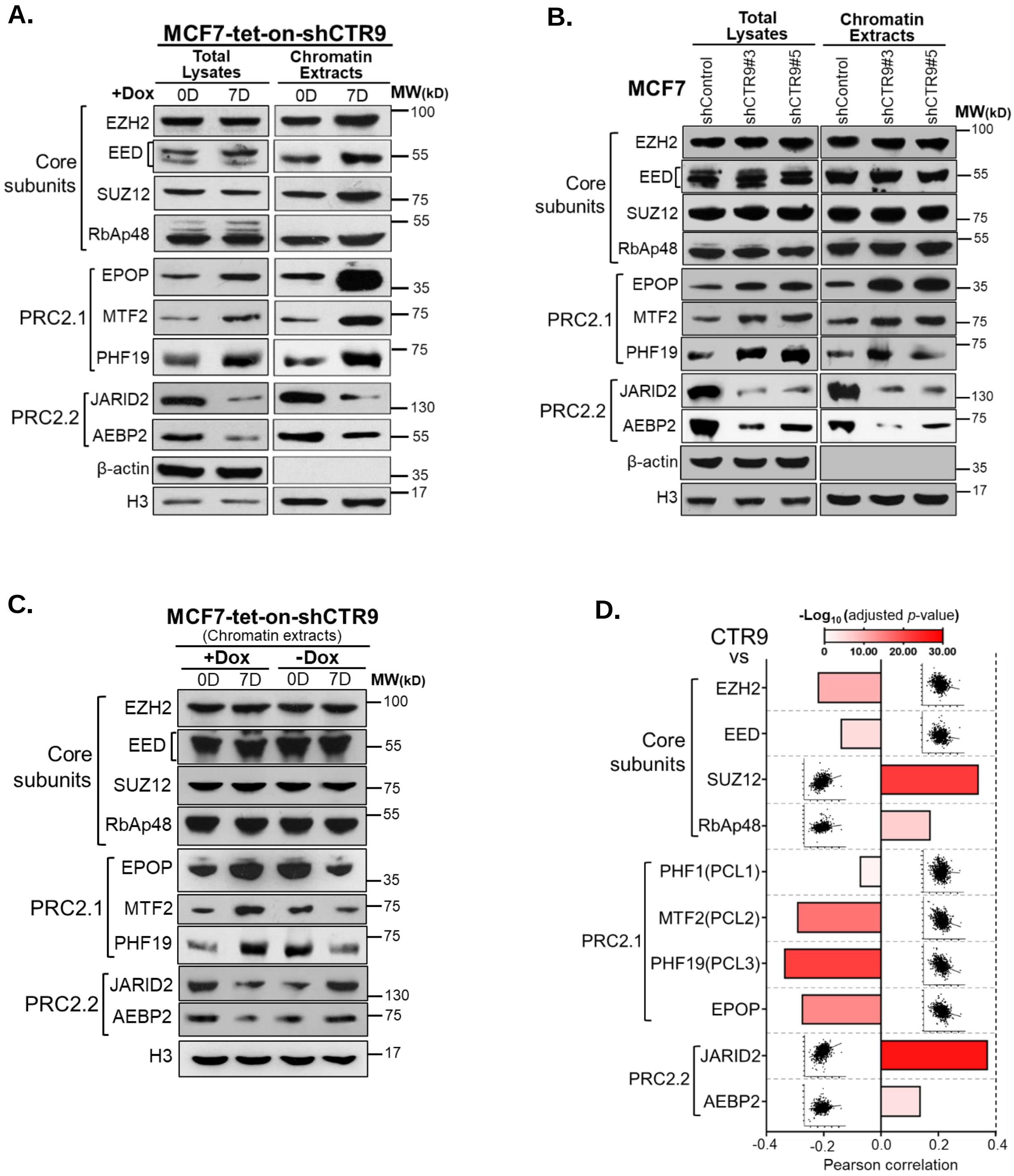
A.
MCF7-tet-on-shCTR9
Total Lysates
Chromatin Extracts
+Dox
0D
7D
0D
7D
MW(kD)
Core subunits
EZH2
EED
SUZ12
RbAp48
PRC2.1
EPOP
MTF2
PHF19
PRC2.2
JARID2
AEBP2
β-actin
H3
100
55
75
55
35
75
75
130
55
35
17
B.
MCF7
Total Lysates
Chromatin Extracts
shControl
shCTR9#3
shCTR9#5
shControl
shCTR9#3
shCTR9#5
MW(kD)
Core subunits
EZH2
EED
SUZ12
RbAp48
PRC2.1
EPOP
MTF2
PHF19
PRC2.2
JARID2
AEBP2
β-actin
H3
100
55
75
55
35
75
75
130
75
35
17
C.
MCF7-tet-on-shCTR9
(Chromatin extracts)
+Dox
-Dox
0D
7D
0D
7D
MW(kD)
Core subunits
EZH2
EED
SUZ12
RbAp48
PRC2.1
EPOP
MTF2
PHF19
PRC2.2
JARID2
AEBP2
H3
100
55
75
55
35
75
75
130
75
17
D.
CTR9 vs
-Log10 (adjusted p-value)
0
10.00
20.00
30.00
Core subunits
EZH2
EED
SUZ12
RbAp48
PRC2.1
PHF1(PCL1)
MTF2(PCL2)
PHF19(PCL3)
EPOP
PRC2.2
JARID2
AEBP2
-0.4
-0.2
0.0
0.2
0.4
Pearson correlation

Figure 2-12.

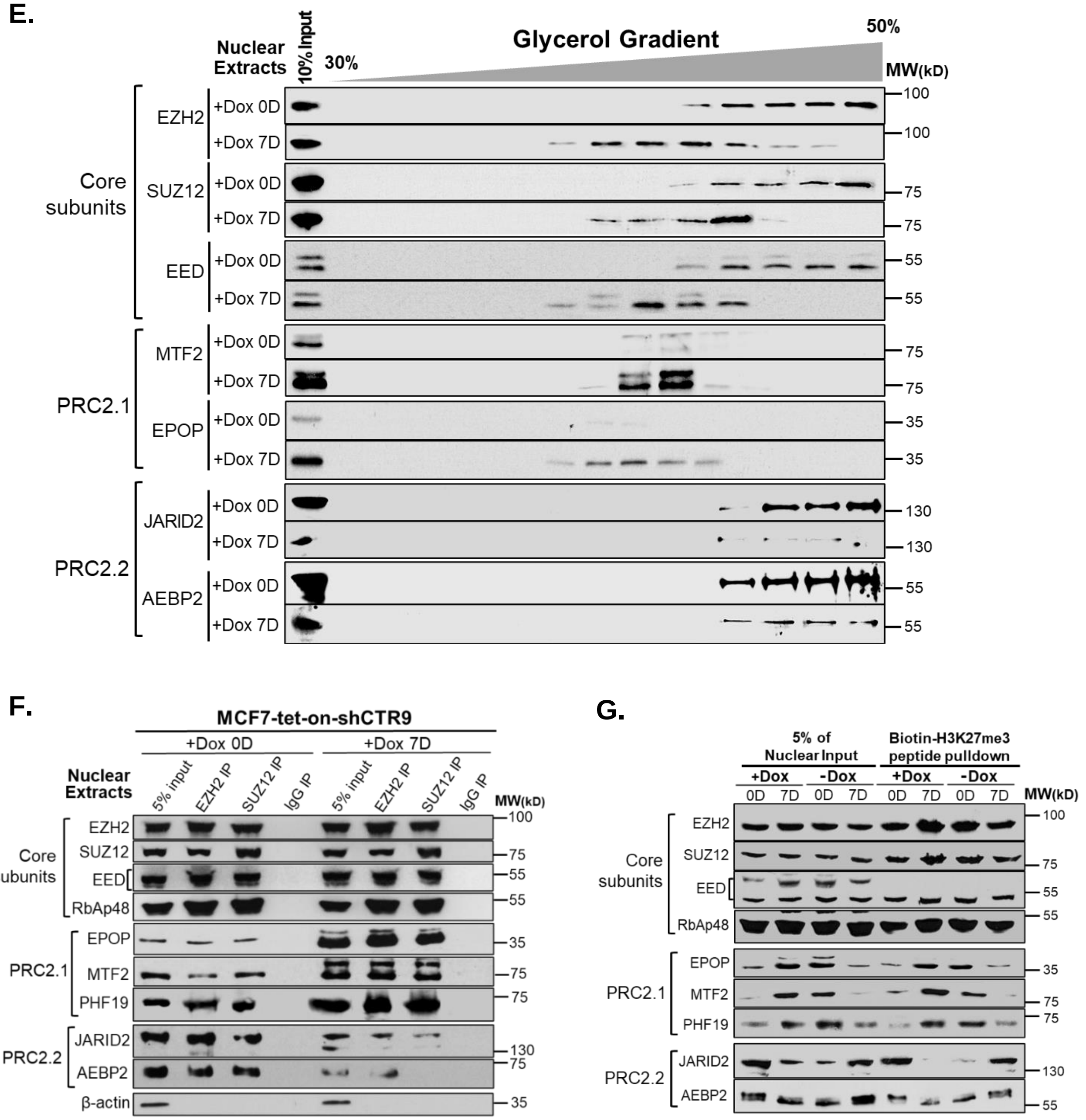
E.
Nuclear Extracts
10% Input
30%
Glycerol Gradient
50%
MW(kD)
Core subunits
EZH2
+Dox 0D
+Dox 7D
100
100
SUZ12
+Dox 0D
+Dox 7D
75
75
EED
+Dox 0D
+Dox 7D
55
55
PRC2.1
MTF2
+Dox 0D
+Dox 7D
75
75
EPOP
+Dox 0D
+Dox 7D
35
35
PRC2.2
JARID2
+Dox 0D
+Dox 7D
130
130
AEBP2
+Dox 0D
+Dox 7D
55
55
F.
MCF7-tet-on-shCTR9
+Dox 0D
+Dox 7D
Nuclear Extracts
5% input
EZH2 IP
SUZ12 IP
IgG IP
5% input
EZH2 IP
SUZ12 IP
IgG IP
MW(kD)
Core subunits
EZH2
SUZ12
EED
RbAp48
PRC2.1
EPOP
MTF2
PHF19
PRC2.2
JARID2
AEBP2
β-actin
100
75
55
55
35
75
75
130
75
35
G.
5% of Nuclear Input
Biotin-H3K27me3 peptide pulldown
+Dox
-Dox
+Dox
-Dox
0D
7D
0D
7D
0D
7D
0D
7D
MW(kD)
Core subunits
EZH2
SUZ12
EED
RbAp48
PRC2.1
EPOP
MTF2
PHF19
PRC2.2
JARID2
AEBP2
100
75
55
55
35
75
75
130
55

Figure 2-12.

- **A.** Western blot analysis of PRC2 core subunits (i.e., EZH2, SUZ12, EED and RbAp48) and facultative subunits EPOP/MTF2/PHF19 for PRC2.1 and JARID2/AEBP2 for PRC2.2 in total lysates and chromatin fractions in MCF7-tet-on-shCTR9 cells treated with Dox. β-actin and histone H3 were used as loading controls for total lysates and chromatin extracts, respectively.
- **B.** Western blotting analysis of PRC2 core and facultative subunits in total lysates and chromatin fraction of MCF7-shControl/shCTR9#3/shCTR9#5 cells. β-actin and Histone H3 were used as loading controls for total lysates and chromatin extracts, respectively.
- **C.** Western blot analysis of PRC2 core subunits and facultative components in chromatin extracts from MCF7-tet-on-shCTR9 cells treated with Dox. Histone H3 served as a loading control.
- **D.** Bar chart showing the Pearson correlation of CTR9 and PRC2 core and facultative subunits expression in 817 primary ER-positive breast tumor samples from TCGA. Adjusted p-values were transformed in -log10 manner and shown as red scale-bars.
- **E.** Glycerol gradient sedimentation to separate PRC2.1 and PRC2.2 subtypes in nuclear extracts of MCF7-tet-on-shCTR9 cells after Dox treatment (*Left*). Molecular weight of individual PRC2 subunits were shown (*Right*).
- **F.** Co-Immunoprecipitation of PRC2 auxiliary components with the core subunits (EZH2 or SUZ12) using nuclear extracts from MCF7-tet-on-shCTR9 treated with Dox for 0 day or 7 days. β-actin was used as a loading control for input.
- **G.** Western Blot analyses of PRC2 core and facultative subunits pulled down by biotinylated H3K27me3 peptide (aa 21-40) from nuclear extracts.

Figure 2-13.

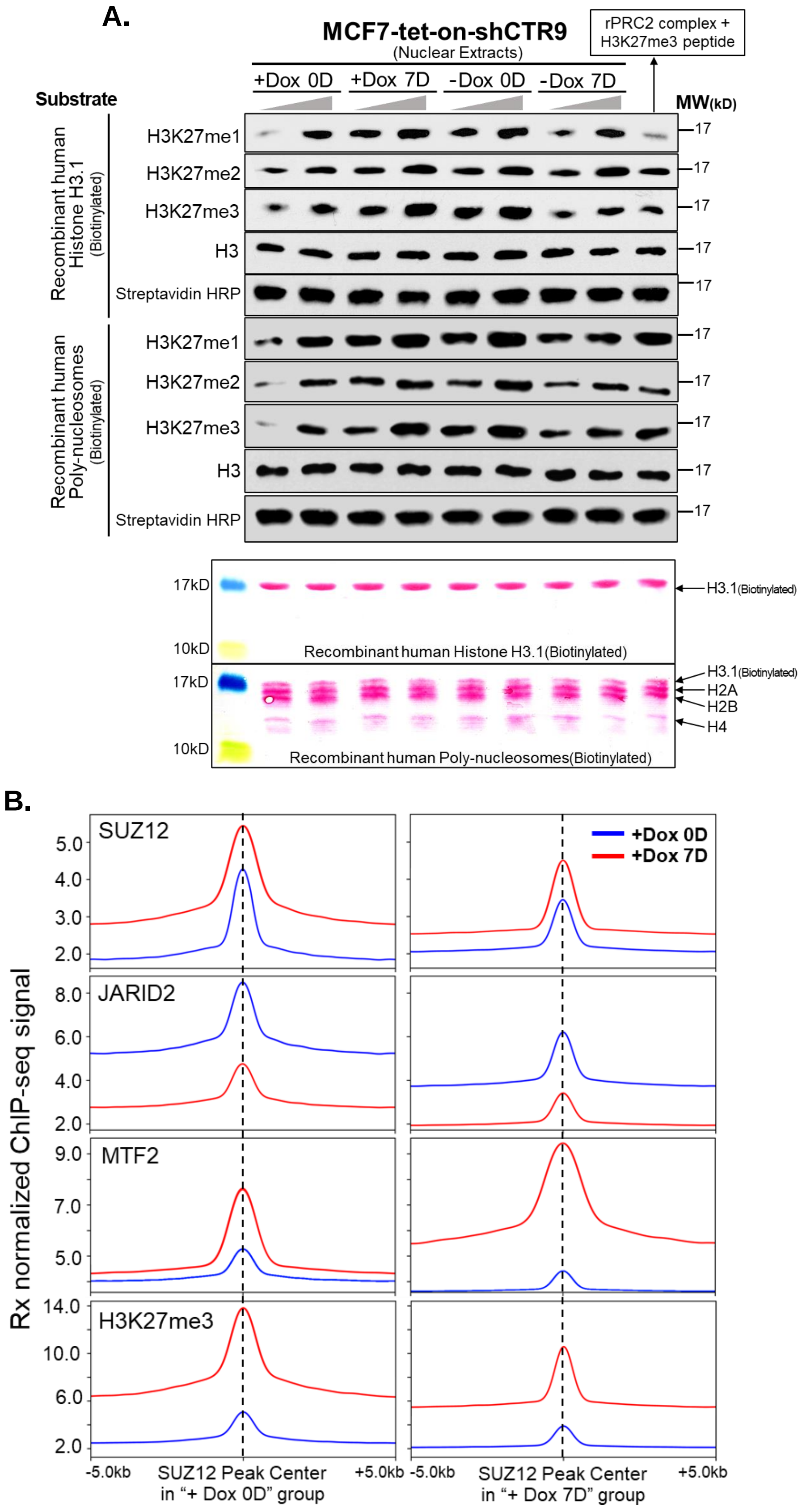
A.
MCF7-tet-on-shCTR9
(Nuclear Extracts)
rPRC2 complex + H3K27me3 peptide
+Dox 0D
+Dox 7D
-Dox 0D
-Dox 7D
Substrate
MW(kD)
Recombinant human Histone H3.1 (Biotinylated)
H3K27me1
H3K27me2
H3K27me3
H3
Streptavidin HRP
Recombinant human Poly-nucleosomes (Biotinylated)
H3K27me1
H3K27me2
H3K27me3
H3
Streptavidin HRP
17
17kD
10kD
H3.1(Biotinylated)
Recombinant human Histone H3.1(Biotinylated)
H3.1(Biotinylated)
H2A
H2B
H4
Recombinant human Poly-nucleosomes(Biotinylated)
B.
Rx normalized ChIP-seq signal
SUZ12
JARID2
MTF2
H3K27me3
+Dox 0D
+Dox 7D
2.0
3.0
4.0
5.0
6.0
8.0
7.0
9.0
10.0
14.0
-5.0kb
+5.0kb
SUZ12 Peak Center in “+ Dox 0D” group
SUZ12 Peak Center in “+ Dox 7D” group

Figure 2-13.

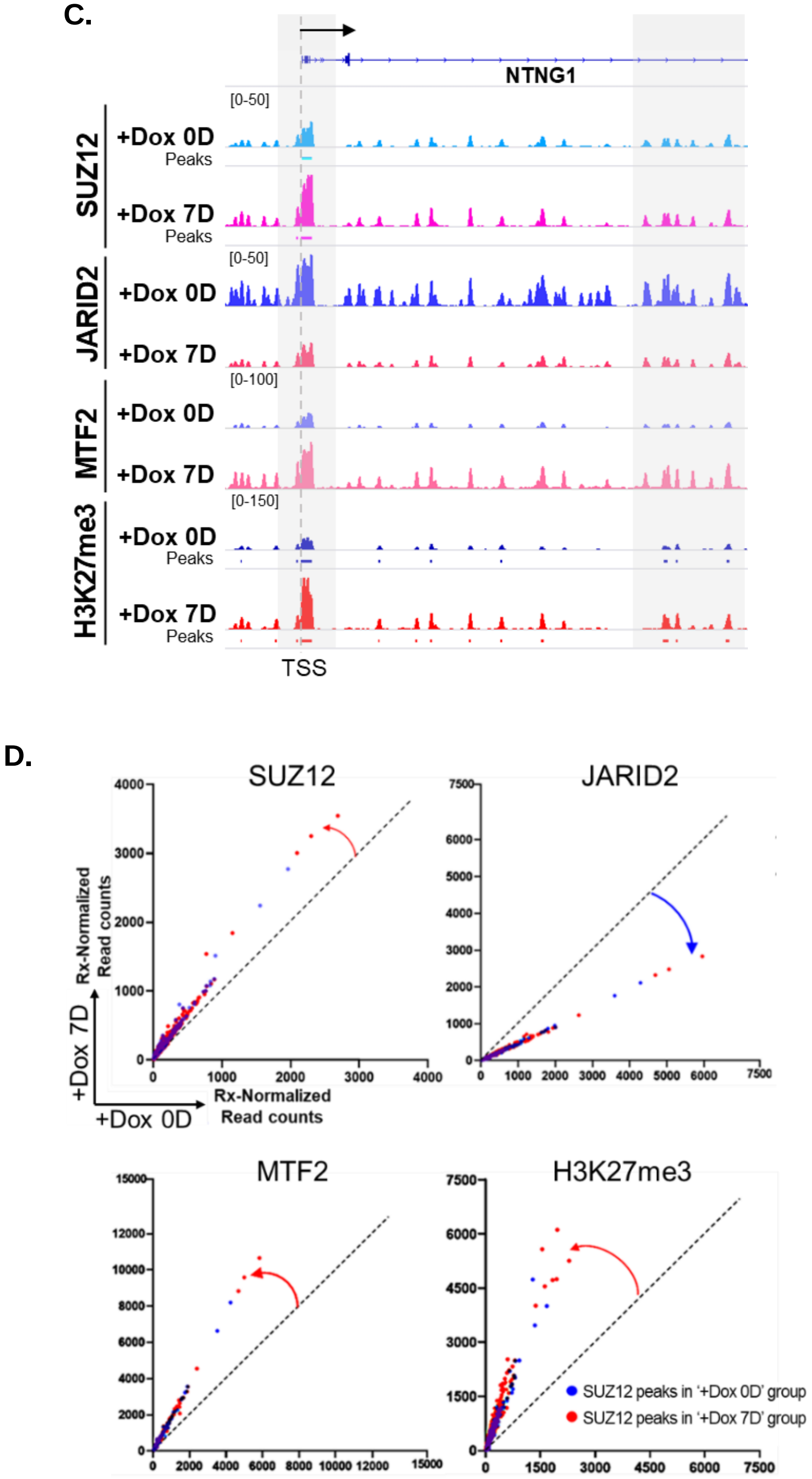
C.
NTNG1
SUZ12
[0-50]
+Dox 0D
Peaks
+Dox 7D
Peaks
JARID2
[0-50]
+Dox 0D
+Dox 7D
MTF2
[0-100]
+Dox 0D
+Dox 7D
H3K27me3
[0-150]
+Dox 0D
Peaks
+Dox 7D
Peaks
TSS
D.
SUZ12
JARID2
MTF2
H3K27me3
+Dox 7D
Rx-Normalized Read counts
+Dox 0D
Rx-Normalized Read counts
0
1000
2000
3000
4000
5000
6000
7500
8000
10000
12000
15000
1500
4500
SUZ12 peaks in '+Dox 0D' group
SUZ12 peaks in '+Dox 7D' group

Figure 2-13.

- **A.** *In vitro* H3K27 histone methyltransferase assay (HMT) using recombinant human biotinylated histone H3.1 or human biotinylated poly-nucleosomes as substrates. The ascending amounts of nuclear extracts from MCF7-tet-on-shCTR9 cells under indicated conditions were used as enzyme sources. Recombinant PRC2 complex and H3K27me3 peptide were used as a positive control (*Up*). Ponceau S staining of HMT substrates that pre-bound on streptavidin beads (*Bottom*).
- **B.** Composite profile of SUZ12, JARID2, MTF2, and H3K27me3 ChIP-Rx signals in ±5.0kb range of SUZ12 peak centers.
- **C.** Representative genome browser snapshot of ChIP-Rx signals for SUZ12, JARID2, MTF2, and H3K27me3 from MCF7-tet-on-shCTR9 cells treated with Dox for 0 day or 7 days. Each signal track represents the mean of two biological replicates.
- **D.** Dot plots of Rx-normalized read counts on SUZ12 peaks from MCF7-tet-on-shCTR9 cells treated with Dox for 0 day or 7 days. Blue dots represent SUZ12 peaks identified in ‘+Dox 0D’ group, and red dots represent SUZ12 peaks found in ‘+Dox 7D’ group.

Figure 2-14.

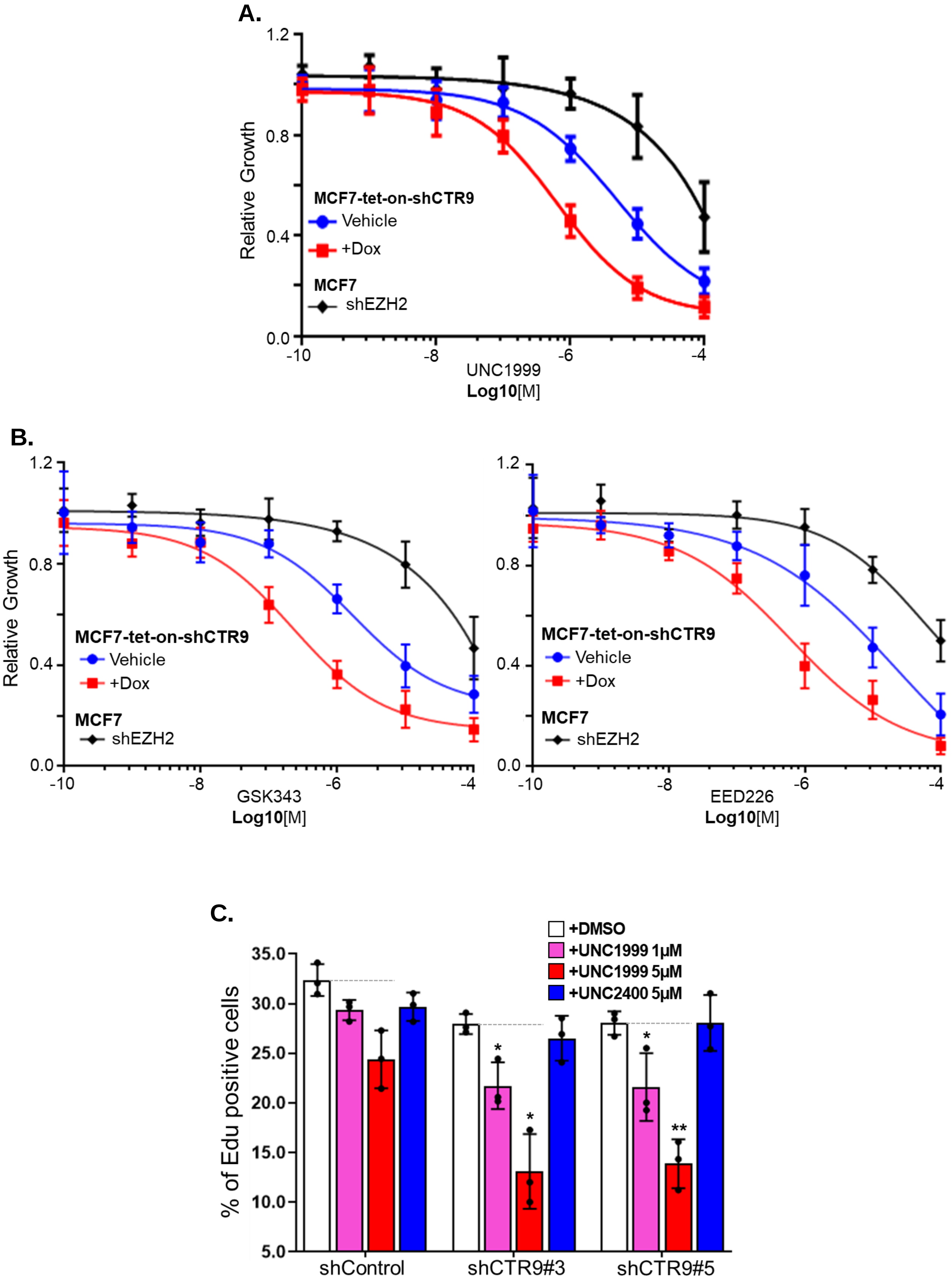
A.
1.2
0.8
0.4
0.0
Relative Growth
MCF7-tet-on-shCTR9
Vehicle
+Dox
MCF7
shEZH2
-10
-8
-6
-4
UNC1999
Log10[M]
B.
1.2
0.8
0.4
0.0
Relative Growth
MCF7-tet-on-shCTR9
Vehicle
+Dox
MCF7
shEZH2
-10
-8
-6
-4
GSK343
Log10[M]
1.2
0.8
0.4
0.0
MCF7-tet-on-shCTR9
Vehicle
+Dox
MCF7
shEZH2
-10
-8
-6
-4
EED226
Log10[M]
C.
+DMSO
+UNC1999 1μM
+UNC1999 5μM
+UNC2400 5μM
35.0
30.0
25.0
20.0
15.0
10.0
5.0
% of Edu positive cells
*
*
*
**
shControl
shCTR9#3
shCTR9#5

Figure 2-14.

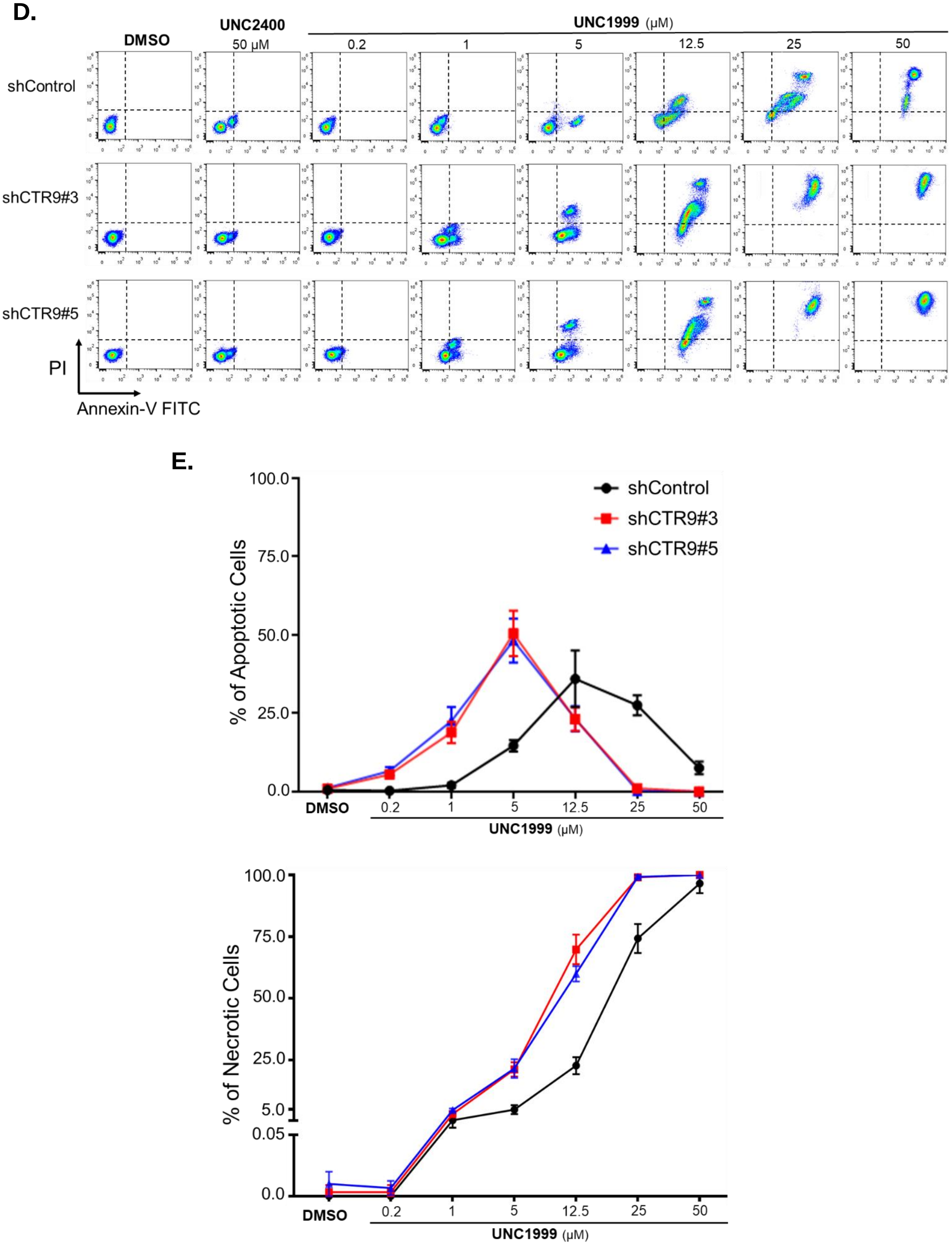
D.
DMSO
UNC2400
50 μM
UNC1999 (μM)
0.2
1
5
12.5
25
50
shControl
shCTR9#3
shCTR9#5
PI
Annexin-V FITC
E.
% of Apoptotic Cells
100.0
75.0
50.0
25.0
0.0
shControl
shCTR9#3
shCTR9#5
DMSO
0.2
1
5
12.5
25
50
UNC1999 (μM)
% of Necrotic Cells
100.0
75.0
50.0
25.0
5.0
0.05
0.0
DMSO
0.2
1
5
12.5
25
50
UNC1999 (μM)

Figure 2-14.

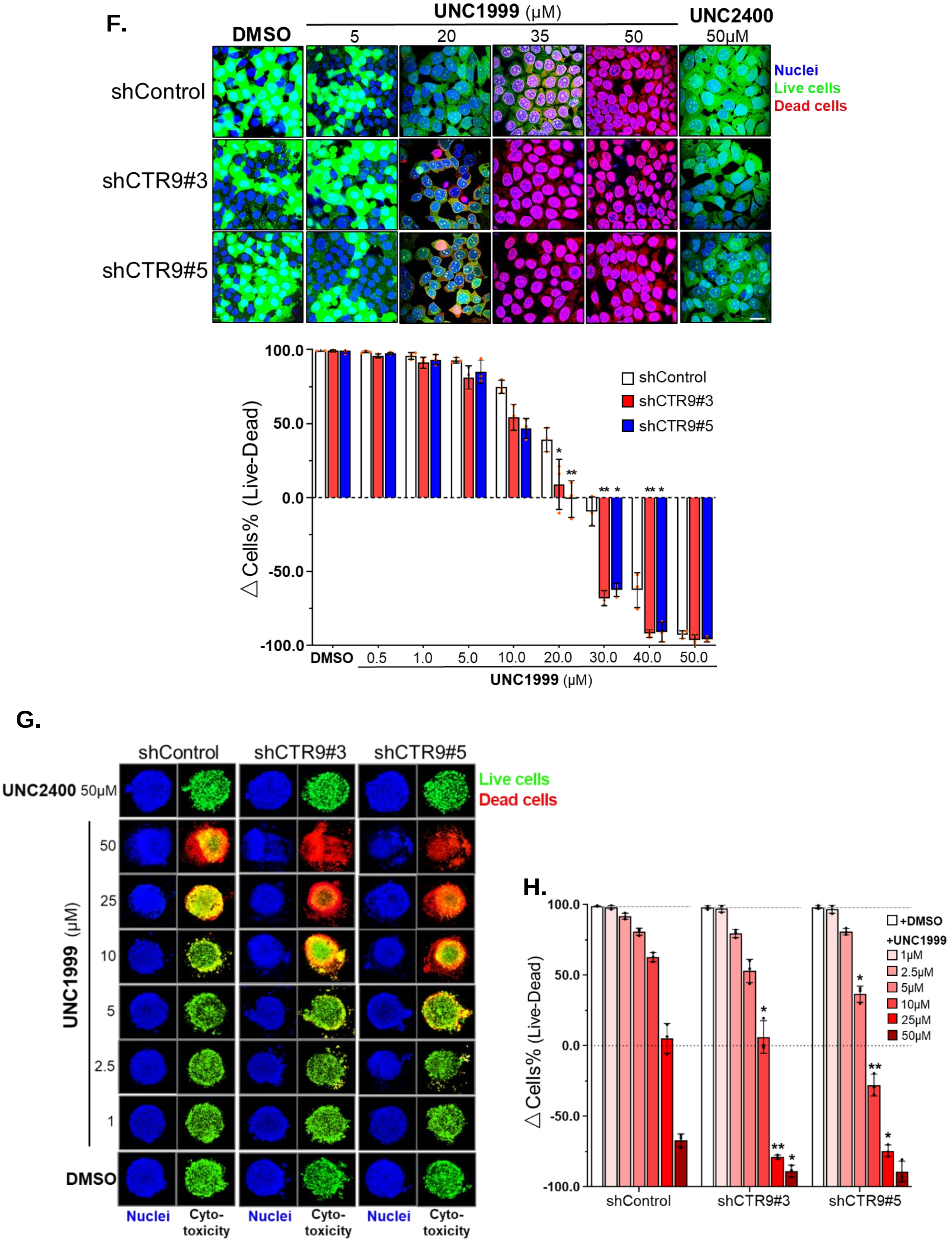
F.
DMSO
UNC1999 (μM)
5
20
35
50
UNC2400
50μM
shControl
shCTR9#3
shCTR9#5
Nuclei
Live cells
Dead cells
100.0
50.0
0.0
-50.0
-100.0
△Cells% (Live-Dead)
□ shControl
🟥 shCTR9#3
🟦 shCTR9#5
*
**
** *
** *
DMSO
0.5
1.0
5.0
10.0
20.0
30.0
40.0
50.0
UNC1999 (μM)
G.
shControl
shCTR9#3
shCTR9#5
UNC2400 50μM
Live cells
Dead cells
UNC1999 (μM)
50
25
10
5
2.5
1
DMSO
Nuclei
Cyto-toxicity
Nuclei
Cyto-toxicity
Nuclei
Cyto-toxicity
H.
100.0
50.0
0.0
-50.0
-100.0
△Cells% (Live-Dead)
□ +DMSO
+UNC1999
1μM
2.5μM
5μM
10μM
25μM
50μM
*
**
*
*
**
*
shControl
shCTR9#3
shCTR9#5

Figure 2-14.

A. Cell viability measured by MTT assays after treating MCF7-shEZH2 or MCF7-tet-on-shCTR9 cells (Vehicle or Dox) with increasing doses of UNC1999. Data are represented as mean ± SD (n=6). IC_{50} were calculated through non-linear regression against log(inhibitor) response model. (IC50: Vehicle = 4.6 ± 0.3μM; +Dox = 1.0 ± 0.1μM)

B. Cell viability measured by MTT assays after treating MCF7-shEZH2 or MCF7-tet-on-shCTR9 cells (Vehicle or Dox) with increasing doses of GSK343 (left) or EED226 (right). Data are represented as mean ± SD (n=6).

C. Quantification of % EdU positive cells from control shRNA or shCTR9 (#3 and #5) MCF7 cells treated with DMSO, UNC1999 or UNC2400. Data are represented as mean ± SD (n=3). The difference of % EdU positive cells between DMSO and each group of UNC1999 treatment were calculated and corresponding p-value of Welch's t-test were shown (*: $p < 0.05$; **: $p < 0.01$).

D. Flow cytometry analyses of apoptotic and necrotic cells using PI uptake and annexin-V FITC labeling. MCF7-shControl or MCF7-shCTR9#3 or shCTR9#5 cells were treated with DMSO, 0.2 to 50 μM UNC1999, or 50 μM UNC2400 for 2 days.

E. Quantification of % apoptotic cells with Annexin-V^+**/**PI^- (*Top*) and % necrotic cells with Annexin-V^+**/**PI^+ (*Bottom*) in shRNA or shCTR9 expressing MCF7 cells treated with DMSO or ascending concentrations of UNC1999. (n=3)

F. Representative confocal images of MCF7-shControl, MCF7 shCTR9#3 or shCTR9#5 cells after treating with DMSO or the ascending concentrations of UNC1999 for 2 days. UNC2400 (negative paralog) serves as a negative control. Nuclei were stained in blue. Live cells with ubiquitous esterase activity were shown in green. Dead cells with impaired cell membrane were shown in red (*Top*). Quantification of cytotoxicity in MCF7-shControl, MCF7shCTR9#3 or shCTR9#5 cells treated with ascending concentration of UNC1999. The differences between live cells and dead cells percentages were plotted. Comparative value between DMSO and each group of UNC1999 treatment were calculated and corresponding p-value of Welch's t-test were shown (*: $p < 0.05$; **: $p < 0.01$) (*Bottom*).

G. Representative confocal images of 3D spheroids of shRNA or shCTR9 expressing MCF7 cells after treatment with DMSO or increasing doses of UNC1999 for 24 hours. UNC2400 (negative paralog) serves as a negative control. Nuclei (blue), live cells with ubiquitous esterase activity (green) and dead cells with impaired cell membrane (red) were shown by immunofluorescence staining.

H. Quantification of the cytotoxic response of shRNA or shCTR9 expressing MCF7 cells grew in 3D spheroids against UNC1999. The difference of live cells percentage and dead cells percentage were measured by fluorescence absorbance of calcein AM and EthD-1, respectively. Data are shown in mean ± SD. (n=3) *$p < 0.05$; ** $p < 0.01$.

Figure 2-15.

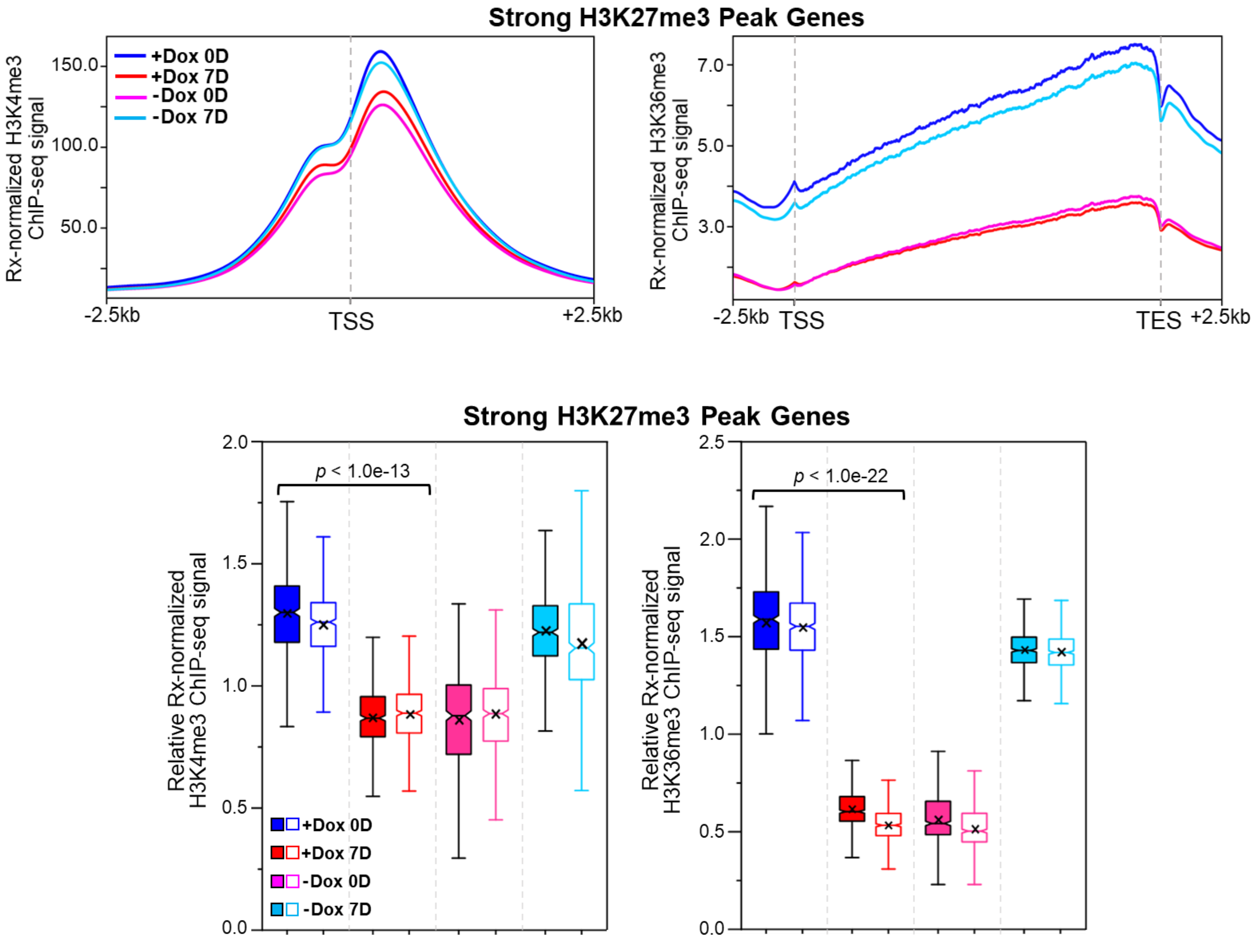

Figure 2-15.

(*Top*) Average profiles of Rx-normalized H3K4me3 (left) and H3K36me3 (right) ChIP-seq signals at ±2.5kb of TSS or TSS-TES regions of the strong H3K27me3 peak associated genes (n=11,483). (*Bottom*) Notched boxplot of relative Rx-normalized H3K4me3 (left) and H3K36me3 (right) ChIP-seq signals of strong H3K27me3 peak genes (n=2). Paired Student’s t test was used to calculate statistical significance among groups.

Figure 2-16.

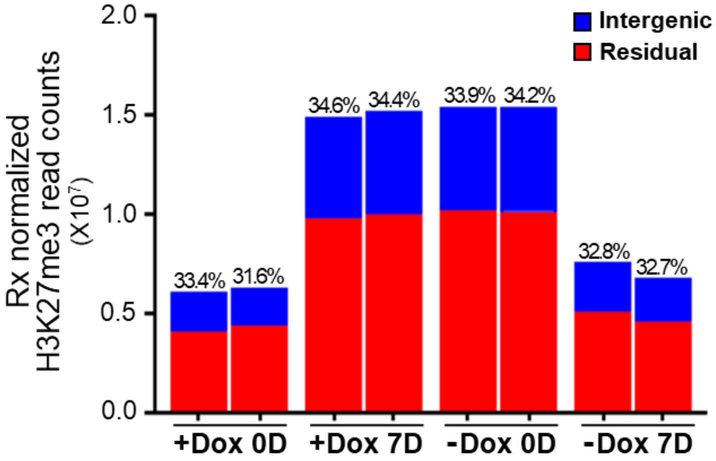

Figure 2-16.

Rx-normalized H3K27me3 ChIP-seq read counts in intergenic regions (blue) as well as residual genomic regions (red) upon Dox addition and removal in MCF7-tet-on-shCTR9 cells. Each bar represents individual biological replicate. Percentage (%) of intergenic read counts were shown on the top of each bar.

Figure 2-17.

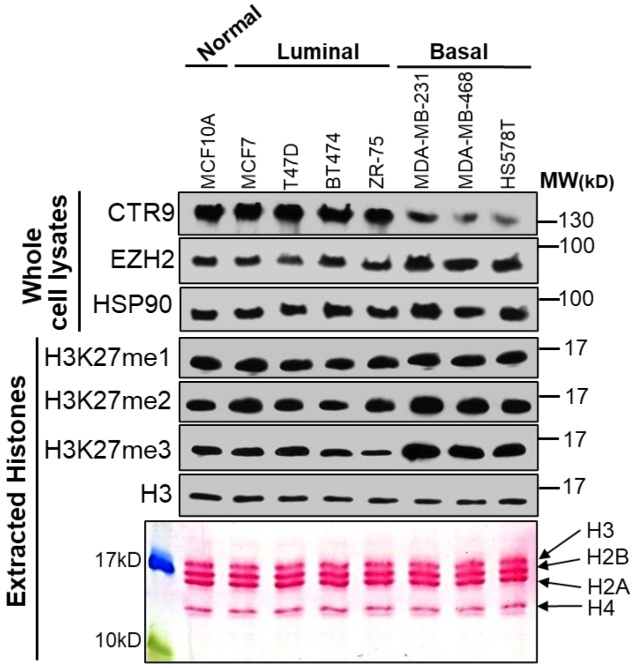

Figure 2-17.

(*Top*) Western blot of CTR9, EZH2 and H3K27me1/2/3 in an immortalized non-transformed mammary epithelial cell line (MCF10A), four ER-positive human breast cancer cell lines, and three TNBC cell lines. HSP90 and histone H3 were loading controls for whole cell lysate and extracted histones, respectively. (*Bottom*) Ponceau S staining of acid extracted histone from above mentioned cell lines.

2.7 TABLES & LEGENDS

Table 1.

Peptide Sequence	**Peptide Peak Area in LC-MS/MS**					
H3(3-8)	**+Dox 0D**-Rep1	**+Dox 0D**-Rep2	**+Dox 0D**-Rep3	**+Dox 7D**-Rep1	**+Dox 7D**-Rep2	**+Dox 7D**-Rep3
T$\mathbf{K}_{4}$QTAR	2.890E+10	2.990E+10	3.230E+10	1.800E+10	8.970E+09	1.230E+10
T$\mathbf{K}_{4}$**(me1)**QTAR	4.180E+09	4.230E+09	4.580E+09	2.100E+09	1.050E+09	1.420E+09
T$\mathbf{K}_{4}$**(me2)**QTAR	4.860E+08	5.230E+08	5.580E+08	2.330E+08	1.220E+08	1.730E+08
T$\mathbf{K}_{4}$**(me3)**QTAR	1.630E+08	1.650E+08	2.290E+08	1.160E+08	6.610E+07	8.120E+07
T$\mathbf{K}_{4}$**(ac)**QTAR	5.950E+07	6.730E+07	6.840E+07	1.980E+07	3.710E+06	2.770E+06
H3(9-17)	**+Dox 0D**-Rep1	**+Dox 0D**-Rep2	**+Dox 0D**-Rep3	**+Dox 7D**-Rep1	**+Dox 7D**-Rep2	**+Dox 7D**-Rep3
$\mathbf{K}_{9}$STGG$\mathbf{K}_{14}$APR	3.860E+09	4.160E+09	4.650E+09	3.570E+09	1.980E+09	2.150E+09
$\mathbf{K}_{9}$**(me1)**STGG$\mathbf{K}_{14}$APR	2.340E+09	2.510E+09	2.900E+09	1.730E+09	1.290E+09	1.210E+09
$\mathbf{K}_{9}$**(me2)**STGG$\mathbf{K}_{14}$APR	4.350E+09	4.810E+09	5.460E+09	3.290E+09	2.210E+09	2.370E+09
$\mathbf{K}_{9}$**(me3)**STGG$\mathbf{K}_{14}$APR	2.690E+09	2.960E+09	3.240E+09	2.120E+09	1.370E+09	2.070E+09
$\mathbf{K}_{9}$STGG$\mathbf{K}_{14}$**(ac)**APR	3.890E+09	3.970E+09	3.480E+09	2.540E+09	2.460E+09	2.210E+09
$\mathbf{K}_{9}$**(me1)**STGG$\mathbf{K}_{14}$**(ac)**APR	2.850E+09	2.920E+09	2.620E+09	1.420E+09	1.420E+09	1.350E+09
$\mathbf{K}_{9}$**(me2)**STGG$\mathbf{K}_{14}$**(ac)**APR	5.490E+09	5.570E+09	5.080E+09	2.540E+09	2.550E+09	2.230E+09
$\mathbf{K}_{9}$**(me3)**STGG$\mathbf{K}_{14}$**(ac)**APR	2.140E+09	2.240E+09	2.110E+09	1.180E+09	1.090E+09	1.210E+09
$\mathbf{K}_{9}$**(ac)**STGG$\mathbf{K}_{14}$**(ac)**APR	2.860E+08	2.030E+08	2.290E+08	9.940E+07	8.550E+07	7.320E+07
H3(18-26)	**+Dox 0D**-Rep1	**+Dox 0D**-Rep2	**+Dox 0D**-Rep3	**+Dox 7D**-Rep1	**+Dox 7D**-Rep2	**+Dox 7D**-Rep3
$\mathbf{K}_{18}$QLAT$\mathbf{K}_{23}$AAR	1.090E+10	1.070E+10	1.240E+10	6.540E+09	7.260E+09	4.870E+09
$\mathbf{K}_{18}$QLAT$\mathbf{K}_{23}$**(me1)**AAR	1.810E+07	2.320E+07	3.090E+07	1.320E+07	2.020E+07	1.550E+07
$\mathbf{K}_{18}$QLAT$\mathbf{K}_{23}$**(ac)**AAR	8.180E+09	6.970E+09	5.510E+09	3.400E+09	3.980E+09	3.910E+09
$\mathbf{K}_{18}$**(ac)**QLAT$\mathbf{K}_{23}$**(ac)**AAR	3.160E+08	3.190E+08	3.320E+08	1.330E+08	2.110E+08	1.750E+08
H3(27-40)	**+Dox 0D**-Rep1	**+Dox 0D**-Rep2	**+Dox 0D**-Rep3	**+Dox 7D**-Rep1	**+Dox 7D**-Rep2	**+Dox 7D**-Rep3
$\mathbf{K}_{27}$SAPATGGV$\mathbf{K}_{36}$KPHR	8.320E+08	9.660E+08	7.520E+08	1.450E+07	6.470E+07	5.270E+07
$\mathbf{K}_{27}$**(me1)**SAPATGGV$\mathbf{K}_{36}$KPHR	2.486E+08	2.715E+08	2.089E+08	1.622E+07	9.851E+07	7.908E+07
$\mathbf{K}_{27}$**(me2)**SAPATGGV$\mathbf{K}_{36}$KPHR	3.472E+08	3.568E+08	3.462E+08	4.823E+08	4.270E+08	3.583E+08
$\mathbf{K}_{27}$**(me3)**SAPATGGV$\mathbf{K}_{36}$KPHR	2.327E+08	2.446E+08	3.185E+08	2.813E+08	2.727E+08	2.146E+08
$\mathbf{K}_{27}$SAPATGGV$\mathbf{K}_{36}$**(me1)**KPHR	7.484E+08	8.785E+08	6.551E+08	4.048E+07	4.849E+07	4.392E+07
$\mathbf{K}_{27}$**(me1)**SAPATGGV$\mathbf{K}_{36}$**(me1)**KPHR	6.234E+08	7.498E+08	5.369E+08	2.470E+07	1.990E+08	1.659E+08
$\mathbf{K}_{27}$**(me2)**SAPATGGV$\mathbf{K}_{36}$**(me1)**KPHR	4.867E+08	4.709E+08	3.288E+08	4.963E+08	4.877E+08	4.084E+08
$\mathbf{K}_{27}$**(me3)**SAPATGGV$\mathbf{K}_{36}$**(me1)**KPHR	6.152E+07	8.251E+07	6.858E+07	7.768E+07	9.330E+07	8.818E+07
$\mathbf{K}_{27}$SAPATGGV$\mathbf{K}_{36}$**(me2)**KPHR	1.019E+09	1.253E+09	9.568E+08	1.299E+07	5.506E+07	5.083E+07
$\mathbf{K}_{27}$**(me1)**SAPATGGV$\mathbf{K}_{36}$**(me2)**KPHR	3.863E+08	5.891E+08	3.952E+08	2.769E+07	1.203E+08	1.016E+08
$\mathbf{K}_{27}$**(me2)**SAPATGGV$\mathbf{K}_{36}$**(me2)**KPHR	4.570E+08	5.370E+08	3.890E+08	5.380E+08	7.000E+08	5.810E+08
$\mathbf{K}_{27}$**(me3)**SAPATGGV$\mathbf{K}_{36}$**(me2)**KPHR	6.445E+07	7.057E+07	4.050E+07	1.444E+08	1.652E+08	1.349E+08
$\mathbf{K}_{27}$SAPATGGV$\mathbf{K}_{36}$**(me3)**KPHR	1.903E+08	2.564E+08	7.448E+07	5.358E+06	2.928E+07	1.541E+07
$\mathbf{K}_{27}$**(me1)**SAPATGGV$\mathbf{K}_{36}$**(me3)**KPHR	7.048E+07	8.149E+07	6.742E+07	2.372E+07	9.570E+07	6.882E+07
$\mathbf{K}_{27}$**(me2)**SAPATGGV$\mathbf{K}_{36}$**(me3)**KPHR	1.525E+07	2.213E+07	1.760E+07	2.543E+07	2.177E+07	1.906E+07
$\mathbf{K}_{27}$**(ac)**SAPATGGV$\mathbf{K}_{36}$KPHR	3.630E+07	3.300E+07	3.660E+07	1.140E+07	1.070E+07	9.190E+06
$\mathbf{K}_{27}$**(ac)**SAPATGGV$\mathbf{K}_{36}$**(me1)**KPHR	3.430E+07	2.650E+07	2.770E+07	4.160E+06	4.870E+06	3.040E+06
$\mathbf{K}_{27}$**(ac)**SAPATGGV$\mathbf{K}_{36}$**(me2)**KPHR	7.860E+07	6.380E+07	7.690E+07	1.440E+07	1.340E+07	1.200E+07
$\mathbf{K}_{27}$**(ac)**SAPATGGV$\mathbf{K}_{36}$**(me3)**KPHR	1.980E+07	1.200E+07	1.220E+07	6.250E+06	6.120E+06	7.270E+06
H3(73-83)	**+Dox 0D**-Rep1	**+Dox 0D**-Rep2	**+Dox 0D**-Rep3	**+Dox 7D**-Rep1	**+Dox 7D**-Rep2	**+Dox 7D**-Rep3
EIAQDF$\mathbf{K}_{79}$TDLR	3.160E+09	1.910E+09	2.060E+09	1.580E+08	3.420E+09	3.380E+09
EIAQDF$\mathbf{K}_{79}$**(me1)**TDLR	3.500E+08	3.310E+08	3.580E+08	2.280E+08	5.450E+08	5.170E+08
EIAQDF$\mathbf{K}_{79}$**(me2)**TDLR	6.410E+07	6.410E+07	6.450E+07	5.790E+07	9.290E+07	8.870E+07

Table 1. Summary of the peptide intensity for each detected histone peptide species for corresponding histone modifications reported in Figure 1B as measured by quantitative tandem mass spectrometry analysis.

Table 2.

Top 15 Epigenetic modulators	Wilcoxon Test statistic	Wilcoxon P-value	Z-score	max AUC
EED	2.982	1.43E-03	3.047	0.813
SSRP1	2.887	1.95E-03	3.995	0.683
RING1B	4.114	1.95E-05	2.642	0.828
TET2	3.763	8.38E-05	2.566	0.773
EZH2	10.499	4.37E-26	1.925	0.95
CTCF	25.995	2.82E-149	1.998	0.752
G9a	2.541	5.53E-03	2.928	0.62
KDM4A	2.81	2.48E-03	2.223	0.704
SUZ12	4.933	4.05E-07	1.349	0.941
JARID2	5.443	2.62E-08	1.308	0.955
JMJD6	3.3	4.84E-04	1.383	0.75
HIRA	1.77	3.83E-02	2.037	0.751
CBX3	1.665	4.79E-02	2.88	0.613
KDM2B	5.118	1.54E-07	0.743	0.752

Top 15 Transcription Factors	Wilcoxon Test statistic	Wilcoxon P-value	Z-score	max AUC
YBX1	36.25	1.45E-04	3.63	0.769
REST	99.23	1.66E-23	3.442	0.709
BMI1	45.07	3.29E-06	3.29	0.739
ZBTB48	58.19	2.97E-09	2.939	0.722
TSC22D4	26.71	3.78E-03	3.313	0.746
ASCL1	59.73	1.16E-09	2.896	0.716
ZTA	23.94	8.34E-03	3.417	0.736
ZNF202	24.32	7.51E-03	3.02	0.739
ZNF207	20.32	2.11E-02	3.393	0.744
GTF2I	49.62	3.50E-07	2.51	0.722
CRY1	17.08	4.39E-02	3.565	0.777
ZNF707	22.64	1.18E-02	3.451	0.678
TCF7L1	38.87	5.08E-05	3.063	0.64
IKZF1	43.51	6.79E-06	2.34	0.775

Table 2. *BART* (Binding Analysis for Regulation of Transcription) results of 11,483 strong H3K27me3 peak genes. Higher the 'Wilcoxon Test statistic' is, more likely this factor regulates the input genes. Higher the 'max AUC', greater association of the dataset with the input genes.

Table 3.

Top 15 Epigenetic modulators	Wilcoxon Test statistic	Wilcoxon P-value	Z-score	max AUC
MBD2	3.567	1.80E-04	2.4	0.899
SUZ12	5.595	1.10E-08	1.582	0.908
EZH2	6.979	1.49E-12	1.262	0.917
TET2	2.959	1.54E-03	2.078	0.889
KDM4A	2.544	5.49E-03	1.948	0.895
JARID2	5.042	2.31E-07	1.19	0.909
KDM2B	5.546	1.46E-08	0.955	0.939
EZH1	2.81	2.48E-03	1.223	0.917
INO80	2.916	1.78E-03	1.096	0.919
TET3	1.772	3.82E-02	1.168	0.921
RNF2	1.871	3.07E-02	1.089	0.921
HDAC2	2.508	6.07E-03	1.193	0.89
BMI1	1.678	4.67E-02	1.524	0.891
BCL11B	3.041	1.18E-03	0.733	0.893
KDM5B	2.115	1.72E-02	1.007	0.891

Top 15 Transcription Factors	Wilcoxon Test statistic	Wilcoxon P-value	Z-score	max AUC
ZFX	3.896	4.88E-05	1.63	0.93
SP1	4.253	1.06E-05	1.718	0.911
ZNF202	1.85	3.22E-02	2.373	0.93
ZBTB48	4.554	2.63E-06	2.364	0.87
TRIM25	2.267	1.17E-02	1.984	0.896
WDR5	3.006	1.32E-03	1.059	0.928
ZBTB7A	4.663	1.56E-06	1.255	0.89
MYC	8.573	5.04E-18	0.698	0.924
ZNF263	2.495	6.30E-03	1.802	0.873
GTF2I	2.653	3.99E-03	1.569	0.876
KLF9	3.279	5.21E-04	1.05	0.888
ZNF687	1.986	2.35E-02	1.827	0.869
ZMYND8	2.419	7.78E-03	1.567	0.869
ZNF592	1.854	3.19E-02	2.421	0.857
SPDEF	1.399	8.10E-02	1.834	0.893

Table 3. *BART* (Binding Analysis for Regulation of Transcription) results of 6,750 confident Flag-CTR9 binding genes.

2.8 REFERENCES

1. Van Oss, S.B., Cucinotta, C.E. and Arndt, K.M. (2017) Emerging Insights into the Roles of the Paf1 Complex in Gene Regulation. *Trends Biochem Sci*, **42**, 788-798.
2. Zhu, B., Mandal, S.S., Pham, A.D., Zheng, Y., Erdjument-Bromage, H., Batra, S.K., Tempst, P. and Reinberg, D. (2005) The human PAF complex coordinates transcription with events downstream of RNA synthesis. *Genes Dev*, **19**, 1668-1673.
3. Chu, X., Qin, X., Xu, H., Li, L., Wang, Z., Li, F., Xie, X., Zhou, H., Shen, Y. and Long, J. (2013) Structural insights into Paf1 complex assembly and histone binding. *Nucleic Acids Res*, **41**, 10619-10629.
4. Vos, S.M., Farnung, L., Boehning, M., Wigge, C., Linden, A., Urlaub, H. and Cramer, P. (2018) Structure of activated transcription complex Pol II-DSIF-PAF-SPT6. *Nature*, **560**, 607-612.
5. Yu, M., Yang, W., Ni, T., Tang, Z., Nakadai, T., Zhu, J. and Roeder, R.G. (2015) RNA polymerase II-associated factor 1 regulates the release and phosphorylation of paused RNA polymerase II. *Science*, **350**, 1383-1386.
6. Tomson, B.N. and Arndt, K.M. (2013) The many roles of the conserved eukaryotic Paf1 complex in regulating transcription, histone modifications, and disease states. *Biochim Biophys Acta*, **1829**, 116-126.
7. Jaehning, J.A. (2010) The Paf1 complex: platform or player in RNA polymerase II transcription? *Biochim Biophys Acta*, **1799**, 379-388.
8. Hanks, S., Perdeaux, E.R., Seal, S., Ruark, E., Mahamdallie, S.S., Murray, A., Ramsay, E., Del Vecchio Duarte, S., Zachariou, A., de Souza, B. *et al.* (2014) Germline mutations in the PAF1 complex gene CTR9 predispose to Wilms tumour. *Nat Commun*, **5**, 4398.
9. Zeng, H. and Xu, W. (2015) Ctr9, a key subunit of PAFc, affects global estrogen signaling and drives ERalpha-positive breast tumorigenesis. *Genes Dev*, **29**, 2153-2167.
10. Zeng, H., Lu, L., Chan, N.T., Horswill, M., Ahlquist, P., Zhong, X. and Xu, W. (2016) Systematic identification of Ctr9 regulome in ERalpha-positive breast cancer. *BMC Genomics*, **17**, 902.
11. Yu, J.R., Lee, C.H., Oksuz, O., Stafford, J.M. and Reinberg, D. (2019) PRC2 is high maintenance. *Genes Dev*, **33**, 903-935.
12. Holoch, D. and Margueron, R. (2017) Mechanisms Regulating PRC2 Recruitment and Enzymatic Activity. *Trends Biochem Sci*, **42**, 531-542.
13. van Mierlo, G., Veenstra, G.J.C., Vermeulen, M. and Marks, H. (2019) The Complexity of PRC2 Subcomplexes. *Trends Cell Biol*, **29**, 660-671.

14. Wu, H., Zeng, H., Dong, A., Li, F., He, H., Senisterra, G., Seitova, A., Duan, S., Brown, P.J., Vedadi, M. *et al.* (2013) Structure of the catalytic domain of EZH2 reveals conformational plasticity in cofactor and substrate binding sites and explains oncogenic mutations. *PLoS One*, **8**, e83737.

15. Antonysamy, S., Condon, B., Druzina, Z., Bonanno, J.B., Gheyi, T., Zhang, F., MacEwan, I., Zhang, A., Ashok, S., Rodgers, L. *et al.* (2013) Structural context of disease-associated mutations and putative mechanism of autoinhibition revealed by X-ray crystallographic analysis of the EZH2-SET domain. *PLoS One*, **8**, e84147.

16. Cao, R. and Zhang, Y. (2004) SUZ12 is required for both the histone methyltransferase activity and the silencing function of the EED-EZH2 complex. *Mol Cell*, **15**, 57-67.

17. Lee, C.H., Yu, J.R., Kumar, S., Jin, Y., LeRoy, G., Bhanu, N., Kaneko, S., Garcia, B.A., Hamilton, A.D. and Reinberg, D. (2018) Allosteric Activation Dictates PRC2 Activity Independent of Its Recruitment to Chromatin. *Mol Cell*, **70**, 422-434 e426.

18. Lee, C.H., Yu, J.R., Granat, J., Saldana-Meyer, R., Andrade, J., LeRoy, G., Jin, Y., Lund, P., Stafford, J.M., Garcia, B.A. *et al.* (2019) Automethylation of PRC2 promotes H3K27 methylation and is impaired in H3K27M pediatric glioma. *Genes Dev*, **33**, 1428-1440.

19. Smits, A.H., Jansen, P.W., Poser, I., Hyman, A.A. and Vermeulen, M. (2013) Stoichiometry of chromatin-associated protein complexes revealed by label-free quantitative mass spectrometry-based proteomics. *Nucleic Acids Res*, **41**, e28.

20. Kasinath, V., Faini, M., Poepsel, S., Reif, D., Feng, X.A., Stjepanovic, G., Aebersold, R. and Nogales, E. (2018) Structures of human PRC2 with its cofactors AEBP2 and JARID2. *Science*, **359**, 940-944.

21. Li, H., Liefke, R., Jiang, J., Kurland, J.V., Tian, W., Deng, P., Zhang, W., He, Q., Patel, D.J., Bulyk, M.L. *et al.* (2017) Polycomb-like proteins link the PRC2 complex to CpG islands. *Nature*, **549**, 287-291.

22. Oksuz, O., Narendra, V., Lee, C.H., Descostes, N., LeRoy, G., Raviram, R., Blumenberg, L., Karch, K., Rocha, P.P., Garcia, B.A. *et al.* (2018) Capturing the Onset of PRC2-Mediated Repressive Domain Formation. *Mol Cell*, **70**, 1149-1162 e1145.

23. Conway, E., Jerman, E., Healy, E., Ito, S., Holoch, D., Oliviero, G., Deevy, O., Glancy, E., Fitzpatrick, D.J., Mucha, M. *et al.* (2018) A Family of Vertebrate-Specific Polycombs Encoded by the LCOR/LCORL Genes Balance PRC2 Subtype Activities. *Mol Cell*, **70**, 408-421 e408.

24. Conway, E., Healy, E. and Bracken, A.P. (2015) PRC2 mediated H3K27 methylations in cellular identity and cancer. *Curr Opin Cell Biol*, **37**, 42-48.

25. Kleer, C.G., Cao, Q., Varambally, S., Shen, R., Ota, I., Tomlins, S.A., Ghosh, D., Sewalt, R.G., Otte, A.P., Hayes, D.F. *et al.* (2003) EZH2 is a marker of aggressive

breast cancer and promotes neoplastic transformation of breast epithelial cells. *Proc Natl Acad Sci U S A*, **100**, 11606-11611.

26. Gong, Y., Huo, L., Liu, P., Sneige, N., Sun, X., Ueno, N.T., Lucci, A., Buchholz, T.A., Valero, V. and Cristofanilli, M. (2011) Polycomb group protein EZH2 is frequently expressed in inflammatory breast cancer and is predictive of worse clinical outcome. *Cancer*, **117**, 5476-5484.

27. Kim, K.H. and Roberts, C.W. (2016) Targeting EZH2 in cancer. *Nat Med*, **22**, 128-134.

28. Hoy, S.M. (2020) Tazemetostat: First Approval. *Drugs*, **80**, 513-521.

29. Grosselin, K., Durand, A., Marsolier, J., Poitou, A., Marangoni, E., Nemati, F., Dahmani, A., Lameiras, S., Reyal, F., Frenoy, O. *et al.* (2019) High-throughput single-cell ChIP-seq identifies heterogeneity of chromatin states in breast cancer. *Nat Genet*, **51**, 1060-1066.

30. Yu, G., Wang, L.G. and He, Q.Y. (2015) ChIPseeker: an R/Bioconductor package for ChIP peak annotation, comparison and visualization. *Bioinformatics*, **31**, 2382-2383.

31. Wang, Z., Civelek, M., Miller, C.L., Sheffield, N.C., Guertin, M.J. and Zang, C. (2018) BART: a transcription factor prediction tool with query gene sets or epigenomic profiles. *Bioinformatics*, **34**, 2867-2869.

32. Campbell, T.M., Castro, M.A.A., de Oliveira, K.G., Ponder, B.A.J. and Meyer, K.B. (2018) ERalpha Binding by Transcription Factors NFIB and YBX1 Enables FGFR2 Signaling to Modulate Estrogen Responsiveness in Breast Cancer. *Cancer Res*, **78**, 410-421.

33. Reddy, B.Y., Greco, S.J., Patel, P.S., Trzaska, K.A. and Rameshwar, P. (2009) RE-1-silencing transcription factor shows tumor-suppressor functions and negatively regulates the oncogenic TAC1 in breast cancer cells. *Proc Natl Acad Sci U S A*, **106**, 4408-4413.

34. Ai, B., Kong, X., Wang, X., Zhang, K., Yang, X., Zhai, J., Gao, R., Qi, Y., Wang, J., Wang, Z. *et al.* (2019) LINC01355 suppresses breast cancer growth through FOXO3-mediated transcriptional repression of CCND1. *Cell Death Dis*, **10**, 502.

35. Litchfield, L.M., Riggs, K.A., Hockenberry, A.M., Oliver, L.D., Barnhart, K.G., Cai, J., Pierce, W.M., Jr., Ivanova, M.M., Bates, P.J., Appana, S.N. *et al.* (2012) Identification and characterization of nucleolin as a COUP-TFII coactivator of retinoic acid receptor beta transcription in breast cancer cells. *PLoS One*, **7**, e38278.

36. Healy, E., Mucha, M., Glancy, E., Fitzpatrick, D.J., Conway, E., Neikes, H.K., Monger, C., Van Mierlo, G., Baltissen, M.P., Koseki, Y. *et al.* (2019) PRC2.1 and PRC2.2 Synergize to Coordinate H3K27 Trimethylation. *Mol Cell*, **76**, 437-452 e436.

37. Yu, Y., Qi, J., Xiong, J., Jiang, L., Cui, D., He, J., Chen, P., Li, L., Wu, C., Ma, T. *et al.* (2019) Epigenetic Co-Deregulation of EZH2/TET1 is a Senescence-Countering, Actionable Vulnerability in Triple-Negative Breast Cancer. *Theranostics*, **9**, 761-777.

38. Konze, K.D., Ma, A., Li, F., Barsyte-Lovejoy, D., Parton, T., Macnevin, C.J., Liu, F., Gao, C., Huang, X.P., Kuznetsova, E. *et al.* (2013) An orally bioavailable chemical probe of the Lysine Methyltransferases EZH2 and EZH1. *ACS Chem Biol*, **8**, 1324-1334.

39. Qi, W., Zhao, K., Gu, J., Huang, Y., Wang, Y., Zhang, H., Zhang, M., Zhang, J., Yu, Z., Li, L. *et al.* (2017) An allosteric PRC2 inhibitor targeting the H3K27me3 binding pocket of EED. *Nat Chem Biol*, **13**, 381-388.

40. Verma, S.K., Tian, X., LaFrance, L.V., Duquenne, C., Suarez, D.P., Newlander, K.A., Romeril, S.P., Burgess, J.L., Grant, S.W., Brackley, J.A. *et al.* (2012) Identification of Potent, Selective, Cell-Active Inhibitors of the Histone Lysine Methyltransferase EZH2. *ACS Med Chem Lett*, **3**, 1091-1096.

41. Chen, S.L., Loffler, K.A., Chen, D., Stallcup, M.R. and Muscat, G.E. (2002) The coactivator-associated arginine methyltransferase is necessary for muscle differentiation: CARM1 coactivates myocyte enhancer factor-2. *J Biol Chem*, **277**, 4324-4333.

42. Massoni-Laporte, A., Perrot, M., Ponger, L., Boucherie, H. and Guieysse-Peugeot, A.L. (2012) Proteome analysis of a CTR9 deficient yeast strain suggests that Ctr9 has function(s) independent of the Paf1 complex. *Biochim Biophys Acta*, **1824**, 759-768.

43. Akanuma, T., Koshida, S., Kawamura, A., Kishimoto, Y. and Takada, S. (2007) Paf1 complex homologues are required for Notch-regulated transcription during somite segmentation. *EMBO Rep*, **8**, 858-863.

44. Chaturvedi, D., Inaba, M., Scoggin, S. and Buszczak, M. (2016) Drosophila CG2469 Encodes a Homolog of Human CTR9 and Is Essential for Development. *G3 (Bethesda)*, **6**, 3849-3857.

45. Zhang, K., Haversat, J.M. and Mager, J. (2013) CTR9/PAF1c regulates molecular lineage identity, histone H3K36 trimethylation and genomic imprinting during preimplantation development. *Dev Biol*, **383**, 15-27.

46. Pasini, D., Bracken, A.P., Jensen, M.R., Lazzerini Denchi, E. and Helin, K. (2004) Suz12 is essential for mouse development and for EZH2 histone methyltransferase activity. *EMBO J*, **23**, 4061-4071.

47. Streubel, G., Watson, A., Jammula, S.G., Scelfo, A., Fitzpatrick, D.J., Oliviero, G., McCole, R., Conway, E., Glancy, E., Negri, G.L. *et al.* (2018) The H3K36me2 Methyltransferase Nsd1 Demarcates PRC2-Mediated H3K27me2 and H3K27me3 Domains in Embryonic Stem Cells. *Mol Cell*, **70**, 371-379 e375.

48. Hosogane, M., Funayama, R., Shirota, M. and Nakayama, K. (2016) Lack of Transcription Triggers H3K27me3 Accumulation in the Gene Body. *Cell Rep*, **16**, 696-706.

49. Riising, E.M., Comet, I., Leblanc, B., Wu, X., Johansen, J.V. and Helin, K. (2014) Gene silencing triggers polycomb repressive complex 2 recruitment to CpG islands genome wide. *Mol Cell*, **55**, 347-360.

50. Laugesen, A., Hojfeldt, J.W. and Helin, K. (2019) Molecular Mechanisms Directing PRC2 Recruitment and H3K27 Methylation. *Mol Cell*, **74**, 8-18.

51. Ballare, C., Lange, M., Lapinaite, A., Martin, G.M., Morey, L., Pascual, G., Liefke, R., Simon, B., Shi, Y., Gozani, O. *et al.* (2012) Phf19 links methylated Lys36 of histone H3 to regulation of Polycomb activity. *Nat Struct Mol Biol*, **19**, 1257-1265.

52. Schmitges, F.W., Prusty, A.B., Faty, M., Stutzer, A., Lingaraju, G.M., Aiwazian, J., Sack, R., Hess, D., Li, L., Zhou, S. *et al.* (2011) Histone methylation by PRC2 is inhibited by active chromatin marks. *Mol Cell*, **42**, 330-341.

53. Peng, J.C., Valouev, A., Swigut, T., Zhang, J., Zhao, Y., Sidow, A. and Wysocka, J. (2009) Jarid2/Jumonji coordinates control of PRC2 enzymatic activity and target gene occupancy in pluripotent cells. *Cell*, **139**, 1290-1302.

54. Grijzenhout, A., Godwin, J., Koseki, H., Gdula, M.R., Szumska, D., McGouran, J.F., Bhattacharya, S., Kessler, B.M., Brockdorff, N. and Cooper, S. (2016) Functional analysis of AEBP2, a PRC2 Polycomb protein, reveals a Trithorax phenotype in embryonic development and in ESCs. *Development*, **143**, 2716-2723.

55. Sanulli, S., Justin, N., Teissandier, A., Ancelin, K., Portoso, M., Caron, M., Michaud, A., Lombard, B., da Rocha, S.T., Offer, J. *et al.* (2015) Jarid2 Methylation via the PRC2 Complex Regulates H3K27me3 Deposition during Cell Differentiation. *Mol Cell*, **57**, 769-783.

56. Perino, M., van Mierlo, G., Karemaker, I.D., van Genesen, S., Vermeulen, M., Marks, H., van Heeringen, S.J. and Veenstra, G.J.C. (2018) MTF2 recruits Polycomb Repressive Complex 2 by helical-shape-selective DNA binding. *Nat Genet*, **50**, 1002-1010.

57. Xu, B., Konze, K.D., Jin, J. and Wang, G.G. (2015) Targeting EZH2 and PRC2 dependence as novel anticancer therapy. *Exp Hematol*, **43**, 698-712.

58. Ezponda, T., Dupere-Richer, D., Will, C.M., Small, E.C., Varghese, N., Patel, T., Nabet, B., Popovic, R., Oyer, J., Bulic, M. *et al.* (2017) UTX/KDM6A Loss Enhances the Malignant Phenotype of Multiple Myeloma and Sensitizes Cells to EZH2 inhibition. *Cell Rep*, **21**, 628-640.

59. Van der Meulen, J., Sanghvi, V., Mavrakis, K., Durinck, K., Fang, F., Matthijssens, F., Rondou, P., Rosen, M., Pieters, T., Vandenberghe, P. *et al.* (2015) The H3K27me3 demethylase UTX is a gender-specific tumor suppressor in T-cell acute lymphoblastic leukemia. *Blood*, **125**, 13-21.

60. Italiano, A., Soria, J.C., Toulmonde, M., Michot, J.M., Lucchesi, C., Varga, A., Coindre, J.M., Blakemore, S.J., Clawson, A., Suttle, B. *et al.* (2018) Tazemetostat, an EZH2 inhibitor, in relapsed or refractory B-cell non-Hodgkin lymphoma and advanced solid tumours: a first-in-human, open-label, phase 1 study. *Lancet Oncol*, **19**, 649-659.

61. Moore, H.M., Gonzalez, M.E., Toy, K.A., Cimino-Mathews, A., Argani, P. and Kleer, C.G. (2013) EZH2 inhibition decreases p38 signaling and suppresses breast cancer motility and metastasis. *Breast Cancer Res Treat*, **138**, 741-752.

62. Kagey, M.H., Newman, J.J., Bilodeau, S., Zhan, Y., Orlando, D.A., van Berkum, N.L., Ebmeier, C.C., Goossens, J., Rahl, P.B., Levine, S.S. *et al.* (2010) Mediator and cohesin connect gene expression and chromatin architecture. *Nature*, **467**, 430-435.

63. Beringer, M., Pisano, P., Di Carlo, V., Blanco, E., Chammas, P., Vizan, P., Gutierrez, A., Aranda, S., Payer, B., Wierer, M. *et al.* (2016) EPOP Functionally Links Elongin and Polycomb in Pluripotent Stem Cells. *Mol Cell*, **64**, 645-658.

64. Langmead, B. and Salzberg, S.L. (2012) Fast gapped-read alignment with Bowtie 2. *Nat Methods*, **9**, 357-359.

65. Ramirez, F., Ryan, D.P., Gruning, B., Bhardwaj, V., Kilpert, F., Richter, A.S., Heyne, S., Dundar, F. and Manke, T. (2016) deepTools2: a next generation web server for deep-sequencing data analysis. *Nucleic Acids Res*, **44**, W160-165.

66. Zhang, Y., Liu, T., Meyer, C.A., Eeckhoute, J., Johnson, D.S., Bernstein, B.E., Nusbaum, C., Myers, R.M., Brown, M., Li, W. *et al.* (2008) Model-based analysis of ChIP-Seq (MACS). *Genome Biol*, **9**, R137.

Chapter 3

CTR9 drives osteochondral lineage differentiation of human mesenchymal stem/stromal cells (MSCs) via counteracting EZH2 activity

Human primary mesenchymal stromal/stem cells were isolated in Prof. Jacques Galipeau's lab and shared with us as a generous gift.

Ectopic bone formation assay using 3D scaffolds was done in collaboration with Ming-Song Lee from Dr. Wan-Ju Li's lab in the Department of Orthopedics.

All the animal surgery work involved in Figure 3-4 were completed by Ming-Song Lee.

3.1 ABSTRACT

Cell-fate determination of human mesenchymal stem/stromal cells (hMSCs) is finely regulated by lineage-specific transcription factors and epigenetic enzymes. Interestingly, we found that CTR9, a key scaffold subunit of PAFc, selectively regulates hMSCs differentiation to osteoblasts, but not to adipocytes. CTR9 knockdown (1) in hMSCs strongly impaired osteogenic differentiation as shown by the attenuated induction of Alkaline Phosphatase activity, decreased osteocalcin secretion and reduced formation of extracellular calcium matrix, whereas adipocyte differentiation was not significantly affected. An *in vivo* ectopic osteogenesis assay confirmed the essentiality of CTR9 expression for hMSC-derived bone formation. The lineage-specific role of CTR9 is not due to modulation of stem cell characteristics of hMSCs. Instead, CTR9 counteracts the activity of EZH2, the epigenetic enzyme that deposits H3K27me3, a crucial histone mark of MSC lineage-specific differentiation. In accordance with the gain of H3K27me3 in CTR9 KD MSCs, the osteogenic differentiation defects of CTR9 KD hMSCs can be partially rescued by treatment with EZH2 inhibitors, supporting a CTR9-driven epigenetic mechanism in regulating MSC lineage differentiation.

3.2 INTRODUCTION

Human mesenchymal stem cells (hMSCs), also known as mesenchymal stromal cells, are the most primitive adult stem cells that can be derived from multiple organs and vascularized tissues. Though initially isolated from bone marrow, MSCs comprise a heterogeneous population of stem cells and lineage commitment progenitors that also reside in other organs and tissues, such as adipose, umbilical cord and pancreas tissue (2-4). Regardless of the original source, MSCs can self-renew and are multipotent and express common cell surface markers such as CD73, CD90, CD105. However, these markers for defining MSCs remain controversial (5,6). As a result, multipotent differentiation remains the hallmark of MSCs. Under appropriate stimuli, MSCs can differentiate into mesodermal lineage cell types, including osteoblasts, adipocytes and chondrocytes, as well as trans-differentiate into ecto/endoderm lineages at a much lower frequency (7,8). Although MSCs can be induced to commit to defined lineages in vitro, the differentiation of MSCs into either adipocytes or osteoblasts is context-dependent and affected by pathological conditions, such as obesity, osteosarcoma and osteoporosis (9). Therefore, a mechanistic understanding of osteogenic and adipogenic differentiation of MSCs could provide insights into metabolic and hematological abnormalities, leading to more effective treatments for bone- and adipose-related diseases.

MSC lineage specification is typically controlled by designated transcription factors (TFs) that either activate or silence lineage specific signaling pathways. For example, the osteogenic differentiation of MSCs is regulated by two master regulators, RUNX2 and Osterix, which sequentially activate osteo-promoting signaling pathways, such as TGF-β and WNT/β-catenin (10,11). Furthermore, numerous bone-matrix protein coding genes, such as osteopontin (OPN) and osteocalcin (OCN), are target genes of RUNX2 and Osterix (12,13). In addition to the induction of osteogenic differentiation, RUNX2 and Osterix inhibit the differentiation of MSCs towards the adipogenic lineage by restraining the expression of PPARγ and C/EBPα, which are the master TFs regulating adipogenesis (14). For example, RUNX2 phosphorylation and transcriptional activity were stimulated by MAPK, which leads to PPARγ repression (15); conversely, ligand activated PPARγ inhibits mRNA expression of RUNX2, as well as physically interacts with RUNX2 to prevent the induction of osteocalcin-encoding genes (16). Moreover, Osterix has been shown to disrupt the transcriptional activity of PPARγ and C/EBPα (17). Thus, reciprocal regulation of osteo- and adipogenesis-specific TFs dictates an interlinked regulatory network, where the induction of one lineage often comes at the expense of the other.

Lineage-priming TFs interact with epigenetic enzymes to establish distinct epigenetic states in favor of cellular differentiation, adding another layer of complexity to the transcriptional regulation of MSC lineage-specific differentiation. For instance, histone H3K9 methyltransferase G9a represses adipogenesis by inhibiting PPARγ expression (18). Histone deacetylase SIRT7 interacts with and transactivates Osterix (19). Chromatin immunoprecipitation (ChIP) analysis showed increased binding of MLL complex and KDM6A on the RUNX2 promoter during osteogenesis. The MLL complex promotes H3K4me3 and KDM6A erases H3K27me3. Thus, their recruitment leads to activation of RUNX2 (20). The coordination between lineage-specific TFs and epigenetic modulators plays important roles in the lineage specification of MSCs.

Emerging evidence shows that a large cohort of lineage priming genes are enriched with H3K27me3, implying that this repressive histone marker also plays a role in establishing different differentiation states. For example, EZH2/H3K27me3 were associated with the promoter regions of osteogenic genes, including RUNX2 and osteopontin (21,22). Cyclin dependent kinase 1 (CDK1) phosphorylates EZH2 to inactivate EZH2, thus suppressing H3K27me3 and leading to osteogenic differentiation (23). EZH2 and KDM6A elicit opposing effects on MSCs osteo- and adipogeneic differentiation. Exogenous expression of EZH2 in MSCs promotes adipogenic and inhibits osteogenic differentiation. In contrast, overexpression of KDM6A, the H3K27me3 eraser, promotes osteogenic and inhibits adipogenic differentiation (24-27).

CTR9/PAFc was previously shown to regulate lineage specific genes that are required for mammalian preimplantation development, such as Eomes, ELF5 and SOX2, through modulating H3K36me3 deposition (28). CTR9 has been shown to regulate pluripotency maintenance and stem cell turnover in mouse and human embryonic stem cells (29,30). Moreover, genome-wide association studies (GWSA) identified CTR9 as a candidate gene involved in the development of osteoporosis-related Kashin-Beck disease, implicating CTR9 in maintaining bone homeostasis (31). In Chapter 2, we uncovered a novel function of CTR9 to restrain expansion of H3K27me3-mediated repressive chromatin foci by regulating PRC2 subtype equilibrium and KDM6A expression in BrCa cells. Given that the PRC2-H3K27me3-KDM6A axis is critical in lineage commitment of hMSCs, we hypothesize that CTR9 may regulate lineage differentiation of hMSCs via an epigenetic mechanism engaging PRC2-H3K27me3-KDM6A.

In this study, we employed loss-of-function as well as gain-of-function approaches to comprehensively examine the roles of CTR9 in hMSCs, including viability, proliferation, stem cell maintenance, and most importantly, multi-faceted lineage-oriented differentiation. First, we found that loss of CTR9 did not affect viability, growth and stemness of hMSCs. However, loss of CTR9 specifically impaired osteogenic, but not adipogenic differentiation of hMSCs. Knocking down CTR9 in MSCs resulted in slower induction of Alkaline Phosphatase activity, reduced osteocalcin secretion, incomplete extracellular calcium matrix formation and delayed expression of osteoblast genes. On the contrary, knocking down CTR9 in hMSCs neither affected formation of lipid vesicles, nor activation of adipogenic markers, suggesting that CTR9 is dispensable for adipogenesis. Using a differentiation medium switch assay, we further defined the imperative role of CTR9 expression in the early commitment of hMSCs to osteo-lineage progenitors. Second, osteogenic differentiation of hMSCs is CTR9 dose dependent. Restoration of CTR9 expression partially rescued the defective osteogenic phenotypes caused by CTR9 knockdown, whereas overexpression of CTR9 accelerated osteogenesis. Third, CTR9 is essential for *in vivo* mineralization. Knocking down CTR9 in hMSCs significantly reduced deposition and mineralization of bone matrix on *ex vivo* implanted 3D scaffolds, indicating that CTR9 is indispensable for hMSC-derived bone formation *in vivo*. Lastly, hMSCs treated with UNC1999, an EZH2 inhibitor, partially rescued the osteogenic defects in CTR9 KD MSCs, resembling the effect of CTR9 restoration. This result demonstrates that CTR9 regulates osteogenic differentiation of hMSCs via an epigenetic mechanism engaging the PRC2-H3K27me3 axis. Together, our findings reveal the antagonism between a transcription coactivator (i.e., CTR9) and repressor (i.e., EZH2) in shaping epigenetic states during lineage specification.

3.3 RESULTS

3.3.1 CTR9 depletion has negligible effects on the viability and stem cell properties of hMSCs

To examine the functional roles of CTR9 in lineage specification of hMSCs, we first generated hMSC lines stably expressing two distinct CTR9-targeting shRNAs, with a scramble shRNA serving as a negative control (i.e., shControl vs shCTR9#3 or #5). Western blotting results confirmed depletion of CTR9 in hMSCs derived from different donors (H01/H03/H18) at early passages (p3/p4) (Figure 3-1A). In agreement with our previous study in breast cancer cells, CTR9 knockdown (1) in hMSCs also resulted in a significant morphology change measured by immuno-fluorescent staining of the cytoskeleton (F-actin/β-tubulin) (Figure 3-1B). In contrast to the fibroblast-like morphology of shControl MSCs, CTR9 KD cells were enlarged and branched, and cell-cell adhesion was decreased. Despite the morphological changes, cell survival was unaffected. Flow cytometry analysis of PI/Annexin-V uptake showed a moderate increase of apoptotic cells (PI^-/Annexin-V^+) after CTR9 depletion, whereas the necrotic cells (PI^+/Annexin-V^+ were not apparent in either shControl or shCTR9 hMSCs (Figure 3-1C). Silencing of CTR9 resulted in a moderate increase in cell senescence as detected by senescence-associated β-galactosidase staining (Figure 3-1D), and hMSCs in G0/G1 as defined by PI-staining (Figure 3-1E).

We next compared stem cell properties by measuring 3D spheroid formation and stem cell marker expression between shControl and shCTR9 hMSCs. Depletion of CTR9 did not affect 3D spheroid formation after a 48-hour cell inoculation in a 96-well ultra-low attachment plate (Figure 3-1F). Furthermore, CTR9 KD did not result in significant changes on the expression of MSC surface markers and other pluripotency regulatory genes (Figure 3-1G). In summary, although CTR9 KD moderately affected morphology and proliferation of hMSCs, the viability and stem cell properties of hMSCs were not significantly affected by the loss of CTR9.

3.3.2 Knockdown of CTR9 in hMSCs impairs early and late osteogenic differentiation

We next investigated whether depletion of CTR9 affects lineage specification of hMSCs. Several studies implicated that CTR9 level is likely associated with osteogenic potential (30,32). Thus, we compared shControl and shCTR9#3/#5 MSCs in the *in vitro* osteogenic assays where osteogenic induction was initiated when hMSCs reached 80% confluency. The hMSCs were treated with osteogenic induction media for 28 days, during which sequential osteogenic markers were measured at different time points (Figure 3-2A). The increase of Alkaline Phosphatase (AP) activity is generally regarded as a very early osteogenic differentiation marker, suggesting the presence of osteo-progenitor or osteoblast cells (33). We measured the AP activity through BCIP/NBT substrate staining. BCIP is hydrolyzed by alkaline phosphatase to form a blue intermediate, which is then oxidized by NBT to produce a dimer to give an intense purple staining (34). In Figure 3-2B, shControl MSCs elicited much stronger AP activity 7-days post osteogenic induction as compared with shCTR9 hMSCs. The quantification of AP activity normalized by DNA content was shown in Figure 3-2C. In addition to AP activity, increased synthesis and secretion of collagen is another marker during early osteogenesis. Loss of function mutations in *COL1A1* or *COL1A2* genes encoding the pro-α1 or pro-α2 chains of type I collagen were identified in over 90% of the patients with Osteogenesis imperfecta (35).

Picrosirius red staining is commonly used to visualize collagen (36). In Figure 3-2D, strong red staining of collagen fibers was observed in shControl but not in shCTR9 hMSCs after 28-day osteogenic induction. Given that elevated AP activity and enhanced collagen synthesis/secretion are hallmarks of early osteogenesis and are a prerequisite for extracellular calcium matrix (ECM) formation, we conclude that CTR9 KD impedes osteogenic differentiation of hMSCs at the onset of osteogenesis.

Synthesis and secretion of osteo-glycoproteins including osteocalcin/osteonectin/ osteopontin occur at the late stages of osteogenesis. These osteo-glycoproteins are the small non-collagenous proteins to bind to the calcium containing matrix and promote the mineralization and condensation of calcium matrix (37,38). To determine whether CTR9 depletion affects the secretion of osteo-glycoproteins, we performed ELISA for human specific osteocalcin. Both shControl and shCTR9 hMSCs were cultured in osteogenic induction media for 0, 14, and 28 days, followed by serum-free osteoblast growth media for an additional 2 days. Medium was then harvested and used with an osteocalcin ELISA kit. The result showed that CTR9 depletion significantly reduced osteocalcin secretion after 28-day *in vitro* osteo-induction (Figure 3-2E). In addition, we monitored osteogenesis by measuring the decrease of undifferentiated markers CD73/CD90 and the increase of osteocalcin/osteopontin expression using flow cytometry after 28-days of osteogenic induction. shControl hMSCs, but not shCTR9 hMSCs, displayed increased osteocalcin/osteopontin and decreased CD73/CD90 expression (Figure 3-2F). This result was substantiated by immuno-fluorescence staining of CD73/CD90 as well as osteoblast specific proteins RUNX2 and osteocalcin. A substantial increase of RUNX2 expression (green) was observed between 14 to 21 days of osteogenic induction in the shControl group. Similarly, immunofluorescence staining detected initiation of osteocalcin synthesis (39) near endo-reticulum on day 14 of osteogenesis and accumulation in cells on day 28 of osteogenic differentiation. This was accompanied by reduction of CD73/CD90 expression. In contrast, shCTR9 MSCs exhibited delayed RUNX2 activation or osteocalcin synthesis, while maintaining the expression of undifferentiated surface markers, CD73/CD90 (Figure 3-2G). Finally, we measured the formation of extracellular calcium matrix (ECM), as it is a hallmark distinguishing a terminally differentiated osteoblast from a premature one. Mature osteoblasts can secrete large amounts of collagen-proteoglycan matrix, which binds calcium salts (mainly hydroxyapatite, Ca5(PO4)3(OH)), in addition to products of AP and other calcium and phosphate ion metabolic enzymes during osteogenesis (40). This process is fundamental for preboned (osteoid) matrix calcification and subsequent intramembranous ossification during normal bone formation and development processes (41). To quantify ECM formation, we performed Alizarin Red S staining, where Alizarin Red S could trap calcium ions from ECM to form a tertiary insoluble bright red Alizarin Red S-Calcium complex under highly acidic conditions (42). As expected, shControl, but not shCTR9 hMSCs, formed large amounts of ECMs after 28 days of osteo-induction (Figure 3-2H). The quantification of ECM normalized by DNA content is shown in Figure 3-2I. The defects of AP activity and ECM formation in shCTR9 hMSCs were highly reproducible as CTR9 KD in hMSCs derived from different donors (H01/H18) produced the same results (Figure 3-2J). In summary, loss of CTR9 strongly impedes both the early and late stages of osteogenic differentiation, underscoring the essential role of CTR9 in the osteogenic lineage determination of hMSCs.

3.3.3 The expression levels of CTR9 are strongly associated with osteogenic potential

Given that knocking-down CTR9 impairs the osteogenic potential of hMSCs, we next investigated if the osteogenic potential of hMSCs is CTR9 dose-dependent. Flag tagged CTR9 was exogenously expressed in shControl or shCTR9 hMSCs. Western blotting results showed the restoration of CTR9 protein in shCTR9 hMSCs, but overexpression of CTR9 in shControl hMSCs. (Figure 3-3A). When CTR9 expression was restored to the same levels of the parental hMSCs, the osteogenic defects were largely alleviated as shown by the partial rescue of AP activity, osteocalcin secretion, as well as ECM formation, in comparison to the shCTR9 hMSCs expressing vector control (shCTR9#3/#5+Flag-CTR9 vs shCtr9#3/#5+Vector) (Figure 3-3B-D). Notably, overexpression of CTR9 in shControl hMSCs displayed the highest osteogenic potential as compared with shControl hMSCs expressing blank vector (i.e., shControl+Flag-CTR9 vs shControl+Vector) (Figure 3-3B-D). Together, these data strongly suggest that CTR9 is a *bona fide* regulator of osteogenesis and the osteogenic potential of hMSCs is governed by CTR9 levels.

3.3.4 CTR9 is required for *in vivo* bone formation

The osteogenic defects associated with CTR9 loss in hMSCs *in vitro* prompted us to validate the role of CTR9 in modulating MSC-derived bone formation *in vivo* using an ectopic bone formation assay. shControl and shCTR9 hMSCs were harvested when sub-confluent and seeded on the fused filament fabrication (FFF)-printed 3D polycaprolactone (PCL) scaffolds at a density of 10^6 cells/cm^3. After 7-day pre-osteo differentiation *in vitro,* the shControl and shCTR9 hMSC-containing scaffolds were subcutaneously implanted to the bilateral dorsal surface of immuno-deficient mice symmetrically. Mice (n=4) that were only implanted with scaffold medium serve as negative controls. The *in vivo* CT scanning was performed after 4-8 weeks of implantation, followed by harvesting the embedded 3D PCL scaffolds for *ex vivo* CT scanning. Additional analyses such as Alizarin Red S staining and immunostaining of osteogenic markers were performed with a quarter-section of those 3D scaffolds (Figure 3-4A). The *in vivo* CT scanning revealed extensive areas of bone-matrix like calcification in scaffolds containing shControl hMSCs after 4 weeks of *in vivo* implantation, and the mineral density in those areas was further increased after 8-weeks of implantation. In contrast, the scaffolds containing shCTR9 hMSCs exhibited lower levels of calcification and less mineral density as compared with the shControl MSCs after 4-8 weeks of implantation (Figure 3-4B). As expected, the negative control mock group had no detectable signal. The quantification of calcification volume (mm^3) and the mineral density of the scaffolds (mg/cm^3) are shown in Figure 3-4C. The *ex vivo* CT-scan results of the scaffolds retrieved from the mice after 8-weeks of implantation agree with those of the *in vivo* CT-scan (Figure 3-4D). BCIP/NBT and Alizarin Red S staining of the harvested scaffolds also showed that the scaffolds seeded with shControl hMSCs had significantly higher AP activity and ECM deposition compared to the shCTR9 counterparts (Figure 3-4E-F). Moreover, CTR9 KD scaffolds contained less osteocalcin than the shControl group, as measured using an ELISA assay (Figure 3-4G). H&E and Von-Kossa staining of paraffin embedded scaffold further confirmed the reduced ECM formation and scaffold mineralization when CTR9 was depleted (Figure 3-4H-I). Moreover, Picrosirius Red staining also showed decreased collagen fiber consolidation around the nano strings of the scaffolds when CTR9 was knocked down. (Figure 3-4J). Finally, decreased osteocalcin sedimentation (green), as detected by immunofluorescence, across the scaffolds was observed in shCTR9 MSCs as compared to shControl (Figure 3-4K). Together, our results suggest that CTR9 is indispensable for sufficient bone-formation both *in vitro* and *in vivo*.

3.3.5 Loss of CTR9 impairs the chondrogenic differentiation of hMSCs

Although chondrogenesis and osteogenesis were originally considered two separate processes (43), the discovery of osteochondral progenitor cells in bone marrow and the observation that osteoblasts are derived from chondrocytes surrounding the cartilage anlagen, imply that chondrogenesis and osteogenesis are coupled developmental processes (44,45). Many signaling pathways and lineage specific TFs are involved in both processes, such as alkaline phosphatase and RUNX2 (46). Because CTR9 depletion impedes osteogenesis *in vitro* and *in vivo,* we sought to examine if CTR9 KD also hinders chondrogenesis. Unlike osteoblasts, chondrocytes are less stable and easily lose their chondrogenic potential, and dedifferentiate to osteochondral progenitors in 2-D culture conditions (47). Therefore, culturing chondrocytes in 3D spherical cell aggregates was developed and shown to improve the efficiency of chondrogenic differentiation *in vitro* (48). We seeded two to three hundred thousand shControl or shCTR9 hMSCs as single cell suspensions in a 96-well untreated, round bottom plate. hMSCs were observed to self-aggregate and form solid spheroids in suspension in 72 hours (Figure 3-5A). After 21 days of *in vitro* chondrogenic induction, the differentiated chondrocyte spheroids were collected for FFPE preparation. To determine whether shCTR9 hMSCs can be differentiated into chondrocytes completely, we first examined the formation of cartilaginous extracellular matrix (CECM), the distinguished feature of a mature chondrocyte. The major components of CECM including acidic sulfates, carboxylates, and phosphate radicals which were stained using Alcian Blue and Toluidine Blue (49). The results showed that CTR9 KD spheroids exhibited attenuated CECM in comparison with shControl spheroids after 14-21 days of chondrogenesis (Figure 3-5B-C). These data support that CTR9 expression is also important for chondrogenesis of hMSCs and implicate that a subset of genes shared by osteo- and chondrogenesis could be targets of CTR9.

3.3.6 Loss of CTR9 did not alter the adipogenic differentiation of hMSCs

hMSCs are multipotent cells that can give rise to osteoblast, chondrocyte, and adipocyte lineages. Numerous studies have demonstrated that *in vivo* lineage determination is under the control of the niche and regulated by lineage-specific TFs. Promotion of one lineage often comes at the expense of the other. For example, transcription factor TAZ which activates RUNX2 expression during osteogenesis also suppresses PPARγ-mediated gene expression to block adipogenesis (50). Because loss of CTR9 results in decreased osteogenic potential of hMSCs, we next investigated if CTR9 KD hMSCs are more inclined to differentiate into adipocytes. The *in vitro* adipogenic differentiation was performed by sensitizing 2-D cultured hMSCs to adipogenic stimuli for at least 21 days (Figure 3-6A). Large numbers of lipid vesicles are typically visible in mature adipocytes, and the neutral triglycerides and other lipids of those vesicles can be stained with fat-soluble Oil Red O in bright red (51). Figure 3-6B showed that comparable levels of lipid vesicles were observed between shControl and shCTR9 hMSCs after 14-21 days of adipogenic induction. Quantification of lipid vesicles are shown in Figure 3-6C. Moreover, immuno-fluorescence staining as well as flow cytometry analysis confirmed that PPARγ expression was elevated in both shControl and shCTR9 hMSC cells. Concomitantly, accumulation of neutral lipid droplets indicated by BODIPY 493/503 is accompanied by the gradual loss of undifferentiated markers CD73/CD90 after 14-21 days of adipogenic induction (Figure 3-6D-E). Similar observations were made using hMSCs originating from different donors (H01/H18) (Figure 3-6F). Together, we concluded that CTR9 loss does not impair the adipogenic potential of hMSCs and that CTR9 is not required for adipogenic differentiation of hMSCs.

3.3.7 H3K27me3-dependent epigenetic mechanisms underlying CTR9-regulated hMSC osteogenesis

Accumulating evidence suggests that H3K27me3 levels play an essential role in modulating the equilibrium between osteogenesis and adipogenesis in hMSCs (22,24,27,52). In Chapter 2, CTR9 was identified as a novel determinant of cellular H3K27me3 levels in BrCa cells. Loss of CTR9 resulted in a dramatic increase of global H3K27me3 levels, as well as expansion of H3K27me3 repressive domains on chromatin. Interestingly, CTR9 KD also resulted in a significant increase of bulk H3K27me3 levels as shown by immunofluorescence in hMSCs (Figure 3-1B). This implies that CTR9 regulates osteogenesis, at least in part, through epigenetic mechanisms engaging H3K27me3. A recent clinical trial reports a novel strategy to combine EZH2 inhibition with a reduced dose of bone morphogenetic protein 2 (BMP2) *in vivo* for bone regeneration, thus minimizing the adverse effects associated with high doses of BMP2. GSK-246, the small molecule EZH2 inhibitor, stimulated osteogenic differentiation of MSCs on 3D scaffolds *in vitro,* when implanted *in vivo,* enhanced vascularization and bone formation (25). Accordingly, suppression of H3K27me3 using EZH2 inhibitors may reverse the phenotype of stalled osteogenesis caused by CTR9 KD in hMSCs. To test this hypothesis, both shControl and shCTR9 hMSCs were treated with increasing concentrations of EZH2 inhibitor (UNC1999) throughout the osteogenesis process. UNC2400, a structural paralog, and DMSO served as negative and background controls, respectively. Measurement of AP activity showed that UNC1999 treatment increased osteogenesis in the shControl group, and partially rescued the early osteogenic defects in the shCTR9 group, whereas treatment with UNC2400 or DMSO had no effect on the AP activity during osteogenic induction (Figure 3-7A). Quantification of AP activity corresponding to each condition was shown in Figure 3-7B. These data demonstrate that CTR9-governed osteogenic differentiation of hMSCs is regulated, at least in part, by an epigenetic mechanism engaging H3K27me3.

3.4 DISCUSSION

In this chapter, we phenotypically examined the roles of CTR9 in regulating lineage specification of hMSCs. Interestingly, knocking down CTR9 in hMSCs selectively affected osteogenic, but not adipogenic differentiation, whereas cell viability and other stem cell properties were not significantly affected. Our *in vitro* osteogenic induction of hMSCs revealed that loss of CTR9 affects both early and late osteogenic differentiation, as measured by alkaline phosphatase activity and collagen fiber synthesis in early osteogenesis, as well as reduced ECM formation and expression of osteoblast markers including RUNX2/Osterix and osteo-glycoproteins in late-stage osteogenesis. On the contrary, CTR9 KD in hMSCs did not affect any adipogenesis phenotypes. This raised several questions: (1) At which stage does CTR9 affect hMSC lineage-specific differentiation: osteochondral or adipogenic lineage priming, pre-osteogenesis of committed osteochondral progenitors, or osteoblast maturation? (2) The expression levels of several epigenetic regulators (e.g., EZH2) has been shown to regulate the balance between osteogenesis and adipogenesis. However, our results showed that CTR9 loss only impair osteogenesis, whereas adipogenesis was not elevated. Why does CTR9 loss fail to shift the balance between osteogenesis and adipogenesis? (3) What are the transcriptional and epigenetic mechanisms regulated by CTR9 in osteogenesis?

Our results that CTR9 is not involved in balancing osteogenic and adipogenic differentiation implicates that CTR9 is likely not involved in osteochondral and adipocyte lineage priming of hMSCs. Rather, CTR9 only affects formation of committed osteochondral progenitors. To begin to test this hypothesis, I designed a medium-switch experiment (Data not shown), where shControl or shCTR9 hMSCs were pre-treated with osteogenic induction medium, followed by switching to adipogenic medium. If CTR9 is not required for osteogenic lineage commitment, we should observe the same phenotype between shControl and shCTR9 hMSCs. Our results showed that the shControl hMSCs failed to differentiate into adipocytes after pre-treatment with osteogenic induction medium for 7 days. However, the shCTR9 hMSCs could be induced to adipocytes after medium switching, suggesting that CTR9 loss affects whether hMSCs to osteoblastic progenitor cells. This result reconciles the lack of osteogenic differentiation phenotypes of shCTR9 hMSCs. Although this result suggests that CTR9 affects the formation of osteoblastic progenitor cells, we cannot exclude the possibility that CTR9 is also required for early and/or late osteogenic differentiation of committed osteoblastic progenitor cells. To address this question, we will knock down CTR9 from pre-osteoblastic cells including murine cell line MC3T3-E1 (53), human hFOB 1.19 cell line (54), or mature human osteoblasts (HOB) isolated from femoral trabecular bone tissue (PromoCell, C-12760) followed by osteogenic induction. Because these cells are already committed to the osteoblastic lineage, we can directly test if CTR9 is required for the entire process of osteogenesis, including maturation of pre-osteoblasts to osteoblasts, and osteoblast maturation to mineralized osteocytes. If CTR9 is required for either early or late osteogenic differentiation, deficiency of osteoblast maturation will be observed by knocking down CTR9.

In addition to *in vitro* differentiation assays to measure the phenotypic effects of CTR9 in osteogenic differentiation, bulk and single-cell RNA-sequencing of shControl and shCTR9 hMSCs upon osteogenic induction could help delineate transcriptional networks of pro-osteogenic transcription factors and signaling pathways that work in a sequential and coordinated way to activate an osteogenic gene program. A recent review has summarized transcriptional networks that control lineage determination and differentiation of hMSCs (55). Towards this goal, I have harvested mRNAs from shControl and shCTR9 hMSCs before and after short-term (7 days) osteogenic induction for bulk RNA-seq. Based on our finding that CTR9 is required for osteogenic but dispensable for adipogenic differentiation of hMSCs, we speculate that CTR9 affects expression of master regulators and transcription factors for osteogenesis but has no effect on transcription factors regulating adipogenesis. This is supported by our data that RUNX2 mRNA and protein levels were decreased in shCTR9 hMSCs during osteogenic induction as compared to shControl hMSCs (Figure 3-2-F/G). Moreover, ChIP-grade CTR9 antibody has recently become available (56). With the evolving of ChIP-seq to CUT&RUN method, we could map genome CTR9 binding sites on hMSCs during osteogenesis to identify direct target genes of CTR9 that regulate osteogenesis. In addition to affecting lineage-specific transcription factors, we also envision that CTR9 regulates osteogenesis via epigenetic mechanisms. In BrCa cells, we have shown that CTR9 expression affects not only active histone marks (e.g., H3K4me3 and H3K36me3) associated with transcription elongation, but also H3K27me3, the repressive chromatin mark, through counteracting EZH2 activity. Furthermore, the osteogenic defects associated with CTR9 KD hMSCs could be partially rescued by pharmacological inhibition of EZH2, suggesting that PRC2-H3K27me3 mechanisms are likely conserved in different biological systems and govern CTR9-mediated osteogenic differentiation. Our finding is consistent with published work that inhibition or depletion of EZH2 enhanced osteogenesis (24,25,27,57). However, the differential requirement of EZH2 and CTR9 in adipogenic differentiation of hMSCs (i.e., EZH2 promotes adipogenesis whereas CTR9 has no effect) implies that the EZH2-H3K27me3 axis does not account for all biological effects of CTR9. Therefore, profiling of chromatin-bound histone markers, such as H3K4me3, H3K27me3, and PRC2 subunits over the course of osteogenesis or adipogenesis will further elucidate the epigenetic mechanisms involved in lineage-specific differentiation. By integrating data from RNA-seq and CUT & RUN, we hope to identify key transcriptional factors as well as epigenetic modulators that are most affected by CTR9 ablation in early osteogenic commitment.

Due to the poorly defined cell surface markers and heterogenous population of precursor cells in hMSCs, single cell genomic sequencing (scRNA-seq and scATAC-seq) has become a powerful tool to determine cell identity based on the expression profiles of a large number of genes. We could employ these technologies to investigate how CTR9 affects chromatin accessibility, in particular, on the osteoblast-specific genes, during osteogenic induction at single cell resolution. We expect that hMSCs will form distinct gene expression clusters in the scRNA-seq data due to heterogeneity. The scATAC-seq results will inform us of the gene signatures, as well as cis-regulatory networks, that are most susceptible to CTR9 loss at different stages of osteogenesis. By integrating scRNA-seq with scATAC-seq data, we may identify a subpopulation of hMSCs that differ by CTR9 levels and exhibit different osteogenic trajectories. These results will delineate transcriptional networks and chromatin structure changes regulated by CTR9 in true adult skeletal muscular stem cells during osteogenesis.

In summary, the phenotypic studies in this chapter reveal the previously unknown role of CTR9 in the osteogenic differentiation of hMSCs, and open opportunities for in-depth mechanistic studies. Because CTR9 SNPs were associated with osteoporosis-related Kashin-Beck disease (31), and this study shows that pharmacological inhibition of EZH2 activity partially rescues the osteogenic defects of CTR9 loss, our results suggest that EZH2 inhibitors might be applicable for osteoporosis treatment caused by genetic alteration of CTR9. Our mechanistic studies of CTR9 in Chapter 2 and phenotypic studies of CTR9 function in hMSCs lineage-specific differentiation in Chapter 3 led us to investigate the *in vivo* function of CTR9 in bone and cartilage formation via collaboration with Dr. Deneen Wellik. These projects will be discussed in Chapter 4.

3.5 MATERIALS & METHODS

Culture of human MSCs

Human MSCs in this study were isolated from bone marrow of different donors and obtained from Dr. Jacques Galipeau's Lab (Department of Stem Cell & Regenerative Medicine, UW-Madison) in early passage (H01/H03/H18, p3-p4). hMSCs from each donor were cultured and assayed independently. Isolated hMSCs were cultured in basal medium composed of low-glucose MEMα (Corning), 10% fetal bovine serum (FBS, VWR), and 1% antibiotics (Gibco™ Penicillin-Streptomycin, ThermoFisher Scientific) and maintained at 37°C under a humidified atmosphere of 5% CO_2. When reaching over 90% confluency, cells were trypsinized using TrypLE™ Express Enzyme (ThermoFisher Scientific) and replated at 1000 cells/cm^2. Cell culture medium was changed twice a week. Senescent hMSCs with over 7 passages will be discarded.

Virus packaging, infection, and preparation of hMSCs with stable CTR9 KD or overexpression

Stable knockdown or overexpression in hMSCs were generated by lentivirus infection. The virus packaging vectors pME-VSVG and psPAX2 were purchased from Open Biosystems. For lentivirus packaging, 4 µg pME-VSVG, 4 µg psPAX2 or 8 µg lentiviral shCTR9 expression (pLKO.1-shCTR9-Puro) vectors or Flag-CTR9 expression vector (pHAGE-PGK-eGFP-IRES-Flag-CTR9) were co-transfected into HEK293T cells cultured in one 10-cm dish using transIT-LT1 reagent (Mirus Bio) according to the manufacturer's protocol. Medium was replaced with fresh DMEM supplemented with 10% FBS/ 1%P/S 8-10 hours post transfection. 48 hours after transfection, the supernatant containing the virus particles was collected by centrifugation (1500 rpm, 5 minutes) and subsequent filtered through a 0.45 µm syringe filter (Thermo Scientific). Approximately 1/5 volume of Lenti-X concentrator (Clonetech) was added to concentrate the virus tilter overnight at 4°C. For infection, 1 mL of virus was mixed with 1 mL of fresh cell culture medium, and polybrene was added at a final concentration of 8 µg/mL to increase the infection efficiency. After overnight infection, the culture medium was changed. Cells were selected with 2 µg/mL puromycin for at least one week or send out for high GFP+ inclusion by flow cytometry sorter for generation of stable CTR9 KD or overexpression in hMSCs, respectively.

In Vitro Differentiation Assay

Expanded hMSCs with shControl and shCTR9#3/#5 were cultured in either osteogenic, adipogenic or chondrogenic medium to induce the lineage specific differentiation *in vitro*. For osteogenesis, hMSCs were induced in osteogenic medium composed of 1x MEMα, 10% FBS, 1% antibiotics, 10 mM β-glycerophosphate, 50 mg/ml L-ascorbic acid–2-phosphate, and 0.1 mM dexamethasone (Sigma Aldrich) for up to 28 days.

For adipogenesis, hMSCs were induced in adipogenic medium consisting of 1x MEMα, 10% FBS, 1% antibiotics, 1 mM dexamethasone, 0.5 mM 3-isobutyl-1-methylxanthine (IBMX) and 1 mg/ml insulin (Sigma Aldrich) for up to 21 days.

For chondrogenesis, 1.5-3X10^5 cells were collected and centrifuged at 600 g for 5 min to form a high-cell-density pellet before induced by chondrogenic medium containing 1x MEMα, 10% FBS, 1% antibiotics, ITS Premix (Corning), 0.9 mM sodium pyruvate, 50 mg/ml L-ascorbic acid-2- phosphate, 40 mg/ml L-proline, 0.1 mM dexamethasone (Sigma Aldrich), and 10 ng/ml transforming growth factor-b 1 (PeproTech) for up to 21 days. Medium was changed every 3 days during the induction period.

Western Blot analysis

Cells were harvested after trypsinization, washed with 1x Dulbecco's phosphate buffer saline (DPBS) (Life Technologies), and lysed in lysis buffer [50 mM Tris-HCl pH 8.0, 400 mM NaCl, 10% glycerol, 0.5% Triton X-100 and 1 x protease inhibitor cocktail (Sigma-Aldrich)]. After a brief sonication, total lysate was centrifuged, and the supernatant was quantified using the BioRad Protein Assay (BioRad). Approximately 30 µg protein was resolved by SDS-PAGE. Proteins were transferred to a nitrocellulose membrane for 1.5 hours at 350 mA. Membranes were blocked with 5% nonfat milk or 5% BSA at room temperature for 1 hour and incubated overnight with diluted primary antibody at 4°C. Membranes were then washed and incubated with HRP-conjugated goat-anti-rabbit or mouse IgG secondary antibody for 1 hour at room temperature. Membrane was incubated with enhanced chemiluminescence reagents (ThermoFisher Scientific) followed by exposure to X-ray films.

Total RNA extraction and Quantitative real-time PCR

Total RNA was extracted from cells using the E.Z.N.A™ HP Total RNA extraction kit (Omega). The quantity and quality of total RNA were measured by Nanodrop 1000 (Thermo Fisher Scientific) before the RNA was reverse transcribed using the SuperScript First strand cDNA synthesis kit with 6-mer random oligos (Invitrogen). The mRNA expression of genes of interest was determined using the iQSYBR Green Premix (Bio-Rad) with corresponding primers. The level of mRNA expression was calculated using the $2^{-\triangle Ct}$ method with reference to the control 18s rRNA.

Immunofluorescence staining of cell skeletons and H3K27me3 in hMSCs

hMSCs with shControl or shCTR9#3/#5 were seeded on 3.5 cm petri dishes with glass bottom. Cells were fixed in 4% formaldehyde for 15 mins, and then washed with DPBS three times. Subsequently, cells were permeabilized in 0.3% Triton X-100 in PBS for 10 mins, blocked with 3% BSA in PBST [PBS + 0.1% Triton X-100] for 1hr, and incubated with Tubulin (Thermo) and H3K27me3 primary antibody (Cell signaling technology) at room temperature for 2 hours. Cells were then washed with PBST, followed by incubation with secondary antibody (FITC- goat anti-mouse IgG (H+L), Cy5-goat anti-rabbit IgG (H+L), 1:250; Bethyl) for 45 mins at room temperature. After being washed twice in PBST, cells were incubated with 50 nM Alexa Fluor 555 Phalloidin (Cell Signaling Technology) and 10 mg/ml of Hoechest 33342 (Cell Signaling Technology) at 37°C for 15 mins, then washed twice in DPBS. Fluorescence was detected using a Nikon A1R confocal microscope at appropriate wavelengths at the UW imaging core.

Cell cycle profiling and senescence-associated β-galactosidase staining

To assess the cell cycle distribution, hMSCs were collected by trypsinization, fixed in cold 95% ethanol, and washed in PBS. The fixed cells were then resuspended in propidium iodide staining solution (200 µg/mL RNase A, 50 µg/mL propidium iodide, 0.1% [v/v] Triton X-100 in PBS + 1% BSA) and incubated overnight at 4°C. Samples were analyzed by flow cytometry at the University of Wisconsin Flow Cytometry Laboratory. Data were analyzed using FlowJo software (V10, Tree Star). For senescence-associated β-galactosidase staining, cells were fixed in a 2% formaldehyde/0.2% glutaraldehyde solution for 5 min and then stained overnight at 37°C with an X-Gal-containing staining buffer. After two PBS washes, cells were imaged on a Leica inverted microscope using the Leica Application Suite software.

3D spheroids formation

150,000 — 300,000 cells of hMSC-shControl/shCTR#3/#5 were fully resuspended in 200 – 250 µl of MEM α medium and seeded in 96-well round bottom plates with ultralow attachment (Corning), followed by a centrifugation at 500g for 10 minutes. 3D spheroid cultures were grown at 37°C in a humidified atmosphere with 5% CO_2. Brightfield images were taken within 48 hours range after cell seeding by Leica Quick-Check inverted microscopy. 3D spheroids were harvested after 72 hours and subject to FFPE slides preparation and H&E staining.

Annexin V and PI Staining by Flow Cytometry

Collect trypsinizied cells from a 6 cm dish. Wash cells with 1X cold PBS and carefully remove the supernatant. Re-suspend the cells in binding buffer [10 mM HEPES pH 7.4, 140 mM NaCl and 2.5 mM $CaCl_2$] at a concentration of ~1 × 10^6 cells/ml. After a brief centrifugation, cells were resuspended and incubated for 10 min with 0.5 µg/ml Annexin V-FITC and 2 µg/mL PI in 400 µL binding buffer. The cells were immediately placed on ice and analyzed by flow cytometry. Cell fragments were removed by morphological gating. Cells negative for Annexin V-FITC and PI were considered viable, Annexin V-FITC positive and PI negative considered apoptotic, and Annexin V-FITC positive and PI positive considered necrotic.

Phenotypic Measurement of Osteogenesis

A. BCIP/NBT substrate staining of Alkaline Phosphatase Activity

Cells were fixed in formalin for 2 mins after a brief wash of DPBS. Enough BCIP/NBT substrate solution [one BCIP/NBT tablet (Sigma Aldrich) in 10 ml distilled water] were covered and incubate at room temperature at dark for 10 mins. Discard BCIP/NBT substrate solution and wash with DPBS for 2 times. After image analysis, cells were scarped down in ice-cold DPBS, and 1/5 volume of the final suspension were serially diluted in PBS for absorbance measurement at OD 595nm on a microplate reader. And 1/2 volume of the final suspension were subjected to DNA extraction for Pico Green Assay.

B. Picrosirius red staining of collagen

Cells were fixed in formalin for 10 mins followed by an incubation in 0.1% Picrosirius Red solution for 1 h at room temperature. After washing twice in 0.5% acetic acid and distilled water, samples were mounted with DPX mounting medium (Invitrogen).

C. Alizarin Red S staining of Calcium mineralization

Cells were fixed in 60% isopropanol and stained with Alizarin Red S staining solution (20 mg/ml Alizarin Red S, pH 4.1-4.3, 0.22 µm filtered) for 45 mins in dark followed by 5 times of DPBS wash. After image analysis, calcium deposits were extracted using 0.5 M hydrochloric acid and then measured by the LiquiColor Kit (Stanbio) according to the manufacturer’s instructions. 10% of the input were subjected to DNA extraction for Pico Green Assay.

D. Human Osteocalcin ELISA

Serum free medium supernatant as well as 1 ml PBS that rinsed with monolayer surface were collected and concentrated using a Amicon Ultra 3K MWCO Centrifugal Filters (Millipore Sigma) at 4 ℃. Concentrated supernatant was resuspended in ice-cold PBS in a final volume of 100ul and subjected to Osteocalcin Human ELISA Kit (Invitrogen) for measurement of Osteocalcin secretion per manufacturer’s protocol. Monolayer cells on the culture dish were scarped down for genomic DNA extraction followed by Pico Green quantification.

Phenotypic Measurement of Adipogenesis

A. Oil Red O staining of lipid droplets

Cells were fixed in 4% formaldehyde and then stained with freshly made Oil Red O staining solution [3mg/ml Oil Red O (Sigma Aldrich), 60% isopropanol, 0.8 µm filtered]. After image analysis, 100% isopropanol was used to dissolve the Oil Red O stain, and absorbance of the resulting solution at 656 nm was measured by a spectrophotometer to determine lipid content. 10% of the input were subjected to DNA extraction for Pico Green Assay.

Phenotypic Measurement of Chondrogenesis

A. Preparation of 3D spheroids embedding FFPE

Cell pellets were fixed in 4% formaldehyde, dehydrated by a series of gradient ethanol, infiltrated with xylene, and then embedded in paraffin. Embedded cell pellets were cut into 8-mm sections with a microtome.

B. Alcian Blue staining

Deparaffinize FFPE slides and rehydrate through a series of gradient ethanol to distilled water at the final. Stain the spheroid sections in Alcian Blue Solution [1mg/ml Alcian Blue 8GX (ThermoFisher Scientific), 3% Acetic Acid, pH 2.5] for 30 mins with 2 mins rinse in running tap water afterwards. Counterstain the sections in Nuclear Fast Red Solution [1mg/ml Nuclear Fast Red (Sigma Aldrich), 5% Aluminum sulfate (Fisher Scientific), 0.8 um filtered, and 1% thymol preservative (Sigma Aldrich) added]. Wash the slides in running tap water for 1 min. Dehydrate the slides through 70% -- 100% ethanol and clear in xylene. Coverslip the slides with resinous mounting medium at last.

C. Toluidine blue staining

Deparaffinize FFPE slides and rehydrate through a series of gradient ethanol to distilled water at the final. Stain the spheroid sections in toluidine blue working solution [1mg/ml Toluidine Blue O (Sigma Aldrich), 7% EtOH, 1% NaCl, pH 2.3-2.5] for 3 mins with 3 times wash of distilled water afterwards. Quickly dehydrate the slides through 70% -- 100% ethanol and clear in xylene. Coverslip the slides with resinous mounting medium at last.

Flow Cytometry analysis of osteo-/adipogenic markers

hMSCs with Control KD or CTR9 KD were incubated in osteogenic or adipogenic induction medium for 28 days or 21 days, respectively. Cells were harvested after disassociation using TrypLE™ express Enzyme, washed in PBS, and fixed in 4% paraformaldehyde for 15 mins. Subsequently, cells were permeabilized with 0.3% Triton X-100 in PBS for 10 mins, blocked with 3% BSA in PBST for 1 hour and incubated with corresponding antibodies in 1% BSA in PBST for 1hr. For analysis of osteogenic markers, cells were incubated with APC conjugated CD73/CD90 antibodies (eBioscience) as well as Alexa-Fluor®488 conjugated Osteopontin/Osteocalcin antibodies (Abcam). For analysis of adipogenic markers, cells were incubated with APC conjugated CD73/CD90 antibodies (eBioscience) as well as Dylight®488 conjugated PPAR γ antibody (Cell Signaling Technology) followed by BODIPY 493/503 labeling. After washing with PBST, cells were subjected to flow cytometry analysis.

Immunofluorescence staining of osteo-/adipogenic markers

hMSCs with Control KD or CTR9 KD were seeded on 3.5 cm petri dishes with glass bottom and cultured in osteogenic or adipogenic induction medium for 28 days or 21 days, respectively. Cells were fixed in 4% formaldehyde for 15 mins, and then washed with DPBS three times. Subsequently, cells were permeabilized in 0.3% Triton X-100 in PBS for 10 mins, blocked with 3% BSA in PBST [PBS + 0.1% Triton X-100] for 1hr, and incubated with corresponding antibodies at 4°C overnight. Cells were then washed with PBST, followed by incubation with fluorophore conjugated secondary antibodies with matched host species (Fab Fragments or whole IgG (H+L)). Nuclei were visualized by 1 µg/ml Hoechst 33342 staining at 37°C for 15 mins. For analysis of osteogenic markers, cells were first incubated with RUNX2 (Rabbit, Cell Signaling Technology) and osteocalcin (Mouse, Novus Biologicals) primary antibodies sequentially followed by incubation of corresponding FITC-conjugated or Cy3-conjugated Fab Fragments secondary antibodies (Alexa Fluor®488 AffiniPure Fab Fragment Goat Anti-Rabbit IgG (H+L), Cy3 AffiniPure Fab Fragment Goat Anti-Mouse IgG (H+L), Jackson ImmunoResearch). APC conjugated CD73/CD90 antibodies (Mouse, eBioscience) and corresponding secondary antibody (Cy5-goat anti-mouse IgG (H+L), Bethyl) were lastly applied. For analysis of adipogenic markers, Triton X-100 was removed in antibody incubation buffer as well as PBST wash was replaced by DPBS wash. Cells were simultaneously incubated with PPARγ (Rabbit, Cell Signaling Technology) and APC conjugated CD73/CD90 primary antibodies (Mouse, eBioscience) followed by corresponding secondary antibodies (Cy3-goat anti-rabbit IgG (H+L); Cy5-goat anti-mouse IgG (H+L), Bethyl) incubation. Lipid droplets were further stained by 2µM BODIPY 493/503 at 37°C for 15 mins followed by 3 times of DPBS wash. Fluorescence was detected using a Nikon A1R confocal microscope at appropriate wavelengths at the UW imaging core.

3D scaffolds-based experiments

A. Ectopic Bone Formation

hMSCs (1 X10^6) with control knockdown (shControl) or CTR9 knockdowns (shCTR9#3 / shCTR9#5) were seeded on the top of 3D PCL scaffolds (1cm diameter, 1.6mm thickness; 3D Bio-tek, #PCL305048-16) followed by 4 hours sitting in 37°C， 5% CO_2 cell culture incubator. And the scaffolds were implanted subcutaneously into the dorsal surface of 8–10 weeks old immune-deficient male mice after 7 days of osteo-induction *in vitro*. The whole mice were subjected to *in vivo* CT scanning after 4 or 8 weeks of implantation. The implants were harvested, fixed in 4% paraformaldehyde for micro-CT, then quarter sectioned and decalcified, and embedded in paraffin or sent to other downstream analysis. Thin histological sections (8 mm) were stained with hematoxylin and eosin (H&E).

B. Alizarin Red S staining

Quarter sectioned scaffolds were fixed with 3.7% formaldehyde for 24 hours at 37°C and then stained with Alizarin Red S (10 mg/mL) for 1 hour. Scaffolds were washed 5 times with distilled water to remove excess stain and air dried. Digital images of stained scaffolds were acquired using a high-resolution scanner for integral view or using stereomicroscope for zoom in view. Two fields of view at high magnification were randomly selected and captured for each specimen and representative images are shown in the figures.

C. BCIP/NBT substrate staining

Quarter sectioned scaffolds were fixed with 3.7% formaldehyde for 5 mins and then stained with BCIP/NBT staining solution (1 pill/ 10mL) for 15 mins. Scaffolds were washed 3 times with PBST to remove excess stain and air dried. Digital images of stained scaffolds were acquired using a high-resolution scanner.

D. Osteocalcin ELISA

Levels of osteocalcin protein in the quarter-sectioned scaffolds were measured by ELISA (Osteocalcin Human ELISA Kit, Invitrogen # KAQ1381). Quarter sectioned scaffolds were rinsed with PBS and frozen until assay. For ELISA assay, thawed scaffolds were incubated in 0.5 mL of 0.5 M HCl for 30 mins at 37℃. After 30 min, the pH was neutralized with 1M NaOH and amount of osteocalcin in extracts was measured by ELISA based assay according to manufacturer’s protocols. A standard curve using control osteocalcin was used to determine concentration.

E. Von-Kossa staining

Deparaffinize scaffold sections and rehydrate through a series of gradient ethanol to distilled water at the final. After rinsing the slides in several changes of distilled water, incubate sections with 1% aqueous silver nitrate solution in a clear glass jar placed under ultraviolet light bulb for 1 hour (60-100 watt). Wash the slides in several changes of distilled water and remove the residual silver on the sections with 5% sodium thiosulfate for 5 mins. After another wash of distilled water, counterstain the scaffold sections with Nuclear Fast Red solutions [1mg/ml Nuclear Fast Red (Sigma Aldrich), 5% Aluminum sulfate (Fisher Scientific), 0.8 um filtered, and 1% thymol preservative (Sigma Aldrich) added] for 5 mins. Rinse the slides in distilled water followed by the dehydration through a graded alcohol and clearance in xylene. Coverslip the sections using permanent mounting medium.

F. Picrosirius Red staining

Deparaffinize scaffold sections and rehydrate through a series of gradient ethanol to distilled water at the final. After rinsing the slides in several changes of distilled water, stain nuclei with Weigert's hematoxylin (Sigma Aldrich) for 8 minutes, and then wash the slides for 10 minutes in running tap water. Stain the collagen of scaffold sections in picrosirius red solution [1mg/ml Direct Red 80 in saturated aqueous solution of picric acid (Sigma Aldrich)] for 1 hour followed by wash of acidifies water (0.5% acetic acid) for 2 times. Physically remove most of the water from the slides by vigorous shaking and dehydrate the sections in three changes of 100% ethanol. Clear in xylene and mount in a resinous medium

G. Immuno-fluorescence staining

Cells on scaffolds were fixed with 3.7% formaldehyde for 15 mins, washed in DPBS and permeabilized with 0.2% Triton X-100 for 10 mins. Samples were rinsed with DPBS and stained with human specific osteocalcin antibody (Novus Biologicals #MAB1419) at 4°C for overnight. Next day, FITC conjugated secondary antibody (FITC-goat anti-mouse IgG

(H+L), Bethyl) was used to detect osteocalcin staining. Alexa Fluor 555-Phalloidin (100nM in PBS) and Hoechst (1µg/mL in PBS buffer) to stain for F-actin and nuclei, respectively (Invitrogen). Scaffolds were washed with DPBS before confocal microscopy imaging.

H. Confocal microscopy of scaffolds

Confocal microscopy (Nikon Upright FN1 microscope) was used to measure osteocalcin enrichment as well as mineralization using scaffolds soaked in DPBS (not air-dried). High resolution z-stack images were captured with a 10x/0.80 air immersion objective (1 mm z-step size) for nuclei (Hoechst 33342), F-actin (Alexa Fluor 555-Phalloidin) and Human specific Osteocalcin (Novus Biologicals, human specific osteocalcin antibody)

Data availability

The Inveon Research workspace 4.2 (Simens Healthineers) was used to analysis all raw CT data. The GraphPad Prism 7.04 software (GraphPad Software, Inc. San Diego, CA, http://www.graphpad.com) was used for the statistical analyses. Statistical significance was assessed by unpaired two-tailed Student’s t test with corresponding correction and stated as exact *p*-value.

3.6 FIGURES & LEGENDS

Figure 3-1.

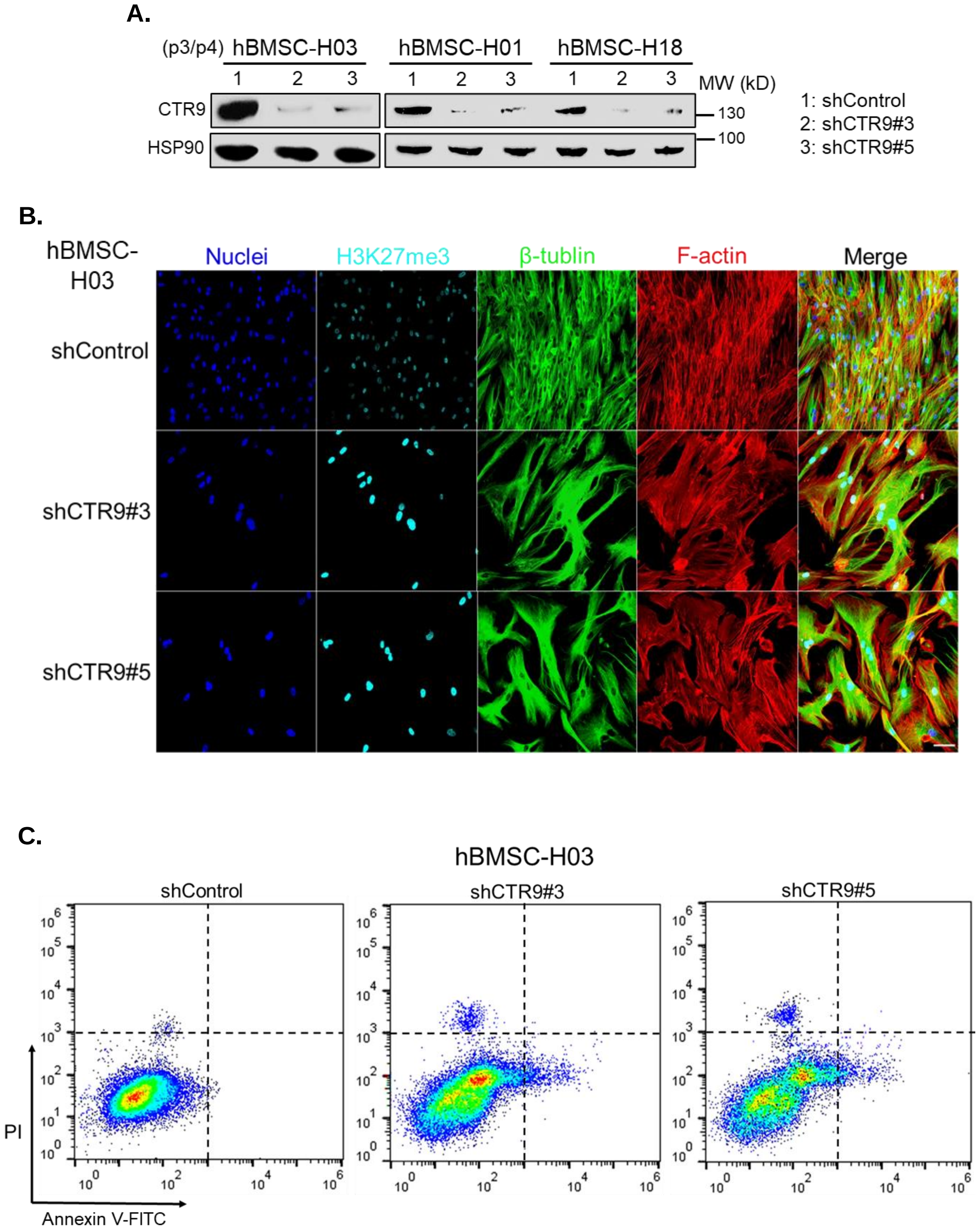

Figure 3-1.

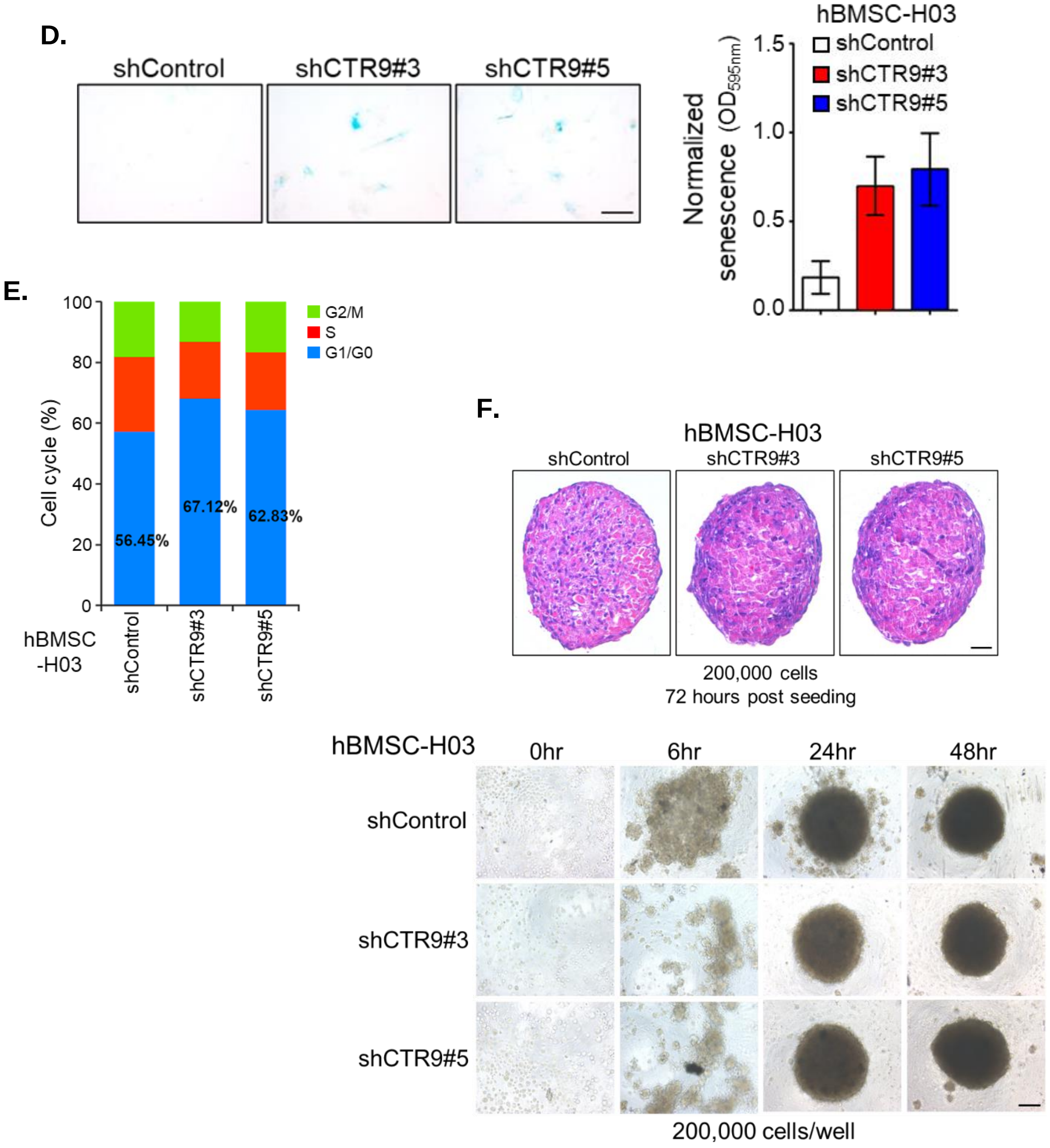
D.
shControl
shCTR9#3
shCTR9#5
hBMSC-H03
shControl
shCTR9#3
shCTR9#5
Normalized senescence (OD595nm)
0.0
0.5
1.0
1.5
E.
Cell cycle (%)
0
20
40
60
80
100
G2/M
S
G1/G0
56.45%
67.12%
62.83%
hBMSC -H03
shControl
shCTR9#3
shCTR9#5
F.
hBMSC-H03
shControl
shCTR9#3
shCTR9#5
200,000 cells
72 hours post seeding
hBMSC-H03
0hr
6hr
24hr
48hr
shControl
shCTR9#3
shCTR9#5
200,000 cells/well

Figure 3-1.

G.

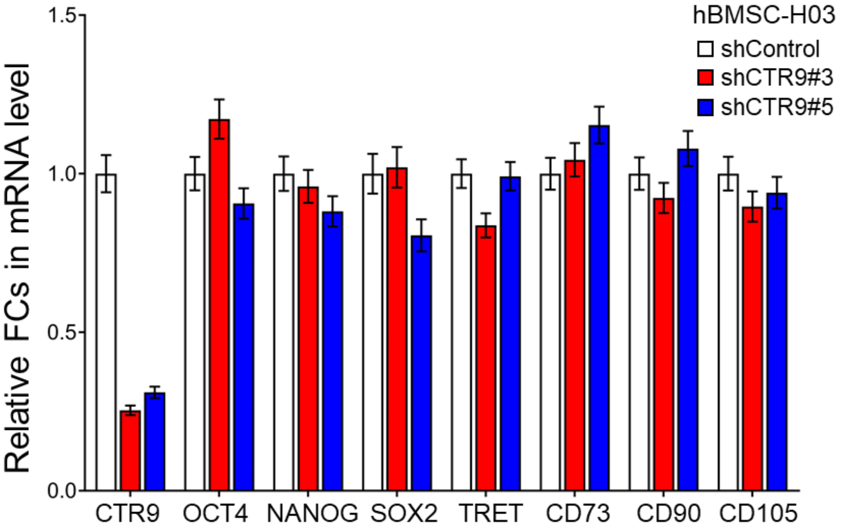

Figure 3-1.

A. Western Blot analyses showing the knockdown efficacies of two different shCTR9 in early passage (p3/p4) of hMSCs derived from different donors (H01/H03/H18), as compared with hMSCs expressing shControl. β-actin was the loading control.

B. Comparison of the morphology of shControl and shCTR9 hMSCs in high confluency by immuno-fluorescence staining of cytoskeleton proteins. (Nuclei: blue; F-actin: red; β-tubulin: green; H3K27me3: cyan)

C. Measurement of cell viability of shControl and two shCTR9 MSC lines (shCTR9#3 and shCTR9#5) by PI staining and annexin V-GFP in flow cytometry.

D. (*Left*) Representative images showing the senescence-associated β-galactosidase staining (light blue) in shControl and shCTR9 KD (shCTR9#3/#5) hMSCs. (*Right*) Quantification of β-galactosidase staining intensities using OD_{595nM} absorbance normalized with the respective DNA content. Data are represented as mean ± SD (n=3).

E. Cell cycle profiles of shControl or shCTR9 hMSCs assessed by propidium iodide (PI) staining followed by flow cytometry.

F. (*Up*) Representative H&E staining of 3D spheroids of shControl or shCTR9 MSCs (shCTR9#3/#5) cultured in non-adherent 96-well plate 72-hour post-seeding. (*Bottom*) Representative images of 3D spheroids formed by equal numbers of shControl or shCTR9 MSCs (shCTR9#3/#5) on non-adherent 96-well plate 48-hour post seeding.

G. qPCR analyses of the mRNA levels of CTR9, stemness genes (OCT4/NANOG/SOX2/TRET) and MSC specific surface antigens (CD73/CD90/CD105) in shControl and shCTR9 hMSCs. Relative fold change in mRNA levels is represented as means ± SD (n = 3) and were normalized to β-actin. Values in shControl group were set as 1.

Figure 3-2.

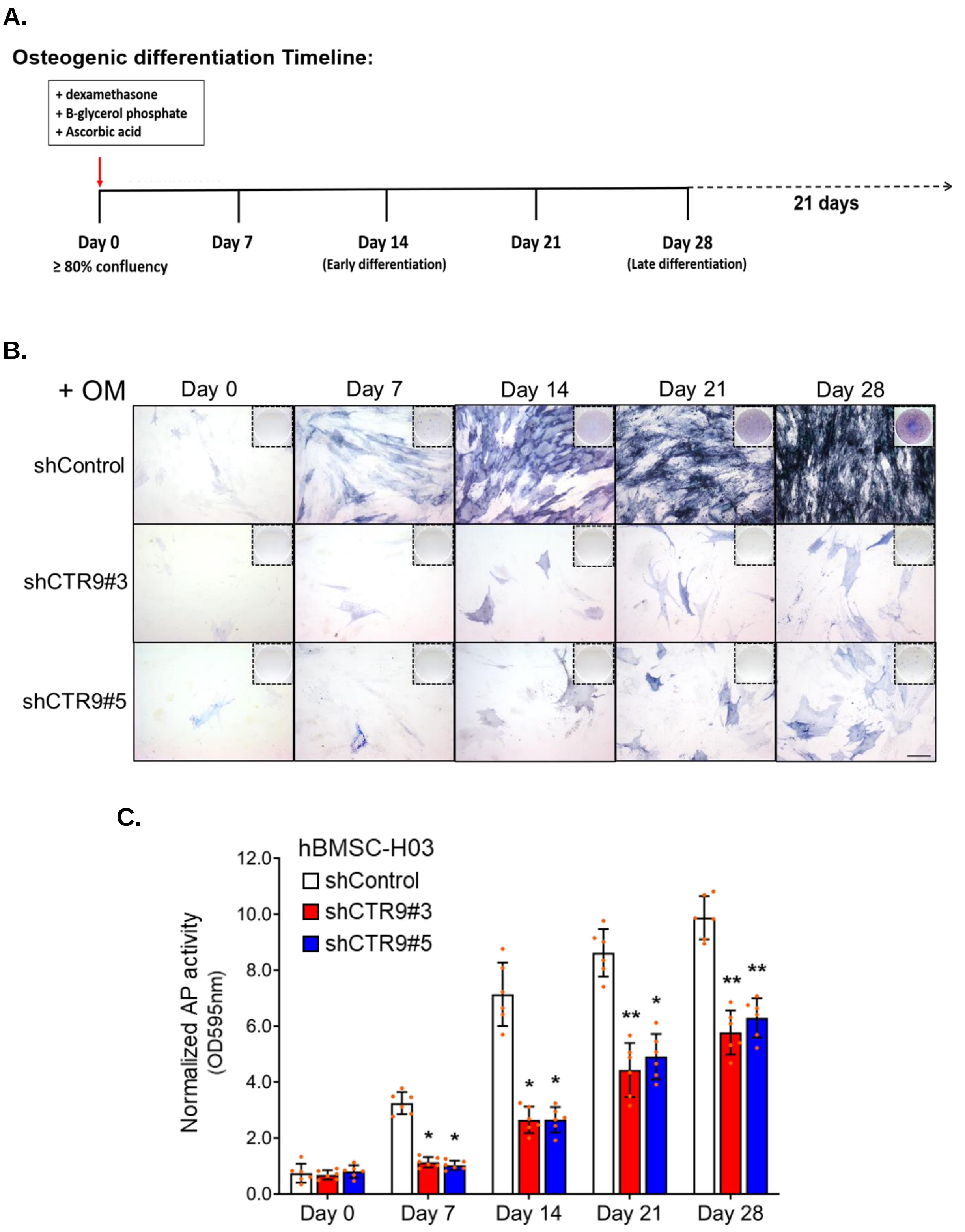
A.
Osteogenic differentiation Timeline:
+ dexamethasone
+ B-glycerol phosphate
+ Ascorbic acid
21 days
Day 0
≥ 80% confluency
Day 7
Day 14
(Early differentiation)
Day 21
Day 28
(Late differentiation)
B.
+ OM
Day 0
Day 7
Day 14
Day 21
Day 28
shControl
shCTR9#3
shCTR9#5
C.
hBMSC-H03
□ shControl
🟥 shCTR9#3
🟦 shCTR9#5
Normalized AP activity (OD595nm)
12.0
10.0
8.0
6.0
4.0
2.0
0.0
Day 0
Day 7
Day 14
Day 21
Day 28
*
**

Figure 3-2.

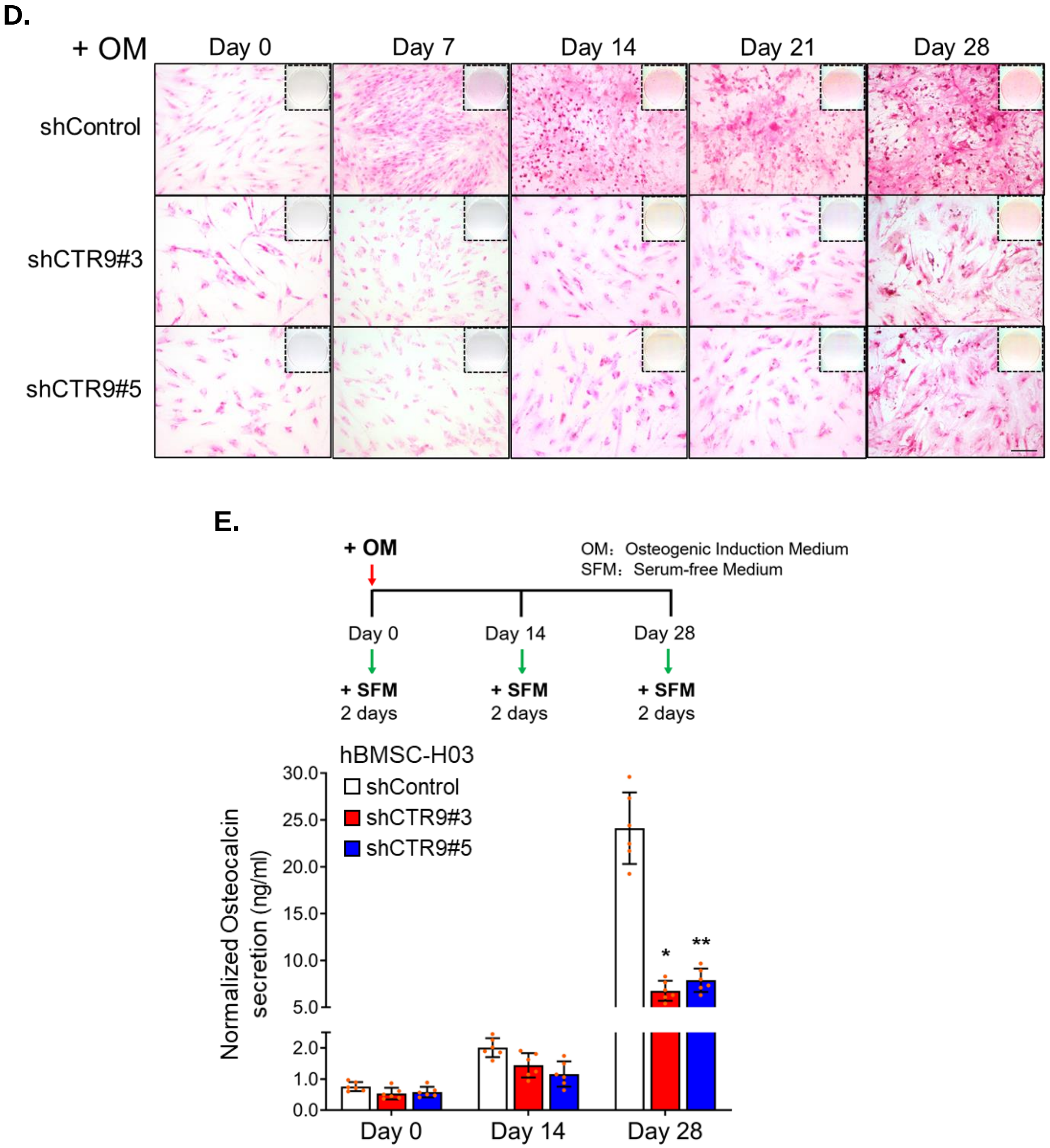
D.
+ OM
Day 0
Day 7
Day 14
Day 21
Day 28
shControl
shCTR9#3
shCTR9#5
E.
+ OM
OM：Osteogenic Induction Medium
SFM：Serum-free Medium
Day 0
Day 14
Day 28
+ SFM
2 days
+ SFM
2 days
+ SFM
2 days
hBMSC-H03
shControl
shCTR9#3
shCTR9#5
Normalized Osteocalcin secretion (ng/ml)
30.0
25.0
20.0
15.0
10.0
5.0
2.0
1.0
0.0
*
**
Day 0
Day 14
Day 28

Figure 3-2.

F.

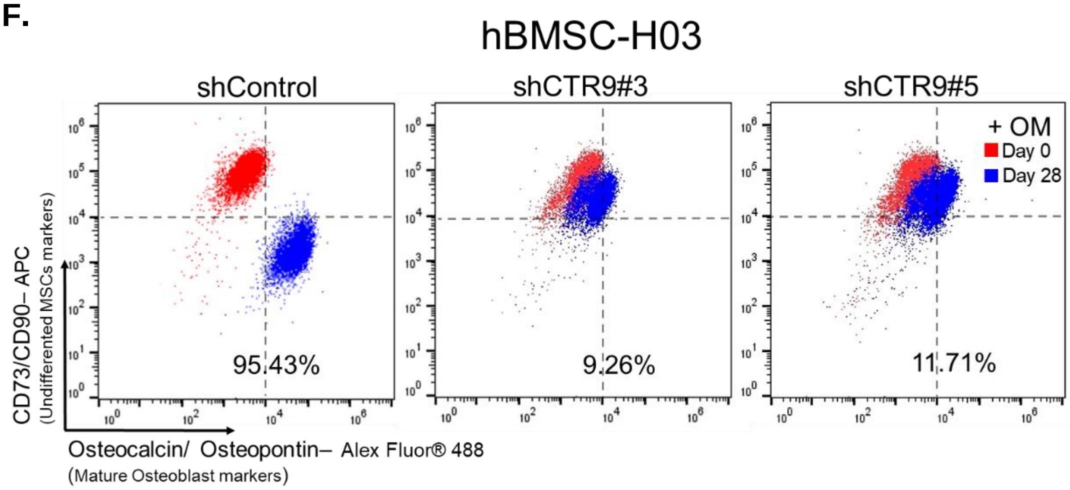
hBMSC-H03
shControl
shCTR9#3
shCTR9#5
+ OM
Day 0
Day 28
95.43%
9.26%
11.71%
CD73/CD90– APC
(Undifferented MSCs markers)
Osteocalcin/ Osteopontin– Alex Fluor® 488
(Mature Osteoblast markers)
10^0
10^1
10^2
10^3
10^4
10^5
10^6

G.

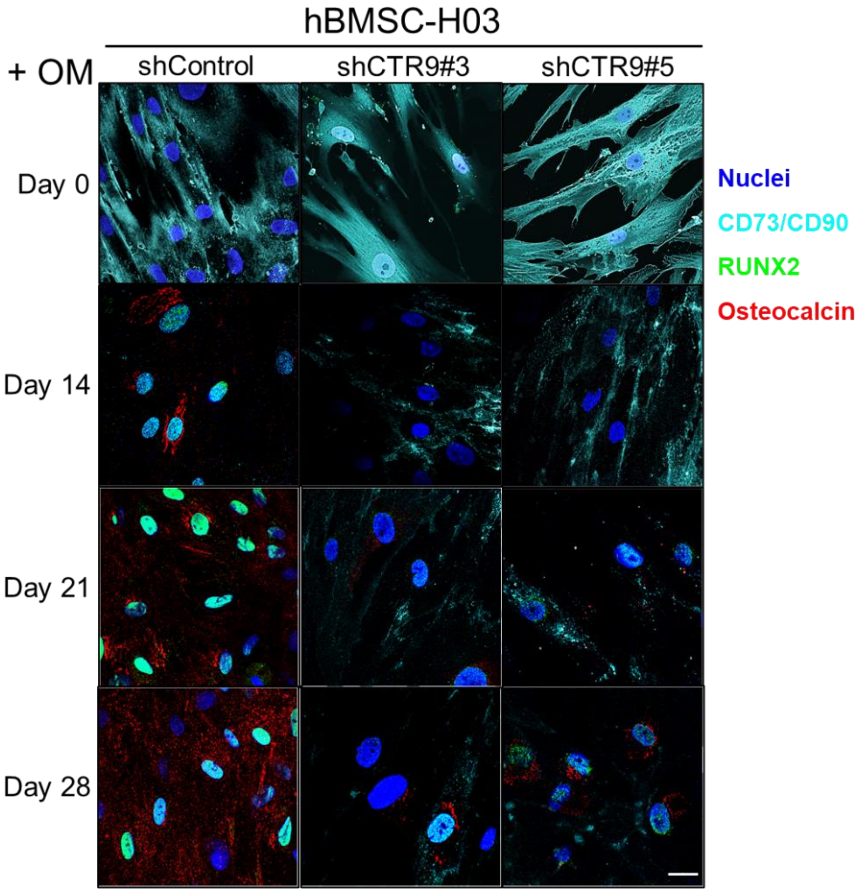
hBMSC-H03
+ OM
shControl
shCTR9#3
shCTR9#5
Day 0
Day 14
Day 21
Day 28
Nuclei
CD73/CD90
RUNX2
Osteocalcin

Figure 3-2.

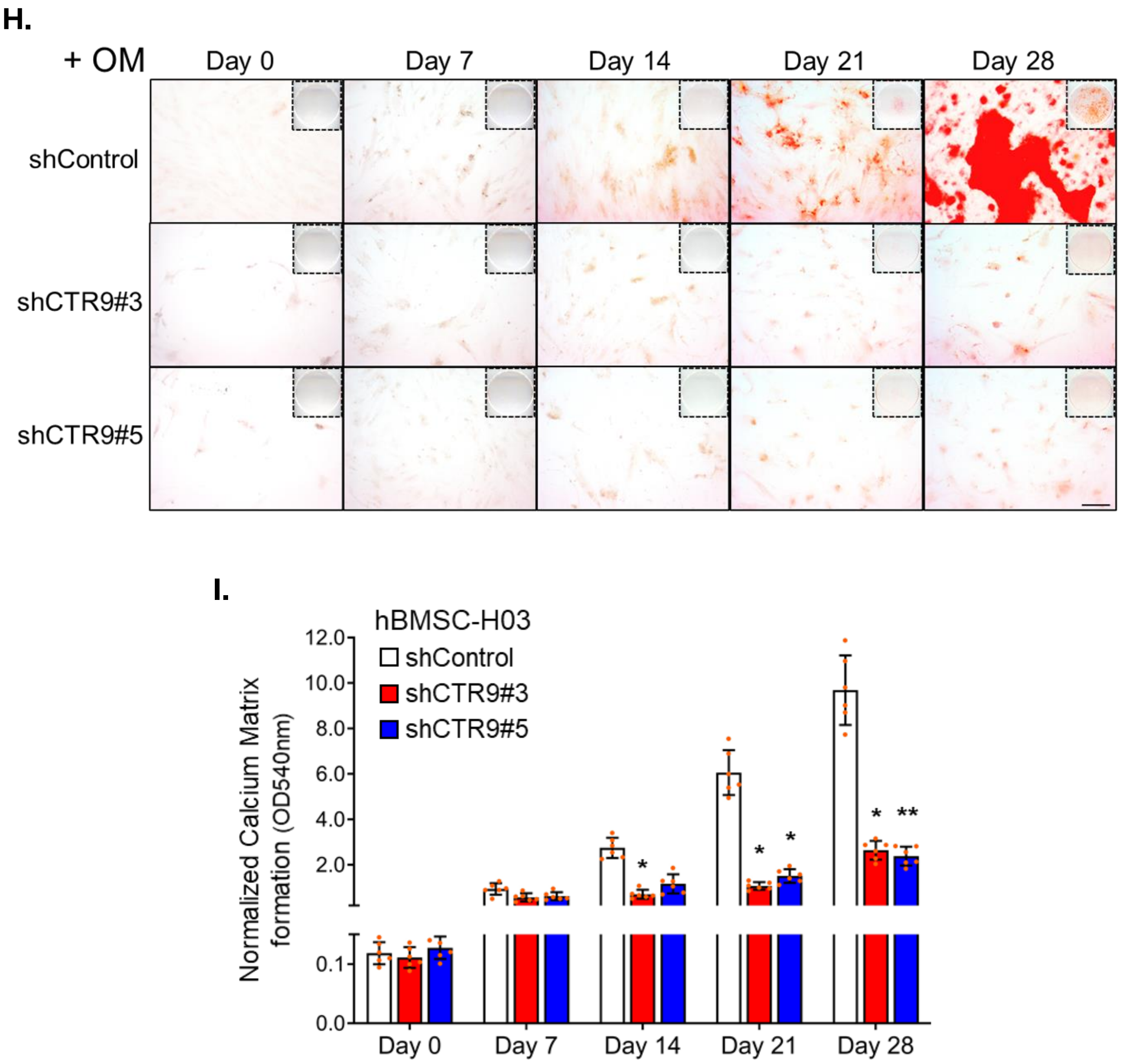
H.
+ OM
Day 0
Day 7
Day 14
Day 21
Day 28
shControl
shCTR9#3
shCTR9#5
I.
hBMSC-H03
☐ shControl
🟥 shCTR9#3
🟦 shCTR9#5
Normalized Calcium Matrix formation (OD540nm)
12.0
10.0
8.0
6.0
4.0
2.0
0.1
0.0
*
*
*
*
**
Day 0
Day 7
Day 14
Day 21
Day 28

Figure 3-2.

J.

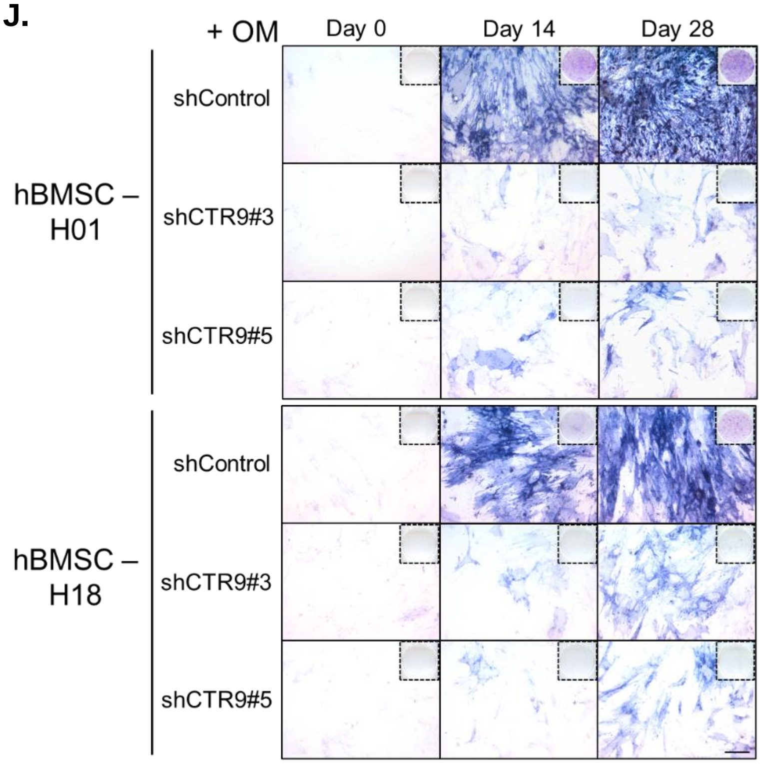
+ OM
Day 0
Day 14
Day 28
hBMSC – H01
shControl
shCTR9#3
shCTR9#5
hBMSC – H18
shControl
shCTR9#3
shCTR9#5

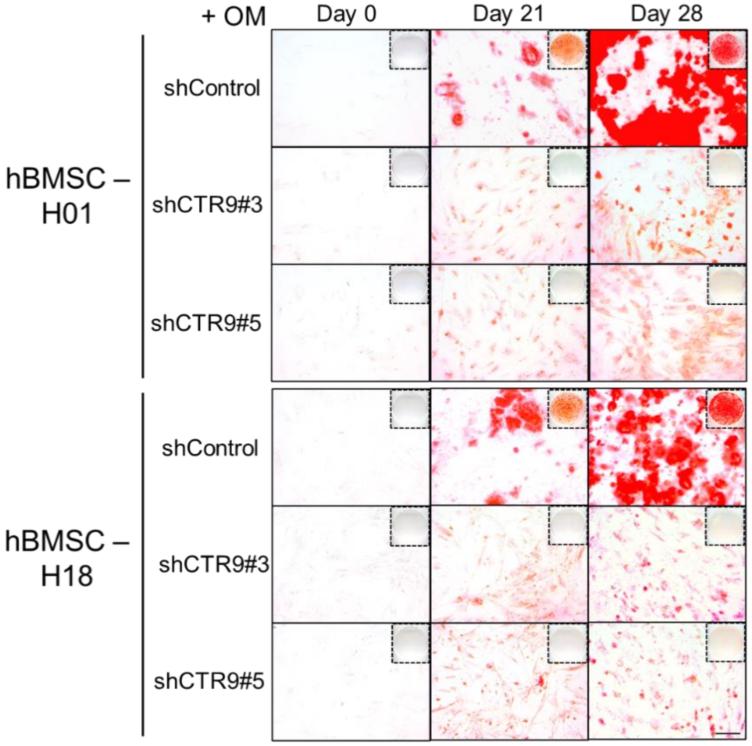
+ OM
Day 0
Day 21
Day 28
hBMSC – H01
shControl
shCTR9#3
shCTR9#5
hBMSC – H18
shControl
shCTR9#3
shCTR9#5

Figure 3-2.

A. Schematic workflow of osteogenic induction of hMSCs.
B. Representative images showing the Alkaline phosphatase (AP) activity-associated BCIP-NBT staining (violet blue) of shControl or shCTR9 hMSCs (shCTR9#3/#5) from 0 to 28 days of osteogenic induction.
C. Quantification of AP activity by OD_{595nM} absorbance normalized with respective DNA content. Data are represented as mean ± SD (n=3). p values were calculated by two tails T-test with * < 0.05 and ** < 0.01. OM: osteogenic induction medium
D. Representative images showing Picrosirius Red-stained collagenous matrix (pink) of shControl or shCTR9 hMSCs (shCTR9#3/shCTR9#5) from day 0 to day 28 of osteogenic induction.
E. Osteocalcin secretion of shControl or shCTR9 hMSCs (shCTR9#3/#5) measured using the human Osteocalcin ELISA kit after 0, 14 or 28 days of osteogenic induction followed by two-day culture in serum-free medium. Data which normalized by respective DNA content are represented as mean ± SD (n=6). p values were calculated by two tails t-test with * < 0.05 and ** < 0.01.
F. Flow cytometry analyses of CD73/CD90, the undifferentiated hMSCs markers, and Osteocalcin/Osteopontin, the osteogenic differentiated hMSCs markers, in shControl or shCTR9 hMSCs (shCTR9#3/#5) on day 0 and day 28 of osteogenic induction.
G. Immuno-fluorescence imaging of CD73/CD90 (Cyan), RUNX2 (Green) and Osteocalcin (39) in shControl or shCTR9 hMSCs (shCTR9#3/#5) from 0 to 28 days of osteogenic induction. Nucleus were stained by Hoechst 33342 in blue.

H. Representative images showing the ECM formation stained with Alizarin Red S (39) of shControl or shCTR9 hMSCs (shCTR9#3/#5) from day 0 to day 28 of osteogenic induction.

I. Quantification of ECM formation by OD_{540nM} absorbance normalized with the respective DNA content. Data are represented as mean ± SD (n=3). p values were calculated by two tails t-test with * < 0.05 and ** < 0.01.

J. BCIP/NBT staining of AP activity (*Up*) and Alizarin Red S staining of ECM formation (*Bottom*) in shControl or shCTR9 hMSCs (shCTR9#3/#5) derived from two different donors (H01/H18) from day 0 to day 28 of osteogenic induction.

Figure 3-3.

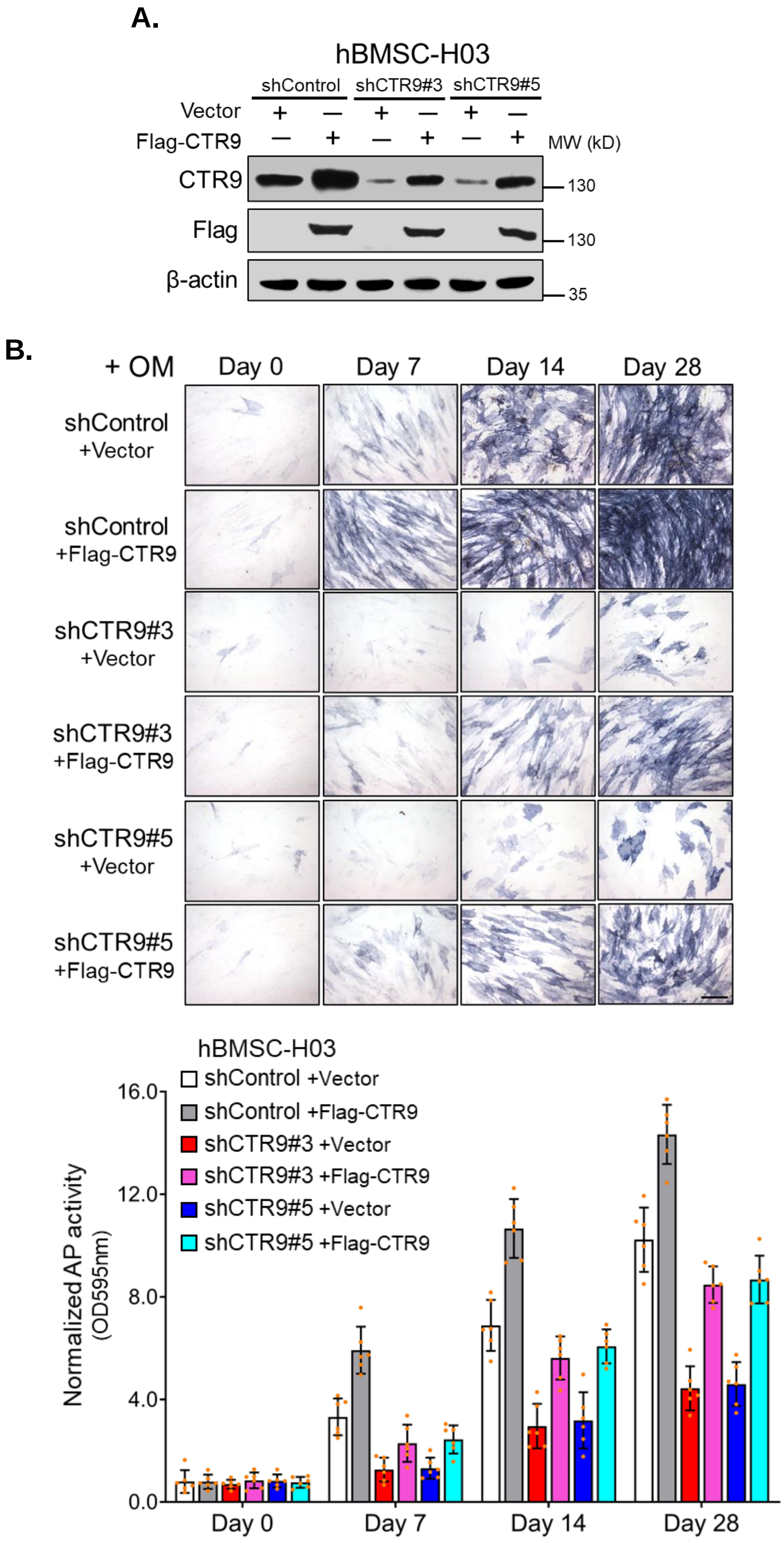
A.
hBMSC-H03
shControl
shCTR9#3
shCTR9#5
Vector + — + — + —
Flag-CTR9 — + — + — +
MW (kD)
CTR9
130
Flag
130
β-actin
35
B.
+ OM
Day 0
Day 7
Day 14
Day 28
shControl +Vector
shControl +Flag-CTR9
shCTR9#3 +Vector
shCTR9#3 +Flag-CTR9
shCTR9#5 +Vector
shCTR9#5 +Flag-CTR9
hBMSC-H03
shControl +Vector
shControl +Flag-CTR9
shCTR9#3 +Vector
shCTR9#3 +Flag-CTR9
shCTR9#5 +Vector
shCTR9#5 +Flag-CTR9
Normalized AP activity (OD595nm)
16.0
12.0
8.0
4.0
0.0
Day 0
Day 7
Day 14
Day 28

Figure 3-3.

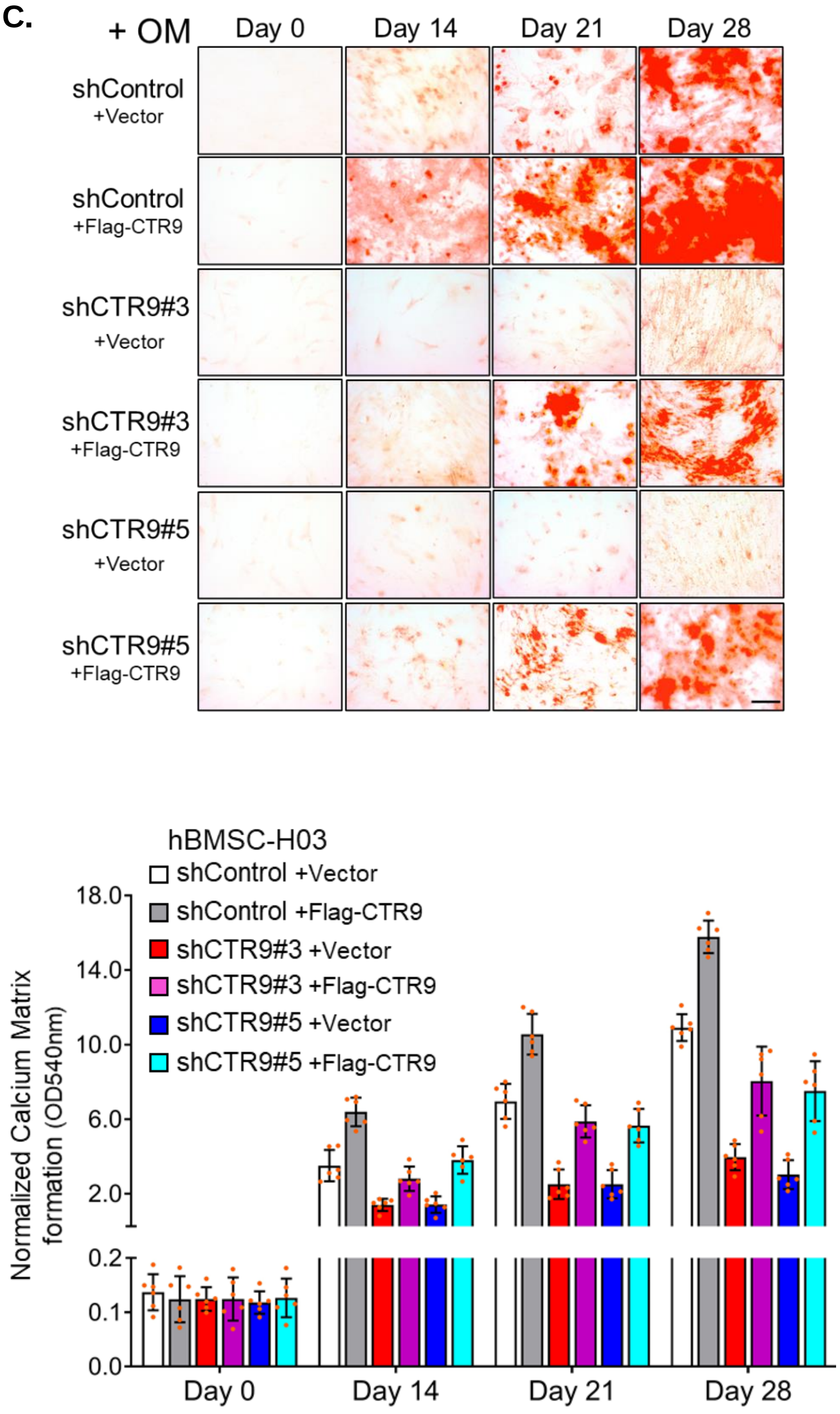
C.
+ OM
Day 0
Day 14
Day 21
Day 28
shControl +Vector
shControl +Flag-CTR9
shCTR9#3 +Vector
shCTR9#3 +Flag-CTR9
shCTR9#5 +Vector
shCTR9#5 +Flag-CTR9
hBMSC-H03
shControl +Vector
shControl +Flag-CTR9
shCTR9#3 +Vector
shCTR9#3 +Flag-CTR9
shCTR9#5 +Vector
shCTR9#5 +Flag-CTR9
Normalized Calcium Matrix formation (OD540nm)
18.0
14.0
10.0
6.0
2.0
0.2
0.1
0.0
Day 0
Day 14
Day 21
Day 28

Figure 3-3.

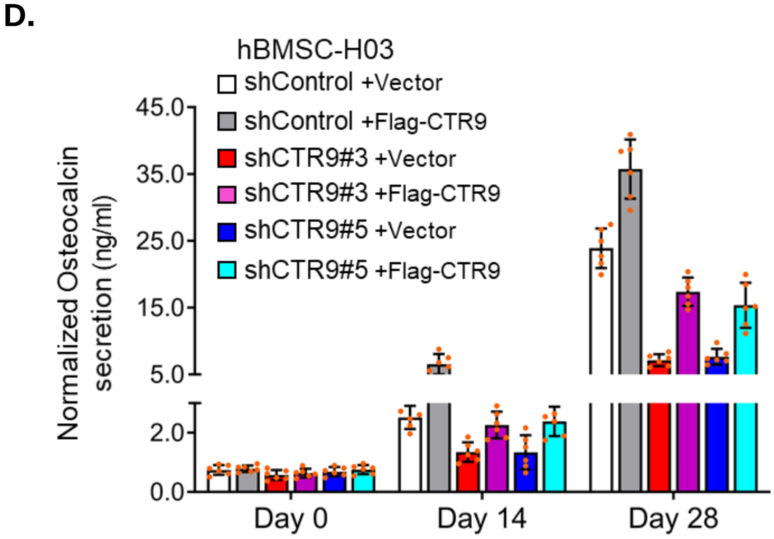

Figure 3-3.

A. Western blot analyses of CTR9 levels in shControl or shCTR9 hMSCs (shCTR9#3/#5) exogenously express Flag-CTR9. Blank vectors were transfected as controls (+Vector).

B. (*Up*) Representative images of BCIP-NBT staining (violet blue) of shControl or shCTR9 hMSCs (shCTR9#3/#5) transfected with blank vector (+Vector) or Flag-CTR9 plasmid (+ Flag-CTR9) from day 0 to day 28 of osteogenic induction. (*Bottom*) Quantification of AP activity by OD_{595nM} absorbance normalized with respective DNA content. Data are represented as mean ± SD (n=3). (OM: osteogenic induction medium).

C. (*Up*) Representative images showing the ECM formation with Alizarin Red S staining (39) of shControl or shCTR9 hMSCs (shCTR9#3/shCTR9#5) transfected with blank vector (+Vector) or Flag-CTR9 plasmid (+ Flag-CTR9) from day 0 to day 28 of osteogenic induction. (*Bottom*) Quantification of ECM formation by OD_{540nM}

absorbance normalized with respective DNA content. Data are represented as mean ± SD (n=3).

D. Quantification of osteocalcin secretion using the human Osteocalcin ELISA kit in shControl or shCTR9 hMSCs (shCTR9#3**/**#5) transfected with blank vector (+Vector) or Flag-CTR9 plasmid (+ Flag-CTR9) after 0, 14 or 28 days of osteogenic induction followed by two-day culture in serum-free medium. Data normalized by respective DNA content are represented as mean ± SD (n=6).

Figure 3-4.

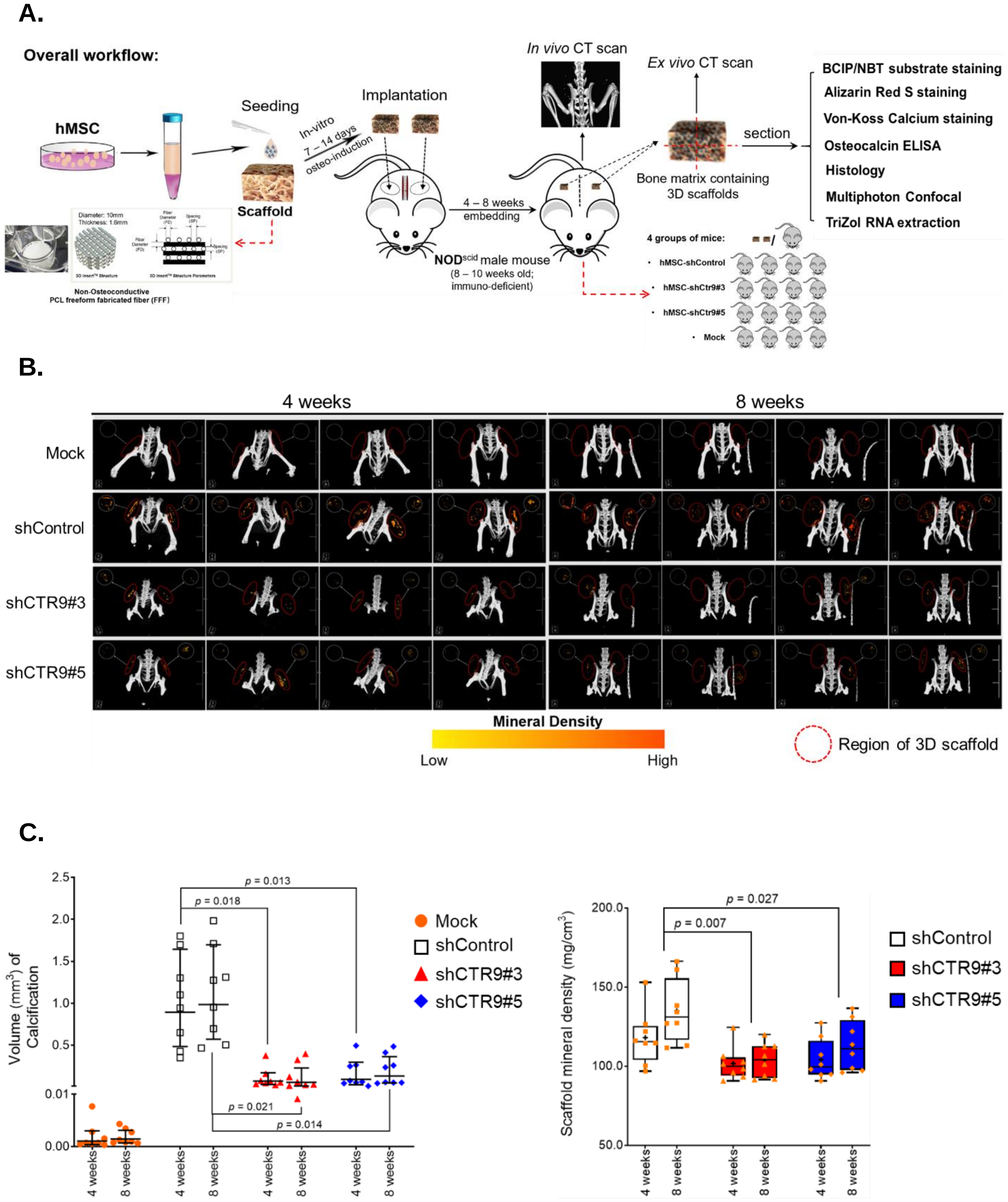
A.
Overall workflow:
hMSC
Seeding
Scaffold
In-vitro
7 – 14 days
osteo-induction
Implantation
Diameter: 10mm
Thickness: 1.6mm
Fiber Diameter (FD)
Spacing (SP)
3D Insert™ Structure
3D Insert™ Structure Parameters
Non-Osteoconductive
PCL freeform fabricated fiber (FFF)
4 – 8 weeks
embedding
NOD^{scid} male mouse
(8 – 10 weeks old;
immuno-deficient)
In vivo CT scan
Ex vivo CT scan
section
Bone matrix containing
3D scaffolds
4 groups of mice:
hMSC-shControl
hMSC-shCtr9#3
hMSC-shCtr9#5
Mock
BCIP/NBT substrate staining
Alizarin Red S staining
Von-Koss Calcium staining
Osteocalcin ELISA
Histology
Multiphoton Confocal
TriZol RNA extraction
B.
4 weeks
8 weeks
Mock
shControl
shCTR9#3
shCTR9#5
Mineral Density
Low
High
Region of 3D scaffold
C.
Volume (mm^3) of Calcification
2.5
2.0
1.5
1.0
0.5
0.01
0.00
p = 0.013
p = 0.018
p = 0.021
p = 0.014
4 weeks
8 weeks
Mock
shControl
shCTR9#3
shCTR9#5
Scaffold mineral density (mg/cm^3)
200.0
150.0
100.0
50.0
p = 0.027
p = 0.007
shControl
shCTR9#3
shCTR9#5

Figure 3-4.

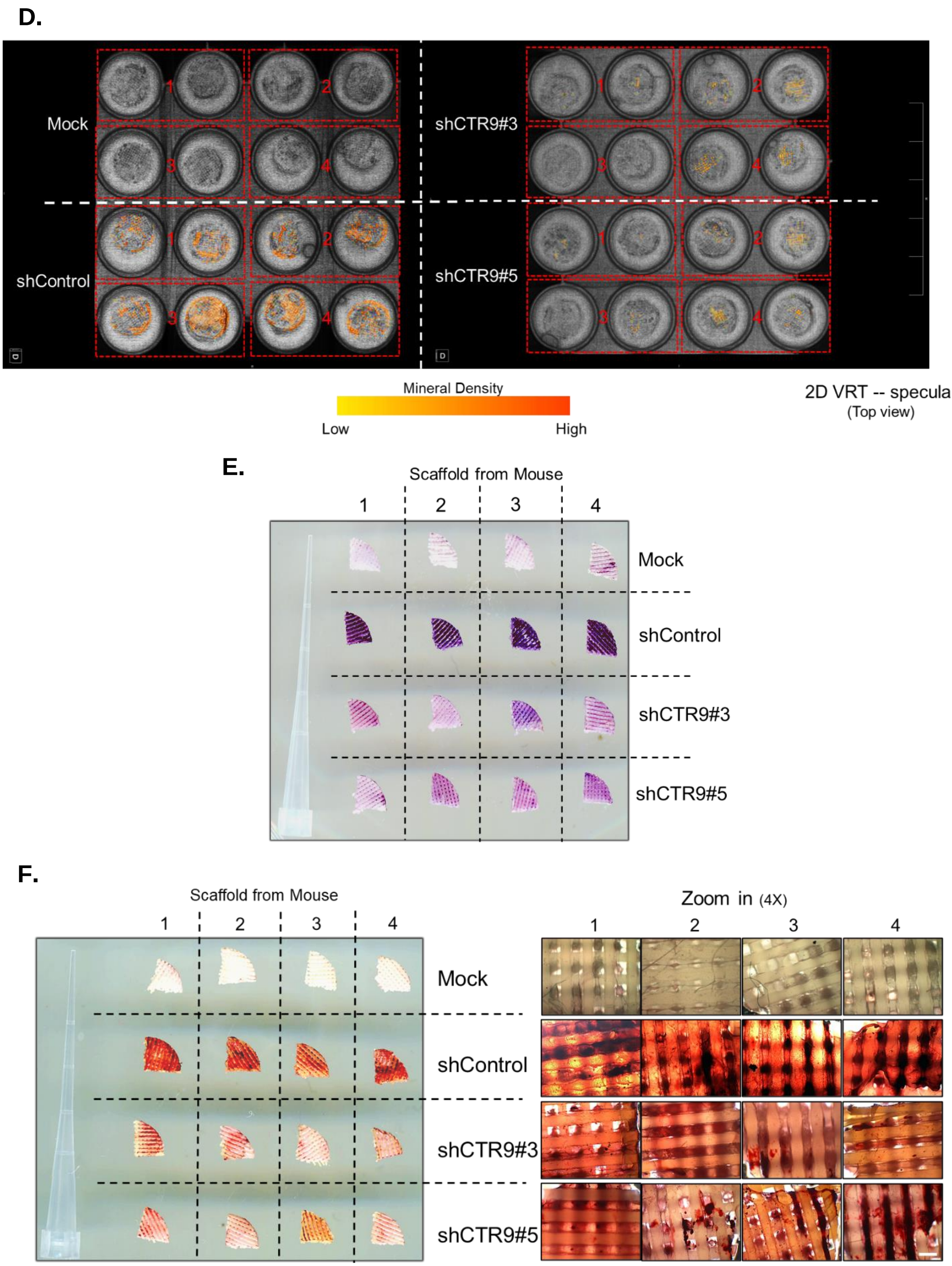
D.
Mock
shCTR9#3
shControl
shCTR9#5
1
2
3
4
Mineral Density
Low
High
2D VRT -- specular
(Top view)
E.
Scaffold from Mouse
1
2
3
4
Mock
shControl
shCTR9#3
shCTR9#5
F.
Scaffold from Mouse
1
2
3
4
Mock
shControl
shCTR9#3
shCTR9#5
Zoom in (4X)
1
2
3
4

Figure 3-4.

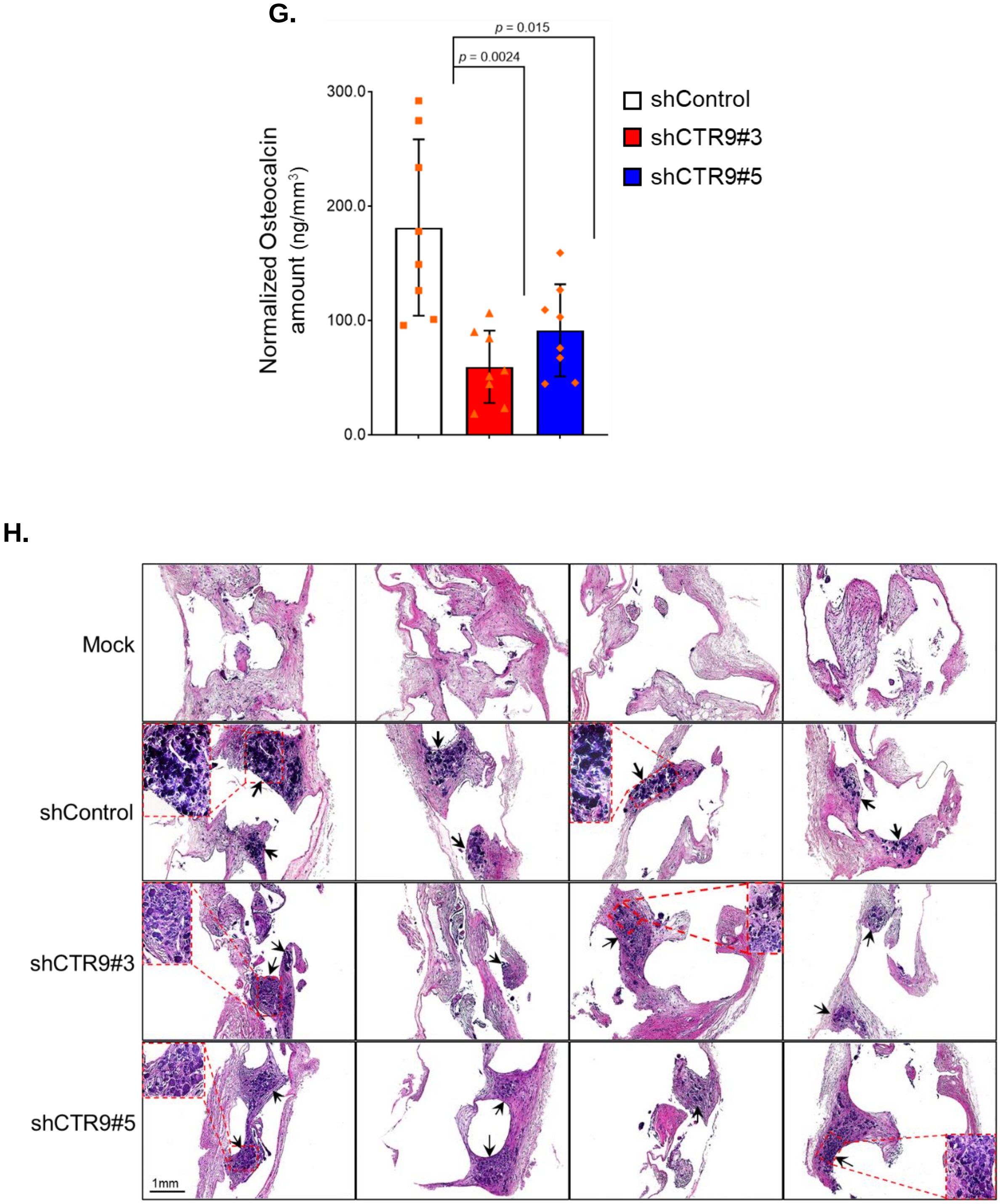
G.
p = 0.015
p = 0.0024
300.0
200.0
100.0
0.0
Normalized Osteocalcin amount (ng/mm^3)
□ shControl
🟥 shCTR9#3
🟦 shCTR9#5
H.
Mock
shControl
shCTR9#3
shCTR9#5
1mm

Figure 3-4.

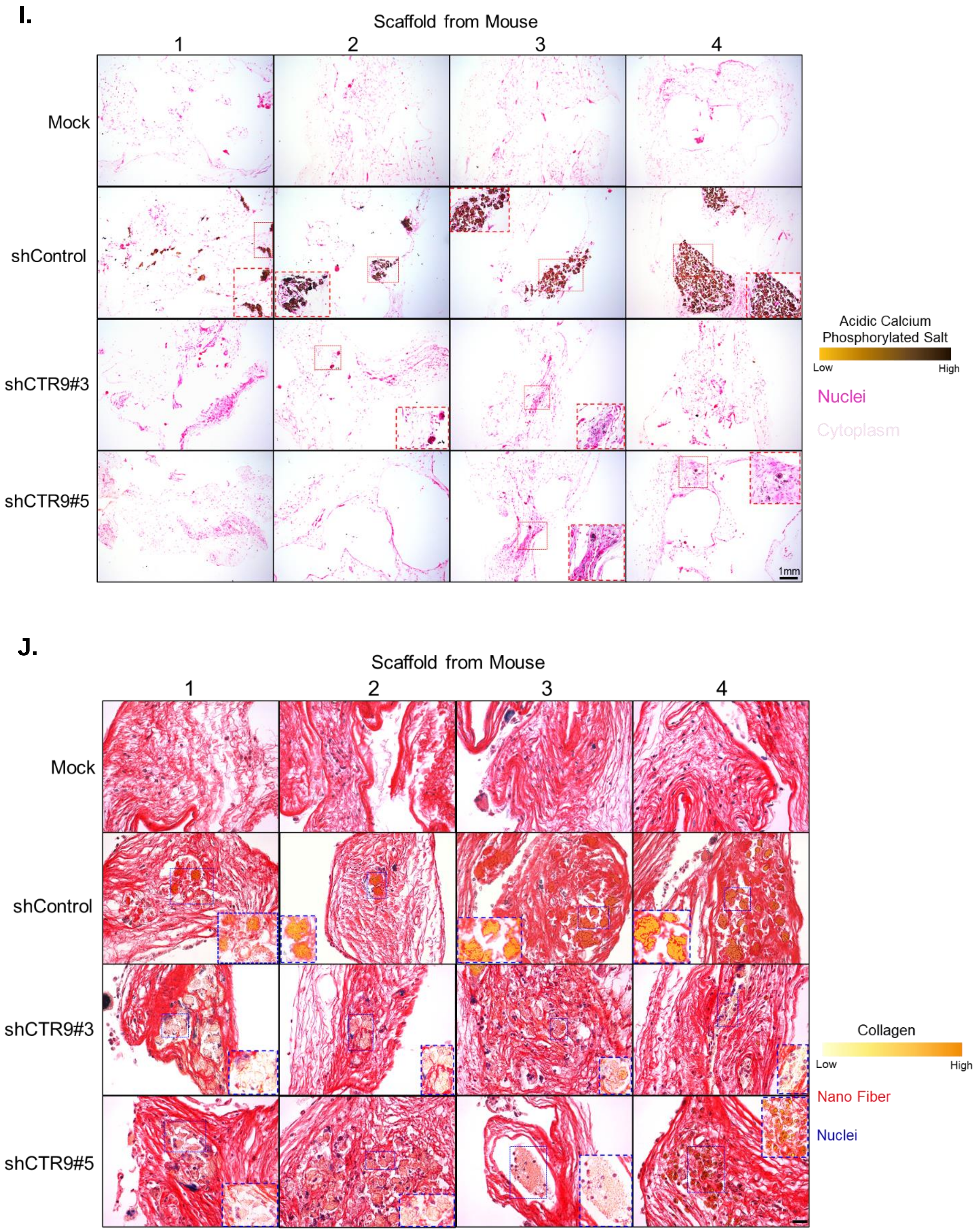
I.
Scaffold from Mouse
1
2
3
4
Mock
shControl
shCTR9#3
shCTR9#5
Acidic Calcium Phosphorylated Salt
Low
High
Nuclei
Cytoplasm
1mm
J.
Scaffold from Mouse
1
2
3
4
Mock
shControl
shCTR9#3
shCTR9#5
Collagen
Low
High
Nano Fiber
Nuclei

Figure 3-4.

K.

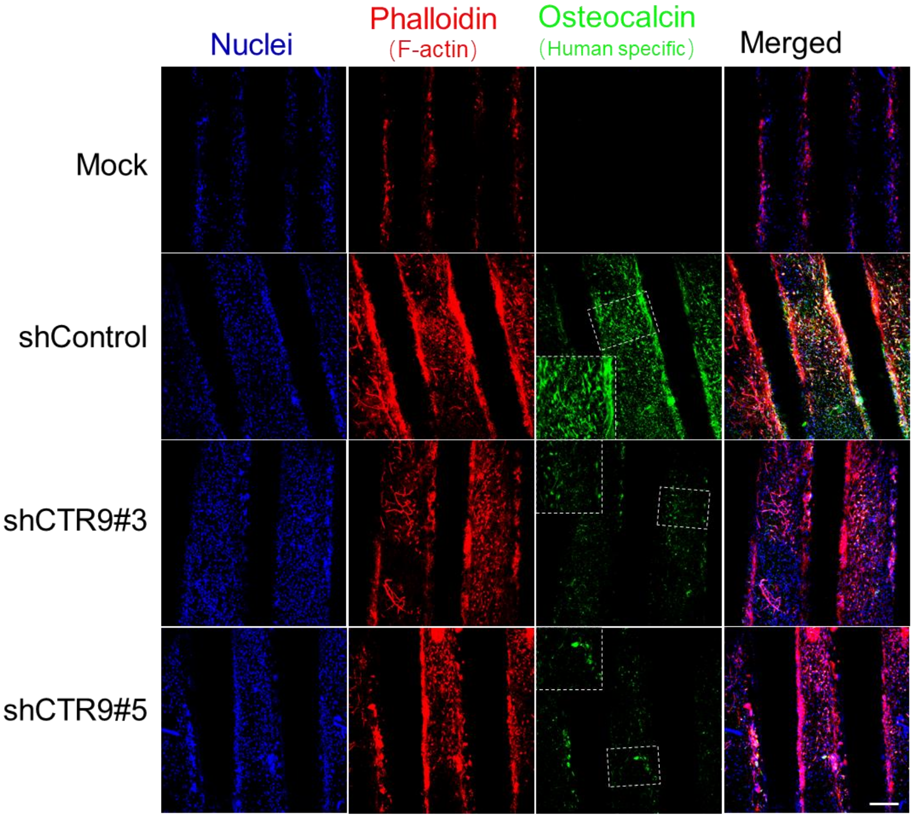
Nuclei
Phalloidin
(F-actin)
Osteocalcin
(Human specific)
Merged
Mock
shControl
shCTR9#3
shCTR9#5

Figure 3-4.

A. Schematic workflow for *in vivo* ectopic bone formation assay using mock, shControl, shCTR#3 or shCTR9#5 MSCs. In brief, cultured hMSCs were seeded on 3D PCL–FFF scaffolds and *pre* osteo-differentiate *in vitro* for 14 days followed by subcutaneous implantation into the dorsal surface of immuno-deficient mice (8-10 weeks old NOD^{scid} male mice) (n=4). After 4-8 weeks of implantation, whole mice were subjected to *in vivo* CT scanning. The embedded 3D PCL scaffolds were then harvested and subjected to *ex vivo* CT scanning. Additional analyses such as Alizarin Red S staining and histology were performed with a quarter-section of the 3D scaffolds.

B. Representative *in vivo* CT images of ectopic bone formation (38) on implanted 3D scaffolds in 3D MIP view after 4- or 8-week implantation. ShControl or shCTR9 hMSCs (shCTR9#3/shCTR9#5) were seeded on scaffolds before implantation. Blank 3D scaffolds (mock) serve as negative controls. Scale bars were shown at the right side of each image.

C. (*Left*) Scatter dot plot showing the calculated volume (mm^3) of calcification within the implanted 3D scaffolds of each group derived from *in vivo* CT scanning. Data are depicted in means ± SD (n=8). 2 tailed t-test *p*-value were shown. (*Right*) Box plot showing the converted mineral density (mg/cm^3) of calcification within the implanted 3D scaffolds of each group derived from *in vivo* CT scanning. Box and whiskers depict 5-95 percentile, and error lines depict the min to max (n=8). Mean was labeled with “+”. 2 tailed t-test *p*-value were shown.

D. Representative 2D VRT view of *ex vivo* CT images of 3D PCL scaffolds. Mineral density of calcification is shown in lava spectrum in each scaffold. Scale bar was shown on the right. Scaffolds from different mice in different groups were highlighted with red or white dash lined rectangles.

E. Alkaline phosphatase activity staining in quarterly sectioned scaffolds seeded with shControl or shCTR9 hMSCs after 8 weeks of implantation in mice. Mock group serves as a background control. 10µl tip at the left serves as the scale bar in the integral view.

F. Integral photographs (*Left*) or zoom-in stereomicrographs (*Right*) of calcium matrix-deposition staining (Alizarin Red S) for osteogenesis in quarterly sectioned scaffolds seeded with shControl or shCTR9 hMSCs after 8 weeks of implantation in mice. Mock group serves as a background control. Scale bar in zoom in view applied to all images. 10µl tip at the left serves as the scale bar in the integral view.

G. Quantification of osteocalcin expression by ELISA in quarter sectioned scaffolds seeded with shControl or shCTR9 hMSCs after 8 weeks of implantation in mice. Mock group serves as a background control. Data were pre-normalized with respective dry weight of 3D scaffolds and presented as mean ± SD (n=8). 2 tailed t-test *p*-value with Welch correction were shown.

H. Representative H&E staining on 3D scaffolds after 8 weeks of implantation. Calcification spots were depicted with black arrowheads. Scale bar applied to all images.

I. Representative Von-Kossa staining on 3D scaffolds after 8 weeks of implantation. Areas with high calcification were highlighted in zoomed dash-boxes. Scale bar applied to all images.

J. Representative images of Von-Kossa staining on 3D scaffolds after 8 weeks of implantation. Areas with clustered collagen enrichment were highlighted in zoomed dash-boxes. Scale bar applied to all images.

K. Fluorescence confocal micrographs (10x) of scaffolds seeded with shControl or shCTR9 hMSCs after 8 weeks of implantation in mice. Mock group serves as a background control. Nuclei were stained in blue (Hoechst 33342), and F-actin were stained in red (Alexa Fluor 555 – Phalloidin). Human specific osteocalcin was shown in green. Images were shown in 2D MIP view (Z-range: 400-500um). Scale bar applied to all images.

Figure 3-5.

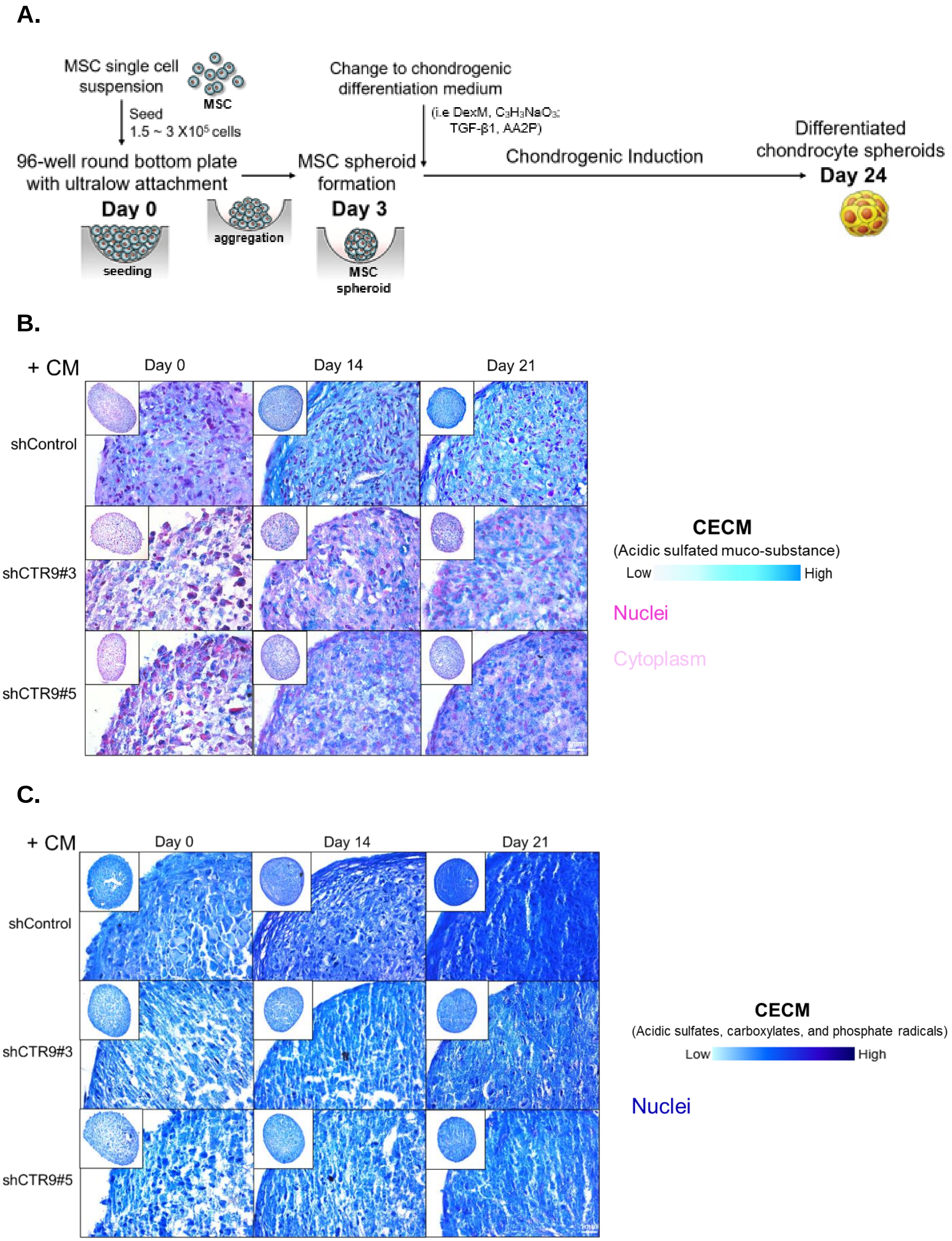
A.
MSC single cell suspension
MSC
Seed
1.5 ~ 3 X10^5 cells
96-well round bottom plate with ultralow attachment
Day 0
seeding
aggregation
MSC spheroid formation
Day 3
MSC spheroid
Change to chondrogenic differentiation medium
(i.e DexM, $C_3H_3NaO_3$;
TGF-β1, AA2P)
Chondrogenic Induction
Differentiated chondrocyte spheroids
Day 24
B.
+ CM
Day 0
Day 14
Day 21
shControl
shCTR9#3
shCTR9#5
CECM
(Acidic sulfated muco-substance)
Low
High
Nuclei
Cytoplasm
C.
+ CM
Day 0
Day 14
Day 21
shControl
shCTR9#3
shCTR9#5
CECM
(Acidic sulfates, carboxylates, and phosphate radicals)
Low
High
Nuclei

Figure 3-5.

A. Schematic workflow of chondrogenic induction of hMSCs.
B. Representative images of Alcian Blue (pH2.5) staining on 3D spheroids of shControl or shCTR9 hMSCs (shCTR9#3/#5) after 0-21 days of chondrogenic induction. Extracellular Cartilage Matrix was stained in light blue. Nuclei were stained in pink, and cytoplasm were stained in pale pink.
C. Representative images of Toluidine blue staining of 3D spheroids of shControl and shCTR9 hMSCs (shCTR9#3/#5) after 0-21 days of chondrogenic induction. Extracellular Cartilage Matrix was stained in dark blue. Nuclei were stained in violet blue.

Figure 3-6.

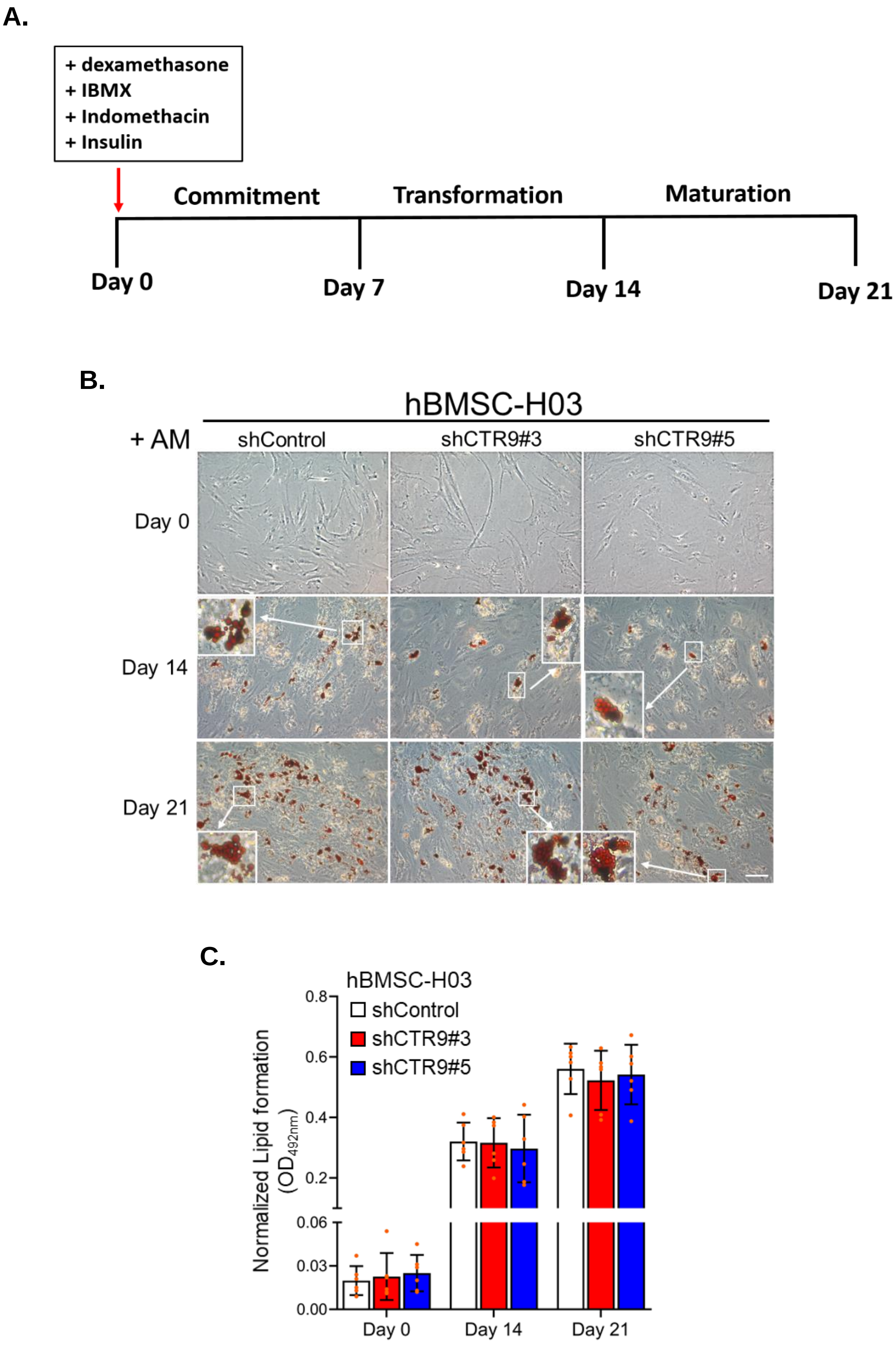
A.
+ dexamethasone
+ IBMX
+ Indomethacin
+ Insulin
Commitment
Transformation
Maturation
Day 0
Day 7
Day 14
Day 21
B.
hBMSC-H03
+ AM
shControl
shCTR9#3
shCTR9#5
Day 0
Day 14
Day 21
C.
hBMSC-H03
shControl
shCTR9#3
shCTR9#5
Normalized Lipid formation
(OD_{492nm})
0.8
0.6
0.4
0.2
0.06
0.03
0.00
Day 0
Day 14
Day 21

Figure 3-6.

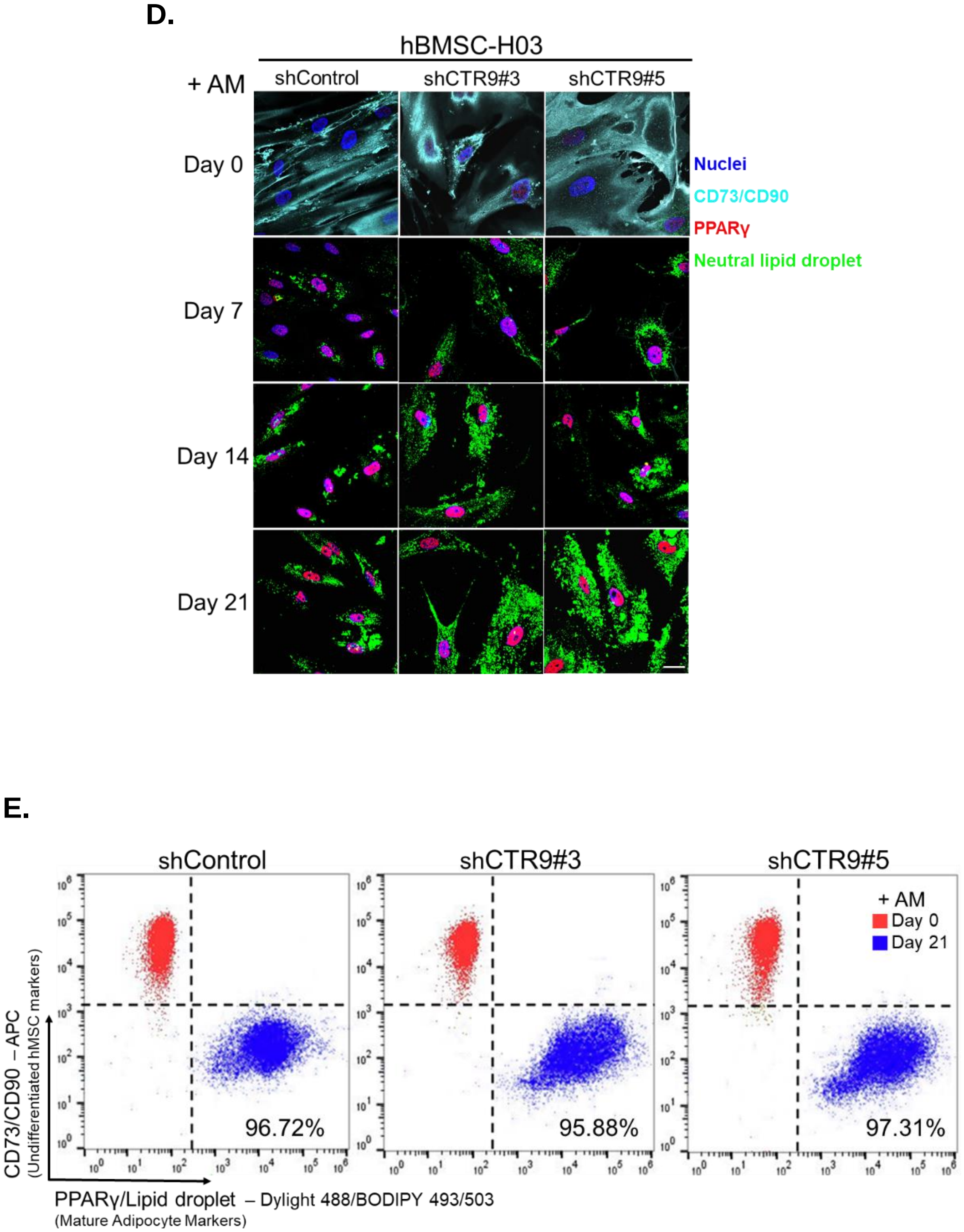
D.
hBMSC-H03
+ AM
shControl
shCTR9#3
shCTR9#5
Day 0
Day 7
Day 14
Day 21
Nuclei
CD73/CD90
PPARγ
Neutral lipid droplet
E.
shControl
shCTR9#3
shCTR9#5
+ AM
Day 0
Day 21
96.72%
95.88%
97.31%
CD73/CD90 – APC
(Undifferentiated hMSC markers)
PPARγ/Lipid droplet – Dylight 488/BODIPY 493/503
(Mature Adipocyte Markers)

Figure 3-6.

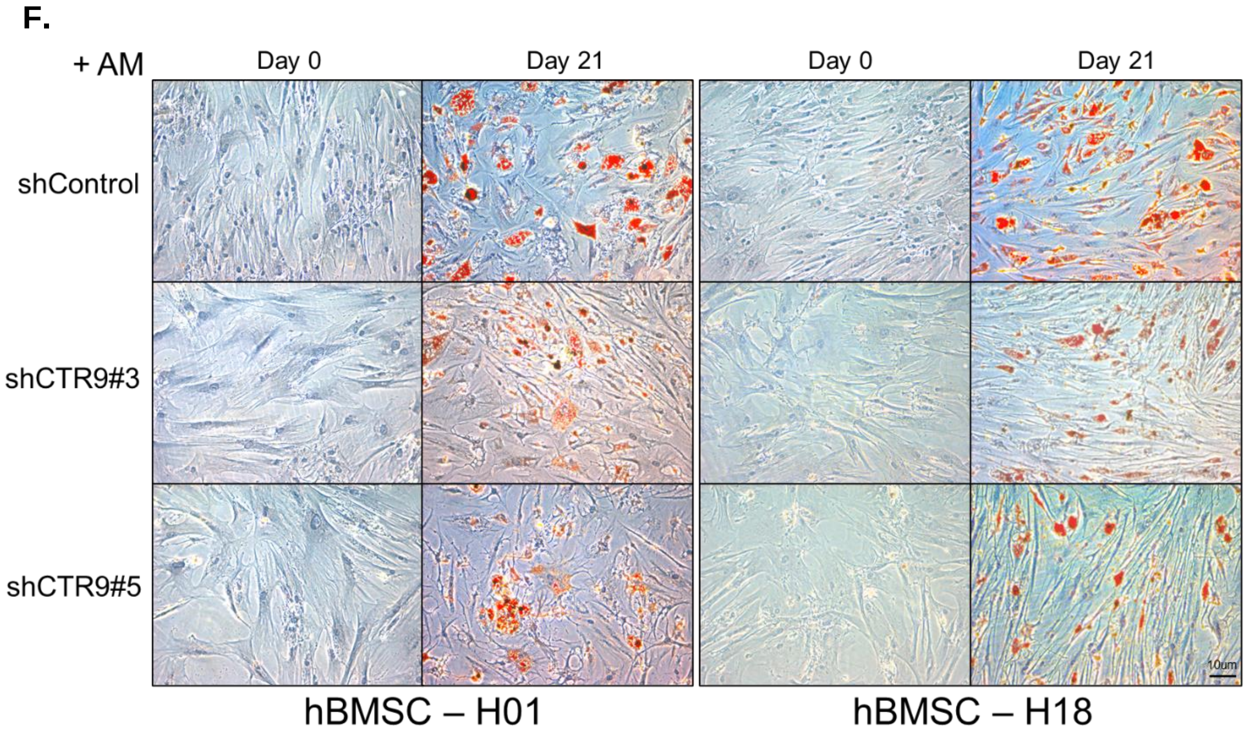
F.
+ AM
Day 0
Day 21
Day 0
Day 21
shControl
shCTR9#3
shCTR9#5
10um
hBMSC – H01
hBMSC – H18

Figure 3-6.

A. Schematic workflow of adipogenic induction of hMSCs *in vitro*.
B. Representative images showing the lipid vesicles formation with Oil Red O staining (39) on shControl or shCTR9 hMSCs (shCTR9#3/#5) after 0-21 days of adipogenic induction. (AM: adipogenic induction medium)
C. Quantification of lipid vesicles measured by OD_{492nM} absorbance normalized with respective DNA content. Data are represented as mean ± SD (n=3).
D. Immuno-fluorescence imaging of undifferentiated hMSCs markers CD73/CD90 (Cyan), adipogenic differentiated MSCs markers PPARγ (39), as well as neutral lipid droplets (Green) in shControl or shCTR9 hMSCs (shCTR9#3/#5) after 0 - 21 days of adipogenic induction. Nucleus were stained by Hoechst 33342 in blue.
E. Flow cytometry analyses of CD73/CD90 and PPARγ/Lipid droplet in shControl or shCTR9 hMSCs (shCTR9#3/#5) after 0 - 21 days of adipogenic induction.
F. Representative images showing the lipid vesicles formation with Oil Red O staining (39) of shControl or shCTR9 hMSCs (shCTR9#3/#5) derived from different donors (H01/H18) after 0-21 days of adipogenic induction.

Figure 3-7.

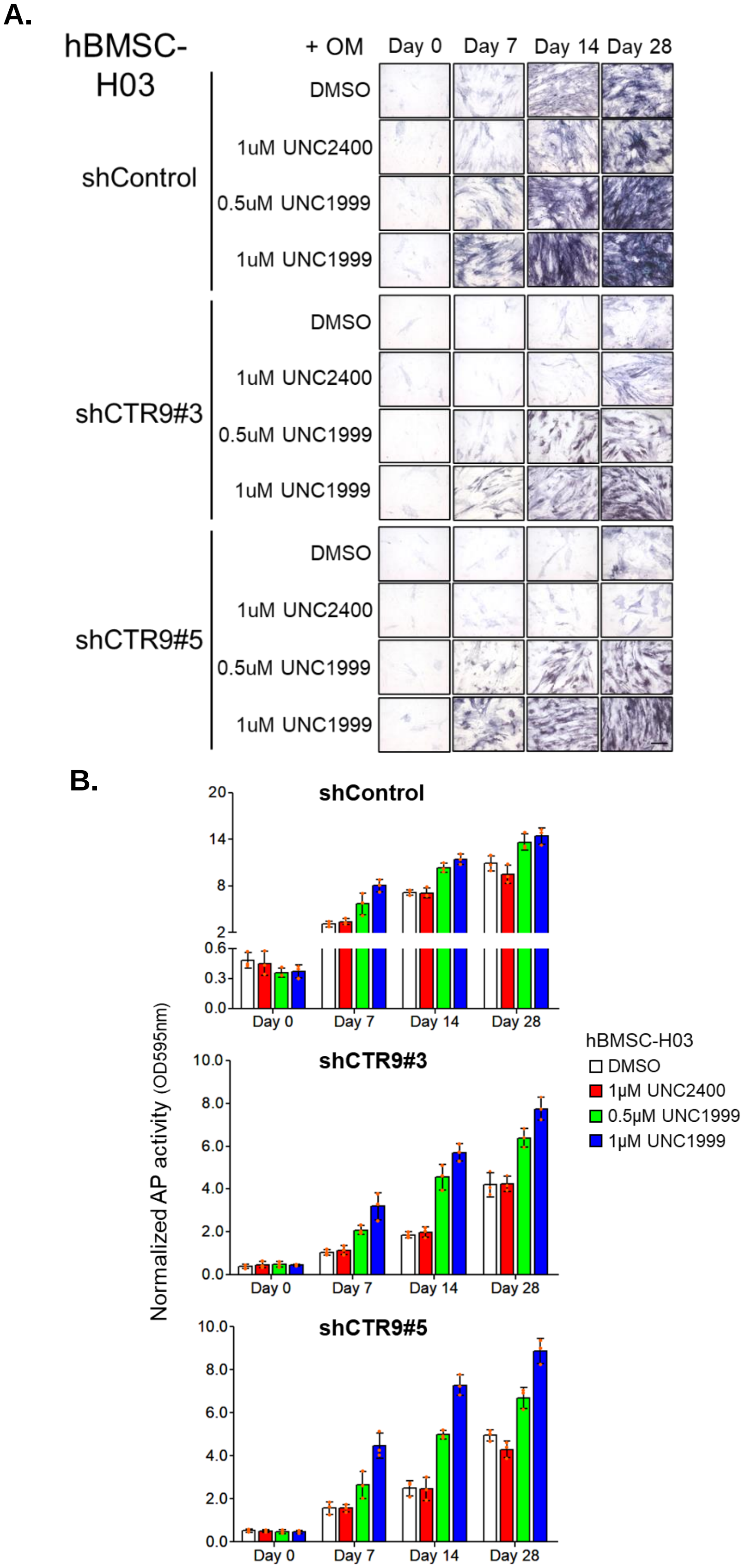
A.
hBMSC-H03
+ OM
Day 0
Day 7
Day 14
Day 28
shControl
shCTR9#3
shCTR9#5
DMSO
1uM UNC2400
0.5uM UNC1999
1uM UNC1999
B.
shControl
shCTR9#3
shCTR9#5
Normalized AP activity (OD595nm)
20
14
8
2
0.6
0.3
0.0
10.0
8.0
6.0
4.0
2.0
0.0
Day 0
Day 7
Day 14
Day 28
hBMSC-H03
□ DMSO
🟥 1μM UNC2400
🟩 0.5μM UNC1999
🟦 1μM UNC1999

Figure 3-7.

A. Representative images showing the Alkaline phosphatase (AP) activity-associated BCIP-NBT staining (violet blue) on shControl or shCTR9 hMSCs (shCTR9#3/#5) treated with DMSO, 1uM UNC2400 or 0.5uM/1uM UNC1999 during 0 - 28 days of osteogenic induction.
B. Quantification of AP activity (right) by OD_{595nM} absorbance normalized with respective DNA content. Data are represented as mean ± SD (n=3).

3.7 REFERENCES

1. Grijzenhout, A., Godwin, J., Koseki, H., Gdula, M.R., Szumska, D., McGouran, J.F., Bhattacharya, S., Kessler, B.M., Brockdorff, N. and Cooper, S. (2016) Functional analysis of AEBP2, a PRC2 Polycomb protein, reveals a Trithorax phenotype in embryonic development and in ESCs. *Development*, **143**, 2716-2723.
2. Feng, J., Mantesso, A., De Bari, C., Nishiyama, A. and Sharpe, P.T. (2011) Dual origin of mesenchymal stem cells contributing to organ growth and repair. *Proc Natl Acad Sci U S A*, **108**, 6503-6508.
3. Marquez-Curtis, L.A., Janowska-Wieczorek, A., McGann, L.E. and Elliott, J.A. (2015) Mesenchymal stromal cells derived from various tissues: Biological, clinical and cryopreservation aspects. *Cryobiology*, **71**, 181-197.
4. Owen, M. and Friedenstein, A.J. (1988) Stromal stem cells: marrow-derived osteogenic precursors. *Ciba Found Symp*, **136**, 42-60.
5. Maleki, M., Ghanbarvand, F., Reza Behvarz, M., Ejtemaei, M. and Ghadirkhomi, E. (2014) Comparison of mesenchymal stem cell markers in multiple human adult stem cells. *Int J Stem Cells*, **7**, 118-126.
6. Sarugaser, R., Hanoun, L., Keating, A., Stanford, W.L. and Davies, J.E. (2009) Human mesenchymal stem cells self-renew and differentiate according to a deterministic hierarchy. *PLoS One*, **4**, e6498.
7. Sheng, G. (2015) The developmental basis of mesenchymal stem/stromal cells (MSCs). *BMC Dev Biol*, **15**, 44.
8. Song, L. and Tuan, R.S. (2004) Transdifferentiation potential of human mesenchymal stem cells derived from bone marrow. *FASEB J*, **18**, 980-982.
9. Hoshiba, T., Kawazoe, N. and Chen, G. (2012) The balance of osteogenic and adipogenic differentiation in human mesenchymal stem cells by matrices that mimic stepwise tissue development. *Biomaterials*, **33**, 2025-2031.
10. Choi, H., Kim, T.H., Yang, S., Lee, J.C., You, H.K. and Cho, E.S. (2017) A Reciprocal Interaction between beta-Catenin and Osterix in Cementogenesis. *Sci Rep*, **7**, 8160.
11. Bennett, C.N., Hodge, C.L., MacDougald, O.A. and Schwartz, J. (2003) Role of Wnt10b and C/EBPα in spontaneous adipogenesis of 243 cells. *Biochemical and Biophysical Research Communications*, **302**, 12-16.
12. Jang, W.G., Kim, E.J., Kim, D.K., Ryoo, H.M., Lee, K.B., Kim, S.H., Choi, H.S. and Koh, J.T. (2012) BMP2 protein regulates osteocalcin expression via Runx2-mediated Atf6 gene transcription. *J Biol Chem*, **287**, 905-915.
13. Villanueva, F., Araya, H., Briceno, P., Varela, N., Stevenson, A., Jerez, S., Tempio, F., Chnaiderman, J., Perez, C., Villarroel, M. *et al.* (2019) The cancer-related transcription factor RUNX2 modulates expression and secretion of the matricellular protein osteopontin in osteosarcoma cells to promote adhesion to endothelial pulmonary cells and lung metastasis. *J Cell Physiol*, **234**, 13659-13679.
14. Madsen, M.S., Siersbaek, R., Boergesen, M., Nielsen, R. and Mandrup, S. (2014) Peroxisome proliferator-activated receptor gamma and C/EBPalpha synergistically activate key metabolic adipocyte genes by assisted loading. *Mol Cell Biol*, **34**, 939-954.

15. Ge, C., Cawthorn, W.P., Li, Y., Zhao, G., Macdougald, O.A. and Franceschi, R.T. (2016) Reciprocal Control of Osteogenic and Adipogenic Differentiation by ERK/MAP Kinase Phosphorylation of Runx2 and PPARgamma Transcription Factors. *J Cell Physiol*, **231**, 587-596.
16. Jeon, M.J., Kim, J.A., Kwon, S.H., Kim, S.W., Park, K.S., Park, S.W., Kim, S.Y. and Shin, C.S. (2003) Activation of peroxisome proliferator-activated receptor-gamma inhibits the Runx2-mediated transcription of osteocalcin in osteoblasts. *J Biol Chem*, **278**, 23270-23277.
17. Han, Y., Kim, C.Y., Cheong, H. and Lee, K.Y. (2016) Osterix represses adipogenesis by negatively regulating PPARgamma transcriptional activity. *Sci Rep*, **6**, 35655.
18. Wang, L., Xu, S., Lee, J.E., Baldridge, A., Grullon, S., Peng, W. and Ge, K. (2013) Histone H3K9 methyltransferase G9a represses PPARgamma expression and adipogenesis. *EMBO J*, **32**, 45-59.
19. Dudakovic, A., Evans, J.M., Li, Y., Middha, S., McGee-Lawrence, M.E., van Wijnen, A.J. and Westendorf, J.J. (2013) Histone deacetylase inhibition promotes osteoblast maturation by altering the histone H4 epigenome and reduces Akt phosphorylation. *J Biol Chem*, **288**, 28783-28791.
20. Rojas, A., Sepulveda, H., Henriquez, B., Aguilar, R., Opazo, T., Nardocci, G., Bustos, F., Lian, J.B., Stein, J.L., Stein, G.S. *et al.* (2019) Mll-COMPASS complexes mediate H3K4me3 enrichment and transcription of the osteoblast master gene Runx2/p57 in osteoblasts. *J Cell Physiol*, **234**, 6244-6253.
21. Sepulveda, H., Aguilar, R., Prieto, C.P., Bustos, F., Aedo, S., Lattus, J., van Zundert, B., Palma, V. and Montecino, M. (2017) Epigenetic Signatures at the RUNX2-P1 and Sp7 Gene Promoters Control Osteogenic Lineage Commitment of Umbilical Cord-Derived Mesenchymal Stem Cells. *J Cell Physiol*, **232**, 2519-2527.
22. Cao, Y., Li, L. and Fan, Z. (2021) The role and mechanisms of polycomb repressive complex 2 on the regulation of osteogenic and neurogenic differentiation of stem cells. *Cell Prolif*, **54**, e13032.
23. Wei, Y., Chen, Y.H., Li, L.Y., Lang, J., Yeh, S.P., Shi, B., Yang, C.C., Yang, J.Y., Lin, C.Y., Lai, C.C. *et al.* (2011) CDK1-dependent phosphorylation of EZH2 suppresses methylation of H3K27 and promotes osteogenic differentiation of human mesenchymal stem cells. *Nat Cell Biol*, **13**, 87-94.
24. Hemming, S., Cakouros, D., Isenmann, S., Cooper, L., Menicanin, D., Zannettino, A. and Gronthos, S. (2014) EZH2 and KDM6A act as an epigenetic switch to regulate mesenchymal stem cell lineage specification. *Stem Cells*, **32**, 802-815.
25. Dudakovic, A., Samsonraj, R.M., Paradise, C.R., Galeano-Garces, C., Mol, M.O., Galeano-Garces, D., Zan, P., Galvan, M.L., Hevesi, M., Pichurin, O. *et al.* (2020) Inhibition of the epigenetic suppressor EZH2 primes osteogenic differentiation mediated by BMP2. *J Biol Chem*, **295**, 7877-7893.
26. Yang, D., Okamura, H., Teramachi, J. and Haneji, T. (2015) Histone demethylase Utx regulates differentiation and mineralization in osteoblasts. *J Cell Biochem*, **116**, 2628-2636.
27. Wang, L., Jin, Q., Lee, J.E., Su, I.H. and Ge, K. (2010) Histone H3K27 methyltransferase Ezh2 represses Wnt genes to facilitate adipogenesis. *Proc Natl Acad Sci U S A*, **107**, 7317-7322.

28. Zhang, K., Haversat, J.M. and Mager, J. (2013) CTR9/PAF1c regulates molecular lineage identity, histone H3K36 trimethylation and genomic imprinting during preimplantation development. *Dev Biol*, **383**, 15-27.
29. Onal, P., Grun, D., Adamidi, C., Rybak, A., Solana, J., Mastrobuoni, G., Wang, Y., Rahn, H.P., Chen, W., Kempa, S. *et al.* (2012) Gene expression of pluripotency determinants is conserved between mammalian and planarian stem cells. *EMBO J*, **31**, 2755-2769.
30. Aaronson, Y., Livyatan, I., Gokhman, D. and Meshorer, E. (2016) Systematic identification of gene family regulators in mouse and human embryonic stem cells. *Nucleic Acids Res*, **44**, 4080-4089.
31. Wen, Y., Guo, X., Hao, J., Xiao, X., Wang, W., Wu, C., Wang, S., Yang, T., Shen, H., Chen, X. *et al.* (2016) Integrative analysis of genome-wide association studies and gene expression profiles identified candidate genes for osteoporosis in Kashin-Beck disease patients. *Osteoporos Int*, **27**, 1041-1046.
32. <Integrated transcriptomic, phenotypic, and functional study reveals tissue-specific immune properties of mesenchymal stromal cells.pdf>.
33. Hoemann, C.D., El-Gabalawy, H. and McKee, M.D. (2009) In vitro osteogenesis assays: influence of the primary cell source on alkaline phosphatase activity and mineralization. *Pathol Biol (Paris)*, **57**, 318-323.
34. Halbhuber, K.J., Krieg, R., Geidel, O. and Dietz, W. (2004) A modified Ce/Mg-BCIP-NBT formazan/indigoblue technique for demonstration of non-specific alkaline phosphatase activity. *Cell Mol Biol (Noisy-le-grand)*, **50 Online Pub**, OL507-514.
35. Basel, D. and Steiner, R.D. (2009) Osteogenesis imperfecta: recent findings shed new light on this once well-understood condition. *Genet Med*, **11**, 375-385.
36. Lattouf, R., Younes, R., Lutomski, D., Naaman, N., Godeau, G., Senni, K. and Changotade, S. (2014) Picrosirius red staining: a useful tool to appraise collagen networks in normal and pathological tissues. *J Histochem Cytochem*, **62**, 751-758.
37. Lin, X., Patil, S., Gao, Y.G. and Qian, A. (2020) The Bone Extracellular Matrix in Bone Formation and Regeneration. *Front Pharmacol*, **11**, 757.
38. Malaval, L., Modrowski, D., Gupta, A.K. and Aubin, J.E. (1994) Cellular expression of bone-related proteins during in vitro osteogenesis in rat bone marrow stromal cell cultures. *J Cell Physiol*, **158**, 555-572.
39. Reddy, B.Y., Greco, S.J., Patel, P.S., Trzaska, K.A. and Rameshwar, P. (2009) RE-1-silencing transcription factor shows tumor-suppressor functions and negatively regulates the oncogenic TAC1 in breast cancer cells. *Proc Natl Acad Sci U S A*, **106**, 4408-4413.
40. Nishimura, R., Hata, K., Matsubara, T., Wakabayashi, M. and Yoneda, T. (2012) Regulation of bone and cartilage development by network between BMP signalling and transcription factors. *J Biochem*, **151**, 247-254.
41. Jiang, Z., Von den Hoff, J.W., Torensma, R., Meng, L. and Bian, Z. (2014) Wnt16 is involved in intramembranous ossification and suppresses osteoblast differentiation through the Wnt/beta-catenin pathway. *J Cell Physiol*, **229**, 384-392.
42. Gregory, C.A., Gunn, W.G., Peister, A. and Prockop, D.J. (2004) An Alizarin red-based assay of mineralization by adherent cells in culture: comparison with cetylpyridinium chloride extraction. *Anal Biochem*, **329**, 77-84.

43. Zhou, X., von der Mark, K., Henry, S., Norton, W., Adams, H. and de Crombrugghe, B. (2014) Chondrocytes transdifferentiate into osteoblasts in endochondral bone during development, postnatal growth and fracture healing in mice. *PLoS Genet*, **10**, e1004820.
44. Jing, Y., Jing, J., Ye, L., Liu, X., Harris, S.E., Hinton, R.J. and Feng, J.Q. (2017) Chondrogenesis and osteogenesis are one continuous developmental and lineage defined biological process. *Sci Rep*, **7**, 10020.
45. Liu, Z., Xu, J., Colvin, J.S. and Ornitz, D.M. (2002) Coordination of chondrogenesis and osteogenesis by fibroblast growth factor 18. *Genes Dev*, **16**, 859-869.
46. Robert, A.W., Marcon, B.H., Dallagiovanna, B. and Shigunov, P. (2020) Adipogenesis, Osteogenesis, and Chondrogenesis of Human Mesenchymal Stem/Stromal Cells: A Comparative Transcriptome Approach. *Front Cell Dev Biol*, **8**, 561.
47. Merceron, C., Portron, S., Masson, M., Lesoeur, J., Fellah, B.H., Gauthier, O., Geffroy, O., Weiss, P., Guicheux, J. and Vinatier, C. (2011) The effect of two- and three-dimensional cell culture on the chondrogenic potential of human adipose-derived mesenchymal stem cells after subcutaneous transplantation with an injectable hydrogel. *Cell Transplant*, **20**, 1575-1588.
48. Markway, B.D., Tan, G.K., Brooke, G., Hudson, J.E., Cooper-White, J.J. and Doran, M.R. (2010) Enhanced chondrogenic differentiation of human bone marrow-derived mesenchymal stem cells in low oxygen environment micropellet cultures. *Cell Transplant*, **19**, 29-42.
49. Terry, D.E., Chopra, R.K., Ovenden, J. and Anastassiades, T.P. (2000) Differential use of Alcian blue and toluidine blue dyes for the quantification and isolation of anionic glycoconjugates from cell cultures: application to proteoglycans and a high-molecular-weight glycoprotein synthesized by articular chondrocytes. *Anal Biochem*, **285**, 211-219.
50. <TAZ, a Transcriptional Modulator of Mesenchymal Stem Cell Differentiation.pdf>.
51. Koopman, R., Schaart, G. and Hesselink, M.K. (2001) Optimisation of oil red O staining permits combination with immunofluorescence and automated quantification of lipids. *Histochem Cell Biol*, **116**, 63-68.
52. Thornton, S.R., Butty, V.L., Levine, S.S. and Boyer, L.A. (2014) Polycomb Repressive Complex 2 regulates lineage fidelity during embryonic stem cell differentiation. *PLoS One*, **9**, e110498.
53. Wang, D., Christensen, K., Chawla, K., Xiao, G., Krebsbach, P.H. and Franceschi, R.T. (1999) Isolation and characterization of MC3T3-E1 preosteoblast subclones with distinct in vitro and in vivo differentiation/mineralization potential. *J Bone Miner Res*, **14**, 893-903.
54. Yen, M.L., Chien, C.C., Chiu, I.M., Huang, H.I., Chen, Y.C., Hu, H.I. and Yen, B.L. (2007) Multilineage differentiation and characterization of the human fetal osteoblastic 1.19 cell line: a possible in vitro model of human mesenchymal progenitors. *Stem Cells*, **25**, 125-131.
55. Rauch, A., Haakonsson, A.K., Madsen, J.G.S., Larsen, M., Forss, I., Madsen, M.R., Van Hauwaert, E.L., Wiwie, C., Jespersen, N.Z., Tencerova, M. *et al.* (2019) Osteogenesis depends on commissioning of a network of stem cell transcription factors that act as repressors of adipogenesis. *Nat Genet*, **51**, 716-727.

56. Varshney, D., Lombardi, O., Schweikert, G., Dunn, S., Suska, O. and Cowling, V.H. (2018) mRNA Cap Methyltransferase, RNMT-RAM, Promotes RNA Pol II-Dependent Transcription. *Cell Rep*, **23**, 1530-1542.
57. Dudakovic, A., Camilleri, E.T., Xu, F., Riester, S.M., McGee-Lawrence, M.E., Bradley, E.W., Paradise, C.R., Lewallen, E.A., Thaler, R., Deyle, D.R. *et al.* (2015) Epigenetic Control of Skeletal Development by the Histone Methyltransferase Ezh2. *J Biol Chem*, **290**, 27604-27617.

Chapter 4

Conclusions, Discussion and Future Directions

4.1 Conclusions

My research focused on dissecting the role of CTR9 protein, the key scaffold protein of human RNA Polymerase Associated Factor Complex (hPAFc), in regulating transcriptional and epigenetic networks in breast cancer cells and human mesenchymal stem cells (hMSCs). Although additional investigation is required to elucidate how CTR9 modulates transcription and epigenetic states during breast tumorigenesis, as well as hMSCs lineage specification, the work presented in this dissertation provides a framework and valuable insights that could help advance research in these fields.

In Chapter 2, by using inducible CTR9 knockdown MCF7 cells (MCF7-tet-on-shCTR9) and several ER+ luminal breast cancer cell lines with CTR9 stably knocked down, we unmasked a novel role of CTR9 in governing the establishment of H3K27me3 repressive domains, beyond its well-characterized functions in transcriptional regulation and transcription-coupled histone modification (i.e., H2Bub, H3K4me3, H3K36me3). Proteomic quantification of histone modifications revealed a significant increase of H3K27me3 upon loss of CTR9. Global ChIP-RX analyses showed that loss of CTR9 induces a gradual reduction of H3K4me3 and H3K36me3 in gene bodies, followed by a genome-wide increase of H3K27me3 levels. This effect is likely attributed to the switch from the less potent PRC2 subtype, PRC2.2, to the more potent subtype, PRC2.1, which has higher H3K27me3 activity. Moreover, using 3xFlag tag knock-in MCF7 cells, we identified over 6,500 genes with putative Flag-CTR9 binding sites. Approximately 50% of these genes are subjected to epigenetic regulation by PRC2-H3K27me3. Consequently, CTR9 depletion generates vulnerability that renders breast cancer cells hypersensitive to PRC2 inhibitors. Collectively, our study in this chapter uncovers a unique mechanism by which a transcriptional elongation factor demarcates the PRC2-mediated H3K27me3 domains in breast cancer cells (Figure 4-1). This mechanism is likely conserved across cell types. Moreover, CTR9-dependent response to EZH2 inhibitors provides a therapeutic vulnerability for breast cancer treatment.

In Chapter 3, by employing similar loss/gain-of-function approaches, we evaluated the roles of CTR9 in regulating multiple aspects of hMSC biology, including viability, proliferation, basic stem cell properties, and importantly, multi-faceted lineage-specific differentiation. We discovered that CTR9 knockdown in hMSCs did not severely interfere with the viability, growth and stemness of hMSCs. Rather, loss of CTR9 impaired MSC differentiation to osteoblasts and chondrocytes while not affecting adipogenesis. Deletion of CTR9 in hMSCs resulted in delayed alkaline phosphatase activity, reduced osteocalcin secretion, incomplete extracellular calcium matrix formation and attenuated expression of osteoblast genes. In contrast, hMSCs with CTR9 KD did not affect lipid vesicle formation and activation of adipogenic markers. Inspection of osteogenic phenotypes by switching differentiation medium suggests that CTR9 expression is imperative for early commitment of hMSCs to osteo-lineage progenitors. Moreover, restoration of CTR9 expression partially rescued osteogenic defective phenotypes caused by CTR9 knockdown, whereas overexpression of CTR9 accelerated osteogenesis *in vitro*. Loss of CTR9 expression significantly reduced deposition and mineralization of bone matrix on ex vivo implanted 3D scaffolds, indicating that CTR9 is also essential for hMSC-derived bone formation *in vivo*. Lastly, EZH2 inhibitor UNC1999 partially rescued the osteogenic defects caused by CTR9 KD, suggesting that the PRC2-H3K27me3 axis is involved in CTR9-dependent osteogenic differentiation of hMSCs (Figure 4-2). These observations made in two different biological systems, breast cancer cells and hMSCs, collectively support the antagonisms between transcription coactivators and silencers in maintaining the epigenetic states required for lineage-specific differentiation.

4.2 Discussion

4.2.1. Transcriptional regulatory roles of CTR9 during evolution and beyond PAFc

The discoveries described in Chapter 2 and Chapter 3 provide an explanation for the discrepancy between the phenotypes observed in lower eukaryotes (i.e., yeast) and multicellular organisms when CTR9 is depleted. While CTR9 is not an essential gene in *S. cerevisiae* (1,2), CTR9 knockout causes early embryonic lethality in higher eukaryotic organisms such as Drosophila, zebrafish and mouse (3-5). CTR9-deficient mouse embryos exhibit significant defects in Inner Cell Mass (ICM) outgrowth and differentiation of the trophectoderm during the blastula stage, indicating that CTR9 is involved in maintaining chromatin states for cell fate specification (5). The CTR9 KO defects in preimplantation resemble the phenotypes resulting from knocking out the core PRC2 subunits SUZ12, EZH2 and EED in mice (6-8). While PRC2 and H3K27me3 play crucial roles in establishing repressive chromatin regions and safeguarding cell identity in multicellular organisms (9-11), neither PRC2, nor histone H3K27me3, exist in yeast (12). Therefore, our results might suggest a hypothesis that, while CTR9 regulates transcription across species, controlling PRC-repressive domains is a new function acquired over the course of evolution. We speculate that the embryonic lethality of CTR9-null metazoans is more likely attributed to deregulated H3K27me3 than transcription inhibition *per se.*

CTR9 is not among the 148 PRC2 interacting partners that are enriched in EZH2 and SUZ12 immunoprecipitants in ESCs (13). Therefore, the significantly elevated levels of PRC2.1 subunits and genome-wide distribution of H3K27me3 upon loss of CTR9 is unexpected, which implies that, despite no physical interaction with the PRC2 complex, CTR9 functionally antagonizes PRC2.

Our findings that CTR9 levels determine PRC2-mediated H3K27me3 levels and genomic distribution explain how chromatin is converted from transcriptionally active to repressive states when general transcription is disrupted. It is intriguing that while PAF1 and CTR9 are both required for overall PAFc integrity (14,15), silencing of CTR9, but not the other PAFc subunits, results in increased H3K27me3. Furthermore, our lab has previously reported that knocking down CTR9, but not PAF1, impairs estrogen signaling in breast cancer cells (2,16). This evidence supports PAFc-independent functions of CTR9, which is further substantiated by proteomic quantification of PAFc subunits in a CTR9Δ yeast strain. Yeast is estimated to have more than 200,000 molecules of CTR9, as compared to 20,000 molecules of other PAFc components per cell. Moreover, a CTR9Δ yeast strain tends to lose chromosomes at a high frequency, whereas the strains lacking PAF1 did not show this phenotype (2). Collectively, our results support that CTR9 has an autonomous transcriptional regulatory role outside of PAFc.

4.2.2. Functions of CTR9 in osteochondral lineage differentiation *in vivo*

The bone marrow-derived human MSCs that we used in Chapter 3 are postnatal stem cells that can differentiate to multiple skeletal tissues and myelo-supportive stroma, including osteoblasts/osteocytes, adipocytes, chondrocytes, and myocytes (17,18). MSC lineage determination is regulated by a complex network of signaling pathways such as WNT, Notch, BMP (19), and the expression of key lineage specific transcription factors (TFs). RUNX2/Osterix, PPARγ/C-EBPα, SOX9 are regarded as critical TFs driving hMSC differentiation to osteogenic, adipogenic and chondrogenic cells, respectively (20). The activation of these signaling pathways and transcription factors is dependent on the chromatin states, which determines either activation or suppression of lineage specific factors and their downstream targets. Therefore, it is important to identify epigenetic modifiers essential for the regulation of hMSC lineage specification.

The role of PRC2, in particular its core enzymatic subunit – EZH2, in MSC lineage specification has been well-documented. Overexpression of EZH2 in hMSCs is found to constrain osteogenic differentiation, whereas EZH2 knockdown or chemical inhibition of EZH2 methyltransferase activity promotes osteogenesis and inhibits adipogenesis (21-24). In addition to the *in vitro* evidence, dysregulation of PRC2-EZH2 also results in abnormal bone formation, skeletal maturation, and remodeling. Conditional EZH2 knockout in early limb bud mesenchyme results in defective skeletal patterning in mice due to dysregulation of HOX genes (25). Deletion of EZH2 in embryonic postnatal bone results in shorter limbs with decreased growth plate size, whereas the trabeculae patterning was promoted in long bones (26). These findings collectively suggest that EZH2 deficiency impacts the patterning and trabeculae microarchitecture, while promoting osteoblast differentiation and activity in long bones. Our collaborative work with Dr. Deneen Wellik’s laboratory showed that CTR9 is continuously expressed during the entire process of skeletal embryogenesis (Data not shown). Interestingly, the onset of CTR9 expression synchronizes with the reported emergence and expansion of an embryonic MSC-like population in the mesodermal fraction of early limb at E11.5 (27). Moreover, embryonic CTR9 colocalizes with HOX proteins only in authentic MSC progenitor cells possessing trilineage differentiation potential (Data not shown). PAFc/CTR9 has previously been shown to synergize with the MLL complex at HOX loci to promote leukemogenesis (28). Disruption of Hox11 gene function in mice leads to skeletal patterning defects (29,30), which resemble the bone phenotypes caused by EZH2 loss. These data support the role of CTR9 in skeletal development and postnatal bone remodeling *in vivo*. We posit that CTR9 at least partially functions in bone development by regulating PRC2-H3K27me3 activity and modulating HOX gene transcriptional activity. The skeletal-specific knockout of CTR9 using HOXA11-Cre-mediated targeting is in progress. Generation of this genetically engineered mouse model will facilitate tracing the spatial and dynamic expression of CTR9 in mesenchymal stem cells in early embryos.

4.3 Future Directions

4.3.1 Identification of CTR9 interacting partners in breast cancer cells

Tetratricopeptide repeat (TPR) domains are found in a large number of proteins and serve as protein-protein interaction modules (31). The human CTR9 protein contains 19 TPRs (residues 41-650), which form two antiparallel α-helices at the N terminus (32). Due to recent advances, tools including affinity-capture, proximity label mass spectrometry and in-silico prediction, and proteomic mapping have identified > 150 CTR9-interacting proteins to date in different biological systems (33,34). Although not all interacting partners are co-expressed with CTR9 in breast cancer cells, some may mediate PAFc-independent functions of CTR9 in regulating transcription and the epigenome in breast cancer cells.

To identify CTR9-interacting proteins in breast cancer cells, Dr. Gui Ma in the Xu lab has successfully knocked in a 3 X Flag epitope tag at the CTR9-endogenous locus in MCF7 cells, which can be used for pulling down CTR9-interacting proteins in MCF7 cells. Anti-Flag M2 beads will be incubated with nuclear extracts. Proteins will be eluted with Flag peptide, resolved by SDS-PAGE, visualized by silver staining, followed by in gel digestion for mass spectrometry analysis. The other PAFc subunits are expected to be pulled down by CTR9 and will serve as positive control. To visualize the presence of CTR9 in different complexes, the eluate will be fractionated on a Superdex 200 size-exclusion column. The putative CTR9 binding partners not in PAFc will be identified and validated by reciprocal Co-IP.

4.3.2 Delineate the requirement of CTR9 during normal mammary gland development

CTR9 is highly expressed in ER+ luminal breast cancer (BrCa) as compared to ER- BrCa. Using inducible and stable CTR9 knockdown (35) breast cancer cell lines, we have shown that loss of CTR9 led to reduction of >90% of estrogen responsive transcription. Furthermore, substantial growth inhibition and changes in morphology were observed in CTR9 KD luminal BrCa cells, accompanied by a decrease of ER protein (16,36), suggesting that CTR9 is essential for ER-dependent transcription and maintenance of luminal lineage. Since CTR9 regulates ER stability and ER is essential for mammary gland ductal structure formation (16,36), we predict that loss of CTR9 in mammary gland tissue affects normal development of breast, including lobule and duct formation.

To evaluate the role of CTR9 in mammary gland development, we will generate mammary gland-specific CTR9 KO mice by breeding CTR9 floxed mice with the MMTV-Cre strain where Cre expression is restricted to mammary epithelial cells. To examine if CTR9 is essential for mammary gland duct formation during puberty, mammary glands from MMTV-cre$^{+/-}$CTR9$^{f/f}$ and MMTV-Cre$^{+/-}$, CTR9$^{wt/wt}$ mice at 6-weeks (mid-puberty) and 12-weeks (adult) of age will be collected for a whole-mount assay and H&E staining as previously described (37). ImageJ will be used to count the number of ducts and acini (alveoli) and to measure the areas of ducts and acini (duct or acini coverage) on a tissue section. To evaluate the role of CTR9 in pregnancy-associated mammary gland branching and lobule formation, we will harvest mammary glands from CTR9 mammary-specific KO and control pregnant female mice on pregnancy day 7 and lactation day 2 to perform whole-mount assay.

Because CTR9 KD in BrCa cells resulted in a global increase of H3K27me3 peaks and intensities, CTR9 KO may affect mouse mammary gland development via controlling H3K27me3 levels and genomic distribution. To determine if CTR9 knockout causes global changes of H3K27me3 to influence the lineage-specific differentiation of mammary glands, we will first perform H3K27me3 IHC staining on mammary tissues from CTR9 KO and age matched control mice. The results will be informative as to whether CTR9 KO affects the levels of H3K27me3 in various cell types of mammary gland (i.e., ductal luminal cells, alveolar lactocytes, and basal myoepithelial cells). If CTR9 affects H3K27me3 in a specific cell population, we will sort cells by FACS and isolate chromatin for H3K27me3 ChIP-Rx to identify CTR9-regulated genes as described in Chapter 2. Second, we will extract total mRNA from the mammary epithelial cells of 12-week-old

Control and CTR9 KO mice to perform RNA-sequencing. Integrated analysis of H3K27me3 ChIP-Rx and RNA-seq will reveal the essential gene regulatory networks controlled by CTR9 during luminal lineage differentiation through epigenetic mechanism.

4.3.3 Determine whether CTR9 and H3K27me3 are predictive biomarkers for EZH2i sensitivity in ER+ BrCa

Although EZH2 is the sole mammalian enzyme catalyzing the formation of H3K27me3, expression levels of EZH2 does not correlate with abundance of H3K27me3 in two large-cohort studies (38,39), implying that EZH2 activity, rather than expression level *per se*, should be evaluated for designing EZH2 based epigenetic therapy. Our finding that CTR9 KD in ER+ BrCa cell lines resulted in increased H3K27me3 levels and enhanced sensitivity to EZH2 inhibitors lead to the hypothesis that CTR9-low tumors are addicted to H3K27me3 and are, therefore, sensitive to EZH2 inhibitors.

To determine if CTR9 knockdown cells also gain sensitivity to EZH2 inhibitors *in vivo*, we will use our previously generated CTR9 inducible knockdown MCF7 cell line for xenograft studies. We will test if Dox-induced CTR9 KD MCF7 cells gain sensitivity to EZH2 inhibitors *in vivo*. The commercially available EZH2 inhibitor UNC1999 and its negative paralog UNC2400 will be employed in this study. Another potent EZH2 inhibitor that was recently approved by FDA, tazemetostat (40,41), will also be included to optimize in vivo response. The global and genomic-loci specific increase of H3K27me3 will be measured by ChIP-Rx and correlated with gene expression changes in response to EZH2 inhibitor treatment. In addition, we will compare several ER+ PDX models (a generous gift from Alana Welm, University of Utah) with divergent CTR9 expression (High vs Median vs Low) to study the correlation of CTR9 levels with the sensitivity to EZH2 inhibitors. However, PDX tumors will potentially elicit heterogeneous responses towards EZH2 inhibitors which add additional complexity to correlating CTR9 levels and EZH2 inhibitor sensitivity. To overcome this hurdle, we will perform single cell RNA-seq of PDX tumors before and after EZH2 inhibitor treatment and analyze cell states and gene expression in clusters.

4.3.4 Assess the essentiality of CTR9 during skeletal development

In Chapter 3, we found that CTR9 is essential for hMSC-derived bone formation in the in vivo ectopic bone formation assay. However, the function of CTR9 in bone development at different embryonic stages is largely unknown. Genetically engineered mouse models are needed to elucidate the roles of CTR9 in skeletal development, postnatal bone remodeling, and MSC fate determination in vivo. Considering that the systematic knockout of CTR9 is an embryonic lethal in mice, inducible or conditional (mesenchyme or bone specific) CTR9 knockout mice are needed. To study the function of CTR9 in early skeletal patterning and lineage specification of bone marrow-derived mesenchymal cells, we will breed transgenic strains expressing CTR9 floxed (European Mouse Mutant Archive) with tamoxifen-inducible Cre recombinase under the control of the PRRX1 enhancer (CTR9$^{fl/fl:}$ As:Prx1CreER-GFP, Jackson) (42). PRRX1 is the primary marker of primitive mesenchyme which is responsible for early limb bud development and is thought to give rise to bone marrow stromal/stem cells (BMSCs) within the newly formed skeleton (43,44). We will compare control and CTR9 mesenchymal-specific KO mice for phenotypic measurements of early skeletal development (e.g., newborn limb patterning, trabecular bone microarchitecture and growth plates sizes) as well as examine the expression of osteogenic markers by IHC. The results will be informative as to whether CTR9 affects early bone development and homeostasis. Moreover, primary MSCs from the bone marrow of control or CTR9 KO mice will be subjected to *in vitro* adherent culture to compare osteogenic potential (i.e., BCIP/NBT substrate, Picrosirus Red, Alizarin Red S staining).

It is during the later stages of fetal development that bone formation, osteogenesis, and mineralization occur leading to the transformation of mesenchymal tissue into bone (45,46). To study the function of CTR9 in committed pre-osteoblasts, we will employ an inducible (Tet-off) Osx1-GFP::Cre (Osx-Cre) mouse line that targets osteoblasts or osteoblastic progenitors (47,48). Micro-computed tomography (micro-CT) will be performed to measure the structure of the skulls and clavicles, as well as volume and density of cortical bone and trabecular bone. Cartilage morphologies, which are associated with bone marrow adiposity (49,50) and growth plate size will be measured by histomorphology analysis using Von Kossa and Goldner’s trichrome staining of the distal femora. Moreover, we will isolate pre-committed osteoblastic progenitors as well as mature osteoblasts (GFP positive) from control and CTR9 KO mice for expansion and osteo-lineage differentiation *in vitro*.

4.4 Figure & Legends

Figure 4-1.

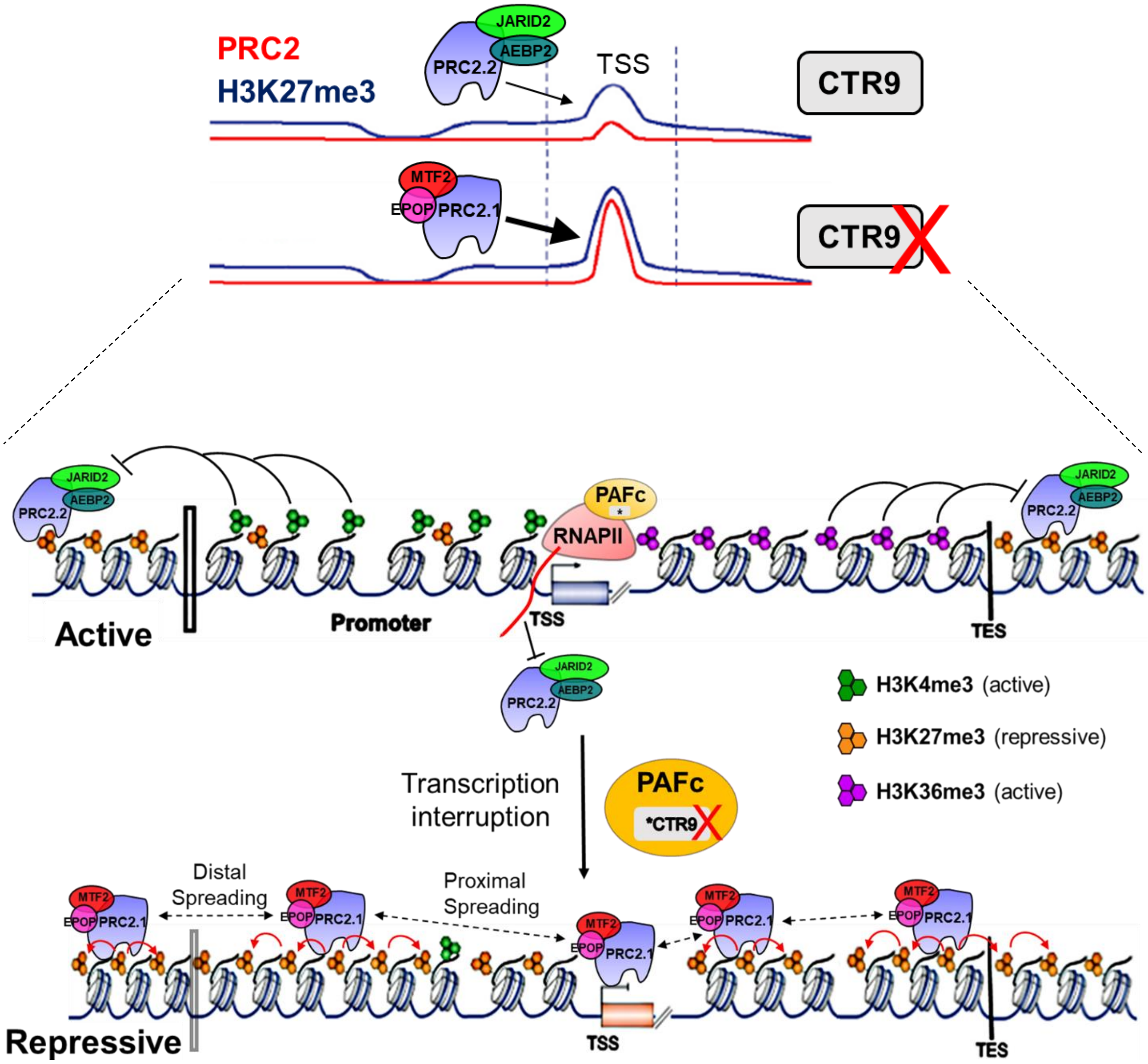

Figure 4-1.

Schematic model summarizing the novel function of CTR9 in refining the distribution of PRC2-mediated H3K27me3 repressive domains through modulating PRC2 subtypes balance in breast cancer cells and loss of CTR9 results in a genome-wide transition from transcriptional active to repressive state. Switch of predominant PRC2 subtypes from less active PRC2.2 to more active PRC2.1 accompanied with eviction of transcriptional active histone markers (i.e., H3K4me3/H3K36me3) facilitates the spreading of H3K27me3 repressive domains in both proximal and distal sites.

Figure 4-2.

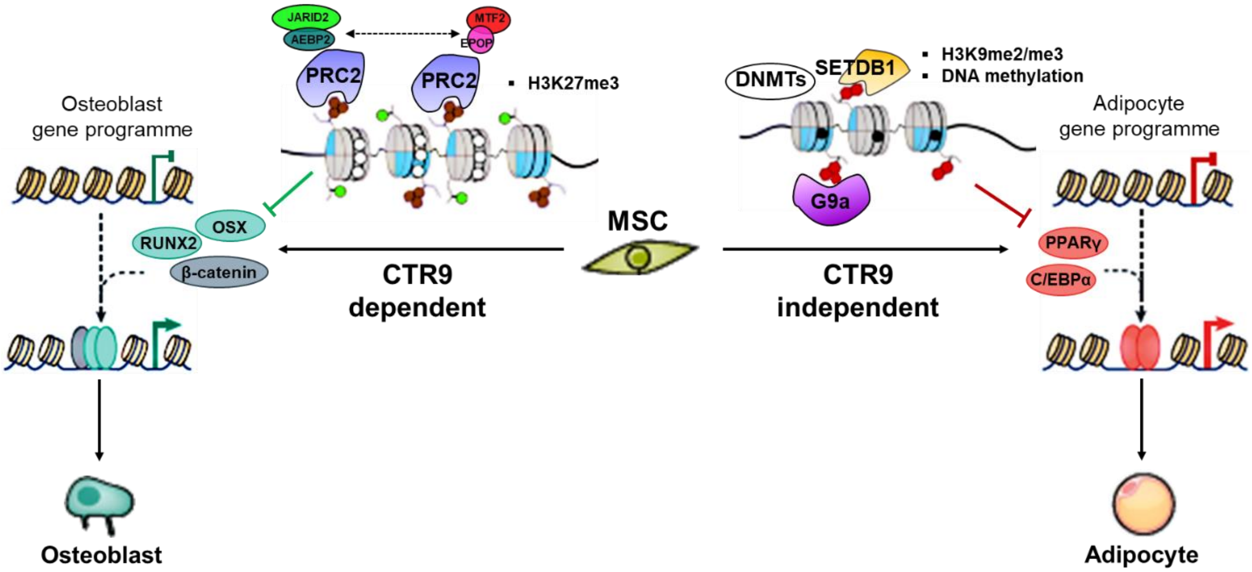

Figure 4-2.

A hypothesized model that CTR9 selectively regulates osteogenic differentiation over adipogenic differentiation by targeting H3K27me3 marks deposited at osteoblastic lineage transcription factors (i.e., RUNX2/OSX/β-catenin) whereas expression of adipogenic lineage transcription factors is regulated by H3K9 methylation and DNA methylation but not affected by H3K27me3, thus not affected by CTR9 levels.

4.5 Reference

1. Chen, S.L., Loffler, K.A., Chen, D., Stallcup, M.R. and Muscat, G.E. (2002) The coactivator-associated arginine methyltransferase is necessary for muscle differentiation: CARM1 coactivates myocyte enhancer factor-2. *J Biol Chem*, **277**, 4324-4333.
2. Massoni-Laporte, A., Perrot, M., Ponger, L., Boucherie, H. and Guieysse-Peugeot, A.L. (2012) Proteome analysis of a CTR9 deficient yeast strain suggests that Ctr9 has function(s) independent of the Paf1 complex. *Biochim Biophys Acta*, **1824**, 759-768.
3. Akanuma, T., Koshida, S., Kawamura, A., Kishimoto, Y. and Takada, S. (2007) Paf1 complex homologues are required for Notch-regulated transcription during somite segmentation. *EMBO Rep*, **8**, 858-863.
4. Chaturvedi, D., Inaba, M., Scoggin, S. and Buszczak, M. (2016) Drosophila CG2469 Encodes a Homolog of Human CTR9 and Is Essential for Development. *G3 (Bethesda)*, **6**, 3849-3857.
5. Zhang, K., Haversat, J.M. and Mager, J. (2013) CTR9/PAF1c regulates molecular lineage identity, histone H3K36 trimethylation and genomic imprinting during preimplantation development. *Dev Biol*, **383**, 15-27.
6. Cai, Q., Niu, H., Zhang, B., Shi, X., Liao, M., Chen, Z., Mo, D., He, Z., Chen, Y. and Cong, P. (2019) Effect of EZH2 knockdown on preimplantation development of porcine parthenogenetic embryos. *Theriogenology*, **132**, 95-105.
7. Ikeda, K., Ueda, T., Yamasaki, N., Nakata, Y., Sera, Y., Nagamachi, A., Miyama, T., Kobayashi, H., Takubo, K., Kanai, A. *et al.* (2016) Maintenance of the functional integrity of mouse hematopoiesis by EED and promotion of leukemogenesis by EED haploinsufficiency. *Sci Rep*, **6**, 29454.
8. Pasini, D., Bracken, A.P., Jensen, M.R., Lazzerini Denchi, E. and Helin, K. (2004) Suz12 is essential for mouse development and for EZH2 histone methyltransferase activity. *EMBO J*, **23**, 4061-4071.
9. Conway, E., Healy, E. and Bracken, A.P. (2015) PRC2 mediated H3K27 methylations in cellular identity and cancer. *Curr Opin Cell Biol*, **37**, 42-48.
10. Holoch, D. and Margueron, R. (2017) Mechanisms Regulating PRC2 Recruitment and Enzymatic Activity. *Trends Biochem Sci*, **42**, 531-542.
11. Lavarone, E., Barbieri, C.M. and Pasini, D. (2019) Dissecting the role of H3K27 acetylation and methylation in PRC2 mediated control of cellular identity. *Nat Commun*, **10**, 1679.
12. Dumesic, P.A., Homer, C.M., Moresco, J.J., Pack, L.R., Shanle, E.K., Coyle, S.M., Strahl, B.D., Fujimori, D.G., Yates, J.R., 3rd and Madhani, H.D. (2015) Product binding enforces the genomic specificity of a yeast polycomb repressive complex. *Cell*, **160**, 204-218.
13. Streubel, G., Watson, A., Jammula, S.G., Scelfo, A., Fitzpatrick, D.J., Oliviero, G., McCole, R., Conway, E., Glancy, E., Negri, G.L. *et al.* (2018) The H3K36me2 Methyltransferase Nsd1 Demarcates PRC2-Mediated H3K27me2 and H3K27me3 Domains in Embryonic Stem Cells. *Mol Cell*, **70**, 371-379 e375.

14. Chu, X., Qin, X., Xu, H., Li, L., Wang, Z., Li, F., Xie, X., Zhou, H., Shen, Y. and Long, J. (2013) Structural insights into Paf1 complex assembly and histone binding. *Nucleic Acids Res*, **41**, 10619-10629.
15. Xie, Y., Zheng, M., Chu, X., Chen, Y., Xu, H., Wang, J., Zhou, H. and Long, J. (2018) Paf1 and Ctr9 subcomplex formation is essential for Paf1 complex assembly and functional regulation. *Nat Commun*, **9**, 3795.
16. Zeng, H. and Xu, W. (2015) Ctr9, a key subunit of PAFc, affects global estrogen signaling and drives ERalpha-positive breast tumorigenesis. *Genes & development*, **29**, 2153-2167.
17. Arthur, A. and Gronthos, S. (2020) Clinical Application of Bone Marrow Mesenchymal Stem/Stromal Cells to Repair Skeletal Tissue. *Int J Mol Sci*, **21**.
18. Mabuchi, Y., Okawara, C., Mendez-Ferrer, S. and Akazawa, C. (2021) Cellular Heterogeneity of Mesenchymal Stem/Stromal Cells in the Bone Marrow. *Front Cell Dev Biol*, **9**, 689366.
19. Lin, G.L. and Hankenson, K.D. (2011) Integration of BMP, Wnt, and notch signaling pathways in osteoblast differentiation. *J Cell Biochem*, **112**, 3491-3501.
20. Rauch, A. and Mandrup, S. (2021) Transcriptional networks controlling stromal cell differentiation. *Nat Rev Mol Cell Biol*, **22**, 465-482.
21. Wei, Y., Chen, Y.H., Li, L.Y., Lang, J., Yeh, S.P., Shi, B., Yang, C.C., Yang, J.Y., Lin, C.Y., Lai, C.C. *et al.* (2011) CDK1-dependent phosphorylation of EZH2 suppresses methylation of H3K27 and promotes osteogenic differentiation of human mesenchymal stem cells. *Nat Cell Biol*, **13**, 87-94.
22. Dudakovic, A., Camilleri, E.T., Paradise, C.R., Samsonraj, R.M., Gluscevic, M., Paggi, C.A., Begun, D.L., Khani, F., Pichurin, O., Ahmed, F.S. *et al.* (2018) Enhancer of zeste homolog 2 (Ezh2) controls bone formation and cell cycle progression during osteogenesis in mice. *J Biol Chem*, **293**, 12894-12907.
23. Hemming, S., Cakouros, D., Isenmann, S., Cooper, L., Menicanin, D., Zannettino, A. and Gronthos, S. (2014) EZH2 and KDM6A act as an epigenetic switch to regulate mesenchymal stem cell lineage specification. *Stem Cells*, **32**, 802-815.
24. Wang, L., Jin, Q., Lee, J.E., Su, I.H. and Ge, K. (2010) Histone H3K27 methyltransferase Ezh2 represses Wnt genes to facilitate adipogenesis. *Proc Natl Acad Sci U S A*, **107**, 7317-7322.
25. Wyngaarden, L.A., Delgado-Olguin, P., Su, I.H., Bruneau, B.G. and Hopyan, S. (2011) Ezh2 regulates anteroposterior axis specification and proximodistal axis elongation in the developing limb. *Development*, **138**, 3759-3767.
26. Hemming, S., Cakouros, D., Codrington, J., Vandyke, K., Arthur, A., Zannettino, A. and Gronthos, S. (2017) EZH2 deletion in early mesenchyme compromises postnatal bone microarchitecture and structural integrity and accelerates remodeling. *FASEB J*, **31**, 1011-1027.
27. Miwa, H. and Era, T. (2018) Tracing the destiny of mesenchymal stem cells from embryo to adult bone marrow and white adipose tissue via Pdgfralpha expression. *Development*, **145**.
28. Muntean, A.G., Tan, J., Sitwala, K., Huang, Y., Bronstein, J., Connelly, J.A., Basrur, V., Elenitoba-Johnson, K.S. and Hess, J.L. (2010) The PAF complex synergizes with MLL fusion proteins at HOX loci to promote leukemogenesis. *Cancer Cell*, **17**, 609-621.

29. Zeytuni, N. and Zarivach, R. (2012) Structural and functional discussion of the tetra-trico-peptide repeat, a protein interaction module. *Structure*, **20**, 397-405.
30. Vos, S.M., Farnung, L., Boehning, M., Wigge, C., Linden, A., Urlaub, H. and Cramer, P. (2018) Structure of activated transcription complex Pol II-DSIF-PAF-SPT6. *Nature*, **560**, 607-612.
31. Colland, F., Jacq, X., Trouplin, V., Mougin, C., Groizeleau, C., Hamburger, A., Meil, A., Wojcik, J., Legrain, P. and Gauthier, J.M. (2004) Functional proteomics mapping of a human signaling pathway. *Genome Res*, **14**, 1324-1332.
32. Liu, Y. and Zhao, H. (2004) A computational approach for ordering signal transduction pathway components from genomics and proteomics Data. *BMC Bioinformatics*, **5**, 158.
33. Zeng, H., Lu, L., Chan, N.T., Horswill, M., Ahlquist, P., Zhong, X. and Xu, W. (2016) Systematic identification of Ctr9 regulome in ERalpha-positive breast cancer. *BMC Genomics*, **17**, 902.
34. Ma, G., Gao, A., Yang, Y., He, Y., Zhang, X., Zhang, B., Zhang, Z., Li, M., Fu, X., Zhao, D. *et al.* (2019) Zfhx3 is essential for progesterone/progesterone receptor signaling to drive ductal side-branching and alveologenesis in mouse mammary glands. *J Genet Genomics*, **46**, 119-131.
35. Bae, W.K., Yoo, K.H., Lee, J.S., Kim, Y., Chung, I.J., Park, M.H., Yoon, J.H., Furth, P.A. and Hennighausen, L. (2015) The methyltransferase EZH2 is not required for mammary cancer development, although high EZH2 and low H3K27me3 correlate with poor prognosis of ER-positive breast cancers. *Mol Carcinog*, **54**, 1172-1180.
36. Holm, K., Grabau, D., Lovgren, K., Aradottir, S., Gruvberger-Saal, S., Howlin, J., Saal, L.H., Ethier, S.P., Bendahl, P.O., Stal, O. *et al.* (2012) Global H3K27 trimethylation and EZH2 abundance in breast tumor subtypes. *Mol Oncol*, **6**, 494-506.
37. Hoy, S.M. (2020) Tazemetostat: First Approval. *Drugs*, **80**, 513-521.
38. Simeone, N., Frezza, A.M., Zaffaroni, N. and Stacchiotti, S. (2021) Tazemetostat for advanced epithelioid sarcoma: current status and future perspectives. *Future Oncol*, **17**, 1253-1263.
39. DeRose, Y.S., Wang, G., Lin, Y.C., Bernard, P.S., Buys, S.S., Ebbert, M.T., Factor, R., Matsen, C., Milash, B.A., Nelson, E. *et al.* (2011) Tumor grafts derived from women with breast cancer authentically reflect tumor pathology, growth, metastasis and disease outcomes. *Nature medicine*, **17**, 1514-1520.
40. Kawanami, A., Matsushita, T., Chan, Y.Y. and Murakami, S. (2009) Mice expressing GFP and CreER in osteochondro progenitor cells in the periosteum. *Biochem Biophys Res Commun*, **386**, 477-482.
41. Balic, A., Adams, D. and Mina, M. (2009) Prx1 and Prx2 cooperatively regulate the morphogenesis of the medial region of the mandibular process. *Dev Dyn*, **238**, 2599-2613.
42. Esposito, A., Wang, L., Li, T., Miranda, M. and Spagnoli, A. (2020) Role of Prx1-expressing skeletal cells and Prx1-expression in fracture repair. *Bone*, **139**, 115521.
43. Kovacs, C.S. (2014) Bone development and mineral homeostasis in the fetus and neonate: roles of the calciotropic and phosphotropic hormones. *Physiol Rev*, **94**, 1143-1218.

44. Verbruggen, S.W., Kainz, B., Shelmerdine, S.C., Hajnal, J.V., Rutherford, M.A., Arthurs, O.J., Phillips, A.T.M. and Nowlan, N.C. (2018) Stresses and strains on the human fetal skeleton during development. *J R Soc Interface*, **15**.
45. Wang, L., Mishina, Y. and Liu, F. (2015) Osterix-Cre transgene causes craniofacial bone development defect. *Calcif Tissue Int*, **96**, 129-137.
46. Chen, J., Shi, Y., Regan, J., Karuppaiah, K., Ornitz, D.M. and Long, F. (2014) Osx-Cre targets multiple cell types besides osteoblast lineage in postnatal mice. *PLoS One*, **9**, e85161.
47. Devlin, M.J. and Rosen, C.J. (2015) The bone-fat interface: basic and clinical implications of marrow adiposity. *Lancet Diabetes Endocrinol*, **3**, 141-147.
48. Sebo, Z.L., Rendina-Ruedy, E., Ables, G.P., Lindskog, D.M., Rodeheffer, M.S., Fazeli, P.K. and Horowitz, M.C. (2019) Bone Marrow Adiposity: Basic and Clinical Implications. *Endocr Rev*, **40**, 1187-1206.